

**OPTIMIZATION ON THE THERMOHYDRAULIC
CHARACTERISTICS OF HIGH TEMPERATURE
SUPERCONDUCTING CABLES USING ENTROPY
GENERATION MINIMIZATION APPROACH**

A Thesis

Submitted in partial fulfillment of the requirements for the
award of the degree of

DOCTOR OF PHILOSOPHY

in

Mechanical Engineering

By

Gadekula Rajesh Kumar

41700250

Supervised By

Dr. Raja Sekhar Dondapati



**LOVELY PROFESSIONAL UNIVERSITY
PUNJAB
2021**

DECLARATION

I declare that the thesis entitled "**Optimization on the Thermohydraulic characteristics of High Temperature Superconducting Cables using Entropy Generation Minimization Approach**" has been prepared by me under the guidance of **Dr. Raja Sekhar Dondapati**, Associate Professor, School of Mechanical Engineering, Lovely Professional University, Phagwara, Punjab. No part of this thesis has formed the basis for the award of any degree or fellowship previously.

Gadekula Rajesh Kumar

Registration No.41700250

School of Mechanical Engineering

Lovely Professional University

Phagwara, Punjab

Date:

CERTIFICATE

I certify that **Gadekula Rajesh Kumar** bearing Registration no. **41700250** has prepared his thesis entitled "**Optimization on the Thermohydraulic characteristics of High Temperature Superconducting Cables using Entropy Generation Minimization Approach**" for the award of PhD degree of Lovely Professional University, under my guidance. He has carried out the work at the School of Mechanical Engineering, Lovely Professional University.

Dr. Raja Sekhar Dondapati (17715)

Associate Professor

School of Mechanical Engineering

Lovely Professional University

Phagwara, Punjab

India

Date:

ABSTRACT

Turbulence flow is encountered in most of the thermal systems including heat exchangers. However, estimation of friction factors and heat transfer coefficients in turbulent flow regime is still a challenge. A numerous experiments have to be conducted in order to estimate the same. This challenge can be overcome with the help of numerical and computational techniques which are economic to be implemented. In recent years conventional power transmission systems are recommended to be replaced by superconducting power transmission systems with High Temperature Superconducting (HTS) cables. These cables have potential merits of large current carrying capacity and compactness with reduced transmission losses and Right-of-way (ROW) compared to conventional transmission power cables. However, internal forced convective cooling is used to cool HTS cables using cryogenic coolant such as liquid nitrogen (LN_2) to retain the superconductivity for efficient power transmission. However, flow of LN_2 in the corrugated steel pipe (former) of HTS cable is found to be turbulent. Hence, the present work aims at estimating pressure drop and heat transfer in turbulent flow regime using Computational Fluid Dynamics (CFD). Due to forced convective cooling, inevitable pressure drop will occur in these cables and result in development of temperature and velocity gradients. Further, the accounted temperature and velocity gradients in HTS cables lead to volumetric entropy generation.

The present work focuses at investigating the volumetric entropy generation rate in HTS cable. Further, entropy generation minimization (EGM) technique is used as an optimization tool to estimate the minimum volumetric entropy generation rate to optimize thermohydraulic characteristics in HTS cables. Furthermore, pumping power and cooling capacity at minimum entropy generation rate are calculated. Computational Fluid Dynamics (CFD) is used to analyze the pressure drop and heat transfer rate for different flow rates to estimate the friction factor, pumping power and cooling capacity with LN_2 flow in corrugated former in HTS cable. A 3D computational geometry is developed and simulated the flow domain of LN_2 in commercial ANSYS. K-epsilon turbulent scheme is used to signify the validity of turbulence model to practical experimental conditions. The simulated results are validated with the results available in literature.

Chapter 1 introduces the high temperature superconductivity, critical parameters of Superconductor, characteristics of Superconductor, cryogenics and applications of

superconductivity such as Superconducting cables, Superconducting motors, Superconducting generators, Superconducting Magnetic Energy Storage (SMES), Superconducting Transformers and Superconducting Fault Current Limiters (SFCL).

Chapter 2 begins with the exhaustive survey of available literature on the development of HTS cables, losses encountered by the HTS cables during normal operation. The implemented cooling strategies to compensate the heat loads due to the losses and the thermohydraulic characteristics in HTS cables. Further, a typical review on entropy generation rate in various engineering applications is presented. From the literature, research gaps are identified and research objectives are framed from the gaps.

Chapter 3 illustrates the mathematical formulation for solving the thermohydraulic characteristics and entropy generation rate in HTS Cables employing the governing equations such as conservation of mass, momentum and energy that are required for solving the closure problem. Further, the thermohydraulic characteristics and entropy generation rate for internally forced cooled HTS cables are computationally investigated using the time averaged Reynolds Averaged Navier-Stokes (RANS) equations. The Finite Volume Method of discretization with $\kappa - \varepsilon$ turbulence equations are used as closure to the RANS equations is discussed in this chapter.

Chapter 4 describes the hydraulic studies in HTS cables under the influence of mass flow inlet ranging from 11 L/min to 20 L/min, heat loads ranging from 1 W/m to 3 W/m and inlet temperature ranging from 65 K to 77 K. The pressure gradients, velocity gradients developed in the computational domain are predicted and results are utilized for estimating the entropy generation rate due to velocity gradients in the HTS cables. Further, the hydraulic characteristics such as Friction factor, pressure drop and pumping power are estimated at different flow rates, heat loads and inlet temperatures in this chapter.

Chapter 5 describes the thermal studies in HTS cables under the influence of mass flow inlet ranging from 11 L/min to 20 L/min, heat loads ranging from 1 W/m to 3 W/m and inlet temperature ranging from 65 K to 77 K. The temperature gradients and the temperature profile developed in the computational domain are predicted and results are utilized for estimating the entropy generation rate due to thermal gradients in the HTS cables. Further, the thermal characteristics such as Nusselt number, Temperature difference and cooling are estimated at different flow rates, heat loads and inlet temperatures in this chapter.

Chapter 6 includes the results of entropy generation rate in HTS cables under the influence of mass flow inlet ranging from 11 L/min to 20 L/min, heat loads ranging from 1 W/m to 3 W/m and inlet temperature ranging from 65 K to 77 K. The entropy generation rate due to velocity gradients and entropy generation rate due to thermal gradients developed in the computational domain are predicted and results are utilized for estimating the entropy generation rate in the HTS cables. Further, the entropy generation rate developed in the HTS cables are utilized for optimization at different flow rates, heat loads and inlet temperatures.

Chapter 7 deals investigations on entropy generation minimization in HTS cables under the influence of mass flow rates ranging from 11 L/min to 20 L/min, heat loads ranging from 1 W/m to 3 W/m and inlet temperatures ranging from 65 K to 77 K. The objective of the present work is to estimate the volumetric entropy generation rate for optimizing the thermohydraulic performance of HTS cable with higher heat transfer rate and lower pumping power. To achieve the objectives, hydraulic and thermal characteristics that are calculated in chapter 4 and chapter 5 are utilized along with the results of entropy generation rate discussed in chapter 6 for optimization.

Chapter 8 deals with the summary and conclusion of study such as thermohydraulic characteristics, entropy generation rate and entropy generation minimization results. Further, the future scope of the study is discussed.

Entropy generation minimization is the approach that signifies the optimum thermohydraulic performance of HTS cable for efficient operation under various heat loads, inlet temperature and flow rate. The hydraulic performance and the entropy generation rate due to velocity gradients at different heat loads are not significantly increased for various flow rates. From the performance evaluation, the maximum possible cooling capacity is observed at 14 L/min and 16 L/min at an AC loss of 1.5 W/m and 2.5 W/m respectively. Further, it is concluded that, at an operating condition of 77K and 2.7 bar with a heat of 2.1 W/m, flow rate of 14 L/min is optimum with lower pumping power and higher cooling capacity. Furthermore, the contribution to volumetric entropy generation rate from thermal gradients is higher than the velocity gradients in HTS cable. The present analysis will assist to select the flow rate that is required to overcome the quench of HTS tape under heat loads due to heat in leaks from ambient and AC losses in HTS cables. Since, the thermohydraulic performance is optimized, it helps in cooling the HTS cable with less pumping power and it is worth of minimizing the total entropy

generation. Further, recommends that the flow rate required for operating the HTS cable under various heat loads with minimum pumping power and higher cooling capacity.

ACKNOWLEDGEMENTS

The author has great privilege to express his immense sense of gratitude to **Dr. Raja Sekhar Dondapati**, Associate Professor and Research Coordinator, School of Mechanical Engineering, Lovely Professional University, Phagwara, for his valuable guidance and untiring efforts throughout the tenure of the work. He has been an inspiring force where targets appeared to be difficult during the course of work. His timely help, construction criticism and painstaking efforts made the author capable to compile the thesis in its present form.

It is a matter of great privilege and pride for me to express my sincere thanks and immense gratitude to **Mrs. Preeti Rao Usurumarti**, P.V.K.Institute of Technology, Ananthapur, Andhra Pradesh, who has supported me throughout my thesis with her patience, knowledge, valuable advice, uninterrupted active supervision and constant encouragement throughout the tenure of this work.

I am thankful to **Mr. Gaurav Vyas**, Assistant Professor, School of Mechanical Engineering, Lovely Professional University, Punjab who continuously motivated, clearing concepts and encouraged me to do this research work.

Deep sense of gratitude is expressed to authorities of Lovely Professional University, Phagwara, for permitting the author to pursue his research work and extending necessary facilities during the experimental and analysis work. I also express my sincere thanks to **Dr. Vijay Kumar Singh**, Head, School of Mechanical Engineering Lovely Professional University, Phagwara, for their cooperation and support.

I would like to thank my panel members who provided valuable suggestions during the course and all the staff members of School of Mechanical engineering who have been very patient and co-operative with us.

I would also like to extend my gratitude to friends **Mr. Rahul Agarwal** and **Mr. Venkata Ramana Uppada**, my senior **Mr. Mohit Kalisa** and my junior **Mr. Mohan Sukumar Tiruveedula** who always encouraged and supported me in this thesis work.

I would like to thank **Lovely Professional University** for giving me opportunity to use their resource and work in such a challenging environment. I am grateful to the individuals whom contributed their valuable time towards my thesis.

I humbly dedicate this work to my father **Mr. Gadekula Krishnaih**, my mother **Mrs. Gadekula Padmavathi** and my brother **Gadekula Naresh Kumar**, who are the source of inspiration and encouragement behind this research work. The author sincerely acknowledge the help extended by them during the tenure of this work by sacrificing their comforts and always supported me throughout all my studies at university and encouraged me with their best wishes.

About all, author is highly indebted to Great and Gracious almighty God who blessed me with spiritual support and courage at each and every stage of this work.

GADEKULA RAJESH KUMAR

NOMENCLATURE

\bar{e}_{ij}	Steady mean rate of deformation
e'_{ij}	Fluctuation component of rate of deformation
\bar{T}	Time averaged temperature (K)
$\bar{u}, \bar{v}, \bar{w}$	Time averaged components of velocity in x, y, z directions (m/s)
u, v, w	Components of velocity in x, y, z directions (m/s)
u'	Fluctuation in velocity (m/s)
ψ'	Fluctuation in flow property
Φ	Time averaged component of mean flow property
T_{ref}	Reference temperature (K)
k	Thermal Conductivity of LN ₂ (W/m-K)
h_c	Convective heat transfer coefficient (W/m ² K)
\bar{p}	Average pressure of LN ₂ (Pa)

Greek Symbols

ρ	Density of LN ₂ (kg/m ³)
κ	Turbulent kinetic energy (m ² /s ²), $\kappa = \overline{u'^2} / 2$
ε	Dissipation rate per unit mass (m ² /s ³), $\varepsilon = 2\nu\overline{e'_{ij}.e'_{ij}}$
μ	viscosity of LN ₂ (Pa-s)
φ	Viscous dissipation rate function
σ_k	Turbulent Kinetic Energy (TKE) Prandtl number
σ_ε	Turbulence Dissipation Rate (TDR) Prandtl number
μ_t	Turbulent viscosity (Pa-s), $\mu_t = \rho C_\mu (\kappa^2 / \varepsilon)$

ABBREVIATIONS

HTS	High Temperature Superconductor
T_c	Critical Temperature
I_c	Critical Current
J_c	Critical Current Density
H_c	Critical Magnetic Field
LTS	Low Temperature Superconductors
MTS	Medium Temperature Superconductors
PPLP	Poly Propylene Laminated Paper
XLPE	Cross Linked Polyethylene Paper
PVC	Poly Vinyl Chloride
P_c	Critical Pressure
LN_2	Liquid Nitrogen
CSP	Corrugated Steel Pipe
h_c	Convective Heat Transfer Coefficient
CFD	Computational Fluid Dynamics
SMES	Superconducting Magnetic Energy Storage
SFCL	Superconducting Fault Current Limiters
YBCO	Yttrium Barium Copper Oxide
BSCCO	Bismuth Strontium Calcium Copper Oxide
Be	Bejan Number (-)
EGR	Entropy Generation Rate (W/m^3K)
EGV	Entropy Generation Rate due to Velocity Gradients (W/m^3K)
EGT	Entropy Generation Rate due to Thermal Gradients (W/m^3K)
RANS	Reynolds Averaged Navier-Stokes
FVM	Finite Volume Method
TKE	Turbulence kinetic energy
TDR	Turbulence dissipation rate

TABLE OF CONTENTS

<i>DECLARATION</i>	<i>ii</i>
<i>CERTIFICATE</i>	<i>iii</i>
<i>ABSTRACT</i>	<i>iv</i>
<i>ACKNOWLEDGEMENTS</i>	<i>viii</i>
<i>NOMENCLATURE</i>	<i>x</i>
<i>ABBREVIATIONS</i>	<i>xi</i>
<i>TABLE OF CONTENTS</i>	<i>xii</i>
<i>LIST OF TABLES</i>	<i>xvi</i>
<i>LIST OF FIGURES</i>	<i>xvii</i>
CHAPTER I.....	1
1 INTRODUCTION.....	1
1.1 High Temperature Superconductivity.....	1
1.2 Cryogenics.....	5
1.3 Application.....	8
1.3.1 Superconducting Cables.....	8
1.3.2 Superconducting Motors and Superconducting Generators.....	10
1.3.3 Superconducting Magnetic Energy Storage (SMES).....	11
1.3.4 Superconducting Transformers.....	12
1.3.5 Superconducting Fault Current Limiters (SFCL).....	13
CHAPTER II.....	15
2 LITERATURE REVIEW.....	15
2.1 Introduction.....	15
2.2 Literature review on HTS Cables.....	15
2.2.1 Losses encountered by HTS cables.....	16

2.2.2	Thermohydraulic characteristics	33
2.3	Literature review on Entropy generation rate	39
2.3.1	Fusion grade magnets	41
2.3.2	Micro channels	41
2.3.3	Heat Exchangers.....	42
2.3.4	Refrigeration.....	43
2.3.5	Storage applications.....	43
2.3.6	Power plants.....	44
2.3.7	Solar and nano fluid applications	44
2.4	Recent studies on HTS cables and Entropy generation rate	45
2.5	Research gaps	51
2.6	Objectives of the present work.....	52
CHAPTER III.....		53
3	MATHEMATICAL FORMULATION	53
3.1	Introduction	53
3.2	General conservation equations.....	53
3.2.1	Conservation of mass.....	54
3.2.2	Conservation of momentum.....	55
3.2.3	Conservation of energy	57
3.2.4	Generalized entropy generation equation for fluid flow.....	60
3.3	Flow through HTS cables	61
3.4	Boundary conditions.....	65
3.4.1	Temperature dependent thermophysical properties.....	67
3.5	Closure problem	70
3.6	Solution procedure.....	72
3.6.1	Thermohydraulic characteristics	94
3.6.2	Volumetric entropy generation rate.....	96

3.7	Grid independence study	97
CHAPTER IV		99
4	HYDRAULIC CHARACTERISTICS OF HTS CABLES.....	99
4.1	Introduction.....	99
4.2	Validation	100
4.3	Velocity profiles.....	102
4.4	Velocity gradients	104
4.4.1	Axial Velocity gradients.....	104
4.4.2	Radial velocity gradients	107
4.5	Pressure gradients.....	108
4.5.1	Axial Pressure gradients	109
4.5.2	Radial Pressure gradients.....	110
4.6	Friction factor.....	112
4.7	Pressure drop.....	113
4.8	Pumping power	115
CHAPTER V.....		117
5	THERMAL CHARACTERISTICS OF HTS CABLES.....	117
5.1	Introduction.....	117
5.2	Temperature profile.....	118
5.3	Temperature gradients	120
5.3.1	Axial temperature gradients.....	120
5.3.2	Radial temperature gradients	122
5.4	Temperature difference	124
5.5	Nusselt number	125
5.6	Cooling capacity.....	126
CHAPTER VI		129
6	ENTROPY GENERATION RATE IN HTS CABLES.....	129

6.1	Introduction	129
6.2	Volumetric entropy generation rate due to velocity gradients	130
6.3	Volumetric entropy generation rate due to thermal gradients.....	136
6.4	Bejan Number.....	140
CHAPTER VII		145
7 ENTROPY GENERATION MINIMIZATION IN HTS CABLES		145
7.1	Introduction	145
7.2	Entropy Generation Minimization.....	147
CHAPTER VIII		159
8	SUMMARY AND CONCLUSIONS	159
9	REFERENCES	163
10	PUBLICATIONS FROM PRESENT WORK.....	185
11	VITAE	187

LIST OF TABLES

Table 1.1 Classification of superconductors depends on critical temperatures [1].....	5
Table 1.2 Cryogenic coolants used in Superconductivity applications and their Critical Temperatures and Critical Pressures	7
Table 2.1 HTS cable projects and their specifications in different countries.....	16
Table 2.2 Summary of various investigations on different components of AC losses in HTS cables	21
Table 2.3 Summary of various investigations on AC losses in different HTS cables	22
Table 2.4 Different geometries and expressions for perpendicular magnetic field	27
Table 2.5 Recent studies on AC losses by various researchers	29
Table 2.6 Thermohydraulic analysis summaries on HTS cables.....	35
Table 2.7 Summary of studies on thermohydraulic characteristics of HTS cables	36
Table 2.8 Recent studies on thermohydraulic characteristics, issues encountered by HTS cable during operation and entropy generation rate in superconducting applications	45
Table 3.1 Boundary conditions imposed on the computational domain for analyzing different cases	66
Table 3.2 Analytical functions and their coefficients for density of LN ₂ at different operating temperature used in analysis.....	67
Table 3.3 Analytical functions and their coefficients for specific heat of LN ₂ at different operating temperature used in analysis.....	68
Table 3.4 Analytical functions and their coefficients for thermal conductivity of LN ₂ at different operating temperature used in analysis	69
Table 3.5 Analytical functions and their coefficients for viscosity of LN ₂ at different operating temperature used in analysis.....	69
Table 3.6 Different mesh topologies used for grid independent study	98
Table 7.1 Optimum flow rate at different inlet temperatures and heat loads with minimum entropy generation rate of the HTS cables.....	157

LIST OF FIGURES

Figure 1.1 Comparison between resistance v/s temperature curves of a superconductor and a normal conductor	1
Figure 1.2 Critical parameters of a superconductor.....	2
Figure 1.3 Characteristics of a superconductor and perfect conductor in the presence of an external magnetic field.....	3
Figure 1.4 (a-c) Types of superconducting wires and tapes.....	4
Figure 1.5 Operating temperature and pressure range of Nitrogen to be utilized as liquid cryogen for cooling superconducting cables.....	7
Figure 1.6 Schematic representation of the configurations of HTS cable: (a) warm dielectric and (b) cold dielectric cables.....	9
Figure 1.7 Configuration of a typical synchronous machine employing superconducting field winding on the rotor.....	10
Figure 1.8 Superconducting Magnetic Energy Storage (SMES).....	11
Figure 1.9. Liquid cooling system by natural convection for a superconducting transformer	12
Figure 1.10 Design of SFCL	13
Figure 1.11 V-I characteristics of a normal conductor and a superconductor	14
Figure 2.1 Geometrical arrangement of twisted HTS tapes in HTS cable.....	18
Figure 2.2 Operating range of HTS cable with boiling curve of Liquid Nitrogen (LN ₂)....	33
Figure 2.3 Entropy generation analysis as an optimum tool used in various applications of engineering systems.....	40
Figure 2.4 (a) Schematic of HTS cooling system with LN ₂ as cryogenic coolant (b) HTS cable configuration employed for estimating entropy generation rate and thermohydraulic performance.....	50
Figure 3.1 Control volume considered in the flow field.....	53
Figure 3.2 HTS cable geometry with imposed boundary conditions	66
Figure 3.3 Temperature dependent thermophysical properties of LN ₂ at 77K and 2.7 bar ..	67
Figure 3.4 Selection of modules in the ANSYS workbench.....	73
Figure 3.5 Selection of geometric entities and dimensioning the computational domain ...	73
Figure 3.6 Selection of pattern command for modeling the computational domain	74
Figure 3.7 Selection of linear pattern for modeling the geometry of computational domain	74

Figure 3.8 Selection of mesh with sizing option for generating the mesh	75
Figure 3.9 Final meshed geometry and its statistics for grid independence study.....	75
Figure 3.10 Reading case and data of the final meshed geometry from design modular to Fluent.....	76
Figure 3.11 Activating the energy equation in models to solve conservation of energy equation.....	76
Figure 3.12 Selection of viscous model for solving the turbulence flow in the computational domain	77
Figure 3.13 Defining temperature dependent thermophysical properties of LN ₂	77
Figure 3.14 Selection of Stainless steel material for corrugated former	78
Figure 3.15 Defining the cell zone condition to fluid with operating pressure of 2.7 bar ..	78
Figure 3.16 Defining the inlet boundary condition.....	79
Figure 3.17 Specifying the inlet boundary condition with flow rate of LN ₂ in momentum	79
Figure 3.18 Defining the flow direction with normal to boundary	80
Figure 3.19 Specifying the turbulence specification method with intensity and hydraulic diameter	80
Figure 3.20 Defining the inlet boundary condition with inlet temperature (reference temperature) of 77 K	81
Figure 3.21 Defining the outlet boundary condition.....	81
Figure 3.22 Defining the wall with wall boundary condition.....	82
Figure 3.23 Specifying the wall zone with stationary wall and no slip boundary condition	82
Figure 3.24 Defining the wall boundary condition with uniform heat flux	83
Figure 3.25 Specifying the Pressure-Velocity coupling with SIMPLE scheme.....	83
Figure 3.26 Selection of least square cell based gradients in solution discretization	84
Figure 3.27 Selection of second order pressure discretization	86
Figure 3.28 Selection of second order upwind for momentum discretization.....	86
Figure 3.29 Selection of first order upwind for turbulent kinetic energy in solution discretization.....	87
Figure 3.30 Selection of first order upwind for turbulent dissipation rate in solution discretization.....	87
Figure 3.31 Selection of second order upwind for energy in solution discretization.....	88
Figure 3.32 Initializing the solution with standard initialization and computing from the inlet.....	88

Figure 3.33 Selecting the custom field functions	89
Figure 3.34 Defining the custom field functions for volumetric entropy generation rate ...	89
Figure 3.35 Retrieving the surface heat transfer coefficient contours to observe the heat load distribution in the computational domain.....	90
Figure 3.36 Retrieving the total temperature contours to observe temperature distribution in the computational domain	90
Figure 3.37 Retrieving the heat transfer rate from the wall of the computational domain..	91
Figure 3.38 Retrieving the shear stresses in the computational domain.....	91
Figure 3.39 Retrieving the surface Nusselt number in the computational domain	92
Figure 3.40 Retrieving the total temperature at the inlet and outlet of the computational domain.....	92
Figure 3.41 Retrieving the volumetric entropy generation rate in the computational domain	93
Figure 3.42 Retrieving the bulk temperature of LN ₂ in the computational domain.....	93
Figure 3.43 Flow chart of the methodology used for the analysis	95
Figure 3.44 Velocity profiles at the outlet of the corrugated pipe in HTS cables for different mesh sizes	97
Figure 4.1 Geometry of HTS cable and schematic of corrugated former used for computational analysis with boundary conditions.....	99
Figure 4.2 Validation of present CFD study at different heat loads (a) friction factor versus Reynolds number with simulation results of Gadekula et al. [298] and experiemental results of Ivanov et al. [290] (b) Temperature difference versus flow rate with the simulation results of Gadekula et al. [298] and Kalsia et al. [280]	101
Figure 4.3 Validation of Computational results with the experimental results of Ivanov et al. [290]	101
Figure 4.4 Velocity profiles at various flow rates in HTS cable with a heat load of 2.1 W/m (a) center (b) outlet	102
Figure 4.5 Velocity profiles at various heat loads in corrugated steel former with a flow rate of 19 LPM (a) center (b) outlet.....	103
Figure 4.6 Radial velocity distribution at a distance of z = 0.5 m in the HTS cable (a) for different heat loads at a flow rate of 14 L/min (b) for different flow rates at a heat load of 2 W/m.....	103

Figure 4.7 Radial velocity distribution at a distance of $z = 1$ m in the HTS cable (a) for different heat loads at a flow rate of 14 L/min (b) for different flow rates at a heat load of 2 W/m	104
Figure 4.8 Axial velocity gradients for different flow rates at heat load of 2.1 W/m in (a) x-direction (b) y-direction (c) z-direction	105
Figure 4.9 Transverse axial velocity gradients at different mass flow rates at a heat flux of 2.1 W/m (a-b) x-direction (c-d) y-direction (e-f) z-direction	106
Figure 4.10 Radial Velocity gradients at the flow rate of 14 L/min in (a) x-direction (b) y-direction (c) z-direction	107
Figure 4.11 Transverse radial velocity gradients at a flow rate of 14 L/min and a heat load of 2.1 W/m (a-b) x-direction (c-d) y-direction (e-f) z-direction	108
Figure 4.12 Axial pressure gradient in x-direction for different flow rates at heat load of 2.1 W/m	109
Figure 4.13 Axial pressure gradient in y-direction for different flow rates at heat load of 2.1 W/m	109
Figure 4.14 Axial pressure gradient in z-direction for different flow rates at heat load of 2.1 W/m	110
Figure 4.15 Radial pressure gradient in x-direction for different flow rates at heat load of 2.1 W/m	111
Figure 4.16 Radial pressure gradient in y-direction for different flow rates at heat load of 2.1 W/m	111
Figure 4.17 Radial pressure gradient in z-direction for different flow rates at heat load of 2.1 W/m	112
Figure 4.18 Friction factor versus Reynolds number at different heat loads.....	112
Figure 4.19 Friction Factor versus Reynolds Number at various inlet temperatures.....	113
Figure 4.20 Variation of pressure drop with respect to flow rate for different heat loads	114
Figure 4.21 Pressure drop along the HTS cable at various flow rates and inlet temperatures	114
Figure 4.22 Pumping power versus flow rate for various Heat loads	115
Figure 4.23 Pumping power versus flow rate for various inlet temperatures.....	116
Figure 5.1 High Temperature Superconducting (HTS) cable configuration with heat loads employed for thermal characteristic analysis.....	117

Figure 5.2 Radial temperature distribution at a distance of $z = 0.5$ m in the HTS cable (a) for different heat loads at a flow rate of 14 L/min (b) for different flow rates at a heat load of 2 W/m.....	118
Figure 5.3 Radial temperature distribution at a distance of $z = 1$ m in the HTS cable (a) for different heat loads at a flow rate of 14 L/min (b) for different flow rates at a heat load of 2 W/m.....	119
Figure 5.4 Axial temperature gradient in x-direction for different flow rates at heat load of 2.1 W/m.....	120
Figure 5.5 Axial temperature gradient in y-direction for different flow rates at heat load of 2.1 W/m.....	121
Figure 5.6 Axial temperature gradient in z-direction for different flow rates at heat load of 2.1 W/m.....	121
Figure 5.7 Radial temperature gradient in x-direction for different flow rates at heat load of 2.1 W/m.....	122
Figure 5.8 Radial temperature gradient in y-direction for different flow rates at heat load of 2.1 W/m.....	123
Figure 5.9 Radial temperature gradient in z-direction for different flow rates at heat load of 2.1 W/m.....	123
Figure 5.10 Temperature difference between the outlet and inlet of HTS cable for different Heat loads and mass flow rates at inlet temperature of 77 K.....	124
Figure 5.11 Temperature difference between the outlet and inlet of HTS cable for different inlet temperatures and mass flow rates at heat load of 2.5 W/m.....	125
Figure 5.12 Nusselt Number versus Reynolds Number at different heat loads	125
Figure 5.13 Nusselt Number versus Reynolds Number at different inlet temperatures	126
Figure 5.14 Cooling capacities versus flow rate for different Heat loads.....	127
Figure 5.15 Cooling capacities versus flow rate for different inlet temperatures	127
Figure 6.1 Schematic of HTS cable and computational domain used for estimating the entropy generation rate.....	129
Figure 6.2 Entropy generation due to velocity gradients for different flow rates (a) at the center and (b) at the outlet at a heat load of 2.1 W/m.....	131
Figure 6.3 Entropy generation due to velocity gradients for different heat loads at a flow rate of 19 L/min (a) at the center and (b) at the outlet	132
Figure 6.4 Entropy generation rate due to velocity gradients for different flow rates and heat loads.....	133

Figure 6.5 Entropy generation rate due to velocity gradients at a distance of $z = 1\text{m}$ in the HTS cable (a) for different heat loads at a flow rate of 14 L/min (b) for different flow rates at a heat load of 2 W/m.....	134
Figure 6.6 Volumetric entropy generation rate due to velocity gradients for various heat loads and different flow rates in HTS cable	134
Figure 6.7 Entropy generation rate due to velocity gradients for different flow rates and inlet temperature.....	135
Figure 6.8 Entropy generation due to thermal gradients for different flow rates at a heat load of 2.1 W/m (a) at the center and (b) at the outlet.....	136
Figure 6.9 Entropy generation due to thermal gradients for different heat loads at a flow rate of 19 LPM (a) at the center and (b) at the outlet	137
Figure 6.10 Entropy generation rate due to thermal gradients for different flow rates and heat loads	138
Figure 6.11 Entropy generation rate due to thermal gradients at a distance of $z = 1\text{m}$ in the HTS cable (a) for different heat loads at a flow rate of 14 L/min (b) for different flow rates at a heat load of 2 W/m.....	139
Figure 6.12 Entropy generation rate due to thermal gradients for various heat loads and different flow rates	139
Figure 6.13 Entropy generation rate due to thermal gradients for different flow rates and inlet temperatures	140
Figure 6.14 Bejan number contours at the inlet, center and outlet for flow rate of 14 L/min and heat load of 2.1W/m.....	141
Figure 6.15 Bejan number for different flow rates (a) at the center and (b) at the outlet at a heat load of 2.1 W/m	141
Figure 6.16 Bejan number for different heat loads at a flow rate of 19 L/min at center...	142
Figure 6.17 Bejan number for different heat loads and flow rates at an inlet temperature of 77K	142
Figure 6.18 Bejan number versus Reynolds number at different heat loads	143
Figure 6.19 Bejan number for different flow rates and inlet temperatures at a heat load of 2.5 W/m	144
Figure 7.1 Entropy generation analysis (EGA) interdisciplinary fields.....	146
Figure 7.2 Entropy generation due to velocity gradients, Entropy generation due to thermal gradients and Total Entropy Generation, for different flow rates at a heat load of 2.1 W/m	148

Figure 7.3 Total Entropy Generation, pumping power and cooling capacity for different flow rates at a heat load of 2.1 W/m	149
Figure 7.4 Total entropy generation rate for various heat loads and flow rates.....	149
Figure 7.5 Total entropy generation rate at a flow rate of 16 L/min for different inlet temperatures and heat loads	150
Figure 7.6 Total entropy generation rate at a heat load of 2.5 W/m for different inlet temperatures and flow rates.....	150
Figure 7.7 Total entropy generation rate for various heat loads and different flow rates in HTS cable.....	151
Figure 7.8 Total entropy generation rate for various inlet temperatures and flow rates....	152
Figure 7.9 Entropy generation rate due to velocity gradients, Entropy generation rate due to thermal gradients and Total Entropy Generation rate, for different flow rates at an inlet temperature of 65 K	153
Figure 7.10 Entropy generation rate due to velocity gradients, Entropy generation rate due to thermal gradients and Total Entropy Generation rate, for different flow rates at an inlet temperature of 69 K	153
Figure 7.11 Entropy generation rate due to velocity gradients, Entropy generation rate due to thermal gradients and Total Entropy Generation rate, for different flow rates at an inlet temperature of 73 K	154
Figure 7.12 Entropy generation rate due to velocity gradients, Entropy generation rate due to thermal gradients and Total Entropy Generation rate, for different flow rates at an inlet temperature of 77 K	155
Figure 7.13 Total Entropy Generation, pumping power and cooling capacity for different flow rates at a heat load of 2.5 W/m and inlet temperature of 65 K.....	155
Figure 7.14 Total Entropy Generation, pumping power and cooling capacity for different flow rates at a heat load of 2.5 W/m and inlet temperature of 69 K.....	156
Figure 7.15 Total Entropy Generation, pumping power and cooling capacity for different flow rates at a heat load of 2.5 W/m and inlet temperature of 73 K.....	156
Figure 7.16 Total Entropy Generation, pumping power and cooling capacity for different flow rates at a heat load of 2.5 W/m and inlet temperature of 77 K.....	158

CHAPTER I

1 INTRODUCTION

1.1 High Temperature Superconductivity

In the early 1900s, soon after the method of liquefaction of helium by Kamerlingh Onnes, further investigation concerning the electrical resistance of pure metals at low temperature initiated. At that instance, the electric resistance characteristic at low temperature was unexplored and unknown. The existing prediction ranged from the continuous linear decrease of electrical resistance towards, leveling at some residual resistance value, or an increase at some point due to electron scattering mechanisms.

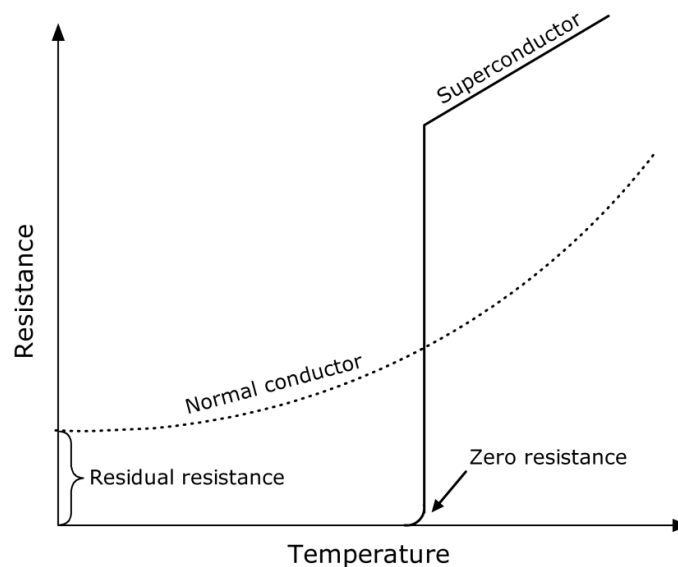


Figure 1.1 Comparison between resistance v/s temperature curves of a superconductor and a normal conductor

At that time, one of the purest metals available was Mercury. Kamerlingh Onnes, in 1911, measured the electrical resistance of pure mercury as a function of temperature and discovered that the mercury's resistance abruptly drops to zero below 4 K (operating temperature of liquid helium). A new realization came that below 4 K, mercury enters a new state, which he called "superconductivity". Such remarkable and fascinating features had not been predicted, which still intrigues today. Since then, many materials were subsequently discovered in order to show the phenomenon of superconductivity at low temperature. Since then, a vast categorical device, which takes majority of the field of

physics, is in the continuous state of development. A typical dependence of resistance on the temperature of a superconductor and a normal conductor is shown in Figure 1.1.

The resistance of a superconductor drops to zero when the temperature reduces to a certain value below the critical temperature (T_c), which is due to the non-scattering by crystal lattice, resulting in no dissipation of energy when operating with DC. However, for a normal conductor upon decreasing temperature, some resistance in the material is observed. There are three fundamental parameters, namely, critical temperature T_c , critical external magnetic field H_c , and critical current density J_c , as shown in Figure 1.2. These three are the most important parameters which define the state of superconductivity in a superconductor.

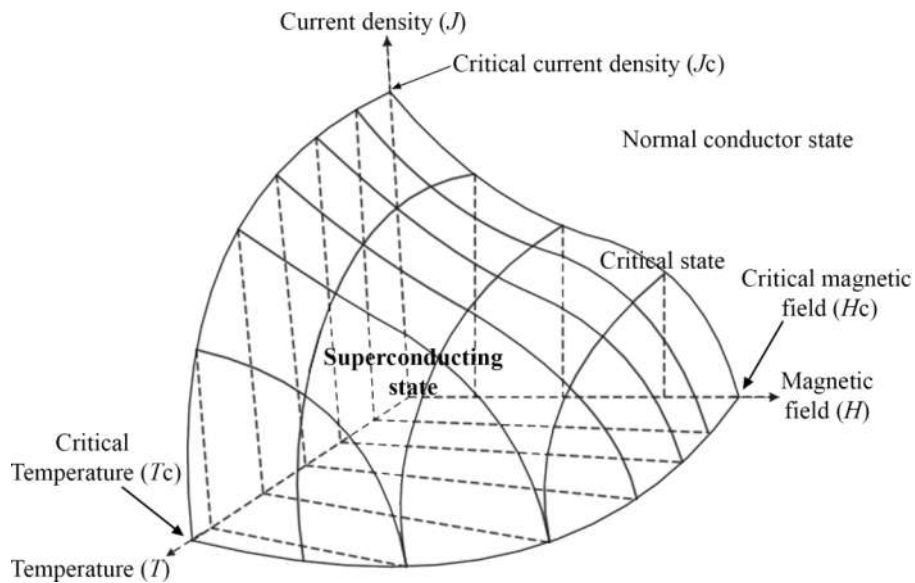


Figure 1.2 Critical parameters of a superconductor

The development of superconductors in large scale made a revolutionary changes in superconducting power applications such as Superconducting cables, SMES, superconducting motors, superconducting generators, superconducting transformer and superconducting fault current limiters. The superconductors are premium than normal conductors because they exhibit zero resistivity and handles higher current density at lower volumes. The superconductors are manufactured either in wire or tape using different superconducting materials. The superconducting wires are manufactured using a thin superconducting material enclosed within Aluminum, Copper, Silver alloy matrix to enhance the strength and to protect the wire from quench. The parameters such as critical magnetic field (B_c), critical temperature (T_c) and critical current density (J_c)

characterize the superconducting material. At cryogenic temperatures, there is a direct dependency within these three parameters to achieve higher magnetic field and higher current densities.

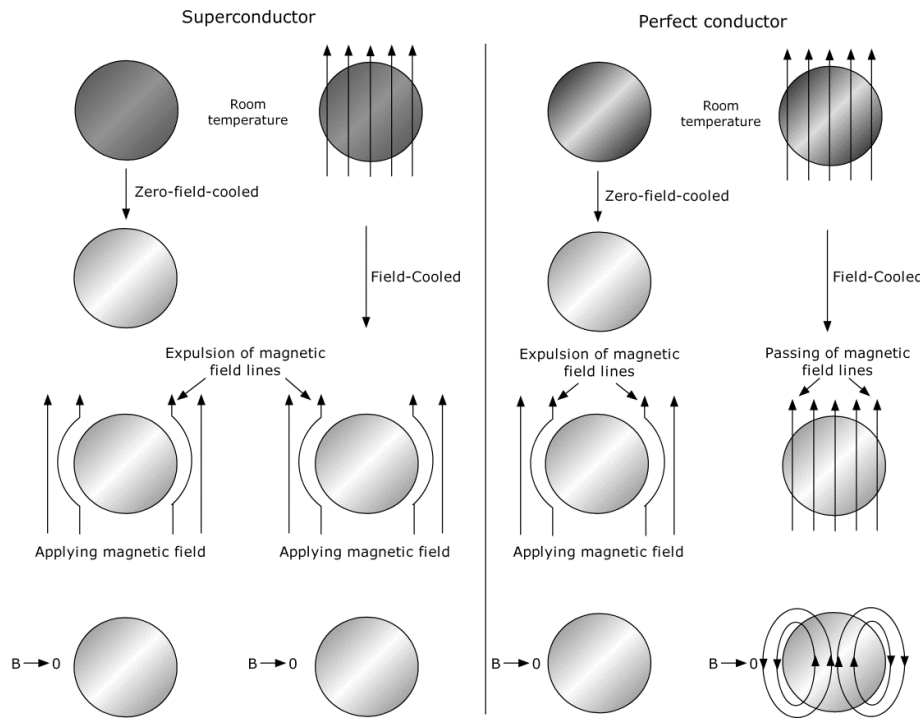


Figure 1.3 Characteristics of a superconductor and perfect conductor in the presence of an external magnetic field

For instance, for SMES higher magnetic fields are required to achieve higher storage capacities, consequently the critical current density and the critical temperature are changed accordingly. The SMES are operated at the temperature of 4.5 K, even the critical temperatures of different superconductors are higher than 20 K (See Table 1.1).

In 1933, Meissner and Ochsenfeld began an investigation on Type I superconductors. They discovered that on cooling a superconductor below its superconducting transition temperature, placed in an applied steady-state magnet field, the magnetic field lines were completely expelled from the interior of the superconductor. This phenomenon is called Meissner effect. Such behavior is possible under magnetization in the opposite sense ($M = -H$); a perfect diamagnetism is exhibited. Such type of magnetization measurement is sometimes referred to as the field-cooled (FC) experiment and is schematically shown in Figure 1.3 (left). However, this characteristic is far different from a zero-field-cooled (ZFC) experiment and cannot be simply explained by assuming that a superconductor is a

perfect conductor (infinite mean free path). Instead, the Meissner effect implies that the flux density inside the material is zero ($B = 0$) for temperature below its critical transition temperature (T_c). If the superconductor would simply be a perfect conductor with infinite conductivity ($\sigma = \infty$) and was cooled below T_c in the presence of a steady-state magnetic field (H), there would be no magnet flux expulsion ($B = 0$) at T_c . Such a perfect conductor cooled in the background steady-state magnet field would simply pass through it. If the perfect conductor was cooled in a zero magnetic field, upon subsequently applying the magnetic field, the perfect conductor would repel flux. The whole process is illustrated in Figure 1.3. Hence, perfect diamagnetism under FC magnetization is the true signature of superconductivity.

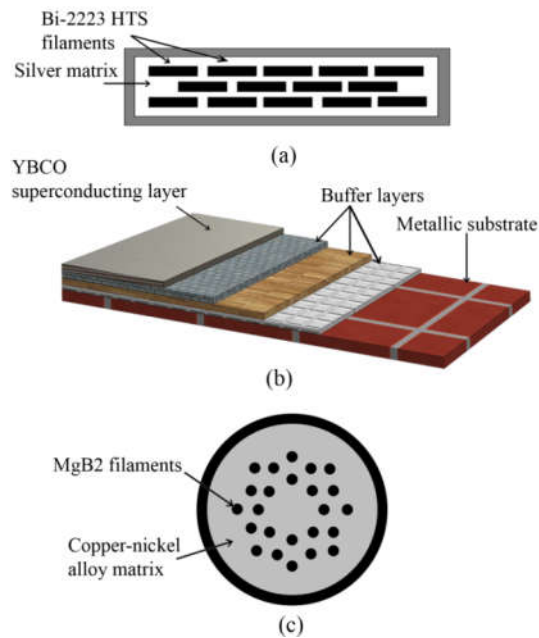


Figure 1.4 (a-c) Types of superconducting wires and tapes

Similarly in HTS cable applications, higher current densities are required. Consequently the critical magnetic field and the critical temperature are changed accordingly. The HTS cables are operated at operating range of 65-77K depends on the type of superconducting material used. The cryogenic coolants to be used for cooling the superconductors are made up of different materials with respect to critical temperature range is given in Table 1.1.

The superconductors are classified into two categories depends on the behavior of superconductor in the magnetic field at critical temperature and the critical temperature of the superconducting material. Based on the magnetic field, superconductors are either Type I or Type II. In Type I, superconductors acts as a perfect diamagnetic and repels the

magnetic field when it maintained below critical temperature and unable to sustain higher magnetic fields. In Type II, superconductors exhibit a mixed state around the critical temperature and can sustain higher magnetic fields without exhibiting the quench behavior. The superconducting materials used in different projects based on the operating temperature are shown in Figure 1.4.

Table 1.1 Classification of superconductors depends on critical temperatures [1]

Superconducting material	Superconductors (Critical temperature (K))	Cryogenic coolant (Boiling temperature (K) @ 1 atm)	Critical temperature of coolant (K)	Critical Pressure of coolant (K)	Latent heat of vaporization (kJ/kg)
LTS	NbTi (9.8)	Helium (4.2)	5.2	2.3	21
	Nb ₃ Al (18)				
	Nb ₃ Sn (18.1)	Hydrogen (20.3)	32.9	12.8	445
MTS	MgB ₂ (39)	Hydrogen (20.3)	32.9	12.8	445
		Neon (27.1)	44.4	26.5	86
HTS	BSCCO-2212 (85)	Nitrogen (77.3)	126.3	34	199
	BSCCO-2223 (110)	Argon (87.302)	150.69	48.630	163
	YBCO (93)	Oxygen (90.2)	154.6	50.4	213

1.2 Cryogenics

The word cryogenics is defined as the study of low-temperature phenomena. However, the temperature level at which refrigeration in the conventional sense ends and cryogenics begins is somewhat arbitrary. The temperature separating cryogenics from conventional refrigeration that is suggested by the workers at the National Institute for Standards and Technology in Boulder, Colorado, is -150°C (123 K). The significance of heat transfer in cryogenic systems is illustrated by a variety of its applications. Some applications are discussed as follows

- 1) For land-based service design of Cryogenic fluid storage vessels (Dewars), the rate of heat transfer through the insulation must be as low as practical. In order to minimize the gaseous conduction, cryogenic insulations are generally evacuated. Moreover, multi-layer insulation (MLI) is used to minimize radiation heat transfer, and low thermal conductivity spacers are used to minimize conduction through solids. In addition, the suspension system utilized for providing support to the inner vessel within the outer vessel must minimize the heat conducted through support.

Hence, for vessel suspension purpose, high-strength stainless steel rods are often used due to its low thermal conductivity.

- 2) In Superconducting Magnetic Energy Storage Systems (SMES), conduction heat transfer along the current leads into the superconducting magnetic energy systems may be detrimental for the operation of magnet refrigeration system due to the associated thermal load.
- 3) In the late 1960's marked the commercial development of superconducting electrical cables, which was made possible after the Nb-Ti and Nb₃Sn alloys became available in large-scale lengths. Cables that are constructed from LTS were cooled to a temperature on the order of 4 K using LHe. However, the accompanied heat transfer caused extensive evaporation of LHe. Such a problem is solved by shielding helium circuits with LN₂-cooled thermal shields.
- 4) In an air separation system involving the production of LN₂, liquid oxygen (LOX), and liquid argon (LAr), high-performance heat exchangers are required. For the economical operation of these heat exchangers, the effectiveness must be approximately 95% or higher. Moreover, recuperative heat exchangers allow the incoming warm air stream to be cooled by the outgoing cold gas stream, thereby reducing the need for external refrigeration.
- 5) The duration of aerospace missions may be as long as five years. Therefore, thermal protection for cooling instrumentation carrying any refrigerant liquid, such as LHe, must be provided. Such protection can be achieved by thermal shields, which are actively cooled by Stirling cycle refrigerators or thermoelectric coolers for maintaining an extremely low heat transfer rate to the coolant, thereby ensuring adequate mission duration.
- 6) Cryosurgery systems: All practical surgical specialties, such as gynecological surgery, ophthalmological surgery, and neurosurgery, involve freezing a small region of the defective tissue for destroying the offending material. For such devices that involve the cooling process by either cryogens or small cryocoolers, thermal analysis of the tissue is of critical importance in order to predict the extent of the frozen lesion.

In Superconductivity applications, Cryogenics plays a vital role in order to retain the superconductivity by cooling the superconductors below to its critical temperatures based on the superconducting material. Table 1.2 provides the data of critical pressure and

critical temperatures of various cryogenic coolants that are used in Superconductivity applications. Although conduction cooling had been attempted in the past, the recent developments are focused on the circulation of LN₂. The usage of other cryogenes, such as helium, hydrogen, neon, and oxygen, is ruled out due to considerations of cost, safety, and temperature range. A circulated LN₂ provides consistent temperature distribution, along with rapid recovery from fault and the benefit of liquid dielectric.

Table 1.2 Cryogenic coolants used in Superconductivity applications and their Critical Temperatures and Critical Pressures

Cryogenes	Critical Temperature (K)	Critical Pressure (bar)
Helium (He)	5.1953	2.2746
Hydrogen (H)	33.190	30.118
Nitrogen (N)	126.19	33.958
Argon (Ar)	150.69	48.630
Oxygen (O ₂)	154.58	50.430

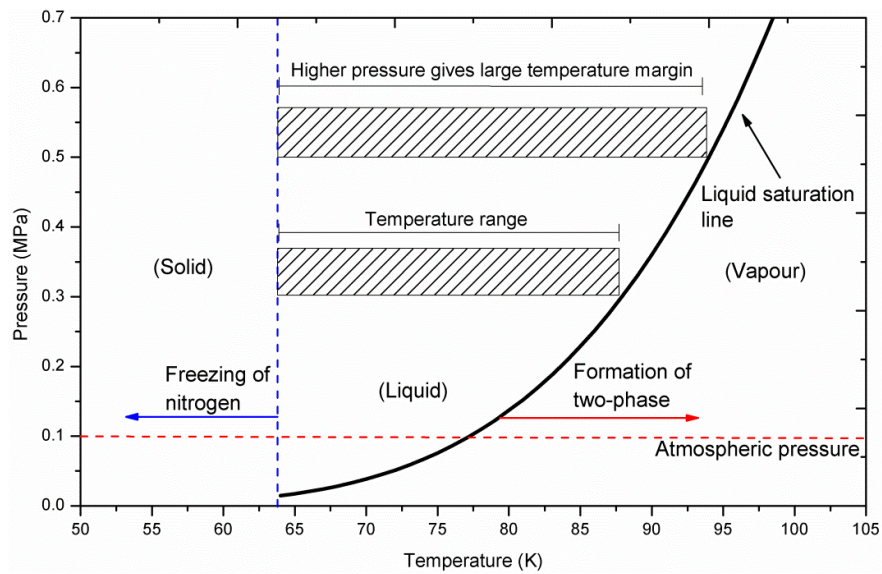


Figure 1.5 Operating temperature and pressure range of Nitrogen to be utilized as liquid cryogen for cooling superconducting cables

Various conceptual designs, such as configurations involving pumping mechanism or circulation using thermo-syphon as well as bath cooling, have been demonstrated. Moreover, LN₂ offers dielectric performance compared to that of oil in a conventional transformer. However, at atmospheric pressure, the operating temperature margin of LN₂ is

narrow (63–77 K). Hence, to prevent the formation of gaseous phase, thereby preserving the dielectric properties, it is desirable to maintain liquid nitrogen in a sub cooled state in high-voltage regions. Further, the cryogen must be pressurized to further increase the boiling point. Furthermore, the preferable cryogen utilized for cooling superconductors to be utilized for power transmission is Liquid Nitrogen and its operating pressure and temperature range is depicted in Figure 1.5.

1.3 Application

In this section, various applications employing High Temperature Superconductors (HTS) are summarized. These applications include cables, motors, generators, SMES, Transformers and SFCL.

1.3.1 Superconducting Cables

The HTS cables are classified into four different categories and a brief description on HTS cables is discussed in this section

- a) Based on electrical insulation – warm and cold dielectric cables
- b) Based on HTS conductors used – First generation (BSCCO) and Second generation (YBCO) cables
- c) Based on the design – Co-axial, tri-axial and concentric cables
- d) Based on power transmission – AC and DC HTS cables

Presently, in various worldwide projects the commercial HTS cables are constructed by using rare earth materials such as YBCO and BSCCO for efficient power transmission. The current carrying capacities of such conductors are high when compared with the conventional conductors. However, these conductors should be cooled at cryogenic temperatures for retaining the superconductivity. At present, there are two principal types of HTS cables. In the first design, the single superconducting layer consisting of HTS tapes is wrapped around a flexible core. This cable design employs an outer dielectric layer (electric insulation) which restricts the flow of current in radial direction. This insulation layer is present at room temperature and is called “warm dielectric” design as shown in Figure 1.6 (a). The cable assembly is contained within a thermal insulation for preventing any heat leakage into the HTS core. The whole HTS core is inserted into a cryostat. Such configuration offers high power density and minimum amount of superconducting material. However, drawbacks are associated with such configuration, such as high electrical losses (increasing refrigeration cost) and higher impedance.

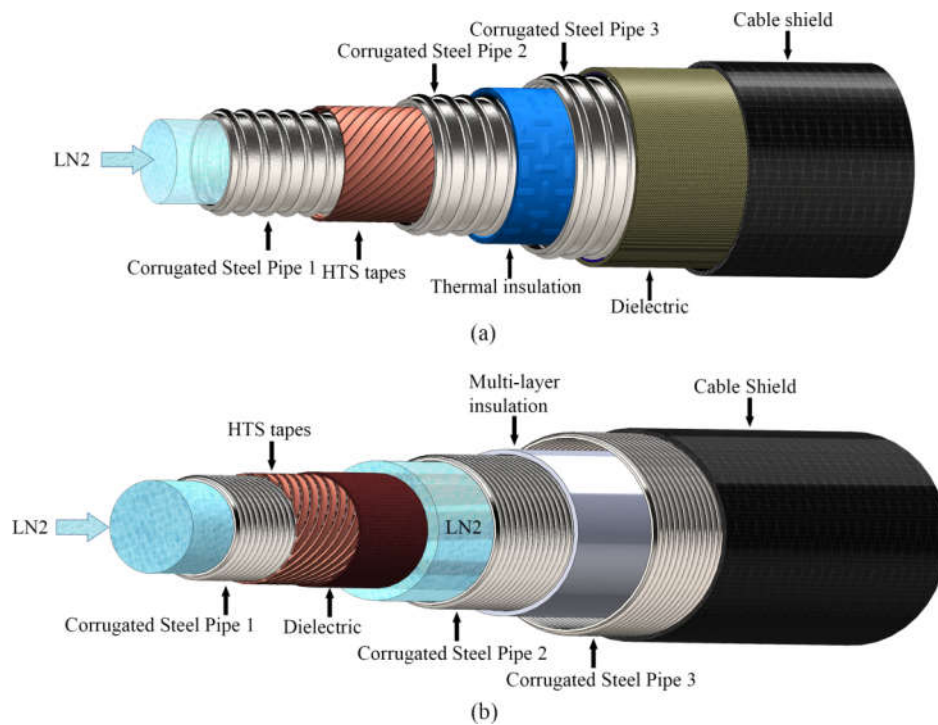


Figure 1.6 Schematic representation of the configurations of HTS cable: (a) warm dielectric and (b) cold dielectric cables

Warm dielectric (WD) design of the HTS cable is most suitable for retrofitting in existing pipe or duct systems. A WD HTS cable has the potential to transport twice the power of a conventional cable with approximately similar losses. The design of the WD HTS cable has many characteristics, which make it attractive for the near future. The absence of a superconducting shield layer results in a lower initial cost. Moreover, the accessories could be derived from conventional designs and has similar handling procedures as a conventional cable. In the cryostat, a vacuum region with radiative multi-layer insulation is provided in order to prevent heat-in-leak from the surrounding. Another configuration is a cold dielectric cable, which as HTS tapes spirally wrapped around a flexible corrugated pipe. A dielectric layer is applied over the HTS tapes and a second layer of HTS tape is applied over the insulation. LN₂ flows over and between the layers, thereby providing dielectric characteristics; such configuration is commonly referred to as the “cold dielectric” design Figure 1.6 (b). Such design utilizes maximum amount of HTS tapes but it offers several advantages, such as reduced AC losses, higher current carrying capacity and complete suppression of stray electromagnetic field outside the cable assembly. The reduction of AC losses further aids in the extension of HTS cables and wider spacing of the cooling stations. Moreover, the inductance of the cold dielectric HTS cable is significantly

lower than a conventional cable. A cold dielectric HTS cable has the greatest level of transmission of transmission capacity and efficiency.

1.3.2 Superconducting Motors and Superconducting Generators

Electrical motors and generators are the most explored topics in electrical engineering. In this section, the principles and characteristics pertaining to superconducting machines will be discussed. Moreover, this chapter is restricted to electromagnetic (EM) motors and generators, due to their relevance to superconducting materials.

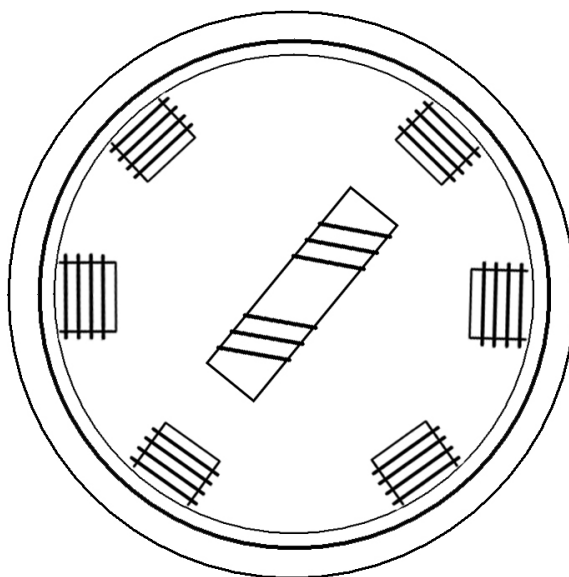


Figure 1.7 Configuration of a typical synchronous machine employing superconducting field winding on the rotor

There are two popular types of electric rotating machines, namely, synchronous and induction. A synchronous rotating machine has two windings: DC winding located on the rotor and AC winding located in the stator. Such a configuration is most commonly available, and the locations of the two windings are interchangeable. An induction motor consists of a squirrel cage or a three-phase wound winding in the rotor. The rotor winding carries AC current at slip frequency, and the rotor frequency is equal to the line frequency when the slip is 1 (rotor stationary) and the slip frequency when the motor is operated at its nominal speed. For low ratings (<500 horsepower), induction motors are very popular; however, for large-scale applications in industries or ships, synchronous motors are preferred.

Moreover, for induction motors, windings (both stator and rotor) experience AC current and are therefore not good candidates for superconducting windings. It should be kept in

mind that superconductor losses are negligible under DC operating conditions. However, losses in the AC environment are large and economically difficult to remove. The involvement of high cost of superconductors and cooling systems limits the primary applications of motors to large sizes (>1000 horsepower) for fan drives and pumps in industrial and utility markets. Figure 1.7 shows the schematic representation of a typical AC synchronous machine. A magnetic field is created due to the rotating HTS field in the copper armature winding. Compared to a conventional motor, the magnitude of this field is typically twice.

1.3.3 Superconducting Magnetic Energy Storage (SMES)

A short circuited superconducting coil of SMES system stores the magnetic field due to DC electrical current as shown in Figure 1.8. These systems work efficiently, when the temperature of the superconductor used in superconducting coil of SMES is maintained below to the critical temperature (T_c) at the high magnetic fields. Hence, cryogenic coolants such as Helium and Nitrogen are employed in the operation of SMES to retain the superconductivity of the superconductor. At cryogenic temperatures (approximately 4.5 K), Ohmic losses are not existing in the coil because the electrical resistance offered by the coil is 0Ω (except at joints). Hence, higher efficiency (>95%) can be achieved.

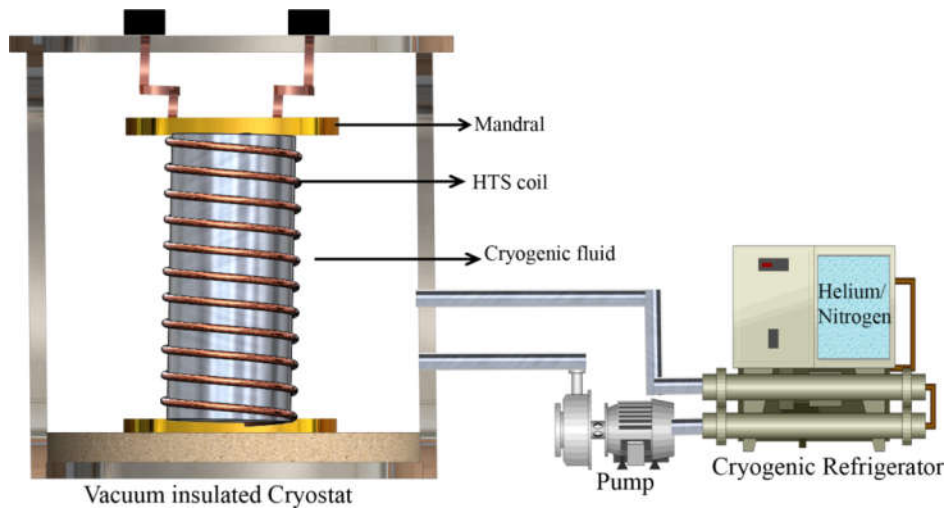


Figure 1.8 Superconducting Magnetic Energy Storage (SMES)

There are four major components in SMES

- **Superconducting coil** made by superconductors such as YBCO, BSCCO, MgB_2 etc. These coils are placed in the vacuum sealed thermally insulated cryogenic environment using a cryostat.

- **Cryogenic system** to maintain the temperature of the superconductor below to its critical temperature. These systems are equipped with cryostat, cryocooler, compressors, vacuum pumps etc.
- **Power conditioning system (PCS)** consists of power electronic devices such as capacitors, transistors and inductors, that provide the interface between the superconducting coil (direct current) and the external grid or load (alternating current). The rated power of the SMES is determined by the power capacity of PCS.
- **Control System** continuously monitor the magnetic protection, cryogenics, power electronics etc. with crucial parameters such as cryogenic coolant operation, coil strain, temperature, pressure. It is vital in the SMES because, it establishes a link between the rated power demands from the external load or grid as well as power flow from and to the superconducting coil.

1.3.4 Superconducting Transformers

A practical cryogenic system for superconducting transformer must be quite, reliable, and efficient in operation. The required cooling power for such a transformer will be of several kilowatts of order at 70 K. Although conduction cooling had been attempted in the past, the recent developments are focused on the circulation of LN₂. The usage of other cryogenes, such as helium, hydrogen, neon, and oxygen, is ruled out due to considerations of cost, safety, and temperature range.

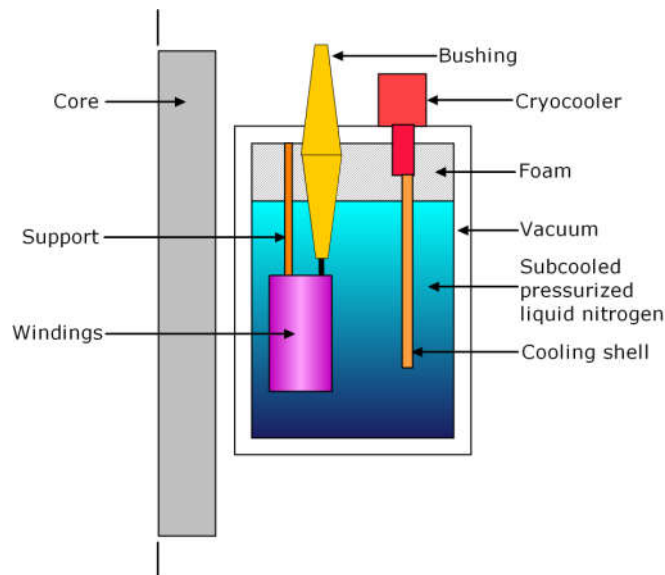


Figure 1.9. Liquid cooling system by natural convection for a superconducting transformer

A circulated LN₂ provides consistent temperature distribution, along with rapid recovery from fault and the benefit of liquid dielectric. Various conceptual designs, such as configurations involving pumping mechanism or circulation using thermo-syphon, as well as bath cooling (Figure 1.9), have been demonstrated. Moreover, LN₂ offers dielectric performance compared to that of oil in a conventional transformer. However, at atmospheric pressure, the operating temperature margin of LN₂ is narrow (63–77 K). Hence, to prevent the formation of gaseous phase, thereby preserving the dielectric properties, it is desirable to maintain liquid nitrogen in a sub cooled state in high-voltage regions. Further, the cryogen must be pressurized to further increase the boiling point.

1.3.5 Superconducting Fault Current Limiters (SFCL)

The conventional fault current limiters such as circuit breakers, switch gears, electromagnetic relays and fuses are not sensitive to detect the short circuit, external triggering is required and expensive in electrical component replacement after fault and are not capable to compensate the fault current without power interruption. **Superconducting Fault Current Limiter (SFCL)** is an innovative electrical power device which is capable of handling the fault current within the half cycle with improved transient stability as well as reduced current stresses and voltage sags efficiently.

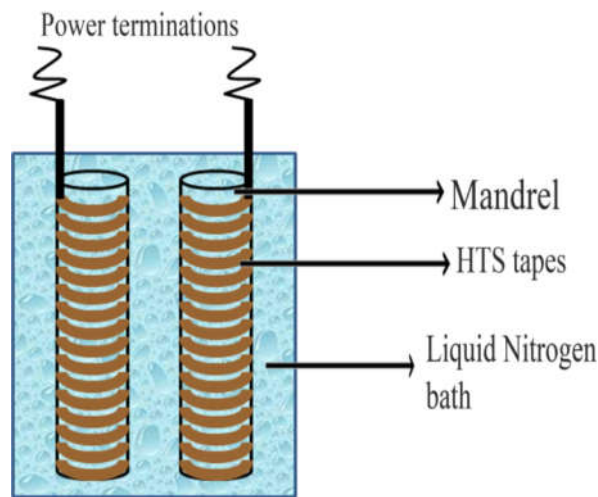


Figure 1.10 Design of SFCL

Figure 1.10 shows the design of the SFCL. The superconducting tapes are wound over a former to replicate a non-inductive coil mandrel. This mandrel is immersed in the Liquid Nitrogen (LN₂) bath to cool the superconducting tapes to retain the superconductivity of the superconductor after fault compensation. SFCL uses the non-linear characteristic and diamagnetism of the superconductor when cooled below to its critical temperature depends

on the type of SFCL for compensating the fault current. The V-I characteristic of normal conductor and the superconductor is shown in Figure 1.11. The superconductor follows the power law during the short circuit and compensates the fault within milli-seconds. When the fault occurs, if the transport current increases than the critical current of the superconductor, the transition from the superconducting state to normal state takes place due to quenching of the superconductor. At this state, the impedance in the line increases and the fault will be limited within the milli-seconds.

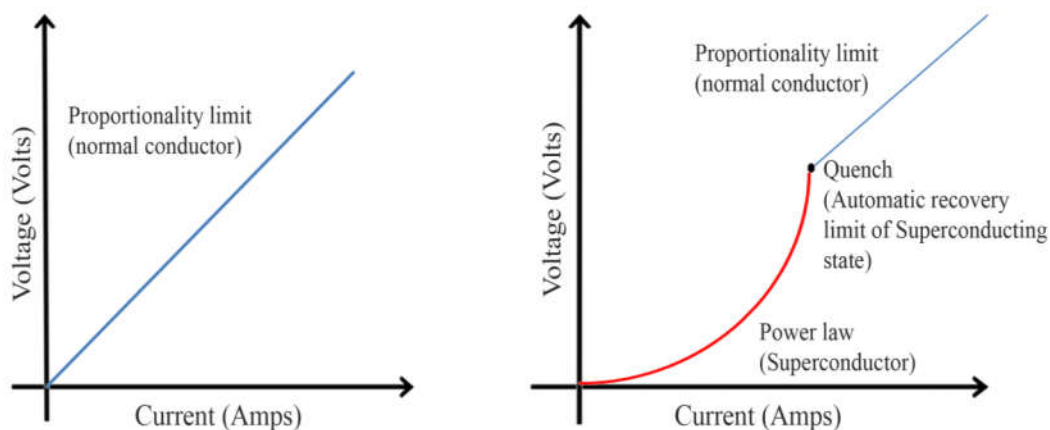


Figure 1.11 V-I characteristics of a normal conductor and a superconductor

For instance, the electrical networks in India operate at 50 Hz and the time taken for a single cycle is 0.02 seconds. The selection of SFCL depends on the fault compensation time and it should be less than 0.02 seconds. The SFCL works on the non-linear V-I characteristics of the superconductor $V \approx (I/I_c)^n$, where, I_c is critical current $I_c = 1\mu\text{V}/\text{cm}$ and n is power law index, for superconductor n ranges from 5-30 [2].

The brief introduction to high temperature superconductivity, cryogenics and their applications are discussed in this chapter. An exhaustive survey of available literature on losses encountered by the HTS cables during normal operation and the cooling strategies implemented to accommodate the heat loads due to the losses are discussed. Further, a typical review on entropy generation rate in various engineering applications is presented in next chapter.

CHAPTER II

2 LITERATURE REVIEW

2.1 Introduction

The conventional power cables are about to upgrade to high temperature superconducting (HTS) cables due to their efficient power transmission with fewer losses and high current carrying capacity. However, the designs of HTS cable is complex and are need to be cooled internally to retain the superconductivity of HTS tapes. This chapter presents the available literature on the development of HTS cables and the implemented cooling strategies. Further, a typical review on entropy generation rate in various engineering applications is presented.

2.2 Literature review on HTS Cables

From the literature, it is evident that Superconductors are employed for efficient power transmission, storage and distribution to meet the power demand with fewer losses. In the past numerous applications were stated by researchers for Low Temperature Superconductors (LTS) [3]–[8] operated at 4K such as Superconducting generators [9]–[12], Superconducting motors [13]–[15], Superconducting Magnetic Energy Storage [16], [17] and High Temperature Superconductors (HTS) operated at 77K such as Superconducting cables [18]–[23] for power transmission and distribution and Superconducting Fault Current limiters [24]–[26] limiting current during fault. In this chapter, a comprehensive review on losses encountered due to various heat loads and thermohydraulic characteristics to be employed for cooling HTS cables are discussed. In this context, the losses encountered by HTS cables from various sources are discussed (mechanical, structural and electrical losses) during installation, transmission and distribution losses during power transmission through HTS tapes. Further, HTS tapes comprises various layers such as Superconductor, stabilizer, intermediate layer and textured metal substrate majorly contribute to total losses in HTS cables [27].

- a) AC losses [28]–[36] in the HTS cables are due to the flow of transport current through the HTS tapes or wires. These losses are categorized as Hysteresis losses (self and external field), eddy current losses in the sheath material edge losses [37] due to gap between the tapes and Coupling losses due to twisting of the HTS tapes wound on the corrugated former.

- b) Dielectric or $\tan\delta$ losses are accounted in HTS cables due to the elevated temperature in dielectric materials such as XLPE, PVC, Polyamides, Polyethylene, PPLP etc [38]–[42].
- c) Thermal losses [43]–[47] in HTS cables are due to convective losses between corrugated steel former and LN_2 flow. In addition, heat-in-leaks from ambient, axial heat leaks from the termination and heat fluxes due to transport current in HTS tapes contributes to thermal losses.
- d) Mechanical losses such as torsion strain [48], twist pitch of HTS tapes wound on corrugated former, fracture toughness [49], [50] and bending radius while installation of HTS cables.

2.2.1 Losses encountered by HTS cables

The efficiency of the HTS cables will be degraded due to AC losses [51], [52] and heat-in-leaks. Further, the electro-thermal behavior of superconducting tapes during transportation of rated current also affects the efficiency of HTS cables. Recently, the electro-thermo mechanical behavior of multilayered superconducting tapes was investigated by using electromagnetic-thermo and mechanical coupling [53]. The major requirements for designing HTS cable depends on application of utility and the factors influence are rated voltage, power, over-current [54] (Short-Circuit Current), Load Factor (LF) of utility, maximum possible outer diameter of the cable and length of the cable to be installed. Further, the maximum electrical field that is possible within the HTS cable can be estimated by calculating the transportation of rated current in HTS tapes (BSCCO[55], [56], YBCO[57], [58]), losses in the HTS cable such as AC losses[59], dielectric losses and cryogenic losses [60]. In the past, the construction and testing of Superconducting cables with BSCCO tapes was discussed in EPRI technical report [61]. The HTS cables developed in different countries and their specifications with manufacturers are shown in Table 2.1 .

Table 2.1 HTS cable projects and their specifications in different countries

Project / Country	HTS cable manufacturer	Specifications
AEP, Coloumbs(2006)[62]	Ultera	13.2 kV, 3 kA, 200m, Tri-axial design, BSSCO 2223 tapes used
LIPA (2007)[63]–[65]	Nexas	138 kV, 574MVA, 2.4kA, 600m, fault current 51kA _{rms} , Single coaxial design

		and BSSCO 2223 tapes used
KEPCO, Gochang, Korea[66]–[68]	LS cable	22.9 kV, 1250 A _{rms} , 50 MVA, 100 m, BSSCO 2223 tapes used (2007) , 500 m field test with YBCO tapes (2011)
AMPACITY project (2014) , Germany[69]	NEXAS	40 MVA, 10 kV, 1 km with SFCL combination
YOKOHAMA, Japan (2007-2011)[70]–[72]	Sumitomo electrical industries	30 m length, 66 kV, 200MVA, 1kA, BSSCO
China (2004)[73]	Innopower Superconductor cable Co. Ltd	35 kV, 2kA, 33 m, Warm dielectric, BSSCO tapes
Shingal,KEPCO, Korea, (2016)[74]	LS cable	AC 154kV, 600MVA, DC 80kV, 500MW, 1 km
SC power cable project ALBANY, USA(2004) [75], [76]	Super Power	34.5 kV, 0.8 kA, 350 m, YBCO tapes, 3-in-1 HTS cable,
Super-ACE, Japan,(2004)[77]	Furukawa Electric	500m, 77kV, 1kA, Ag/Bi-2223 tapes
TEPCO, Tokyo (2001-2002) [78]	SEI	66kV, 114 MVA (1kA _{rms}), 0.1km, three phase cold dielectric, sub cooled LN ₂

2.2.1.1 AC Losses

It is a common belief that superconductors conduct electricity with zero energy loss. In fact superconductors experience losses when transmitting an alternating current. However, direct current (DC) can be transmitted without any losses during normal operation. In power applications, AC and DC [79] transmission requires costly converters at ends of transmission line. Hence, most of the transmission lines are of constructed for AC power transmission. Figure 2.1 shows the geometrical arrangement of the HTS tapes wound around the corrugated former of HTS cable.

The application of AC HTS cables in the applications of power grid was discussed by Malozemoff et al., [80]. An AC HTS power cable can transmit electrical power with fewer loss when compared to conventional power cables. The most important aspect while operating HTS power cable was economical performance of refrigeration system employed for efficient cooling to retain superconductivity of HTS tape which depends on heat loads such as AC losses. These losses [80], [81] are classified as Hysteresis (Self and External field), Eddy current and Coupling losses.

Non-uniform current distribution in the HTS cables due to total AC losses was reported by Zhenget al., 2014 [82]. Later, Ozcivan et al., [83] discussed about the balance current distribution in tri-axial HTS cables and uniform current between the layers of HTS conductor using inter-phase transformers (IPTs) [84].

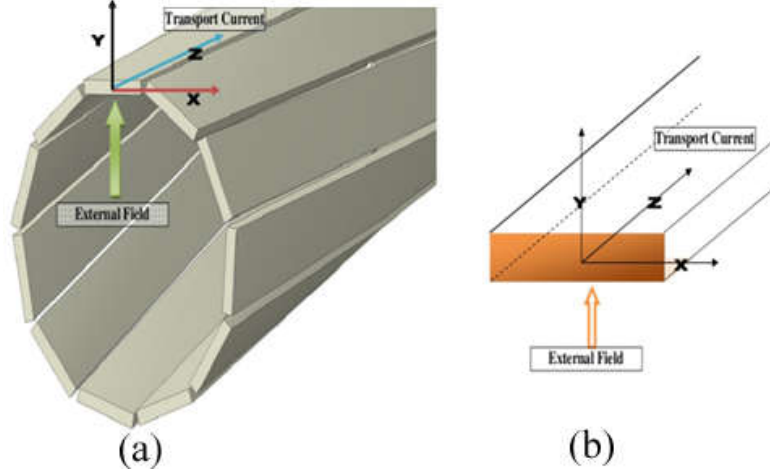


Figure 2.1 Geometrical arrangement of twisted HTS tapes in HTS cable

The AC losses in the HTS cables are given by following equations [6]

$$Q'_{AC} = Q'_{self} + Q'_{Ba} + Q'_{Bc} \quad (2.1)$$

Where, Q'_{self} = self field loss, Q'_{Ba} = axial field loss, Q'_{Bc} = circumferential field loss

According to Furukawa's cable[28]

$$Q'_{AC} = Q'_{Bc} + Q'_{Ba} + Q'_{self} + Q'_{eddy} \quad (2.2)$$

AC losses mainly depends on shape of the conductor. For tapes, the loss per AC cycle per unit length due to self field is predicted by Norris equations. This equation is applicable for elliptical, thin strip cross sections and multi filamentary tapes. Self field AC losses can be calculated by using Norris Equation [7, 23] as follows

For an ellipse

$$Q'_{AC} = \frac{\mu_0 I_c^2 f}{\pi} \left[(1 - \Gamma) \ln(1 - \Gamma) + \Gamma - \frac{\Gamma^2}{2} \right] \quad (2.3)$$

For thin strips [85]

$$Q'_{AC} = \frac{\mu_0 I_c^2 f}{\pi} \left[(1 + \Gamma) \ln(1 + \Gamma) + (1 - \Gamma) \ln(1 - \Gamma) - \Gamma^2 \right] \quad (2.4)$$

AC losses using mono block model can be calculated as [86]

$$Q'_{AC} = \frac{\mu_0 I_c^2 f}{2\pi h^2} \left[(2 - \Gamma h) \Gamma h + 2(1 - \Gamma h) \ln(1 - \Gamma h) \right] \quad (2.5)$$

$$\Gamma = \frac{I_{pk}}{I_c} \text{ for } \Gamma \ll 1 \quad (2.6)$$

$$Q'_{AC} \cong \frac{\mu_0 I_c^2 f \Gamma^3}{6\pi} \quad (2.7)$$

$$\Gamma = \frac{\sqrt{2} I_{rms}}{N F_R I_{c,tape}} \quad (2.8)$$

$$P = V_{rms} I_{rms} \cos\phi \quad (2.9)$$

where, Γ is normalized current, F_R is retention fraction, N is the number of tapes in the cable, V_{rms} is RMS voltage (V), I_{rms} is Transport current (A), $\cos\Phi$ is power factor, μ_0 is permeability in free space, I_{pk} is peak current, I_c is critical current and f is AC frequency.

Voccio et al., [87] reported about the losses in 2G HTS tapes using different models

- a) In Isolated Bean model, losses are measured by treating individual tapes with sufficient space between them.

$$(Q'_{AC})_{isolated} = \left(\frac{\mu}{3\pi} \right) f I_{cable} I_{sw} \Gamma^4 \quad (2.10)$$

- b) In Mono-block model, losses are measured by maintaining no gaps between the tapes and assuming uniform HTS layer in HTS tape

$$(Q'_{AC})_{monoblock} = \left(\frac{\mu}{3\pi} \right) \left(\frac{t}{R} \right) f I_{cable}^2 \Gamma^3 \quad (2.11)$$

- c) In Gap model, losses are measured by considering the gaps between the tapes and width of the individual tape

$$(Q'_{AC})_{gap} = \left(\frac{\pi}{48}\right) \left(\frac{g^2}{w}\right) \mu_0 f I_{cable} I_{sw} \Gamma^4 \quad (2.12)$$

where, I_{sw} is the sheet current (A/cm-width), t is thickness of the HTS layer and R is radius of the former, w is half width of HTS tape and g is gap between the adjacent tapes.

AC losses are measured by using various methods such as electrical circuit method [88], Calorimetric method [89]–[92] and contactless electrical method [93], [94]. Further, Zhu et al., [95] presented about HTS cable AC loss measurement for the large current capacity experimentally by using a lock-in amplifier and compensation coil. In recent past, Mukoyama et al., reported about the AC loss measurement in the conductor with and without shield of HTS cable filled with LN₂ [96]. AC losses without shield can be calculated by using lock-in-amplifier.

$$Q'_{AC} = T^{-1} \int_0^T I(t)V(t) dt = \sum I(t)V(t) = I_e V_e \cos \theta \quad (2.13)$$

where, $I(t)$, $V(t)$ are current in the conductor and voltage difference voltage taps, I_e , V_e are the effective values of current and voltage and θ is phase difference between the $I(t)$, $V(t)$

AC loss measurement with shield can be calculated by using three different methods

a) Each layer individual measurement method

In this method AC losses in each layer was derived by using the relationship between the current and voltage including the shield [96]

$$Q'_{AC} = \int_0^T V_C I dt + \int_0^T V_S I dt = I V_C \cos \theta_C + I V_S \cos \theta_S \quad (2.14)$$

where, V_C , V_S are the voltages in the conductor and shield between the ends

b) Joint part subtraction method

In this method voltage taps between the jointed ends of each conductor with shield in the total system are considered. AC losses are calculated by subtracting the system losses with jointed part AC losses [96]

$$Q'_{AC} = \int_0^T V_1 I dt - \int_0^T V_2 I dt = I V_1 \cos \theta_1 - I V_2 \cos \theta_2 \quad (2.15)$$

c) Joint part differential method

In this method the voltage between the voltage taps of one side of conductor, shield and other side joint part are considered. AC losses are calculated by using phase difference and differential voltage signal [96]

$$Q'_{AC} = I(V_1 - V_2) \cos \theta \quad (2.16)$$

where, V_1 and V_2 voltage between voltage taps of side 1 and side 2

Table 2.2 Summary of various investigations on different components of AC losses in HTS cables

Analysis	Hysteresis Losses			Eddy Current Losses	Coupling Losses	Magnetization Losses
	Self field	External field	Total Hysteresis losses			
Experimental	Hu [97] Kim [98] Elschner [99] Joo[100] Daibo [101]	Ma [102] Kim [103]	Tanaka [104] Magnusson [105]	Yamasaki [106] Siahrang[107] Gouge [108]	Šouc [109] Frank [110] Miyoshi [111]	Zannella[112] Kováč[113] Lakshmi [114]
Simulation	Famakinwa[115] Hong [116] Grilli[117] Hong [116]	Famakinwa [118]	Shen [119]– [121] Zubko[122] Ainslie [123]	Shen[119] Song [124]	Demencik [125]	Majoros[126] Zermeno[127] Sheng [128] Wang [129]
Numerical	Noji [130]– [132] Grilli[133]	Sato [134]	Dresner[135] Malozemoff [136]	Noji[137] Siahrang[107]	N/A	Bykovsky [138] Ogawa [139]

AC losses in different HTS cables such as Warm Dielectric, Cold Dielectric, Co-Axial, Tri-Axial and Triad with type of analysis used is presented in Table 2.3. Grilli et al.,[27] discussed about computational analysis on AC losses in HTS tapes, wires and devices. AC losses in superconductors with complex geometries such as wires [140], twisted filaments[141], twisted multi filamentary [142], twisted stacked tapes [143], [144], stacks [123], helical counter wound [145], polygonal [146], [147], Roebel [148]–[150] cables etc with Hysteresis losses, eddy current losses, Coupling losses and Ferromagnetic losses in the HTS tapes was discussed. Further, Zermeno et al.,[127] reported about calculation of AC losses in the coils and stacks using homogenization method for simulating electromagnetic behavior of HTS tapes using E-J power law. 2D simulations was

performed on the stacks of HTS tapes for evaluating the computational speed and to identify the anisotropic bulk model for large scale applications.

Table 2.3 Summary of various investigations on AC losses in different HTS cables

Superconductor	Author	Analysis	HTS cable	Specifications
BSCCO	Vyas [151]	Numerical	Warm Dielectric	500 MVA / 1.1 kArms, 50Hz
	Wang [152]	Numerical	Co-axial	Bi2223/Ag tape , 125 A self field
	Young [153]	Simulation	Tri-Axial	13.2 kV, 3kA _{rms} and 69 MVA
	Fisher [154]	Simulation	Tri-Axial	1300 A _{rms} , 15 kV, BSCCO 2223
	Gelabert [155]	Simulation	Triad	1175 A, 13.8kV
	Kelley [156]	Experimental	Warm Dielectric	24-kV, 100 MVA, 2400A _{rms}
	Nassi [157]	Experimental	Warm Dielectric	115 kV, 400 MVA, 3300 A
	Dai [158]	Experimental	Three single phases (WD)	75-m long, 10.5 kV/1.5 kA
	Shimoyama [159]	Experimental	Tri-Axial	Bi-2223 tapes, 50 Hz to 500 Hz, 10 A to 25 A
	Gouge [108]	Experimental	Tri-Axial	1.3 and 3 kA _{rms} , 15 kV
YBCO	Zhu [160]	Numerical	Cold Dielectric	110 kV/3 kA, 1km
	Zhu [161]	Simulation	Cold Dielectric	110 kV/3 kA
	Zhou [20]	Simulation	Cold Dielectric	3 kA, 25kA@3s fault current
	Sim [162]	Simulation	Cold Dielectric DC	80kV, 3125 A, 65 K, 5 bar
	Del-Rosario-Calaf [163]	Simulation	Co-axial	138 kV, s 2500 A, I _c = 300 A/cm @ 77K
	Rostila [164]	Simulation	Co-axial	1-10kA _{rms} , YBCO
	Miyagi [165]	Simulation	Tri-Axial	I layer (763A), II layer (791A), III layer (805A), I _c =2359 A
	Chevtchenko [166]	Simulation	Tri-Axial	6 km, 3kA _{rms} , 50 Hz, 0.1W/m AC losses
	Ha [167]	Simulation	Tri-Axial	22.9 kV, 50 MVA, 1,260A _{rms}

	Wang [54]	Simulation	Triad	31.8 kA _{rms} @2.02 s fault current
	Maruyama [168]	Experimental	Co-axial	66 kV/5 kA, 275 kV/3 kA
	Sudheer [169]	Experimental	Co-axial	YBCO, I _c = 120A
	Kitamura [170]	Experimental	Tri-Axial	200 MVA, 22 kV, 3 kA
	Masuda [171]	Experimental	Triad	34.5 kV, 800 Arms, 350m
	Yumura [172]	Experimental	Triad	66 kV, 200 MVA, 10 kA @ 2 sec fault current
	Mukoyama [173]	Experimental	Triad	400 MVA, 66/77 kV class
	Yagi [174]	Experimental	Triad	0.048 W/m AC loss at 1 kA and 50 Hz , 1m
	Yagi [175]	Experimental	Triad	1 kA 66/77 kV, 10 m, YBCO, 50Hz

AC losses in Warm and Cold dielectric HTS cables for DC and AC cable systems was discussed by Jin et al., [176]. Recently, Prestigiacomo et al.,[177] presented about fabrication of scalable progress in 2G HTS tapes (YBCO) with an emulated Rutherford twisted conductor topology for lower AC loss. Yagiet al., [178] discussed about the recent development on AC losses reduction in three layer HTS power cable made of YBCO tapes. The thermal stability of HTS cable depends up on the precise estimation of AC losses and over current. The magneto-thermo coupled analysis was used to investigate the thermal stability in the BSCCO based Co-Axial HTS power cable by Miyagi et al., [179].

Kim et al., [180] reported about performance of HTS AC cable using PSCAD/EMTDC as a simulation tool. Further, author extended his work [181] on AC losses using PSCAD/EMTDC and compared the results with the experimental results under fault condition. Bae et al., [182] performed experiment on stability analysis and estimated AC losses in HTS cables. Electromagnetic analysis on KERI HTS power cable was performed and the procedure for stability at the rated operation was discussed.

2.2.1.2 Eddy Current losses

Eddy current losses are accounted in the metal parts of the superconducting tape due to currents which are induced by magnetic field and circulation. From the literature, it was observed that Grilli et al.,[183] discussed about reduction of AC losses due to eddy currents by electromagnetically uncoupled time varying magnetic fields in the filaments of coated conductor (CC) which are twisted and stratified. The power loss per unit volume due to eddy current was given by

$$(Q'_{AC})_{eddy} = \left(\frac{\pi^2}{6}\right) \left(\frac{w^2}{\rho}\right) (\mu_0 H_a f)^2 \quad (2.17)$$

Wang et al., [184] simulated the Soldered-stacked-square (SSS) wire structure with second generation (2G) HTS tapes for reducing AC losses and observed that 80% more losses are reduced. The AC losses and the eddy current losses are calculated from simulation as follows

$$Q'_{AC} = 2 \int_{I/2}^I \left[\sum_1^N \int_{\Omega} 2\pi r \cdot E_{\phi} \cdot J_{\phi} dr dz \right] dt \quad (2.18)$$

$$(Q'_{AC})_{eddy} = \frac{4\mu_0^2 t w f^2}{\pi \rho} I_c^2 h(i) \quad (2.19)$$

where, I is the cycle of the transport current, N is number of turns of the HTS coil, J_{ϕ} and E_{ϕ} are current density and electrical field and in ϕ direction. ρ , w and t are the resistivity, width and thickness of the stabilizer respectively, μ_0 is the permeability of vacuum, I_c and $h(i)$ are critical current and complex function of normalized peak transport current respectively.

2.2.1.3 Hysteresis losses

Hysteresis losses[185] are accounted in the superconducting material due to movement and penetration of magnetic flux. Power law was used to calculate the hysteresis losses in the HTS cables [4].

$$\rho = kJ^n \quad (2.20)$$

where, J is current density and 'n' is index

Dresner [186] reported AC losses and peak transport current density in slab conductors. Further, by assuming the aspect ratio of HTS tapes approximately as 20 [187],

$$Q'_{AC} = G(n, \beta) \cdot b^{-1} (\nu \cdot \mu_0 / J_c)^{(n+1)(n+2)} \cdot E_c^{1/(n+2)} (J_p \cdot b)^k \quad (2.21)$$

Where, $\beta = J_p / J_c$, $k = (3n + 4) / (n + 2)$, b = tape thickness, ν = frequency, μ_0 = magnetic permeability of free space = $4\pi \times 10^{-7}$ H/m, E_c = criteria for critical current, E_c can be $1\mu\text{V/cm}$ or any other reasonable value

If $\beta < 1$,

$$G(n, \beta) = \frac{1}{6} + 0.17n^{-0.427} \quad (2.22)$$

Here, $Q'_{AC} \propto J_p$ to the $(3n+4)/(n+2)$ -power

If $\beta \gg 1$,

$$G(n, \beta) = D(n) \cdot \beta^{n(n+1)/(n+2)} \cdot \left(E_c / \left[v \mu_0 J_c b^2 \right] \right)^{(n+1)/(n+2)} \quad (2.23)$$

where,

$$D(n) = \Pi^{-0.5} \tau[(n+3)/2] / \tau[(n+4)/2], \tau \text{ is gamma function, } Q'_{AC} \propto (J_p)^{-(n+2)}.$$

From the analysis, the relationship given for AC loss rate from 1 to 3 W/m at $1kA_{rms}$ was

$$P_{cable} \propto I_c^\alpha \cdot (I_p / I_c)^k \quad (2.24)$$

Where, $\alpha = (2n+3)/(n+2)$

Wang et al., [184] simulated the Soldered-stacked-square (SSS) wire structure with second generation (2G) HTS tapes for reducing AC losses and the expression for solving the hysteresis losses was given by

$$(Q'_{AC}) = w_f I_c (\mu_0 H_a f) \quad (2.25)$$

Zhang et al., [188] discussed about the hysteresis losses in the corrugated steel former of HTS cable. An experimental investigation was done to examine the hysteresis loop in the low-magnetic 304 stainless steel and it is identified magnetization of former due flow of transport current. Hysteresis losses estimated are given as follows

$$Q'_{AC} = f \oint H dB = C f H^2 = \left(\frac{\text{loss}}{\text{frequency}} \right)_{\text{alternate magnetic field}} f \left(\frac{H_{\max}}{\text{Alternate magnetic field}} \right) \quad (2.26)$$

$$H_{\max} = \frac{I_{\max}}{\pi \left(\frac{\text{outer dia} + \text{inner dia}}{2} \right)_{\text{former}}} \quad (2.27)$$

where, 'C' is the constant base, f is frequency, I_{\max} is maximum alternating current

2.2.1.4 Coupling losses

Coupling losses are accounted between two or more layers of superconducting filament regions due to flow of current. The coupling losses in the HTS cables occur between the two parallel superconducting wires

$$B_i = B - \tau B \quad (2.28)$$

$$\tau = \frac{\mu_0}{2\rho_i} \left(\frac{l_p}{2\pi} \right)^2 \quad (2.29)$$

For round wire,

$$Q_{AC}''' = \frac{B_{\max}^2}{\mu_0} * \frac{2\pi\omega\tau}{1 + \omega^2\tau^2} \quad (2.30)$$

For flat wire,

$$Q_{AC}''' = \frac{B_{\max}^2}{\mu_0} * \frac{\chi_0\pi\omega\tau}{1 + \omega^2\tau^2} \quad (2.31)$$

Where, $\tau = \tau_{\text{round}} \frac{\chi_0}{2} * A$

Wang et al., [184] simulated the Soldered-stacked-square (SSS) wire structure with second generation (2G) HTS tapes for reducing AC losses and the expression for solving the coupling losses per unit volume was given by

$$(Q'_{AC})_C = \frac{(fL\mu_0 H_a)^2}{4\rho_{\perp}} \quad (2.32)$$

where, L is the length of the tape, ρ_{\perp} is the effective transverse resistivity

2.2.1.5 Magnetization effect on AC losses

Ferromagnetic losses are accounted in the magnetic materials due to hysteresis cycles. The voltage loops are generated in the ferromagnetic material of HTS tapes due to hysteresis losses accounts for voltage loss [34].

$$(Q'_{AC})_H = \pi H_{\text{rms}} V_{H,\text{rms}} \left(\frac{w}{l} \right) \quad (2.33)$$

where, $V_{H,rms}$ is loss voltage in voltage loop in phase with 'H', l and w are length and width of measurement loop.

Table 2.4 Different geometries and expressions for perpendicular magnetic field

Geometry	Expression
Strip (width '2a' and thickness '2b')	$(H_p)_{strip} = J_c \frac{b}{\pi} \left[\ln \left(1 + \frac{a^2}{b^2} \right) + 2 \frac{a}{b} \operatorname{arctg} \frac{b}{a} \right]$
Thin strip ($b \ll a$)	$(H_p)_{strip} = J_c \frac{2b}{\pi} \left[\ln \left(\frac{a}{b} \right) + 1 \right]$
Slab (in parallel field $b = \infty$)	$(H_p)_{strip} = a J_c$
Hollow Cylinder	$(H_p)_{hollowcylinder} = \frac{2}{\pi} \mu_0 J_c (R_0 - R_i)$

Many researchers focused on the reduction of magnetic AC losses by demagnetization. Majoros et al., [126] discussed about the magnetization losses in the YBCO conductor-on-round-core (CORC) cables where the magnetic fields are applied perpendicular to the cable axis. The AC losses due to magnetization was calculated for full penetration field in a perpendicular magnetic field for different geometries

AC losses are calculated by using FEM method and compared with the critical state model for full penetration of magnetic fields in a cylinder

$$Q'_{AC} = \frac{8B_p^2}{3\mu_0} \left(\frac{B_m}{B_p} \right) \left(1 - \frac{B_m}{B_p} \right) \text{ for } B_m \leq B_p \quad (2.34)$$

$$Q'_{AC} = \frac{8B_p^2}{3\mu_0} \left(\frac{B_m}{B_p} - 0.5 \right) \text{ for } B_m \geq B_p \quad (2.35)$$

$$\text{where, } B_m = 0.5B_p \text{ and } B_p = \left(\frac{2}{\pi} \right) \mu_0 J_c R \quad (2.36)$$

Magnetization AC losses on stakes of YBCO coated conductors for reduction of the total losses was investigated by Grilli [32]. Further, different arrangements of multi stacking with BSCCO tapes are considered for describing the effects of magnetization loss and shield effects [189]. Furthermore, Roebel [190] shaped strands of 2G HTS YBCO tapes are

used for characterizing the magnetic AC losses in the absence of coupling currents as a function of field amplitude [191] and it was observed that hysteresis losses dominate the total loss in the superconductor in parallel field. Demencik et al., [125] investigated on striated YBCO tapes with different stabilizer thickness and number of filaments to evaluate AC magnetization losses and transverse resistivity profile. From the study, it was identified that, with reduced stabilizer thickness total losses are reduced significantly and coupling losses are considerably suppressed. Further, Grilli et al., [183] discussed about reduction of AC losses due to electromagnetically uncoupled time varying magnetic fields in the filaments of coated conductor (CC) which are twisted striated. AC losses per unit length was given by

$$(Q'_{AC})_{strip} = 4\mu_0 a^2 J_{cs} H_a g\left(\frac{H_a}{H_c}\right) \quad (2.37)$$

$$(Q'_{AC})_{strip} = 4\mu_0 a^2 J_{cs} (H_a - 1.38H_c) \text{ for } H_a \gg H_c \quad (2.38)$$

AC losses per unit volume was given by

$$(Q''_{AC})_{strip} = 2a\mu_0 J_c H_a \quad (2.39)$$

AC losses per unit volume of twisted striated HTS tapes of CC was given by

$$(Q''_{AC})_{striated\ array} = -\frac{2\mu_0 L_x^2}{\pi w t} \int_0^{H_m} (H_m - 2\xi) \ln \left[1 - \frac{\sin^2\left(\frac{\pi w}{L_x}\right)}{\cosh^2\left(\xi / H_c\right)} \right] d\xi \quad (2.40)$$

where, J_{cs} is the HTS thin sheet critical current density, $H_c = \frac{J_{cs}}{\pi}$, Critical current density

$J_c = \frac{I_c}{(2a)(2b)}$, w is the half width of the filament and t is thickness, L_x is array periodic unit cell.

Tsukamoto et al., 2005 [192] discussed experimentally about a mechanism to decay the trapped magnetic field using AC magnetic field in the HTS bulk (YBCO)

$$Q''_{AC} = \frac{2B_m^2}{\mu_0} \left(\frac{2\delta}{3} - \frac{\delta^2}{3} \right) \text{ for } \delta < 1 \quad (2.41)$$

$$Q_{AC}^m = \frac{2B_m^2}{\mu_0} \left(\frac{2}{3\delta} - \frac{1}{3\delta^2} \right) \text{ for } \delta > 1 \quad (2.42)$$

where, $\delta = \frac{B_m}{B_{mp}}$, B_{mp} is full penetration magnetic field, B_m is magnitude of trapped magnetic field.

Table 2.5 Recent studies on AC losses by various researchers

Mode of analysis	Author, year	Superconductor / cable used	Configuration used	Remarks	
Experimental	Elschneret al., 2015 [99]	Concentric HTS power cables with BSCCO 2223	Helical, Axial, S-shaped for one and two phases	AmpaCity (1 km / 20 kV/2 kA), 77K	
	Ogawa et al., 2018 [193]	Bi2223/Ag	two layer twisted HTS cable	2 mm- thick polystyrene thermal insulators,	
Simulation	H-Formulation	Petrov et al., 2019 [194]	Bi-2223 (1G)	N/A	COMSOL and MATLAB Equivalent circuit
		Escamezet al., 2015 [195]	HTS tube	N/A	Hysteresis losses calculations for self field, external field and combination of both fields
		Shenet al., 2017 [119]	SuperPower tapes(SF12100 and SCS12050)	N/A	COMSOL Multiphysics, Hysteresis losses and eddy-current losses
		Shenet al., 2019 [121]	CroCo cables	Cross-Conductor	COMSOL Multiphysics, Norris's solutions ellipse
		Shenet al., 2017 [120]	Superpower (SF12100 tape)	Parallel HTS tapes	COMSOL Multiphysics, 20 Hz, 150 A, Gap of tapes 2, 4, 6, 8, 10, 12, 14, 16, 18, 20mm
		Yildizet al., 2017 [196]	YBCO	two layers of HTS tapes with	COMSOL Multiphysics, 2400

				a ferromagnetic substrate	A, 50 Hz
T-A Formulation	Wu et al., 2019 [197]	Shanghai, AMSC, SuperPower tapes	twisted stacked tape and stacked conductor	COMSOL Multiphysics	
	Wang et al., 2019 [198]	CORC	multiple-layer structure (striated tapes)	COMSOL Multiphysics	
Other Formulations	Duan et al., 2018 [199]	Cold Dielectric HTS cable with Bi-2223 tapes	cylindrical HTS cable	XFEM method, Magnetic Hysteresis for quasi 3-D transient eddy current field	
	Gouge et al., 2005 [55]	Tri-axial HTS cable / BSCCO-2223	N/A	ANSYS is used for analysis using McFee assumption	
	Zubko et al., 2016 [122]	2G wires	N/A	FEM, APDL and resistivity-adaption algorithm" (RAA)	
Analytical	Samoilenkov et al., 2018 [200]	HTS three phase cable (SuperPower, SuperOx tapes)	coaxial (Polygonal cross section and extended rectangular cross sections)	Medium voltage (10-60kV)	

2.2.1.6 Dielectric Losses

The dielectric losses are also called as “ $\tan\delta$ ” losses. It occurs when the cryogenic fluid supplied cannot able to cool the dielectric material due to the loads such as heat leak from the earth crust through the insulation and protective shield to the dielectric and also from the HTS cable when operated with transport current. This heat will increase the resistivity in the HTS cable and losses are increased these losses are called as dielectric losses. Recently, the fundamental and insulating characteristics of PPLP for HTS cables using LN_2 as a coolant for DC [201] and cold dielectric [202] cables was studied

The dielectric losses per unit length [203] was calculated by

$$P_d = 0.5\omega CU_p^2 \tan \delta = \omega U_p^2 \frac{\pi\epsilon_0}{\ln(r_{od}/r_{id})} \epsilon \tan \delta \quad (2.43)$$

Dielectric losses due to non-ideal electrical insulation [204] was calculated by

$$W_d = \omega CU_0^2 \tan \delta \quad (2.44)$$

Where, C is the capacity of cylindrical capacitor and is given by $C = 2\pi\epsilon\epsilon_0 / \ln(r_{od}/r_{id})$ per unit length, ω is the angular power frequency given by $\omega = 2\pi f$, ϵ is the dielectric constant of the insulation, ϵ_0 is the permittivity of free space, U_p is phase to ground peak voltage, δ is the angle loss, r_{od} is outer diameter, r_{id} is inner diameter. The dielectric losses are also calculated by [39]

$$\frac{P_{ins}}{L} \approx S.\omega \int \partial f \epsilon \epsilon_0 \tan \delta E^2 \quad (2.45)$$

where, S is technical Carnot factor.

When AC voltage is applied within a dielectric material the dielectric loss occurred by a leakage current was calculated by [41]

$$W_{dl} = EI_R = EI_C \tan \delta \quad (2.46)$$

where, W_{dl} is dielectric loss, E is voltage, I_R is leakage current, I_C is charging current, δ is loss angle. LN₂ have good dielectric properties and also used as cryogenic coolant, PPLP [205], [206] have high dielectric strength and low dielectric loss compared with other dielectric material.

The thickness of insulation layer depends on maximum electrical stress in HTS cable was calculated by Kwag et al., [207]

$$t = r_0 \left[\exp\left(\frac{V}{E_{max}.r_0}\right) - 1 \right] \quad (2.47)$$

where, r_0 is the outer radius of the conductor, E_{max} is the maximum design stress (kV_{rms}/mm) and V is the testing voltage

Kikuchi et al., 2015 [208] discussed about the partial discharge characteristics for PPLP material in composite insulation of HTS cables. Gaseous Nitrogen at higher pressure was

used for identifying the PD characteristics in variable size of butt gaps. In recent past, Šoucet et al., 2017 [209] reported aero gel and polyurethane was applied in the Conductor on Round Core (CORC) to provide vacuum less insulation with LN₂ as a cryogenic coolant in cable tube. Zhang et al., [210] discussed about the production and performance of 2G HTS wires in practical applications.

Soika et al., [211] discussed about the mechanical requirements during manufacturing of HTS power cable. The influence of dielectric material on HTS tapes was discussed in the mechanical design of HTS cable. Various forces exerted by the dielectric layer on HTS tapes are given below.

The pressure exerted by the lapped dielectric on HTS tape in phase layer can be calculated by

$$P = \frac{2\sigma_t s}{D} \quad (2.48)$$

The force exerted on HTS tape by the dielectric material

$$F_d = P w \left(0.25 \sqrt{L^2 + \pi^2 D^2} \right) \quad (2.49)$$

The force exerted in the HTS tape to overcome the static friction between the two surfaces to avoid the degradation by slide.

$$F_f = \mu_s P w \left(0.5 \sqrt{L^2 + \pi^2 D^2} \right) \quad (2.50)$$

The tensile stress was given by

$$\sigma = \frac{\mu_s P}{t} \left(0.5 \sqrt{L^2 + \pi^2 D^2} \right) \quad (2.51)$$

where, μ_s is coefficient of static friction, P is pressure, t is tape thickness, D is average diameter, w is tape width, σ_t is hoop stress in the HTS cable and s is dielectric thickness

Demko et al., [212] discussed about the effect of thermal insulation on single phase Cold and Warm dielectric HTS cables. Analysis was carried at 65 K, 200 g/s and 10 bar with LN₂ inlet on above specified cables and cable with cryostat damaged section. It was

observed that thermal insulating system not significantly degraded and cryostat damaged section need large back of refrigeration capacity.

Kottonau et al., [213] reported about the losses in HTS cables due to AC losses, current lead losses and cryostat thermal losses for cold dielectric. The energy losses per year for HTS cables was compared with the conventional overhead line cables.

2.2.2 Thermohydraulic characteristics

HTS cables are renowned for high power density and low transmission losses compared with conventional cables. However, these cables are cooled internally with cryogenic coolants in order to protect to HTS tapes from run-off. From the literature, it is identified that many researchers worked on Liquid Nitrogen (LN_2) [209], [214]–[218] as a cryogenic coolant due to its large latent heat of vaporization, superior economic benefits, low saturation temperature and high safety. In the recent past, various other cryogenic coolants are proposed by researchers for cooling the futuristic HTS cable such as gaseous Helium [219]–[221], Supercritical Nitrogen (SCN) [222], Supercritical Argon (SCAR) [223] and Nano cryogenic coolants [224], [225] These coolant will flows in the corrugated former of HTS cable and maintains the temperature below to the critical temperature of HTS superconductors.

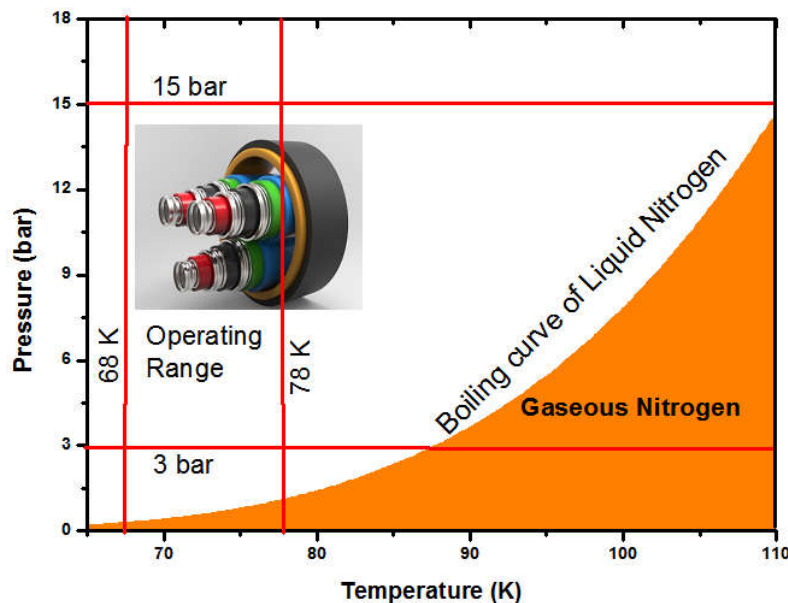


Figure 2.2 Operating range of HTS cable with boiling curve of Liquid Nitrogen (LN_2)

The safe operation of HTS cable depends on the operating pressure and temperature of the cryogenic coolant and high pressure is better in order to avoid the boiling of coolant as

shown in Figure 2.2. Further, under operating environments these HTS cables encounters heat fluxes from various sources such as AC losses and dielectric losses which are discussed in the previous section, heat-in-leaks from the ambient and leads at the termination and boiling of coolant takes place. Due to these losses, one or more cryogenic coolant stations should be installed for cooling HTS cables. Hence, there is a necessity to estimate the thermohydraulic characteristics of cryo-coolant used in the HTS cable between the terminations. The thermal characteristics associate with the temperature drop and the cooling capacity required, the hydraulic characteristics associated with pressure drop, mass flow rate and pumping power required to pump the cryogenic coolant.

The hydraulic characteristics in HTS cables are concerned with estimation of pressure drop and cooling capacity required for cooling HTS tapes. The former and cryostat in HTS cable are corrugated steel pipes with a low bending radius provide an advantage of higher flexibility. Define the operating range of Pressure and Temperature for better design of HTS cable. Figure 2.2 shows the operating range of HTS cable with boiling curve of LN₂ dependent on pressure (bar) and Temperature (K).

In this section various cooling strategy [226] employed for cooling HTS cables was discussed. Further, cooling of HTS cables from the joule heating losses, heat in leaks and dielectric losses are reported with different flows such as Parallel flow, counter flow, force flow, inline flow, conduction cooling, distributed cooling and natural flow (Thermo siphon effect).

Kottonau et al., 2019 [227] discussed about the different cooling strategies to investigate the maximum cable length, cable dimensions, pressure and temperature profiles in three phase concentric HTS cables with LN₂ as a cryogenic coolant. Further, for variable former diameter, cryostat diameter and mass flow rates the maximum possible cable lengths for different strategies was presented.

The Joule heating due to flow of transport current in each phase of three phase HTS cable leads to rise in the temperature corresponds to increased power dissipation. These heat due to electrical dissipation can be analyzed as radial heat conduction and signifies as internal heat source [228].

$$\dot{Q}_g(T) = \frac{Q'_{AC,tape}(T) \cdot f \cdot N_{tape}}{A_{cs}} \quad (2.52)$$

where, $Q'_{AC,tape}(T)$ is AC losses in HTS tape, f is frequency in Hz, N_{tape} is number of tapes, A_{cs} is cross sectional area of HTS phase

The transient three dimensional heat conduction equation of three phase HTS cable in cylindrical coordinates with constant thermal conductivity

$$\frac{d^2T}{dr^2} + \frac{1}{r} \frac{dT}{dr} + \frac{1}{r^2} \frac{d^2T}{d\theta^2} + \frac{d^2T}{dz^2} + \frac{\dot{Q}_g}{k} = \frac{\rho C}{k} \frac{dT}{dt} \quad (2.53)$$

Table 2.6 Thermohydraulic analysis summaries on HTS cables

Author	Analysis	Cable Cooling	Cable type	HTS type	Data	Losses considered
Furuse [46]	Numerical	Counter flow	Three-core CD, three-core WD and concentric	Bi-2223	100MVA class, 66 kVrms	AC losses, Shield current losses and heat in leaks
Fuchino [229]	Numerical	Counter flow	Three phase	N/A	500 MVA, 1.38 W/m losses	Heat in leaks
Demko [47]	Experimental	Counter flow	Tri-Axial	YBCO	1.5 W/m loss, heat load 1000 W each, 1750 g/s	Cryostat loss and termination heat loads
Miyagi [230]	Numerical	Counter flow	Tri-axial	BSCCO	66kV, 2.32 W/m in leaks, 200A	AC losses and heat in leaks
Fuchino [231]	Experimental	Counter flow	Three in one	N/A	160 kPa, 77K	Not considered
Zajaczkowski [43]	Numerical	Inline counter cooling	Three in one	BSCCO, YBCO	65-77K, 1, 1kW cooler	AC losses and thermal loads
Hu [232]	Simulation	Forced flow	Tria-Axial	N/A	66 kV, dielectric loss 0.1 W/(m K)	31.5 kA rms SLG fault current, 2sec
Yasui [233]	Numerical	Forced flow	Three in one	N/A	1.5 W/m heat load, 66kV	fault current of 31.5 kA for 2.0 sec

Maguire [234]	Experimental	Parallel flow	Three phase Cold Dielectric	BSCCO	574 MVA, 138kV, 600m, 2.4kA _{rms}	51 KA _{rms} fault @200ms
Maruyama [235]	Numerical	natural convection, forced flow or static	High voltage (HV)	YBCO	20 liter/min, PPLP, heat inflow 1W/m	AC losses

Many researchers carried out analysis on various HTS cables such as warm dielectric, cold dielectric, Coaxial, Tri axial and Triad. Various flow patterns were used for cooling HTS cables such as counter flow, parallel flow, conduction cooling, distribution, forced flow and natural flow (thermosyphon effect) from the losses that are encountered during operation. Ivanov et al., [236] conducted experiment on natural circulation (thermosyphon effect) and local heating of LN₂ for 200 m DC SC PT line. The dependence of pressure drop on effective temperature and circulation rate of LN₂ was calculated.

In the recent past, Ivanov et al., [237] discussed about the gravity fed of sub-cooled LN₂ using counter flow cooling system. The temperature and pressure profiles are drawn without considering the mechanical stability of HTS cable.

Recently, Chang et al.,[217] discussed about the variation of altitude on the cryogenic cooling system design with LN₂ for cooling the HTS cable. The variations in temperature and pressure are determined by using geographical variations and gravitational effects.

Posada et al., [44] discussed numerically about the axial conduction cooling by considering MgB₂ and BSCCO-2223 superconducting materials. An insulating layer with pure Copper at cryogenic temperature was proposed for designing a HTS cable. Further, the minimization of cable cost for a particular length to radius is discussed through modification of copper layer thickness.

Table 2.7 Summary of studies on thermohydraulic characteristics of HTS cables

Authors, Year	Analysis	Cable / Geometry	Remarks
Thadela et al., [238]	Computational	Warm dielectric cable	Corrugation pitch was varied with constant diameter and length AC losses and heat in leaks are considered
Kottonau	Computational	Concentric Three	Four different cooling strategies were

[227]		Phase	followed for cooling with variable annulus diameters Ratings are 150A, 12kV, HTS tape of 4 mm tape width and 3.4 mm thick PPLP insulation
Sudheer [169]	Experimental	Single phase cold dielectric	2G YBCO HTS tapes are used for 1kA current and low voltage (10V) transmission
Miyagi [230]	Numerical	Tri-axial Cable	For HTS cable operated at 77K, optimum mass flow rate is estimated for lower pressure drop with maximum possible cable length
Maruyama [239]	Experimental and Simulation	Not specified	Eccentric and center positions are used for analysis. Pressure drop in spiral corrugated pipe is 17 times larger than smooth pipe
Shabagin [228]	Numerical	Concentric three phase cable	AC losses, external heat loads and pressure losses are considered. Supply and return flow of LN ₂ and electrical dissipation power under AC currents are considered
Yasui [233]	Numerical (Computer programs)	Three in one	FDM method is used for solving heat transfer and heat conduction equations. Fanning's equation is used for pressure profiles and GASPACK software used to estimate fluid properties
Sato [240]	Computational	Kumatori experiment, Asahi substation models	Cryodata [®] GASPACK software was used for fluid properties. Induction refrigeration system was used for reduction in pressure fluctuations
Li [241]	Computational	Not specified	Variable pitches and depths are used for analyzing the temperature difference for different mass flow rates, heat leaks and AC losses.
Li [23]	Experimental and Computational	Not Specified	Smooth and corrugated pipes are used using Sub-cooled LN ₂ .
Dondapati [242]	Computational	Warm Dielectric Coaxial cable	YBCO and BSSCO tapes are used for analysis. AC and Dielectric losses, Heat in leaks are considered
Maruyama [58]	Numerical	Three core and Single core in one	Parallel flow of LN ₂ was considered in the analysis.
Ivanov [243]	Experimental	Not specified	Mass flow rate 4-17 lit/min was used. Pressure drop is cubic function and specific

			heat is quadratic function of length
Maruyama [168]	Experimental	Three core and Single core in one pipe cables	66 kV/5 kA (570 MVA) LC cable and 275 kV/3 kA (1420 MVA) HV cable are developed
Koh [244]	Experimental	Single large flexible cryostat	Sub cooled LN ₂ operating temperature 65 to 80K using Shell and tube heat exchanger. AC losses and heat leaks are considered
Lee [245]	Computational	2D Axi-symmetrical corrugated pipe	SIMPLE algorithm with QUICK and K-Epsilon models are used. Reynolds number varied from 10,000 to 80,000 for variable P/e ratio
Fuchino [231]	Experimental	Three single phase Coaxially shielded cables	Counter flow sub-cooled liquid nitrogen was used for cooling 10m length. Results are compared for smooth and corrugated pipes

For estimating the thermohydraulic characteristics, the electrical, mechanical and thermal issues are considered for better design and operation of HTS cable. The energy balance of the HTS power transmission cable can be used for determining the temperature distribution due to thermal and AC losses.

$$\rho(C_p)_{HTS} \frac{\partial T_{HTS}}{\partial t} = \left\{ \begin{array}{l} \frac{\partial}{\partial x} \left(K(T) A_{HTS} \frac{\partial T_{HTS}}{\partial x} \right) + \frac{\partial}{\partial y} \left(K(T) A_{HTS} \frac{\partial T_{HTS}}{\partial y} \right) + \\ \frac{\partial}{\partial z} \left(K(T) A_{HTS} \frac{\partial T_{HTS}}{\partial z} \right) + Q'_{AC} - \sum_i Q'_{Conv, LN_2, i} \end{array} \right\} \quad (2.54)$$

For constant thermal conductivity and 1-D energy balance for HTS cable during cryogenic liquid flow can be written as follows[86], [212]

$$\frac{\partial T_{HTS}}{\partial t} = \left(\frac{KA_{HTS}}{\rho(C_p)_{HTS}} \right) \frac{\partial^2 T_{HTS}}{\partial z^2} + Q'_{AC} - \sum_i Q'_{Conv, LN_2, i} \quad (2.55)$$

The energy balance equation for the liquid streams (former, return and annulus flow) in HTS cable can be determined by

$$\rho_i C_{p,i} \frac{\partial T_i}{\partial t} - m \cdot \frac{\partial h_i}{\partial z} - \sum_i Q'_{Conv, LN_2, i} = 0 \quad (2.56)$$

The convective heat transfer coefficient of the inner LN₂ flow solely depends on the inner corrugated former heat transfer while the outer LN₂ flow depends on the outer HTS cable and heat in leaks from the cryostat. The convective heat transfer coefficient can be expressed as

$$Nu = \frac{hD_h}{K_{LN_2}} = 0.023(Re)^{0.8} (Pr)^{0.3} \quad (2.57)$$

The pressure drop with respect to the LN₂ flow along the HTS cable length can be approximated as

$$\rho V dV + \frac{\rho f V^2}{2} \frac{\partial z}{D_h} + dp = 0 \quad (2.58)$$

The rate of heat transfer per unit length of HTS cable cryostat can be determined as [86], [203]

$$Q'_C = \frac{2\pi k_{eff} (T_{ambient} - T_{LN_2,i}(z))}{\ln\left(\frac{(r_0)_C}{(r_i)_C}\right)} \quad (2.59)$$

2.3 Literature review on Entropy generation rate

Entropy generation analysis is globally acknowledged as the most efficient approach for energy balance method in designing and optimizing the process and devices. It is a thermodynamic optimal method that provides convenience to the researchers as direct evaluation parameter for narrowing down the irreversibility in the system by evaluating the entropy generation. In this section, a critical review on entropy generation analysis for various applications in engineering system and fluid flows. The main focus of this work is to contribute the use of entropy generation minimization (EGM) techniques for designing and optimizing the engineering system and fluid flow problems in various geometries. Further, the mathematical formulations on entropy generation using governing equations, type of the analysis carried was presented for different applications and the expressions for Newtonian and Non-Newtonian fluid flows with different models and analysis are briefed. This chapter furthermore provides the importance of entropy generation on thermodynamic, fluid mechanics and heat transfer areas for future research in order to enhance the efficiency and effectiveness of engineering application process and devices.

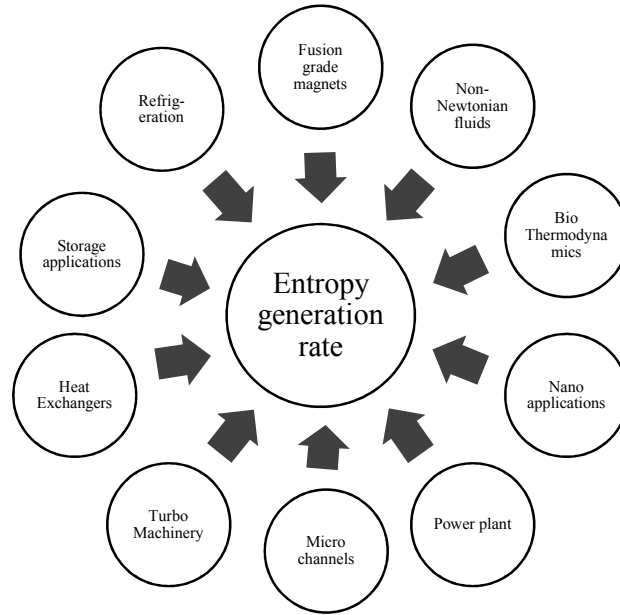


Figure 2.3 Entropy generation analysis as an optimum tool used in various applications of engineering systems

The technological developments in designing and operating the efficient systems are growing interest among the researchers because they are proven to be the most powerful drivers in every field of engineering. The study on available energy, effectiveness, efficiency and conservation of resources became more crucial currently due to unavailability of resources in such systems. In the past, the methods based on second law of thermodynamics set the guidelines to improve and analyze the systems of engineering. This law characterizes the loss of available energy due to irreversibility such as mechanical (vibrations and friction) and thermodynamic (non- equilibrium phenomenon) effects while operating the real system[246]. Further, the proper mathematical formulations on concepts entropy and its production with new breakouts [247] are studied. The generalized thermodynamic formulation of total entropy generation was given by

$$S_{gen}^{\bullet} \geq 0; S_{gen}^{\bullet} = \frac{dS}{dt} - \sum_{j=0}^n \frac{q_j}{T_j} - \sum_{in} m \cdot s + \sum_{out} m \cdot s \text{ (irreversible process)} \quad (2.60)$$

$$S_{gen}^{\bullet} = 0; \text{ (reversible process)}$$

The thermodynamic irreversibility from various sources in the system leads to generation of entropy [248]. The analysis used for determining and minimizing this irreversibility can be stated as entropy generation Analysis (EGA). Entropy Generation Minimization (EGM) is a thermodynamic optimization technique which plays a major role in problem formulation, modeling, designing and optimization using a set of constrains subjected in

operation of specific engineering system [249]. The major objective of the EGM method is to identify the design or configuration with minimal entropy generation rate (EGR) for variable design variables such as operating conditions, dimensions, type of geometries, flow patterns etc. EGR is a function of overall physical characteristics of the subsystems where the entropy is generated at the boundaries due to the heat, mass transfer and fluid flow currents[250].

The focus of this section is only on contributions oriented toward the use of entropy generation analysis as a tool for enhancing the thermodynamic design and optimization of engineering systems by minimizing the entropy generation rate.

In this section a brief literature of EGM in various applications is presented. From the literature it is observed that the role of EGM in optimizing the parameters for increasing the efficiency of system is critical.

2.3.1 Fusion grade magnets

EGM method was used to optimize the mass flow rate of Supercritical Helium (SHe) in fusion grade magnet applications with cable in conduit conductors (CCIC) by Dondapati et al., 2014 [5]. Computational method was used for optimizing mass flow rate of turbulent forced convection using EGM.

$$S_{gen}^{\bullet} = \frac{K}{T^2} \left[\left(\frac{\partial T}{\partial x} \right)^2 + \left(\frac{\partial T}{\partial y} \right)^2 + \left(\frac{\partial T}{\partial z} \right)^2 \right] + \frac{\mu}{T} \left\{ 2 \left[\left(\frac{\partial u}{\partial x} \right)^2 + \left(\frac{\partial v}{\partial y} \right)^2 + \left(\frac{\partial w}{\partial z} \right)^2 \right] + \left(\frac{\partial u}{\partial y} + \frac{\partial v}{\partial x} \right)^2 \right. \\ \left. + \left(\frac{\partial u}{\partial z} + \frac{\partial w}{\partial x} \right)^2 + \left(\frac{\partial w}{\partial y} + \frac{\partial v}{\partial z} \right)^2 \right\} \quad (2.61)$$

2.3.2 Micro channels

Eyuphan Manay et al., 2018 [251], investigated on heat sinks with micro channels using nano fluids (TiO₂+pure water). Entropy generation was calculated experimentally for variable heights of channels and observed that addition of nano particles decrease the rate of entropy generation.

$$S_{gen}^{\bullet} = \underbrace{\frac{q^2 \pi D_h^2}{KT^2 Nu(Re, Pr)}}_{Thermal\ term} + \underbrace{\frac{8m^3 f(Re)}{\pi^2 \rho^2 TD_h^5}}_{Frictional\ term} \quad (2.62)$$

$$Nu = 13.1762(Re.Pr)^{0.154} \left(\frac{H}{W} \right)^{0.339} (1 + \phi)^{20.35} \quad (2.63)$$

$$f = 32.63(\text{Re})^{-0.938} \left(\frac{H}{W} \right)^{-0.02} (1 + \phi)^{17.35} \quad (2.64)$$

Entropy generation in micro channels with steady 3D laminar incompressible nano fluid flow was discussed in the past [252] and the dimensionless numbers are used for presenting the results.

$$S_G = S_{gen} \left(\frac{KT_0^2}{q^2} \right) = (S_{gen,thermal} + S_{gen,frictional}) \left(\frac{KT_0^2}{q^2} \right) \quad (2.65)$$

$$S_{gen,thermal} = \frac{K}{T^2} \left[\left(\frac{\partial T}{\partial x} \right)^2 + \left(\frac{\partial T}{\partial y} \right)^2 + \left(\frac{\partial T}{\partial z} \right)^2 \right] \quad (2.66)$$

$$S_{gen,frictional} = \frac{\mu}{T} \left\{ 2 \left[\left(\frac{\partial u}{\partial x} \right)^2 + \left(\frac{\partial v}{\partial y} \right)^2 + \left(\frac{\partial w}{\partial z} \right)^2 \right] + \left(\frac{\partial u}{\partial y} + \frac{\partial v}{\partial x} \right)^2 + \left(\frac{\partial u}{\partial z} + \frac{\partial w}{\partial x} \right)^2 + \left(\frac{\partial v}{\partial z} + \frac{\partial w}{\partial y} \right)^2 \right\} \quad (2.67)$$

$$S_G = \frac{q^2}{KT_0^2} \left[\underbrace{\frac{16}{Pe^2} \left(\frac{T_0^2}{T} \right)}_{\text{Thermal generation source}} + \underbrace{(2R - R^3) \left(\frac{T_0^2}{T^2} \right) + \frac{\phi T_0 R^2}{T}}_{\text{Frictional source}} \right] \quad (2.68)$$

where, Pe is Peclet number, r_0 is tube radius, R is non dimensionless radius

$$Pe = \frac{2r_0 \rho C_p U}{K}, \phi = \frac{16KT_0 \mu U^2}{q^2 r_0^2}, R = \frac{r}{r_0}$$

2.3.3 Heat Exchangers

Sahiti et al., 2008 [253] discussed the technique of EGM for the heat exchanger with pin fins. Experimental analysis was carried out to determine the pressure drop and heat transfer rate characteristics. Optimization was carried out by considering the flow length of heat exchanger and fin lengths.

$$S_{gen}^* = (m \cdot C_p)_a \ln \left(\frac{T_{a,out}}{T_{a,in}} \right) - m_a R_a \ln \left(\frac{P_{a,out}}{P_{a,in}} \right) + (m \cdot C_p)_w \ln \left(\frac{T_{w,out}}{T_{w,in}} \right) \quad (2.69)$$

Arivazhagan et al., 2013 [254] investigated on the EGM of tubes filled with porous media in a Shell and Tube heat exchanger. Experimental investigation was carried out with chips from machining operations to find the irreversibility considering the Reynolds number.

$$S_{gen}^{\bullet} = \underbrace{\dot{m}_H \Delta S_H + \dot{m}_C \Delta S_C}_{\text{Finite temperature difference}} + \underbrace{\sum (m^{\bullet} C_p)_j \ln \frac{T_0}{T_{j,i}}}_{\text{Fluid mixing}} + \underbrace{\frac{\Delta P}{\rho} m^{\bullet} \frac{\ln \left(\frac{T_0}{T_i} \right)}{T_0 - T_i}}_{\text{Fluid friction}} \quad (2.70)$$

The combined economic and entropy generation for parallel and counter flow heat exchanger was investigated by Genić et al., 2018 [255]. Numerical investigation was carried by considering the NEGU function and compared the results with experimental data using case study.

2.3.4 Refrigeration

EGM was used for assessing the performance of active magnetic regenerator using coupled energy and flow field of liquid and solid phases by Trevizoli et al., 2017 [256]. The working fluid used was water and solid particles are a bed of spherical gadolinium. Variable geometry and Face area are optimized for specified temperature range and cooling capacity.

Vapor Compression Refrigeration System (VCRS) with micro channel condenser and fins of R-134a as refrigerant was studied by Türkakar et al., 2016[257], dimensional optimization of an evaporator in a Micro scale refrigeration cycle using entropy generation was discussed by Göker et al., 2015 [258], thermodynamic analysis of ejector refrigeration cycle with combined kalian cycle was discussed by Seckin 2018 [259] to improve the efficiency. Thu et al.,2013 [260], investigated entropy generation on adsorption cooling cycle of a chiller for different processes such as de-superheating, flushing, heat and mass transfer of liquid refrigerant.

Exergy and energy analysis of Entropy diagram of Absorption refrigeration system with ammonia water mixtures was investigated by Aparecida et al., 2017 [261]. Non-linear regression program was used to calculate the enthalpy of mixtures and the relation between the enthalpy and concentration diagram in liquid phase at 80 °C to -40 °C.

2.3.5 Storage applications

The entropy generation method was used to analyze and optimize the cost factors included in thermal packed bed reservoir for electrical storage applications by White et al., 2016 [262]. The analysis on Latent heat storage systems on molten salt storage Thermo cline [263] and storage tank [264], gas hydrated cool storage [265] and Shell and tube heat

exchanger using phase change material was studied by Guelpa et al., 2013 [266] using the enthalpy method.

2.3.6 Power plants

Laskowski et al., 2016 [267] reported utilization of EGM method to optimize the mass flow rate of cooling water under variable loads in a power plant. Various components such as condenser, cooling water pump and turbine.

For cooling tower

$$S_{gen,CT}^{\bullet} = m_2^{\bullet} C_2 \ln \frac{T_{2,o}}{T_{2,i}} + \frac{\lambda m_2^3}{2T_2 \rho_2^2 F_2^2} \frac{L}{d_{2,i}} \quad (2.71)$$

$$\text{Where, } \lambda = \frac{0.25}{\left[\log \left(\frac{k}{3.72 d_{2,i}} + \frac{5.74}{\text{Re}_2^{0.9}} \right) \right]^2}$$

$$\text{Condenser steam side, } S_{1,gen}^{\bullet} = \frac{-Q^{\bullet}}{T_s} \quad (2.72)$$

$$\text{Turbine, } S_{t,gen}^{\bullet} = m_1^{\bullet} (S_{or} - S_b) \quad (2.73)$$

$$\text{Pump, } S_{p,gen}^{\bullet} = m_2^{\bullet} (S_{po} - S_{pi}) \quad (2.74)$$

Total entropy generation

$$S_{gen}^{\bullet} = S_{2,gen}^{\bullet} - S_{1,gen}^{\bullet} + S_{t,gen}^{\bullet} + S_{p,gen}^{\bullet} \quad (2.75)$$

A critical review on energy and exergy analysis of thermal power plant was done by Kaushik et al., 2011 [268] and efficiency improvement was discussed by Haseli 2018 [269] using specific entropy generation.

2.3.7 Solar and nano fluid applications

The entropy generation rate and Thermohydraulic performance of solar collectors [270] was investigated computationally for two different geometries. Further, entropy generation, fluid flow and heat transfer rate with water alumina nano fluid in solar collector configured with tube on sheet flat plate [271] was investigated. Further, to improve the efficiency of the designed FPSC [272], SiO₂ nano particles with water based fluids are

used and entropy generation method was investigated. Pressure drop and entropy generation are used in plate solar collector [273] to improve the performance using different metal oxide nano fluids.

From the literature, it is observed that various cooling strategies are proposed in the past using liquid nitrogen (LN₂) as a cryogenic coolant. In the working conditions, the HTS cables are encountered with internal heat generation due to the flow of current in the HTS cables, heat in leaks and losses in the various layers of the cable. Due to this, boiling of LN₂ takes place and causes the multiphase flow which adversely creates the challenges in heat transfer rate and thereby the current carrying capacity of HTS cable will be degraded. Hence, there is a huge thrust in designing the HTS cable by considering the thermohydraulic performance and entropy generation rate for better and efficient cooling from the head loads.

2.4 Recent studies on HTS cables and Entropy generation rate

A critical literature was done on the recent studies that discussed about the thermohydraulic issues of different HTS cables at various heat loads, different inlet temperatures and flow rates. Further, issues encountered by the HTS cables during operation such as AC losses, dielectric losses, heat-in-leaks etc was presented. Furthermore, the studies on entropy generation rate in the superconducting applications was discussed. These literature is used for identifying the research gaps for the present work and research objectives are framed. In Table 2.8, recent studies on thermohydraulic characteristics and entropy generation rate in the superconducting applications was presented.

Table 2.8 Recent studies on thermohydraulic characteristics, issues encountered by HTS cable during operation and entropy generation rate in superconducting applications

Authors, Year	Analysis	Study	Remarks	Reference
Dondapati 2020	Computational	Thermohydraulic analysis on futuristic HTS cables with Super Critical Nitrogen (SCN) as cryogenic coolant was presented. For the analysis mass flow rates ranging from 16 L/min to 20 L/min and heat loads due to	SCN can be used as a coolant for cooling the HTS cables at higher critical temperatures because of lower pumping power required for circulation and better cooling capacity due to higher thermal conductivity and specific heat.	[274]

		AC losses and heat intrusions ranging from 1 W/m to 3 W/m are considered.	Further SCN can be used for cooling Hg based superconducting tapes.	
Li et al., 2020	Experimental	Design of three phase cold dielectric HTS cable for 35 kV and 1 kA with YBCO tapes and coolant temperature range of 72 to 77 K. at a pressure of 0.5 MPa was reported.	The AC voltage test and lightning impulse voltage test was conducted and demonstration project was operated stably and successfully for more than 20 months with 20 to 200 A .	[275]
Pi et al., 2020	Experimental and computational	A dielectric insulation design of three phase concentric HTS cable strength of PPLP for a 10 kV with LN ₂ as cryogenic coolant was studied.	AC voltage endurance test and the lightning impulse test are done to investigate the stress cone and main insulation using PPLP at the frequency of 50 Hz. Under the voltage of 30 kV , the design of HTS cable meet the requirements.	[276]
Dondapati et al., 2019	Computational	Entropy generation minimization technique was used to optimize the mass flow rate of Supercritical Helium (She) in CICC at different inlet temperatures and porosities.	For safe and economic operation of CICC, flow rate of 13 g/sec at operating temperature of 4.5 K and porosity of 0.37 to achieve higher heat transfer and lower pumping power.	[277]
Kottonau et al., 2019	Analytical	Thermohydraulic analysis was carried to design the HTS cable for long length with minimal diameter and four different cooling strategies are considered.	The higher cooling capacities can be achieved with the single sided annuls cooling with external return line. Further, the compact cable can be observed with the single sided cooling without annulus side which can reduce the annulus gap by 30 %.	[227]
Lee et al., 2019	Experimental and simulation	The thermal characteristics are studied in HTS cable	From the axial temperature distribution, the maximum	[278]

		with Go- return and external return cooling methods using LN ₂ .	temperature obtained by the HTS cable for 1 km is 73.6 K. Further, it is reported that HTS cable with return line is better option for circulating the LN ₂ .	
Lee et al., 2019	Simulation	Thermohydraulic analysis of HTS cable with sub-cooled LN ₂ using inlet temperature of 70K and flow rate of 0.51 kg/sec was studied using 1D node network analysis and CFD in South Korea. The influence of AC losses and heat penetrations on the HTS cables are considered for the analysis.	The 1D network model analysis shows that the temperature rise and the pressure drop across the cable are 6.98 K and 5.78 bar. Further, it was confirmed that the flow rate of 0.51 kg/sec and inlet temperature of 66.5K meets the demand of HTS cable for the entire route.	[279]
Kalsia et al., 2019	Computational	Thermohydraulic analysis with counter flow cooling in different corrugation topologies such as circular, triangular and rectangular was reported.	Pressure drop in the triangular corrugations are higher than the rectangular and circular corrugations. Higher heat transfer rate was identified with the rectangular corrugations compared to the other corrugations. The influence of heat fluxes on the hydraulic characteristics are not significant for different corrugations.	[280]
Peng et al., 2019	Experimental	The dielectric strength of Kraft paper and PPLP was carried at 0.1MPa with LN ₂ as cryogenic coolant using three parameter Weibull distribution based on grey model GM(1,1) .	The cryogenic dielectric strength of PPLP is higher than the Kraft paper. Hence, PPLP was more suitable according to Breakdown strength under the conditions of DC, AC and impulse lighting.	[281]
Kalsia et	Computational	Thermohydraulic analysis	Hydraulic characteristics are	[282]

al., 2019		with counter flow cooling in circular corrugation geometry under the influence of different heat fluxes and heat generations was studied.	not affected by the influence of heat fluxes and heat generations. Higher pressure drops are observed due to the corrugations at the inner and outer former. However, efficient cooling was possible with the counter flow cooling than parallel flow cooling.	
Thadela et al., 2019	Computational	The influence of Corrugation pitch, AC losses and heat in leaks on thermohydraulic characteristics of HTS was studied to predict the pumping power and cooling capacity at inlet temperatures of 65 K and 77K.	The increase in corrugation pitch of corrugated former increases the pressure drop and decreases the cooling capacity. Higher the bulk temperature of cryogenic coolant higher heat transfer rate and lower pressure drop.	[283]
Kalsia et al., 2019	Analytical	The maximum possible cable length of HTS cable for different heat fluxes ranging from 2.3-2.6 W/m are considered for a flow rate of 20-35 L/min. The analysis was carried to identify the temperature distribution in the cold dielectric HTS cable using 1-D analysis.	Lower heat flux and higher flow rates are required to maintain the LN ₂ without boiling. The maximum temperature attained at the end of the HTS cable is 79.63 K at lower flow rate. The maximum length that HTS can be installed for 2.5 km within the operating ranges.	[284]
Sudheer et al., 2018	Experimental	The voltage – current(V-I) characteristics of Single phase cold dielectric HTS cables at 77K cooled with LN ₂ was discussed	2G YBCO HTS tapes are used for 1kA current and low voltage (10V) transmission.	[169]

Maruyama et al., 2018	Experimental and Simulation	Pressure drop analysis was carried with spiral corrugated cryostat pipe and compared with the smooth pipe.	Eccentric and center positions are used for analysis. Pressure drop in spiral corrugated pipe was 17 times larger than smooth pipe.	[239]
Suttell et al., 2018	Experimental and Simulation	HTS DC cables was operated with Gaseous Helium (GHe) and the performance is optimized to utilize the minimum pumping power with minimum heat loads.	The operating temperature maintained in the cryocooler signifies the thermal efficiency of cryocooler. The optimum flow rate of GHe is observed to be 3.8 g/s with 20.5 % lesser power consumption compared with the original cryostat.	[220]
Anand et al., 2018	Analytical	Thermophysical properties of nano particle based LN ₂ was used in the HTS cables to enhance the thermohydraulic characteristics. Different diameters of CuO, Al ₂ O ₃ and Fe ₂ O ₃ are dispersed with the volume concentration of 1-5 % at operating ranges of 33.9 bar and 65-75 K temperature.	At the volume concentration of 5 %, dispersion of Fe ₂ O ₃ in LN ₂ shows better thermophysical properties at an diameter of 13nm. Density, Viscosity and thermal conductivity are increasing with the increase in the volume concentration and decreases with increase in temperature and opposite trends was observed for specific heat .	[285]
Sousa et al., 2018	Simulation	Transient analysis on installation of SFCL in series with the three phase HTS cable utilizing single direction flow of cryocoolant for protecting the power network with different copper stabilizer thickness was reported.	During fault conditions, the thin layer copper stabilizer reduces the higher faults. However, large increase in the outlet temperature of the coolant was observed. Hence, installation of SFCL will safe guard the HTS tapes from quench by avoiding the	[286]

			boiling of coolant.	
Gadekula et al., 2017	Numerical	Feasibility studies on dispersion of CuO nano particles with volume concentration (1-5%) in LN ₂ for efficient cooling the HTS cable operating at a temperature range of 65-75 K was presented.	Dispersion of 5 % CuO nano particles in the LN ₂ enhances the heat transfer rate compared to LN ₂ . Higher cooling capacities are possible with dispersion of TiO ₂ nano particles in LN ₂ .	[224]

Motivated by the challenges involved in the design of high-temperature superconducting cables and the involved thermohydraulic issues, the present investigation focused on estimation of the entropy generation rate in HTS cables and identified the lowest entropy generation rate at which lower pumping power and higher cooling capacity is possible.

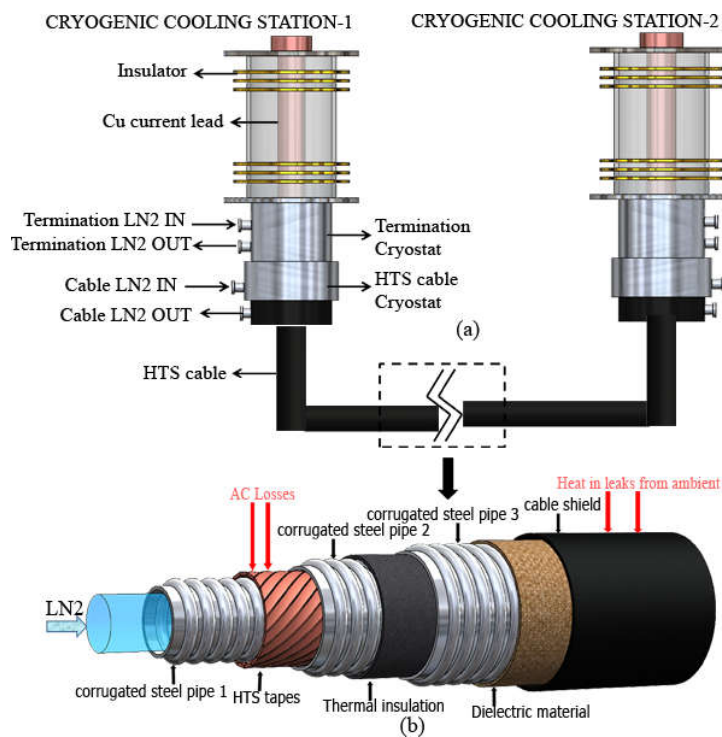


Figure 2.4 (a) Schematic of HTS cooling system with LN₂ as cryogenic coolant (b) HTS cable configuration employed for estimating entropy generation rate and thermohydraulic performance

HTS cables cooled with liquid nitrogen (LN₂) are used for efficient power transmission. A corrugated steel pipe is used as former, around which HTS tapes are wound. These HTS tapes carry large current densities which encounter AC losses [28]–[32], [34]–[36], [287] and dielectric losses [38]–[42]. In addition, losses such as heat-in-leaks [43]–[47] hinders

the thermal performance of HTS cables. Hence, to accommodate such losses higher flow rates of LN₂ is required to cool the HTS cables which require higher pumping power for the circulation of LN₂ between the end terminations.

In this context, the cooling requirement in HTS cables is associated with the estimation of pressure drop and heat transfer rate for predicting the pumping power and cooling capacity. However, the measurement of pumping power and cooling capacity through experimental techniques are expensive and involve complicated instrumentation. Hence, Computational Fluid Dynamics (CFD) is one such alternate approach for predicting the thermohydraulic performance in HTS cables [242]. During the flow of LN₂ through corrugated pipe various dissipative mechanisms are involved, such as the formation of eddies, which results in the development of velocity and temperature gradients leading to entropy generation. Hence, to obtain higher cooling capacity along with minimum pumping power, the estimation of entropy generation is an essential procedure. To author's knowledge, EGM technique has not been performed for HTS cables. Hence, the present work deals with the development of a computational model of HTS cable. Various flow rates of LN₂ under different heat loads are analyzed in order to obtain the optimum performance of HTS cable.

2.5 Research gaps

From the critical review of literature, it is observed that the demand for development of power efficient transmission and distribution of HTS cables in smart power grids is essential.

- ✓ The power demand of Indian power system is expanding exponentially and expected to reach 400GW by 2022. The efficient internally cooled long length HTS cables to handle higher currents instead of large transmission networks with overhead transmission line are under development in India.
- ✓ The various cooling strategies and the optimized operating parameters used in HTS cable are not available under working environment to safeguard the HTS tapes from run-off.
- ✓ Thermo-hydraulic analysis with flow of temperature dependent LN₂ in HTS cable and inherent heat loads due to AC losses and heat-in-leaks with different cable geometries was not done.
- ✓ Entropy generation rate analysis for efficient power transmission to compensate the loss is not available. Optimization of mass flow rate to meet environmental,

technical and socio-economic challenges at cryogenic temperatures in HTS cables is not done.

- ✓ Influence of thermohydraulic performance with return line of cryogenic coolant is not done.
- ✓ Thermohydraulic investigation with SCN in the futuristic HTS cables is not studied.
- ✓ Thermohydraulic investigations on dispersion of nano particles at different heat loads and inlet temperatures are not done.

2.6 Objectives of the present work

The aim of this work is to investigate the entropy generation rate with flow of LN₂ in the HTS cables. Further, the mass flow rate is optimized on the basis of entropy generation rate in HTS cable. The variables considered to achieve the objectives are heat loads on HTS cables, flow rate and inlet temperature of LN₂.

The vital objectives are enlisted as follows

- To estimate Hydraulic characteristics such as velocity, pressure drop, friction factor and pumping power due to flow of temperature dependent LN₂ in HTS cables.
- To estimate Thermal characteristics such as Temperature, heat transfer, Nusselt Number and Cooling capacity due to flow of temperature dependent LN₂ in HTS cables.
- To estimate the Volumetric Entropy Generation Rate (EGR) due to the velocity and temperature gradients in HTS cables.
- Optimization on Pumping Power and Cooling Capacity using Entropy Generation Minimization (EGM) approach.

From the extensive literature review, research gaps are identified and objectives are framed. In order to achieve the objectives of the present work, mathematical formulation for entropy generation through the HTS cable, conservation equations and turbulence equations to study the fluid behavior in the corrugated former of HTS cable are discussed as a closure problem in the next chapter. Further, the boundary conditions considered for the analysis and the temperature dependent thermophysical properties of LN₂ are also discussed.

3 MATHEMATICAL FORMULATION

3.1 Introduction

The research gaps identified from the literature are utilized to frame the research objectives of the present study. Computational Fluid Dynamics is used for achieving the objectives defined in the previous chapter. The mathematical formulation of the governing equations such as conservation of mass, momentum and energy that are required for solving the closure problems are presented in this chapter. The flow of LN_2 through HTS cables encounters turbulences due to corrugations and forced flow through the corrugated former. The thermohydraulic characteristics and entropy generation rate for internally forced cooled HTS cables are computationally investigated using the time averaged Reynolds Averaged Navier-Stokes (RANS) equations. The Finite Volume Method of discretization with $\kappa - \varepsilon$ turbulence equations are used as closure to the RANS equations is discussed in this chapter. Further, boundary conditions imposed on the HTS cable for analyzing thermohydraulic characteristics and entropy generation rate are discussed. Furthermore, the solution procedure employed for achieving the objectives of the present work is discussed.

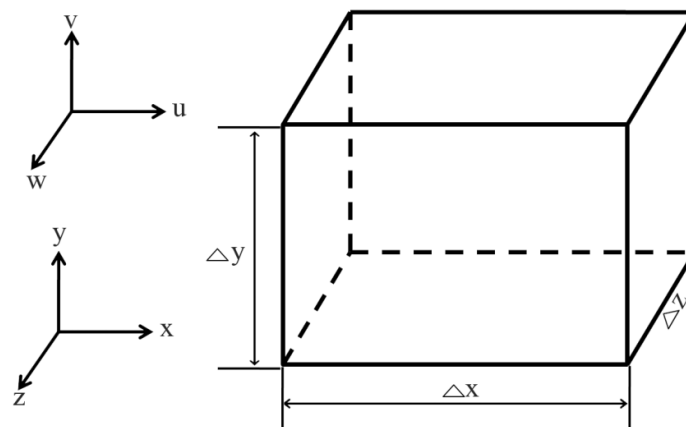


Figure 3.1 Control volume considered in the flow field

3.2 General conservation equations

The general conservation equations applicable for three dimensional flow fields in the control volume are discussed in this section. In a three dimensional flow field the control volume (CV) would be $\Delta x \Delta y \Delta z$ as shown in the Figure 3.1. Considering that u , v and w are velocity components in the x , y and z -directions respectively.

3.2.1 Conservation of mass

The rate of change of mass that is trapped within the control volume is equal to the mass flux crossing the surface

$$\frac{\partial M_{CV}}{\partial t} = \sum \dot{m}_{in} - \sum \dot{m}_{out} \quad (3.1)$$

where, M_{CV} is the mass trapped within the control volume, \dot{m}_{in} and \dot{m}_{out} are the mass flow rate in and out of the control volume.

Solving the above equation

$$\begin{aligned} \frac{\partial}{\partial t}(\rho \Delta x \Delta y \Delta z) = \rho u \Delta y \Delta z + \rho v \Delta x \Delta z + \rho w \Delta x \Delta y - \left[\rho u + \frac{\partial}{\partial x}(\rho u) \Delta x \right] \Delta y \Delta z \\ - \left[\rho v + \frac{\partial}{\partial y}(\rho v) \Delta y \right] \Delta x \Delta z - \left[\rho w + \frac{\partial}{\partial z}(\rho w) \Delta z \right] \Delta x \Delta y \end{aligned} \quad (3.2)$$

Dividing equation (3.2) with the control volume $\Delta x \Delta y \Delta z$,

$$\frac{\partial \rho}{\partial t} = - \frac{\partial(\rho u)}{\partial x} - \frac{\partial(\rho v)}{\partial y} - \frac{\partial(\rho w)}{\partial z} \quad (3.3)$$

Rewriting the above equation

$$\frac{\partial \rho}{\partial t} + \frac{\partial(\rho u)}{\partial x} + \frac{\partial(\rho v)}{\partial y} + \frac{\partial(\rho w)}{\partial z} = 0 \quad (3.4)$$

Solving equation(3.4),

$$\frac{\partial \rho}{\partial t} + u \frac{\partial \rho}{\partial x} + v \frac{\partial \rho}{\partial y} + w \frac{\partial \rho}{\partial z} + \rho \left(\frac{\partial u}{\partial x} + \frac{\partial v}{\partial y} + \frac{\partial w}{\partial z} \right) = 0 \quad (3.5)$$

Equation (3.5) can also be written as

$$\frac{D\rho}{Dt} + \rho \nabla \cdot \mathbf{V} = 0 \quad (3.6)$$

where, \mathbf{V} is velocity vector (u, v, w) and $\frac{D}{Dt}$ is substantial derivative

$$\frac{D(\bullet)}{Dt} = \frac{\partial(\bullet)}{\partial t} + u \frac{\partial(\bullet)}{\partial x} + v \frac{\partial(\bullet)}{\partial y} + w \frac{\partial(\bullet)}{\partial z}$$

For steady flow, equation (3.4) can be written as

$$\frac{\partial(\rho u)}{\partial x} + \frac{\partial(\rho v)}{\partial y} + \frac{\partial(\rho w)}{\partial z} = 0 \quad (3.7)$$

For incompressible ($\rho=c$) and steady flow, equation (3.4) can be written as

$$\frac{\partial u}{\partial x} + \frac{\partial v}{\partial y} + \frac{\partial w}{\partial z} = 0 \quad (3.8)$$

Vector notation of conservation of mass

$$\frac{\partial \rho}{\partial t} + \nabla \cdot (\rho \mathbf{V}) = 0 \quad (3.9)$$

For steady flow,

$$\nabla \cdot (\rho \mathbf{V}) = 0 \quad (3.10)$$

For incompressible ($\rho=c$) and steady flow,

$$\nabla \cdot \mathbf{V} = 0 \quad (3.11)$$

3.2.2 Conservation of momentum

The conservation of momentum can be derived from Newton's Second Law of motion.

These can be solved from the force balance on a control volume.

$$\frac{\partial}{\partial t} (M v_n)_{CV} = \sum F_n + \sum \dot{m}_{in} v_n - \sum \dot{m}_{out} v_n \quad (3.12)$$

where, n is direction considered for analysis, v_n is fluid velocity in n direction, F_n is forces in n direction.

The forces acting on a control volume are volumetric forces and surface forces

1) Volumetric forces are characterized into

a) Gravitational forces due to self weight acting on the fluid, $F_g = \rho F_b dv$

b) Electro and Magnetic forces

In electric field, electromotive force is defined as ratio of electric force to charge in Coulomb

$$\bar{E} = \frac{\bar{F}}{q}$$

Force on a current carrying wire

$$F = Il \times B$$

where, I is current flow in a conductor and l is length of wire

From Lorentz force law,

$$\vec{F} = \underbrace{q\vec{E}}_{\text{Electrical force}} + \underbrace{q\vec{v} \times \vec{B}}_{\text{Magnetic force}}$$

- 2) Surface forces are characterized into Pressure forces and Viscous or frictional forces (Normal and shear forces).

Considering the forces along the x-direction yields

$$\left\{ \begin{array}{l} \frac{\partial}{\partial t}(\rho u \Delta x \Delta y \Delta z) + (\rho u^2) \Delta y \Delta z - \left[\rho u^2 + \frac{\partial}{\partial x}(\rho u^2) \Delta x \right] \Delta y \Delta z + (\rho uv) \Delta x \Delta z \\ - \left[\rho uv + \frac{\partial}{\partial y}(\rho uv) \Delta y \right] \Delta x \Delta z + (\rho uw) \Delta x \Delta y - \left[\rho uw + \frac{\partial}{\partial z}(\rho uw) \Delta z \right] \Delta x \Delta y \\ \sigma_x \Delta y \Delta z - \left(\sigma_x + \frac{\partial}{\partial x} \Delta x \right) \Delta y \Delta z - \tau_{xy} \Delta x \Delta z + \left(\tau_{xy} + \frac{\partial \tau_{xy}}{\partial y} \Delta y \right) \Delta x \Delta z - \tau_{xz} \Delta x \Delta y \\ + \left(\tau_{xz} + \frac{\partial \tau_{xz}}{\partial z} \Delta z \right) \Delta x \Delta y + F_{BX} \Delta x \Delta y \Delta z \end{array} \right\} = 0 \quad (3.13)$$

Dividing equation (3.13) with $\Delta x \Delta y \Delta z$ in the limit $(\Delta x, \Delta y, \Delta z) \rightarrow 0$

$$\rho \frac{Du}{Dt} + u \left[\frac{D\rho}{Dt} + \rho \left(\frac{\partial u}{\partial x} + \frac{\partial v}{\partial y} + \frac{\partial w}{\partial z} \right) \right] = -\frac{\partial \sigma_x}{\partial x} + \frac{\partial \tau_{xy}}{\partial y} + \frac{\partial \tau_{xz}}{\partial z} + F_{BX} \quad (3.14)$$

From conservation of mass equation (3.6)

$$\frac{D\rho}{Dt} + \rho \left(\frac{\partial u}{\partial x} + \frac{\partial v}{\partial y} + \frac{\partial w}{\partial z} \right) = 0$$

Hence, equation (3.14) can be simplified as

$$\rho \frac{Du}{Dt} = -\frac{\partial \sigma_x}{\partial x} + \frac{\partial \tau_{xy}}{\partial y} + \frac{\partial \tau_{xz}}{\partial z} + F_{BX} \quad (3.15)$$

Relating the surface forces to the local flow field

$$\begin{aligned}
\sigma_x &= P - 2\mu \frac{\partial u}{\partial x} + \frac{2}{3}\mu \left(\frac{\partial u}{\partial x} + \frac{\partial v}{\partial y} + \frac{\partial w}{\partial z} \right) \\
\tau_{xy} &= \mu \left(\frac{\partial u}{\partial y} + \frac{\partial v}{\partial x} \right) \\
\tau_{xz} &= \mu \left(\frac{\partial u}{\partial z} + \frac{\partial w}{\partial x} \right)
\end{aligned} \tag{3.16}$$

Substituting equation (3.16) in equation (3.15) yields

$$\begin{aligned}
\rho \frac{Du}{Dt} &= -\frac{\partial P}{\partial x} + \frac{\partial}{\partial x} \left[2\mu \frac{\partial u}{\partial x} - \frac{2\mu}{3} \left(\frac{\partial u}{\partial x} + \frac{\partial v}{\partial y} + \frac{\partial w}{\partial z} \right) \right] + \frac{\partial}{\partial y} \left[\mu \left(\frac{\partial u}{\partial y} + \frac{\partial v}{\partial x} \right) \right] \\
&\quad + \frac{\partial}{\partial z} \left[\mu \left(\frac{\partial u}{\partial z} + \frac{\partial w}{\partial x} \right) \right] + F_{BX}
\end{aligned} \tag{3.17}$$

Considering the fluid flow as compressible and viscosity as constant, equation (3.17) can be written as

$$\rho \left(\frac{\partial u}{\partial t} + u \frac{\partial u}{\partial x} + v \frac{\partial u}{\partial y} + w \frac{\partial u}{\partial z} \right) = -\frac{\partial P}{\partial x} + \mu \left(\frac{\partial^2 u}{\partial x^2} + \frac{\partial^2 u}{\partial y^2} + \frac{\partial^2 u}{\partial z^2} \right) + F_{BX} \tag{3.18}$$

Similarly, conservation of momentum in y-direction and z-direction can be written as

$$\begin{aligned}
\rho \left(\frac{\partial v}{\partial t} + u \frac{\partial v}{\partial x} + v \frac{\partial v}{\partial y} + w \frac{\partial v}{\partial z} \right) &= -\frac{\partial P}{\partial y} + \mu \left(\frac{\partial^2 v}{\partial x^2} + \frac{\partial^2 v}{\partial y^2} + \frac{\partial^2 v}{\partial z^2} \right) + F_{BY} \\
\rho \left(\frac{\partial w}{\partial t} + u \frac{\partial w}{\partial x} + v \frac{\partial w}{\partial y} + w \frac{\partial w}{\partial z} \right) &= -\frac{\partial P}{\partial z} + \mu \left(\frac{\partial^2 w}{\partial x^2} + \frac{\partial^2 w}{\partial y^2} + \frac{\partial^2 w}{\partial z^2} \right) + F_{BZ}
\end{aligned} \tag{3.19}$$

where, F_{BX} , F_{BY} , F_{BZ} are the body forces in x, y and z-directions.

Vector notation of conservation of momentum

$$\rho \frac{D\mathbf{V}}{Dt} = -\nabla P + \mu \nabla^2 \mathbf{V} + \mathbf{F} \tag{3.20}$$

The body force terms such as gravitational forces and electromagnetic forces are neglected while estimating the thermohydraulic characteristics and entropy generation rate in HTS cables.

3.2.3 Conservation of energy

The physical principle of first law of thermodynamics is used for accomplishing the conservation of energy equation. From first law of thermodynamics

$$\underbrace{\left(\begin{array}{l} \text{Rate of energy} \\ \text{accumulated in} \\ \text{control volume} \end{array} \right)}_{(a)} = \underbrace{\left(\begin{array}{l} \text{Net energy transferred} \\ \text{by fluid flow} \end{array} \right)}_{(b)} + \underbrace{\left(\begin{array}{l} \text{Net energy transferred} \\ \text{by conduction} \end{array} \right)}_{(c)} \quad (3.21)$$

$$\underbrace{\left(\begin{array}{l} \text{Rate of internal} \\ \text{heat generation} \end{array} \right)}_{(d)} - \underbrace{\left(\begin{array}{l} \text{Net work transfer from the} \\ \text{control volume to its environment} \end{array} \right)}_{(e)}$$

$$(a) \text{ Rate of energy accumulated in control volume} = \frac{\partial(\rho e)}{\partial t} \Delta x \Delta y \Delta z \quad (3.22)$$

$$(b) \text{ Net energy transferred by fluid flow} = - \left[\frac{\partial(\rho u e)}{\partial x} + \frac{\partial(\rho v e)}{\partial y} + \frac{\partial(\rho w e)}{\partial z} \right] \Delta x \Delta y \Delta z \quad (3.23)$$

$$(c) \text{ Net energy transferred by conduction} = - \left(\frac{\partial q_x''}{\partial x} + \frac{\partial q_y''}{\partial y} + \frac{\partial q_z''}{\partial z} \right) \Delta x \Delta y \Delta z \quad (3.24)$$

$$(d) \text{ Rate of internal heat generation} = q_{gen}''' \Delta x \Delta y \Delta z \quad (3.25)$$

$$(e) \text{ Net work transfer from the control volume to its environment} =$$

$$\left\{ \begin{array}{l} \left(\sigma_x \frac{\partial u}{\partial x} - \tau_{xy} \frac{\partial u}{\partial y} - \tau_{xz} \frac{\partial u}{\partial z} + \sigma_y \frac{\partial v}{\partial y} - \tau_{xy} \frac{\partial v}{\partial x} - \tau_{yz} \frac{\partial v}{\partial z} + \sigma_z \frac{\partial w}{\partial z} - \tau_{xz} \frac{\partial w}{\partial x} - \tau_{yz} \frac{\partial w}{\partial y} \right) \Delta x \Delta y \Delta z \\ + \left[u \frac{\partial \sigma_x}{\partial x} - u \frac{\partial \tau_{xy}}{\partial y} - u \frac{\partial \tau_{xz}}{\partial z} + v \frac{\partial \sigma_y}{\partial y} - v \frac{\partial \tau_{xy}}{\partial x} - v \frac{\partial \tau_{yz}}{\partial z} + w \frac{\partial \sigma_z}{\partial z} - w \frac{\partial \tau_{xz}}{\partial x} - w \frac{\partial \tau_{yz}}{\partial y} \right] \Delta x \Delta y \Delta z \end{array} \right\} \quad (3.26)$$

where, e is specific internal energy, q_x'' , q_y'' and q_z'' are heat flux in x, y and z-direction respectively, q_{gen}''' is internal heat generation or heat dissipation rate.

Substituting equation (3.22) to equation (3.26) in equation (3.21) and using (3.16) yields

$$\rho \frac{De}{Dt} + e \left(\frac{D\rho}{Dt} + \rho \nabla \cdot \mathbf{V} \right) = -\nabla \cdot \mathbf{q}'' + q''' - P \nabla \cdot \mathbf{V} + \mu \phi \quad (3.27)$$

where, ϕ is viscous dissipation function

Using equation(3.6), equation (3.27) can be rewritten as

$$\rho \frac{De}{Dt} = -\nabla \cdot \mathbf{q}'' + q''' - P \nabla \cdot \mathbf{V} + \mu \phi \quad (3.28)$$

Energy in terms of enthalpy can be termed as

$$h = e + \left(\frac{1}{\rho}\right)P \quad (3.29)$$

Applying the substantial derivative to the above equation

$$\frac{Dh}{Dt} = \frac{De}{Dt} + \frac{1}{\rho} \frac{DP}{Dt} - \frac{P}{\rho^2} \frac{D\rho}{Dt} \quad (3.30)$$

From Fourier law of heat conduction, heat fluxes q_x'' , q_y'' and q_z'' in terms of temperature gradients are

$$\mathbf{q}'' = -k\nabla T \quad (3.31)$$

Combining equations (3.27), (3.30) and (3.31)

$$\rho \frac{Dh}{Dt} = \nabla \cdot (k\nabla T) + q''' + \frac{DP}{Dt} + \mu\phi - \frac{P}{\rho} \left(\frac{D\rho}{Dt} + \rho\nabla \cdot \mathbf{V} \right) \quad (3.32)$$

From conservation of mass equation (3.6), equation (3.32) can be written as

$$\rho \frac{Dh}{Dt} = \nabla \cdot (k\nabla T) + q''' + \mu\phi + \underbrace{\frac{DP}{Dt}}_{\text{compressibility effect}} \quad (3.33)$$

For a single phase fluid enthalpy can be expressed as

$$dh = Tds + \frac{1}{\rho} dP \quad (3.34)$$

where, T is absolute temperature and ds is change in the specific entropy

$$ds = \left(\frac{\partial s}{\partial T} \right)_P dT + \left(\frac{\partial s}{\partial P} \right)_T dP \quad (3.35)$$

For incompressible liquid [288]

$$ds = C_p \frac{dT}{T} \quad (3.36)$$

where, C_p is specific heat

$$\left(\frac{\partial s}{\partial T}\right)_p = \frac{C_p}{T} \quad (3.37)$$

Hence, the temperature formulation of conservation of energy equation using first law of thermodynamics for incompressible fluid flow is given by

$$\rho C_p \frac{DT}{Dt} = \nabla \cdot (k \nabla T) + q''' + \mu \phi \quad (3.38)$$

The above equation can be written as

$$\rho C_p \left(\frac{\partial T}{\partial t} + u \frac{\partial T}{\partial x} + v \frac{\partial T}{\partial y} + w \frac{\partial T}{\partial z} \right) = k \left(\frac{\partial^2 T}{\partial x^2} + \frac{\partial^2 T}{\partial y^2} + \frac{\partial^2 T}{\partial z^2} \right) + q''' + \mu \phi \quad (3.39)$$

3.2.4 Generalized entropy generation equation for fluid flow

The discussion of second law of thermodynamics in any engineering systems is important because it is necessary for determining the temperature as well as flow field for formulating the objective and purpose for solving the convection problems. For instance in any engineering systems, the enhanced heat transfer rate and reduced pumping power are necessary to improve the efficiency. Better engineering system design corresponds to efficient thermohydraulic performance, which is possible with minimum entropy generation rate or minimum exergy destruction in the system. Hence, second law of thermodynamics is necessary for evaluating the thermohydraulic performance of engineering system.

The generalized second law of thermodynamics

$$\underbrace{\dot{S}_{gen}}_{\text{Entropy generation rate}} = \underbrace{\frac{ds}{dt}}_{\text{Rate of entropy accumulated in the control volume}} - \underbrace{\sum \frac{q''}{T_{ref}}}_{\text{Entropy transfer rate by heat transfer}} + \underbrace{\sum \dot{m}_{out} s - \sum \dot{m}_{in} s}_{\text{Net entropy flow rate out of control volume by mass flow}} \quad (3.40)$$

The entropy balance for a system with contribution of mass fluxes and energy transfer across the control surface in tensor form can be written as [289]

$$\frac{\partial(\rho s)}{\partial t} + \frac{\partial F_x}{\partial x} + \frac{\partial F_y}{\partial y} + \frac{\partial F_z}{\partial z} \cong S_{gen}'' \geq 0 \quad (3.41)$$

where, S'''_{gen} is entropy generation rate per unit volume, F_x , F_y and F_z are entropy flux components in x, y and z-directions expressed in terms of velocity components and heat flux component

$$\left. \begin{aligned} F_x &= \rho us + \frac{q''_x}{T} \\ F_y &= \rho vs + \frac{q''_y}{T} \\ F_z &= \rho ws + \frac{q''_z}{T} \end{aligned} \right\} \quad (3.42)$$

Solving equation (3.41) by using equation (3.42) yields

$$S'''_{gen} = \rho \left(\frac{\partial s}{\partial t} + u \frac{\partial s}{\partial x} + v \frac{\partial s}{\partial y} + w \frac{\partial s}{\partial z} \right) = \text{div} \left(\frac{q''}{T} \right) + \underbrace{\frac{\phi_v}{T}}_{\text{Frictional entropy generation rate}} + \underbrace{\frac{\phi_T}{T^2}}_{\text{Thermal entropy generation rate}} \quad (3.43)$$

Simplifying the above equation [288],

$$S'''_{gen} = \frac{k(\nabla T \cdot \nabla T)}{T^2} + \frac{\mu \phi}{T} \quad (3.44)$$

The first term in the right hand side represents, entropy generation rate due to finite temperature difference in the fluid subjected to thermal gradients and the second term in the right hand side represents, entropy generation rate due to viscous dissipation in the fluid subjected to velocity gradients.

The above equation can be written as

$$S'''_{gen} = S'''_{gen,Thermal} + S'''_{gen,frictional} \quad (3.45)$$

$$\begin{aligned} S'''_{gen,Thermal} &= \frac{K}{T_{ref}^2} \left[\left(\frac{\partial T}{\partial x} \right)^2 + \left(\frac{\partial T}{\partial y} \right)^2 + \left(\frac{\partial T}{\partial z} \right)^2 \right] \\ S'''_{gen,frictional} &= \frac{\mu}{T_{ref}} \left[2 \left[\left(\frac{\partial u}{\partial x} \right)^2 + \left(\frac{\partial v}{\partial y} \right)^2 + \left(\frac{\partial w}{\partial z} \right)^2 \right] + \left(\frac{\partial u}{\partial y} + \frac{\partial v}{\partial x} \right)^2 + \left(\frac{\partial u}{\partial z} + \frac{\partial w}{\partial x} \right)^2 + \left(\frac{\partial w}{\partial y} + \frac{\partial v}{\partial z} \right)^2 \right] \end{aligned} \quad (3.46)$$

3.3 Flow through HTS cables

The conservation of mass and conservation of momentum derived in the previous section are sufficient for solving the flow component in convection cooling of LN₂ through HTS

cable. The conservation of mass along with force balance is utilized for solving the velocity components and pressure components in x, y and z-directions. However, for solving the temperature distribution for the flow of LN₂ through HTS cable can be evaluated using conservation of energy equation.

The flow of LN₂ through HTS cable encounters turbulences due to corrugated former and forced convection cooling. Hence, the conservation equations derived in the previous section are further solved to obtain the Reynolds Averaged Navier Stokes (RANS) and time averaged equations.

The transformation of conservation equations for time averaged flow through HTS cable can be derived as follows

$$\begin{aligned} u &= \bar{u} + u' & P &= \bar{P} + P' \\ v &= \bar{v} + v' & T &= \bar{T} + T' \\ w &= \bar{w} + w' \end{aligned} \quad (3.47)$$

where \bar{u} , \bar{v} , \bar{w} , \bar{P} and \bar{T} represents the mean components over the entire length of HTS cable, u' , v' , w' , P' and T' are the fluctuating components over the entire length of HTS cable.

The time averaging of mean component can be written as

$$\bar{u} = \frac{1}{t} \int_0^t u dt \quad (3.48)$$

The time averaging of fluctuating component can be written as

$$\int_0^t u' dt = 0 \quad (3.49)$$

From the basics of algebra and writing the conservation equations using(3.47), (3.48) and (3.49)

$$\overline{u + v + w} = \bar{u} + \bar{v} + \bar{w} \quad (3.50)$$

$$\overline{uu'} = 0, \overline{vv'} = 0, \overline{ww'} = 0 \quad (3.51)$$

$$\left. \begin{aligned} \overline{uv} &= \overline{u} \overline{v} + \overline{u'v'} \\ \overline{vw} &= \overline{v} \overline{w} + \overline{v'w'} \\ \overline{uw} &= \overline{u} \overline{w} + \overline{u'w'} \end{aligned} \right\} \quad (3.52)$$

$$\left. \begin{aligned} \overline{u^2} &= \overline{u}^2 + \overline{u'^2} \\ \overline{v^2} &= \overline{v}^2 + \overline{v'^2} \\ \overline{w^2} &= \overline{w}^2 + \overline{w'^2} \end{aligned} \right\} \quad (3.53)$$

$$\frac{\partial \overline{u}}{\partial x} = \frac{\partial \overline{u}}{\partial x} \quad \frac{\partial \overline{v}}{\partial y} = \frac{\partial \overline{v}}{\partial y} \quad \frac{\partial \overline{w}}{\partial z} = \frac{\partial \overline{w}}{\partial z} \quad (3.54)$$

$$\frac{\partial \overline{u}}{\partial t} = 0, \quad \frac{\partial \overline{v}}{\partial t} = 0, \quad \frac{\partial \overline{w}}{\partial t} = 0, \quad \frac{\partial \overline{u}}{\partial t} = 0, \quad \frac{\partial \overline{v}}{\partial t} = 0, \quad \frac{\partial \overline{w}}{\partial t} = 0 \quad (3.55)$$

For steady and incompressible flow of LN₂ through the HTS cable, the RANS conservation of mass equation using equation (3.8) can be written as

$$\frac{\partial \overline{u}}{\partial x} + \frac{\partial \overline{v}}{\partial y} + \frac{\partial \overline{w}}{\partial z} = 0 \quad (3.56)$$

solving the above equation yields,

$$\frac{\partial \overline{u}}{\partial x} + \frac{\partial \overline{u'}}{\partial x} + \frac{\partial \overline{v}}{\partial y} + \frac{\partial \overline{v'}}{\partial y} + \frac{\partial \overline{w}}{\partial z} + \frac{\partial \overline{w'}}{\partial z} = 0 \quad (3.57)$$

Time averaging the above equation can be written as

$$\frac{\partial \overline{u}}{\partial x} + \frac{\partial \overline{v}}{\partial y} + \frac{\partial \overline{w}}{\partial z} = 0 \quad (3.58)$$

For steady and incompressible flow of LN₂ through the HTS cable, the RANS of conservation of momentum equation using equation (3.18) in x-direction can be written as

$$\frac{\partial}{\partial x} (\overline{u^2}) + \frac{\partial}{\partial y} (\overline{uv}) + \frac{\partial}{\partial z} (\overline{uw}) = -\frac{1}{\rho} \frac{\partial \overline{P}}{\partial x} + \frac{\mu}{\rho} \left(\frac{\partial^2 \overline{u}}{\partial x^2} + \frac{\partial^2 \overline{u}}{\partial y^2} + \frac{\partial^2 \overline{u}}{\partial z^2} \right) \quad (3.59)$$

Solving the above equation yields,

$$\begin{aligned} \frac{\partial}{\partial x}(\overline{u^2}) + \frac{\partial}{\partial y}(\overline{uv}) + \frac{\partial}{\partial z}(\overline{uw}) = & -\frac{1}{\rho} \frac{\partial \overline{P}}{\partial x} + \frac{\mu}{\rho} \left(\frac{\partial^2 \overline{u}}{\partial x^2} + \frac{\partial^2 \overline{u}}{\partial y^2} + \frac{\partial^2 \overline{u}}{\partial z^2} \right) - \frac{\partial}{\partial x}(\overline{u'^2}) \\ & - \frac{\partial}{\partial y}(\overline{u'v'}) - \frac{\partial}{\partial z}(\overline{u'w'}) \end{aligned} \quad (3.60)$$

Time average the above equation and using equation (3.58), the left hand side of equation (3.60) can be simplified as

$$\begin{aligned} \overline{u} \frac{\partial \overline{u}}{\partial x} + \overline{v} \frac{\partial \overline{u}}{\partial y} + \overline{w} \frac{\partial \overline{u}}{\partial z} = & -\frac{1}{\rho} \frac{\partial \overline{P}}{\partial x} + \frac{\mu}{\rho} \left(\frac{\partial^2 \overline{u}}{\partial x^2} + \frac{\partial^2 \overline{u}}{\partial y^2} + \frac{\partial^2 \overline{u}}{\partial z^2} \right) - \frac{\partial}{\partial x}(\overline{u'^2}) \\ & - \frac{\partial}{\partial y}(\overline{u'v'}) - \frac{\partial}{\partial z}(\overline{u'w'}) \end{aligned} \quad (3.61)$$

Similarly, the time averaged Reynolds averaged conservation of momentum equations in y and z-directions can be written as

$$\begin{aligned} \overline{u} \frac{\partial \overline{v}}{\partial x} + \overline{v} \frac{\partial \overline{v}}{\partial y} + \overline{w} \frac{\partial \overline{v}}{\partial z} = & -\frac{1}{\rho} \frac{\partial \overline{P}}{\partial x} + \frac{\mu}{\rho} \left(\frac{\partial^2 \overline{v}}{\partial x^2} + \frac{\partial^2 \overline{v}}{\partial y^2} + \frac{\partial^2 \overline{v}}{\partial z^2} \right) - \frac{\partial}{\partial x}(\overline{u'v'}) \\ & - \frac{\partial}{\partial y}(\overline{v'^2}) - \frac{\partial}{\partial z}(\overline{v'w'}) \end{aligned} \quad (3.62)$$

$$\begin{aligned} \overline{u} \frac{\partial \overline{w}}{\partial x} + \overline{v} \frac{\partial \overline{w}}{\partial y} + \overline{w} \frac{\partial \overline{w}}{\partial z} = & -\frac{1}{\rho} \frac{\partial \overline{P}}{\partial x} + \frac{\mu}{\rho} \left(\frac{\partial^2 \overline{w}}{\partial x^2} + \frac{\partial^2 \overline{w}}{\partial y^2} + \frac{\partial^2 \overline{w}}{\partial z^2} \right) \frac{\partial}{\partial x}(\overline{u'w'}) \\ & - \frac{\partial}{\partial y}(\overline{v'w'}) - \frac{\partial}{\partial z}(\overline{w'^2}) \end{aligned} \quad (3.63)$$

For steady and incompressible flow of LN₂ through the HTS cable, the RANS and time averaged conservation of energy equation neglecting the internal heat generation using equation (3.39) can be written as

$$\overline{u} \frac{\partial \overline{T}}{\partial x} + \overline{v} \frac{\partial \overline{T}}{\partial y} + \overline{w} \frac{\partial \overline{T}}{\partial z} = \frac{k}{\rho C_p} \left(\frac{\partial^2 \overline{T}}{\partial x^2} + \frac{\partial^2 \overline{T}}{\partial y^2} + \frac{\partial^2 \overline{T}}{\partial z^2} \right) \quad (3.64)$$

Solving the above equation yields,

$$\begin{aligned} \overline{u} \frac{\partial \overline{T}}{\partial x} + \overline{v} \frac{\partial \overline{T}}{\partial y} + \overline{w} \frac{\partial \overline{T}}{\partial z} = & \frac{k}{\rho C_p} \left(\frac{\partial^2 \overline{T}}{\partial x^2} + \frac{\partial^2 \overline{T}}{\partial y^2} + \frac{\partial^2 \overline{T}}{\partial z^2} \right) - \frac{\partial}{\partial x}(\overline{u'T'}) \\ & - \frac{\partial}{\partial y}(\overline{v'T'}) - \frac{\partial}{\partial z}(\overline{w'T'}) \end{aligned} \quad (3.65)$$

The time averaged entropy generation rate in the HTS cables, from equation (3.43) can be written as

$$\rho \left(\frac{\partial \bar{s}}{\partial t} + \bar{u} \frac{\partial \bar{s}}{\partial x} + \bar{v} \frac{\partial \bar{s}}{\partial y} + \bar{w} \frac{\partial \bar{s}}{\partial z} \right) = \overline{\text{div} \left(\frac{\bar{q}''}{T} \right)} - \rho \left(\frac{\partial \bar{u}'s'}{\partial x} + \frac{\partial \bar{v}'s'}{\partial y} + \frac{\partial \bar{w}'s'}{\partial z} \right) + \frac{\bar{\phi}_v}{T} + \frac{\bar{\phi}_T}{T^2} \quad (3.66)$$

Simplifying the above equation

$$S_{gen}''' = S_{gen,Thermal}''' + S_{gen,frictional}''' \quad (3.67)$$

$$S_{gen,Thermal}''' = \frac{K}{T_{ref}^2} \left[\overline{\left(\frac{\partial T}{\partial x} \right)^2} + \overline{\left(\frac{\partial T}{\partial y} \right)^2} + \overline{\left(\frac{\partial T}{\partial z} \right)^2} \right]$$

$$S_{gen,frictional}''' = \frac{\mu}{T_{ref}} \left[2 \left(\overline{\left(\frac{\partial u}{\partial x} \right)^2} + \overline{\left(\frac{\partial v}{\partial y} \right)^2} + \overline{\left(\frac{\partial w}{\partial z} \right)^2} \right) + \overline{\left(\frac{\partial u}{\partial y} + \frac{\partial v}{\partial x} \right)^2} + \overline{\left(\frac{\partial u}{\partial z} + \frac{\partial w}{\partial x} \right)^2} + \overline{\left(\frac{\partial w}{\partial y} + \frac{\partial v}{\partial z} \right)^2} \right] \quad (3.68)$$

Solving the above equation yields,

$$S_{gen,Thermal}''' = \frac{K}{T_{ref}^2} \left[\overline{\left(\frac{\partial \bar{T}}{\partial x} \right)^2} + \overline{\left(\frac{\partial \bar{T}}{\partial y} \right)^2} + \overline{\left(\frac{\partial \bar{T}}{\partial z} \right)^2} \right] + \frac{K}{T_{ref}^2} \left[\overline{\left(\frac{\partial T'}{\partial x} \right)^2} + \overline{\left(\frac{\partial T'}{\partial y} \right)^2} + \overline{\left(\frac{\partial T'}{\partial z} \right)^2} \right]$$

$$S_{gen,frictional}''' = \frac{\mu}{T_{ref}} \left[2 \left(\overline{\left(\frac{\partial \bar{u}}{\partial x} \right)^2} + \overline{\left(\frac{\partial \bar{v}}{\partial y} \right)^2} + \overline{\left(\frac{\partial \bar{w}}{\partial z} \right)^2} \right) + \overline{\left(\frac{\partial \bar{u}}{\partial y} + \frac{\partial \bar{v}}{\partial x} \right)^2} + \overline{\left(\frac{\partial \bar{u}}{\partial z} + \frac{\partial \bar{w}}{\partial x} \right)^2} + \overline{\left(\frac{\partial \bar{w}}{\partial y} + \frac{\partial \bar{v}}{\partial z} \right)^2} \right]$$

$$\frac{\mu}{T_{ref}} \left[2 \left(\overline{\left(\frac{\partial u'}{\partial x} \right)^2} + \overline{\left(\frac{\partial v'}{\partial y} \right)^2} + \overline{\left(\frac{\partial w'}{\partial z} \right)^2} \right) + \overline{\left(\frac{\partial u'}{\partial y} + \frac{\partial v'}{\partial x} \right)^2} + \overline{\left(\frac{\partial u'}{\partial z} + \frac{\partial w'}{\partial x} \right)^2} + \overline{\left(\frac{\partial w'}{\partial y} + \frac{\partial v'}{\partial z} \right)^2} \right] \quad (3.69)$$

Neglecting the higher order fluctuating terms, the entropy generation rate in the HTS cables can be calculated by [5]

$$S_{gen,Thermal}''' = \frac{K}{T_{ref}^2} \left[\overline{\left(\frac{\partial \bar{T}}{\partial x} \right)^2} + \overline{\left(\frac{\partial \bar{T}}{\partial y} \right)^2} + \overline{\left(\frac{\partial \bar{T}}{\partial z} \right)^2} \right]$$

$$S_{gen,frictional}''' = \frac{\mu}{T_{ref}} \left[2 \left(\overline{\left(\frac{\partial \bar{u}}{\partial x} \right)^2} + \overline{\left(\frac{\partial \bar{v}}{\partial y} \right)^2} + \overline{\left(\frac{\partial \bar{w}}{\partial z} \right)^2} \right) + \overline{\left(\frac{\partial \bar{u}}{\partial y} + \frac{\partial \bar{v}}{\partial x} \right)^2} + \overline{\left(\frac{\partial \bar{u}}{\partial z} + \frac{\partial \bar{w}}{\partial x} \right)^2} + \overline{\left(\frac{\partial \bar{w}}{\partial y} + \frac{\partial \bar{v}}{\partial z} \right)^2} \right] \quad (3.70)$$

3.4 Boundary conditions

The forced convective cooling of the HTS cable with central flow of LN₂ through the corrugated former at an inlet temperatures ranging from 65 K to 77 K and operating

pressure of 2.7 bar is utilized to accommodate the heat loads due to heat intrusions and AC losses. The freezing point of LN₂ at 2.7 bar is 62.1 K. Hence inlet temperature of LN₂ nearer to freezing point i.e., 65 K is utilized for estimating the thermohydraulic characteristics and entropy generation rate in HTS cables. Figure 3.2 shows the boundary conditions imposed on the computational domain similar to the practical conditions encountered by the HTS cable under operation. At the inlet of the HTS cable, mass flow inlet boundary conditions with different inlet temperatures as shown in Table 3.1. The flow rates considered for the analysis are similar to the experiment performed on HTS cables at Chubu university by Ivanov et al.[290].

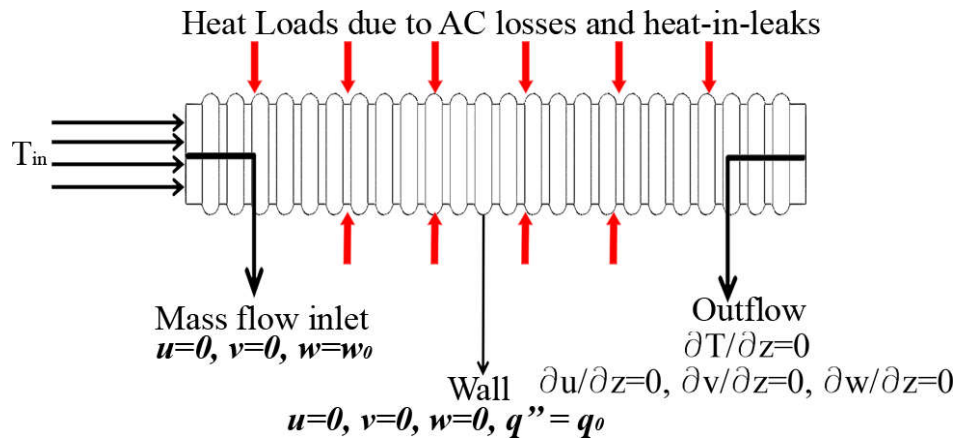


Figure 3.2 HTS cable geometry with imposed boundary conditions

At the outlet, outflow boundary condition is employed that imply the conservation of mass in the computational domain. The heat loads due to transport current in the HTS tapes dissipates the electrical power as AC losses and the heat intrusions from the HTS cable shield are distributed uniformly on the wall of the computational domain. The details of the boundary conditions applied in different cases are shown in Table 3.1. Further, stationary and no slip boundary conditions are imposed on the wall of HTS cable.

Table 3.1 Boundary conditions imposed on the computational domain for analyzing different cases

S.No	Cases analyzed	Heat load (W/m)	Inlet temperature (K)	Flow Rate (L/min)
1	Influence of flow rate	2.1	77	1-20
2	Influence of heat load	1-3	77	11-20
3	Influence of inlet temperature	1-3	65-77	11-20

3.4.1 Temperature dependent thermophysical properties

The temperature dependent thermophysical properties of LN₂ such as density, viscosity, thermal conductivity and specific heat are extracted from the NIST database [291]. Figure 3.3 shows the temperature dependent thermophysical properties of LN₂ at a 77 K and 2.7 bar. Efforts are made to calculate the fitted coefficients for 50 data points of thermophysical properties in the temperature range of 77-86 K. Second order polynomial fitting is performed to calculate the coefficients of thermophysical properties. Similarly, thermophysical properties of LN₂ are extracted for inlet temperatures ranging from 65 K to 77 K and second order polynomial fitting is done. These coefficients are used as inputs in defining the LN₂ properties in ANSYS-FLUENT [292] during the simulation.

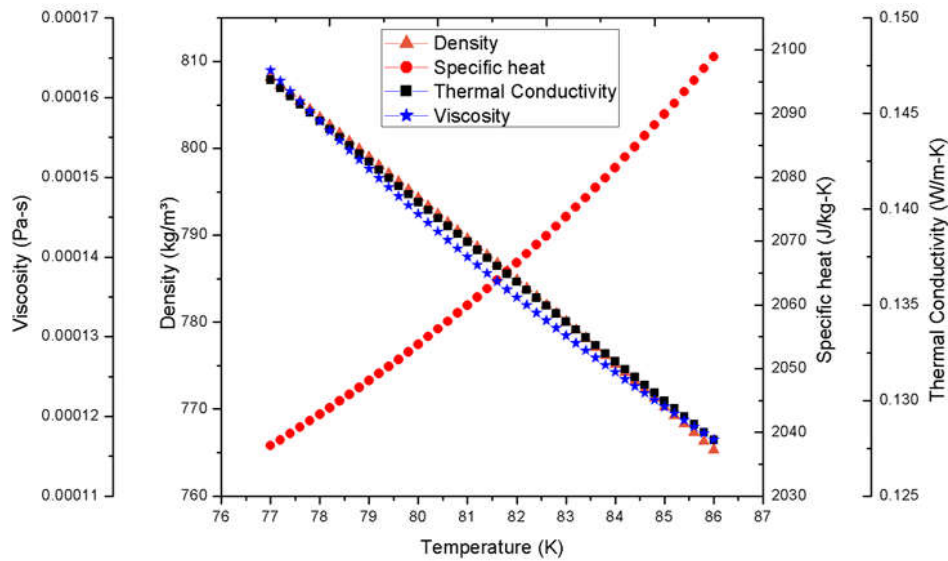


Figure 3.3 Temperature dependent thermophysical properties of LN₂ at 77K and 2.7 bar

1) Density

The analytical functions and their coefficients have been developed for density of LN₂ for different operating temperature ranging from 65 K to 77 K with an increment of 4 K as shown in Table 3.2.

Table 3.2 Analytical functions and their coefficients for density of LN₂ at different operating temperature used in analysis

Property	Operating temperature (K)	Analytical function	Coefficients of analytical function
Density (kg/m ³)	65	$\rho = a_1 + \rho_1 T + \rho_2 T^2$	$a_1 = 1001.73488, \rho_1 = -0.50588, \rho_2 = -0.02609$
	69	$\rho = a_2 + \rho_1 T + \rho_2 T^2$	$a_2 = 1001.73488, \rho_1 = -0.50588, \rho_2 = -0.02609$

73	$\rho = a_3 + \rho_1 T + \rho_2 T^2$	$a_3 = 1001.73488, \rho_1 = -0.50588, \rho_2 = -0.02609$
77	$\rho = a_4 + \rho_1 T + \rho_2 T^2$	$a_4 = 1001.73488, \rho_1 = -0.50588, \rho_2 = -0.02609$

Second order polynomial fitting is performed to calculate the coefficients of temperature dependent density of LN₂. The developed coefficients of analytical functions used as inputs in defining the density of LN₂ in ANSYS-FLUENT during the simulation for different cases specified in Table 3.2.

2) Specific heat

The analytical functions and their coefficients have been developed for specific heat of LN₂ for different operating temperature ranging from 65 K to 77 K with an increment of 4 K as shown in Table 3.3. Second order polynomial fitting is performed to calculate the coefficients of temperature dependent specific heat of LN₂. The developed coefficients of analytical functions used as inputs in defining the specific heat of LN₂ in ANSYS-FLUENT during the simulation for different cases specified in Table 3.3.

Table 3.3 Analytical functions and their coefficients for specific heat of LN₂ at different operating temperature used in analysis

Property	Operating temperature (K)	Analytical function	Coefficients of analytical function
Specific heat (J/kg-K)	65	$C_p = b_1 + C_{p1}x + C_{p2}x^2$	$b_1 = 3219.43549, C_{p1} = -35.10567, C_{p2} = 0.25667$
	69	$C_p = b_2 + C_{p1}x + C_{p2}x^2$	$b_2 = 3219.43549, C_{p1} = -35.10567, C_{p2} = 0.25667$
	73	$C_p = b_3 + C_{p1}x + C_{p2}x^2$	$b_3 = 3219.43549, C_{p1} = -35.10567, C_{p2} = 0.25667$
	77	$C_p = b_4 + C_{p1}x + C_{p2}x^2$	$b_4 = 3219.43549, C_{p1} = -35.10567, C_{p2} = 0.25667$

3) Thermal Conductivity

The analytical functions and their coefficients have been developed for thermal conductivity of LN₂ for different operating temperature ranging from 65 K to 77 K with an

increment of 4 K as shown in Table 3.2. Second order polynomial fitting is performed to calculate the coefficients of temperature dependent thermal conductivity of LN₂. The developed coefficients of analytical functions used as inputs in defining the thermal conductivity of LN₂ in ANSYS-FLUENT during the simulation for different cases specified in Table 3.4.

Table 3.4 Analytical functions and their coefficients for thermal conductivity of LN₂ at different operating temperature used in analysis

Property	Operating temperature (K)	Analytical function	Coefficients of analytical function
Thermal conductivity (W/mK)	65	$K = c_1 + K_1x + K_2x^2$	$c_1 = 0.34223, K_1 = -0.00294, K_2 = 5.2237 \times 10^{-06}$
	69	$K = c_2 + K_1x + K_2x^2$	$c_2 = 0.34223, K_1 = -0.00294, K_2 = 5.2237 \times 10^{-06}$
	73	$K = c_3 + K_1x + K_2x^2$	$c_3 = 0.34223, K_1 = -0.00294, K_2 = 5.2237 \times 10^{-06}$
	77	$K = c_4 + K_1x + K_2x^2$	$c_4 = 0.34223, K_1 = -0.00294, K_2 = 5.2237 \times 10^{-06}$

4) Viscosity

The analytical functions and their coefficients have been developed for viscosity of LN₂ for different operating temperature ranging from 65 K to 77 K with an increment of 4 K as shown in Table 3.5.

Table 3.5 Analytical functions and their coefficients for viscosity of LN₂ at different operating temperature used in analysis

Property	Operating temperature (K)	Analytical function	Coefficients of analytical function
Viscosity (Pa-s)	65	$\mu = d_1 + \mu_1x + \mu_2x^2$	$d_1 = 0.00147, \mu_1 = -2.75384 \times 10^{-05}, \mu_2 = 1.3752 \times 10^{-07}$
	69	$\mu = d_2 + \mu_1x + \mu_2x^2$	$d_2 = 0.00147, \mu_1 = -2.75384 \times 10^{-05}, \mu_2 = 1.3752 \times 10^{-07}$
	73	$\mu = d_3 + \mu_1x + \mu_2x^2$	$d_3 = 0.00147, \mu_1 = -2.75384 \times 10^{-05}, \mu_2 = 1.3752 \times 10^{-07}$
	77	$\mu = d_4 + \mu_1x + \mu_2x^2$	$d_4 = 0.00147, \mu_1 = -2.75384 \times 10^{-05}, \mu_2 = 1.3752 \times 10^{-07}$

Second order polynomial fitting is performed to calculate the coefficients of temperature dependent viscosity of LN₂. The developed coefficients of analytical functions used as inputs in defining the viscosity of LN₂ in ANSYS-FLUENT during the simulation for different cases specified in Table 3.5.

3.5 Closure problem

From the mathematical formulation, the time average conservation equations for flow of LN₂ through the HTS cable are represented by equations (3.58), (3.61) to (3.63), (3.65). In these five equations, there are 17 unknowns (the unknowns are velocity, pressure, temperature components and 12 gradient terms) that forms the closure problem.

The mathematical formulation of the governing equations such as conservation of mass, momentum, energy and turbulent transport which are applicable for single phase, under steady and incompressible flow of LN₂ through HTS cable that are required for solving the closure problem are presented in this section. The analysis is carried out by considering the following assumptions

- 1) In HTS cable, the flow of LN₂ is considered as incompressible and steady.
- 2) The flow of LN₂ is in single phase. Hence the mass transfer due to mass diffusion is neglected (mass transfer is neglected).
- 3) The effect of body forces due to gravitational effects, centrifugal forces and electromagnetic forces are neglected.
- 4) The heat transfer rate due to radiation is considered to be negligible.

The governing equations with the above assumptions are discussed below.

The steady, incompressible time averaged Reynolds Average Navier Stokes (RANS) equations applicable to flow through HTS cable former are as follows.

The continuity equation for flow of LN₂ through HTS cable can be represented as [5], [293], [294]

$$\nabla \cdot (\rho(T) \bar{\mathbf{u}}) = 0 \quad (3.71)$$

where, $\bar{\mathbf{u}}$ is the time averaged velocity vector and $\rho(T)$ is temperature dependent density of LN₂ as shown in Table 3.2.

The conservation of momentum equation applicable to flow through HTS cable with is given by [5], [293], [294]

$$\nabla \cdot (\rho(T) \bar{\mathbf{u}} \bar{\mathbf{u}}) = -\nabla \bar{P} + \mu(T) \nabla^2 (\bar{\mathbf{u}}) + \nabla \cdot (-\rho(T) \overline{\mathbf{u}' \mathbf{u}'}) \quad (3.72)$$

\bar{P} is time averaged pressure, \mathbf{u}' is fluctuating component of velocity vector, $\mu(T)$ is temperature dependent viscosity of LN₂ as shown in Table 3.5. In equation(3.72), the first term on the right hand side is pressure gradient, second term is viscous stress and the last term in represents Reynolds stress tensor.

The conservation of energy equation for flow through HTS cable for determining the rate of heat transfer between the forced flow of LN₂ and the corrugated former surrounded by superconducting HTS tapes is given by [5], [293], [294]

$$\nabla \cdot (\rho(T) \bar{T} \bar{\mathbf{u}}) = \nabla \cdot [k(T) \nabla \bar{T}] + \nabla \cdot (-\rho(T) \overline{\mathbf{u}' T'}) \quad (3.73)$$

where, \bar{T} is the time averaged component of temperature, T' is fluctuation in temperature and $k(T)$ is temperature dependent thermal conductivity of LN₂ as shown in Table 3.4.

The standard κ - ε model is used in the applications of internal flows due to the high accuracy in results. The standard κ - ε model for estimating the thermohydraulic characteristics of HTS cable can be written as [292]

Turbulence kinetic energy (TKE)

$$\nabla \cdot (\rho(T) \kappa \bar{\mathbf{u}}) = \nabla \cdot \left[\left(\mu(T) + \frac{\mu_t(T)}{\sigma_k} \right) \nabla \kappa \right] + 2\mu_t(T) \bar{e}_{ij} \bar{e}_{ij} - \rho(T) \varepsilon \quad (3.74)$$

where, κ is Turbulent kinetic energy (m²/s²), $\kappa = \overline{u'^2} / 2$, $\mu_t(T)$ is turbulent viscosity, $\mu_t(T) = \rho(T) C_\mu (\kappa^2 / \varepsilon)$, σ_k is turbulent kinetic energy (TKE) Prandtl number, \bar{e}_{ij} is steady mean rate of deformation, e'_{ij} is fluctuating component of rate of deformation and ε is dissipation rate per unit mass, $\varepsilon = 2\nu \overline{e'_{ij} e'_{ij}}$

Turbulence dissipation rate (TDR)

$$\nabla \cdot (\rho(T) \varepsilon \bar{\mathbf{u}}) = \nabla \cdot \left[\left(\mu(T) + \frac{\mu_t(T)}{\sigma_\varepsilon} \right) \nabla \varepsilon \right] + C_{1-\varepsilon} 2\mu_t(T) \bar{e}_{ij} \bar{e}_{ij} \frac{\varepsilon}{\kappa} - C_{2-\varepsilon} \rho(T) \frac{\varepsilon^2}{\kappa} \quad (3.75)$$

where, σ_ε is turbulent dissipation rate (TDR) Prandtl number, the standard wall function constants used for the analysis are $C_\mu = 0.09$, $C_{1-\varepsilon} = 1.44$, $C_{2-\varepsilon} = 1.92$, $\sigma_k = 1$ and $\sigma_\varepsilon = 1.3$.

3.6 Solution procedure

The solution of closure problem is analyzed using computational fluid dynamics (CFD) in commercial code software ANSYS-FLUENT [292]. The solution methodology comprise of converting the governing equations stated in section 3.3 into algebraic equations using FVM and are solved using commercial code FLUENT. The results obtained from the FLUENT are used for evaluating the volumetric entropy generation rate and exergy destruction rate for efficient operation of HTS cable.

The solution method includes 3D double precision solver with pressure based, absolute velocity formulation and steady state is used for solving the RANS equation. The viscous turbulence model ($k - \varepsilon$) associated with standard wall function is used for accurate results [5], [283]. FVM is used for converting the governing equations into algebraic equations and solved numerically using FLUENT. The details of discretization schemes used for the analysis of HTS cables are as follows. The least square cell based gradients of discretization is solved because this method of solution compute employ least square assuming the linear variation with the gradients at the cell center. Further, it is less expensive to compute and provides higher order of accuracy. The energy and momentum are discretized with second order upwind in order to predict the solution at higher accuracy. The entropy generation rate accounts due to velocity and temperature gradients are solved in these equations with higher accuracy. Turbulent kinetic energy and turbulent dissipation rate with first order upwind is used because it is less expensive to compute. Further, pressure with second order is used for higher accuracy because the momentum equation constitutes a pressure gradient term which accounts for the flow of LN₂ in the HTS cable and the velocity gradients are varied. The pressure-velocity coupling with Semi Implicit method for pressure linked equation (SIMPLE) algorithm is used because the numerical ability to solve the Navier Stokes equation is superior and it is less expensive to compute.

The procedure for estimating the thermohydraulic characteristics and volumetric entropy generation rate in HTS cable is shown from Figure 3.4 to Figure 3.42. The results retrieved from the FLUENT are used for calculating friction factor, pressure drop, pumping power, temperature difference, cooling capacity, entropy generation rate due to velocity and thermal gradients and volumetric entropy generation rate.

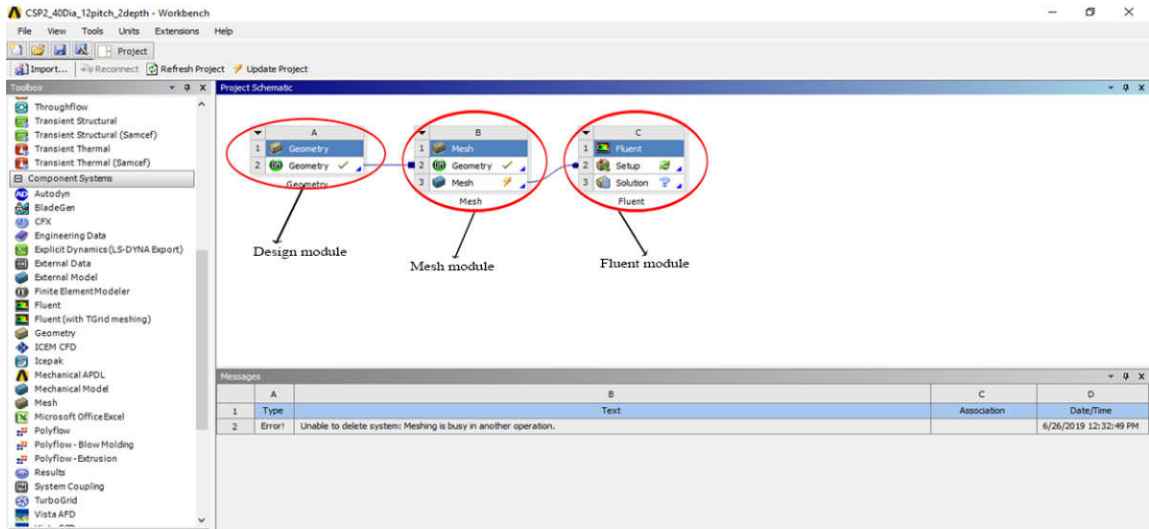


Figure 3.4 Selection of modules in the ANSYS workbench

The thermohydraulic characteristics and entropy generation rate in the HTS cables are analyzed by selecting the Design module for developing the geometry, Mesh module for generating the mesh used for discretization of the developed geometry and Fluent module for analyzing the geometry using Finite Volume Method (FVM) as shown in the Figure 3.4.

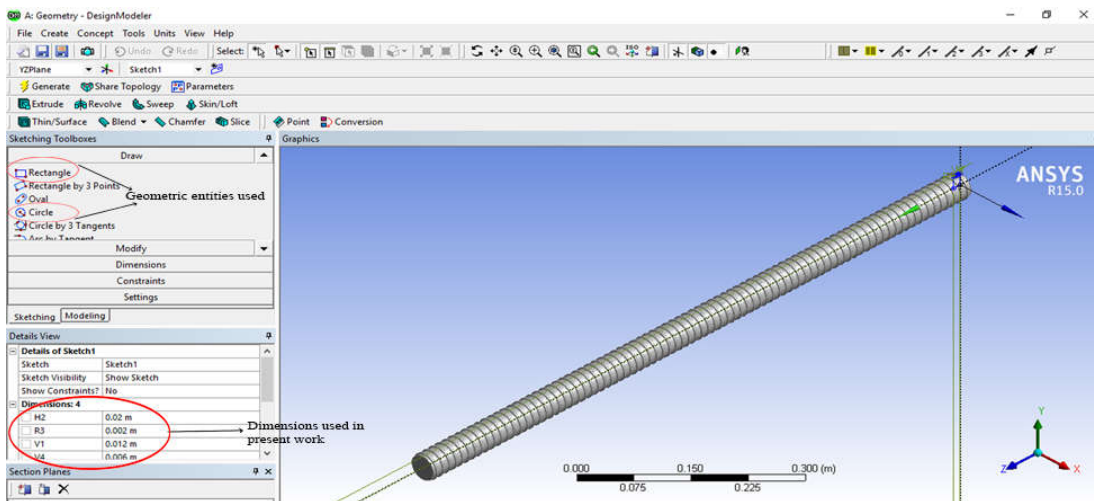


Figure 3.5 Selection of geometric entities and dimensioning the computational domain

The corrugated former in the HTS cable is designed by using rectangle and circle geometric entities. From the draw command, a rectangle with length of 6 mm and breadth of 20 mm was drawn on y-z axis. Later a circle of 2 mm radius was drawn at a distance of 20 mm from the y-axis and at a distance of 3 mm from the z-axis. These geometric entities

are modified into single sketch by using trim and Boolean operation as shown in Figure 3.5. Further, click on generate option in the custom tool bar for generating the final sketch.

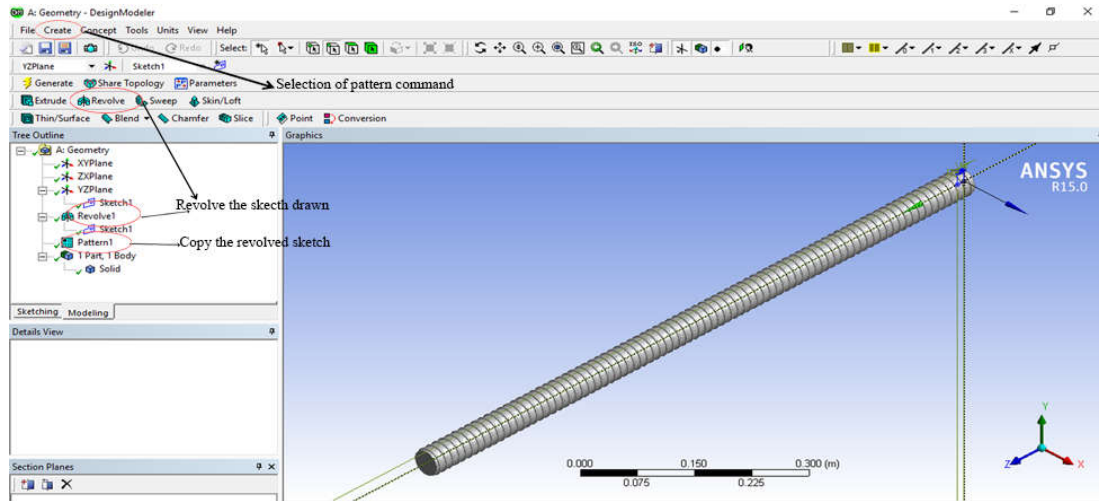


Figure 3.6 Selection of pattern command for modeling the computational domain

The 2-D sketch drawn in the y-z axis is revolved about z-axis to create a 3-D sketch. Select create option and click on revolve. Select the 2-D sketch in the y-z plane and revolve around z-axis with 360° as shown in Figure 3.6. Therefore, a 3-D model of computational domain is generated. The linear pattern command is used for copying the 3-D model of the computational domain. Select pattern option and click on linear pattern in the pattern type. For modeling a 1m cable 83 linear patterns are utilized. The final solid geometry of the computational domain is generated after clicking the generate option as shown in the Figure 3.7.

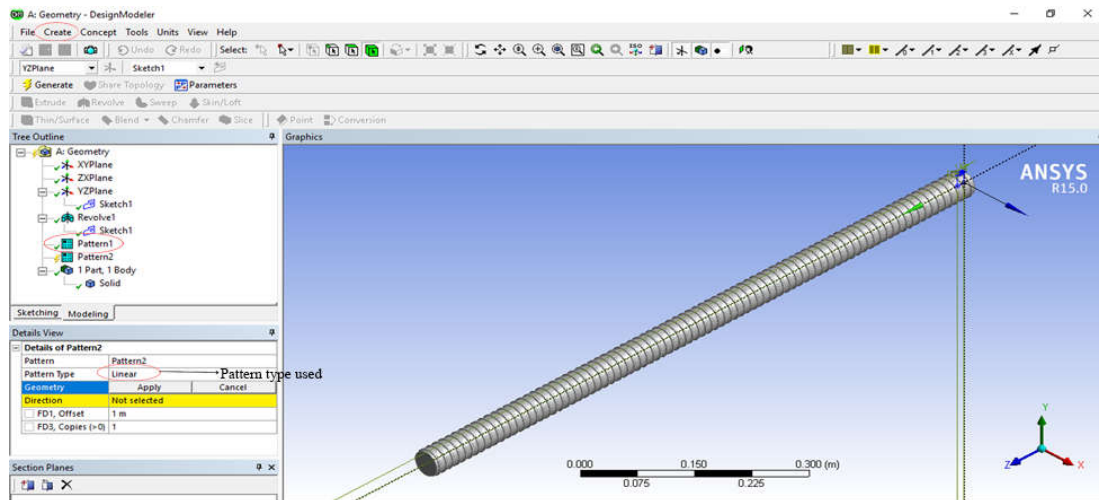


Figure 3.7 Selection of linear pattern for modeling the geometry of computational domain

After creation of the geometry, it is exported to the mesh module. Meshing is termed as discretization of the complex geometry into a simple modules for analyzing. Initially click on sizing option and select element size. Different element sizes are used for studying the grid independency and the element sizes are ranging from 1.1 mm to 0.8 mm are used as shown in Figure 3.8. Then click on generate mesh and update the mesh of the computational domain.

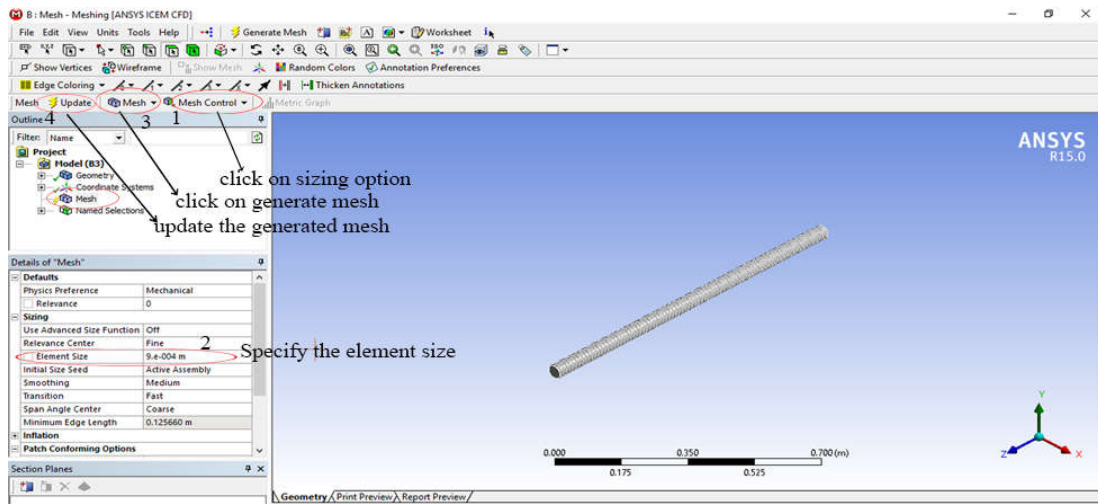


Figure 3.8 Selection of mesh with sizing option for generating the mesh

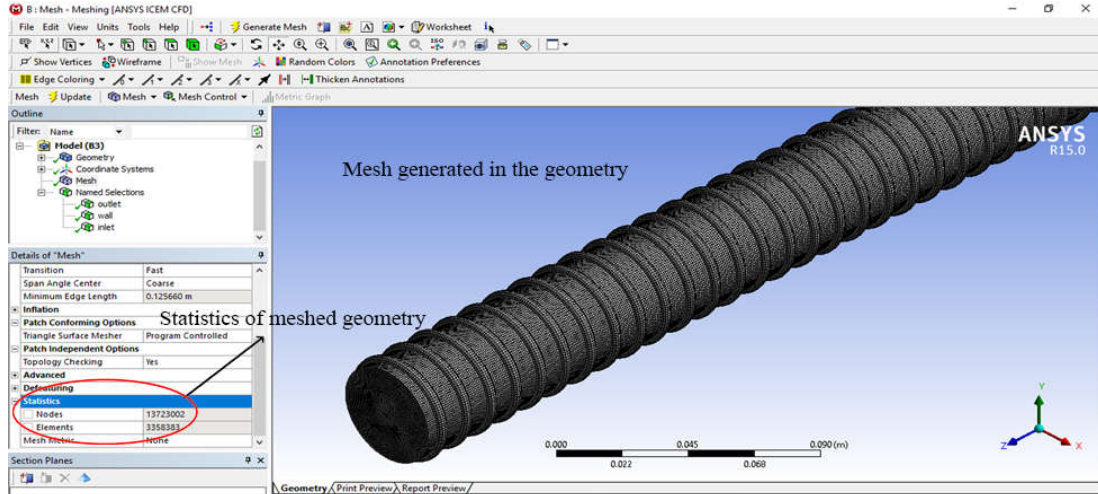


Figure 3.9 Final meshed geometry and its statistics for grid independence study

The final mesh generated in the geometry of the computational domain is shown in Figure 3.9. The statistics of the final mesh are noted for grid independence study. Then from the named selections, select the face at $z=0$ and create the face as inlet. Further select named selections and select the face at $z=1$ and create the face name as outlet. Select the

corrugations and the remaining faces of the computational domain and create the faces name as wall.

The final mesh of the computational domain is exported to fluent module. Click on read option in the file and import the mesh from the design module to Fluent module for analysis as shown in Figure 3.10.

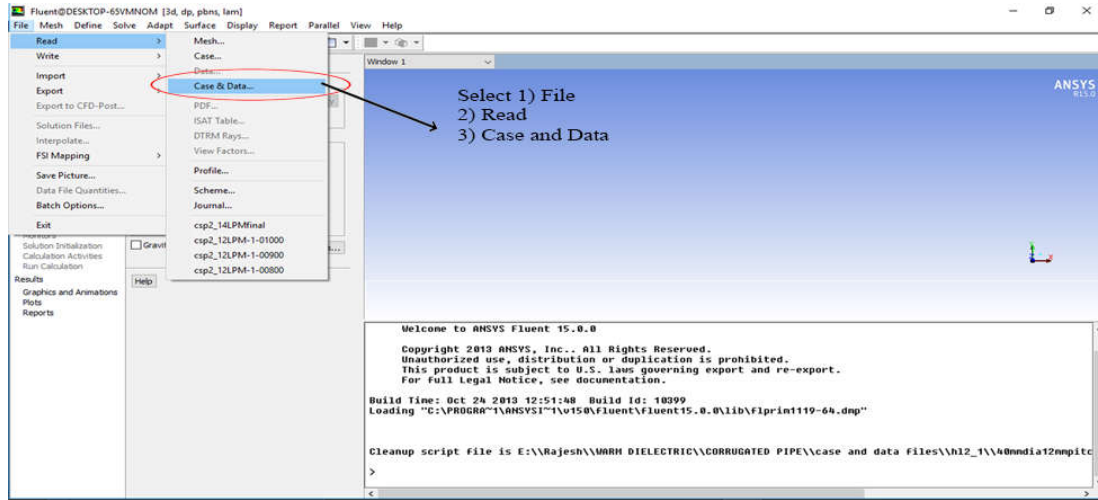


Figure 3.10 Reading case and data of the final meshed geometry from design modular to Fluent

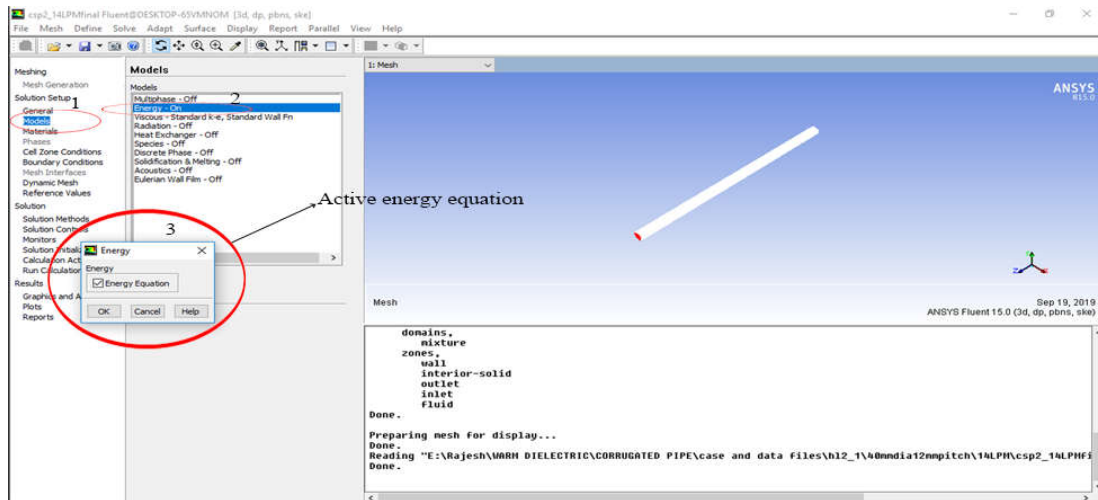


Figure 3.11 Activating the energy equation in models to solve conservation of energy equation

In models select the energy option and activate the energy equation as shown in Figure 3.11. In section 3.2.3 the energy equation derived is utilized in the backend of the fluent module. The energy equation is used for estimating the gradients that are required for calculating the entropy generation rate and thermohydraulic characteristics.

Figure 3.12 shows the selection of the viscous model for solving the turbulent flow in the computational domain. In models activate the viscous model with $\kappa - \varepsilon$ standard and the standard wall function. Click on OK option using the defined model constrains and user-defined functions. The mathematical equations of $\kappa - \varepsilon$ turbulence model is discussed in the closure problem in section 3.5. This mathematical model is used because it provides the accurate results with reference to experimental results.

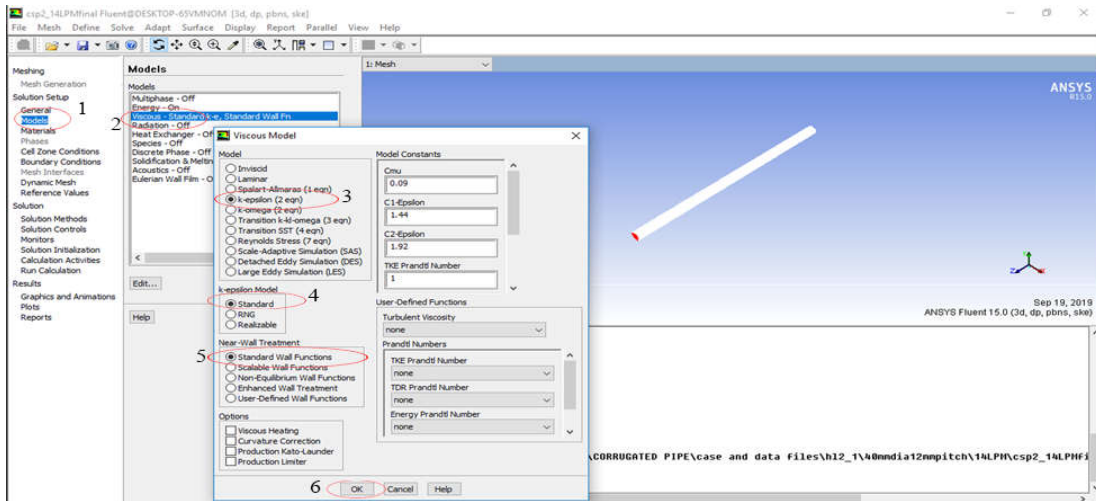


Figure 3.12 Selection of viscous model for solving the turbulence flow in the computational domain

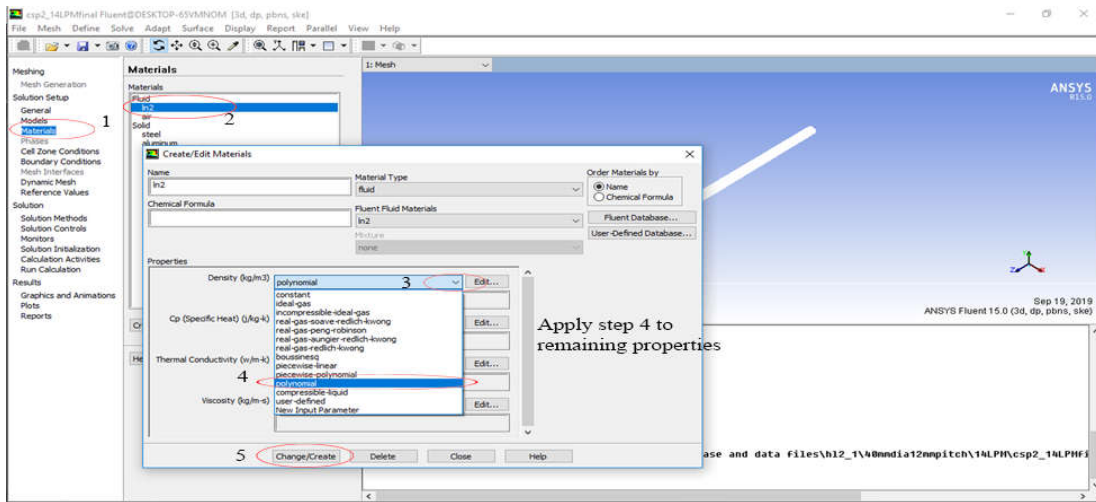


Figure 3.13 Defining temperature dependent thermophysical properties of LN₂

The temperature dependent thermophysical properties at different temperatures discussed in section 3.4.1 are utilized for estimating the thermohydraulic characteristics. In materials create the fluid material as Liquid Nitrogen (LN₂) and click on change or create as shown in Figure 3.13. In properties select each fluid property and click on edit option. Select the polynomial and use the constants that are calculated from the curve fitting as shown in

section 3.4.1. Second order polynomial fitting is performed to calculate the coefficients of thermophysical properties for predicting the thermohydraulic characteristics. The corrugated former of the HTS cable is manufactured with stainless steel. Hence the solid material is selected as steel from the fluent data base instead of Aluminum as shown in Figure 3.14.

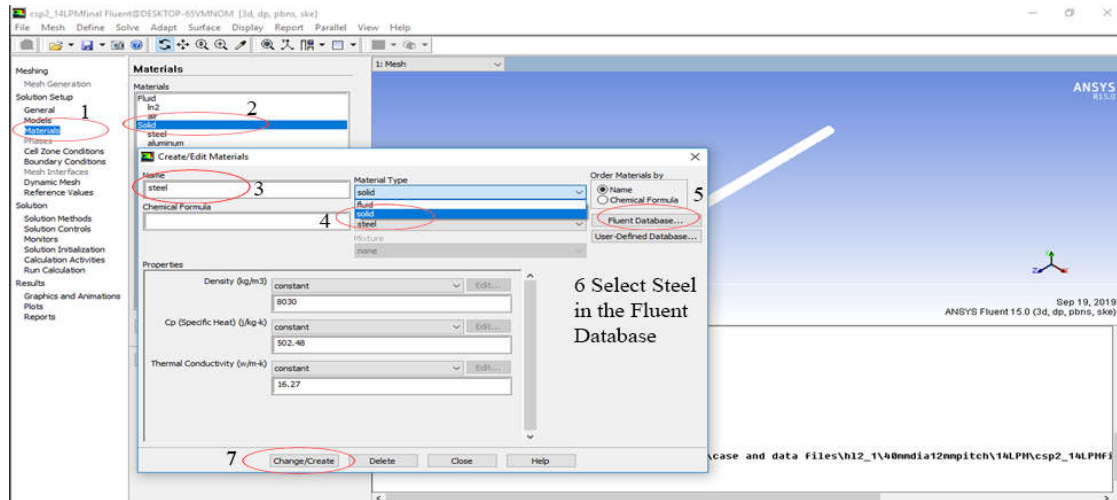


Figure 3.14 Selection of Stainless steel material for corrugated former

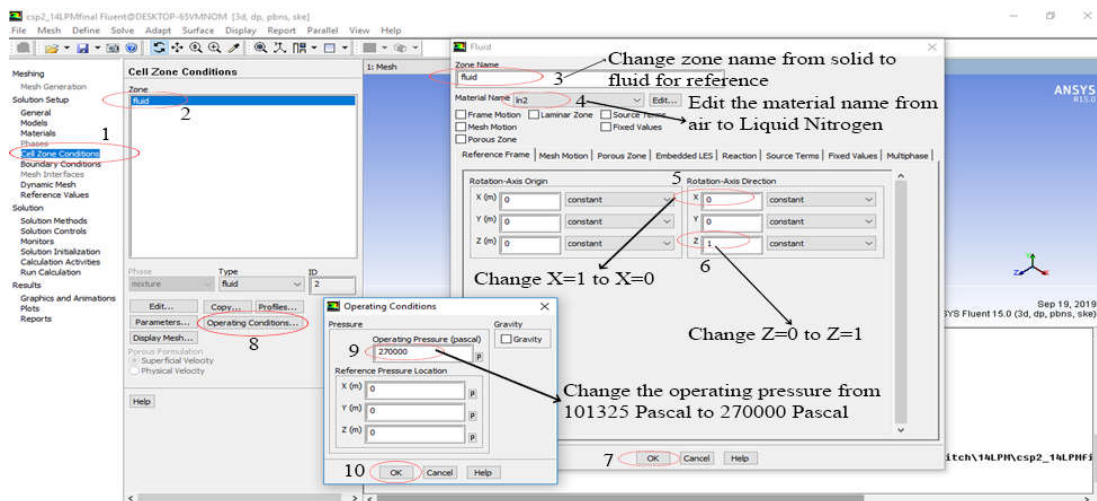


Figure 3.15 Defining the cell zone condition to fluid with operating pressure of 2.7 bar

The temperature thermophysical properties of LN_2 are calculated at an operating of 2.7 bar. In cell conditions the zone name is modified from solid to fluid for reference as shown in Figure 3.15. In material name the named selection is Since the fluid is changed from air to named as LN_2 . Further in rotation axis direction the z-axis is specified from $z=0$ to $z=1$, because the computational domain axis is in the z-direction. Furthermore the operating pressure of the fluid is specified as 2.7 bar.

For solving the thermohydraulic characteristics three boundary conditions are used. At inlet mass flow, at the outlet outflow and on the wall heat fluxes are employed in computational domain for solving the thermohydraulic characteristics. In Figure 3.16, the procedure for specifying the inlet boundary conditions is shown. Click on boundary conditions and select inlet zone. In type select mass flow inlet for defining it.

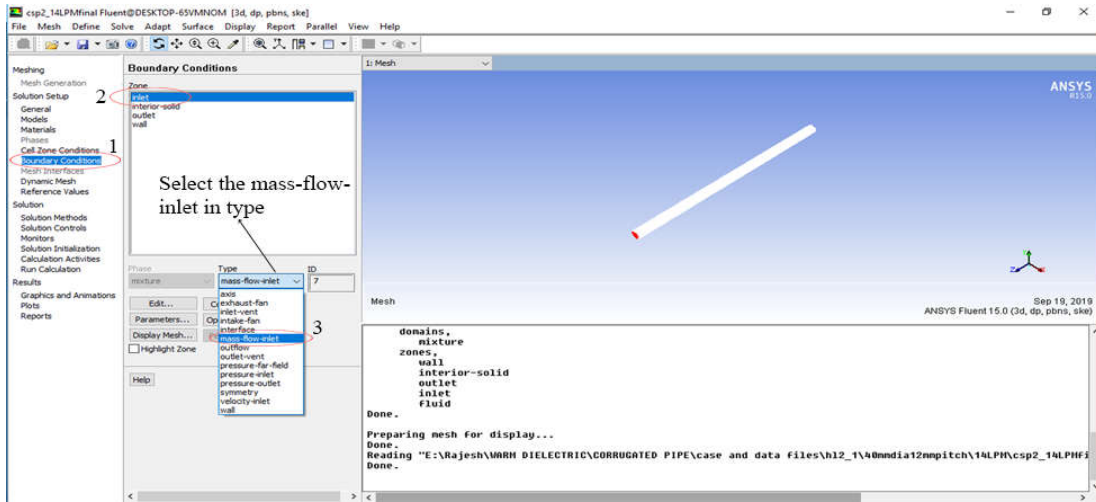


Figure 3.16 Defining the inlet boundary condition

Select the edit option in inlet zone and click on momentum to define the required mass flow rate. The mass flow rate ranging from 1-20 L/min is utilized for solving the thermohydraulic characteristics. The density of the LN₂ is used for converting the mass flow rate from L/min to kg/sec as shown in Figure 3.17.

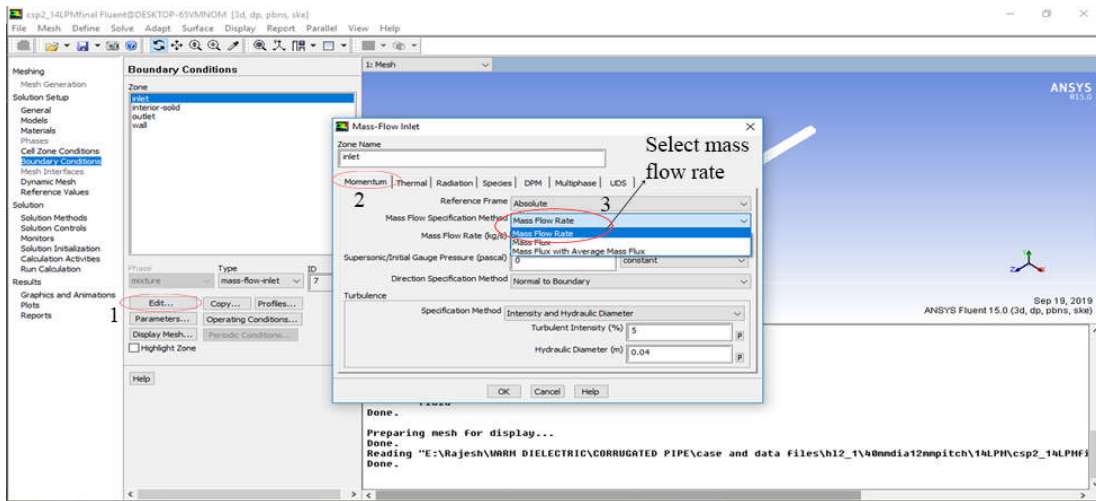


Figure 3.17 Specifying the inlet boundary condition with flow rate of LN₂ in momentum

Further the direction of flow in the computational domain is specified normal to the boundary as shown in Figure 3.18. It specifies that the flow of fluid through the computational domain in the z-direction along the axis from $z=0$ to $z=1$.

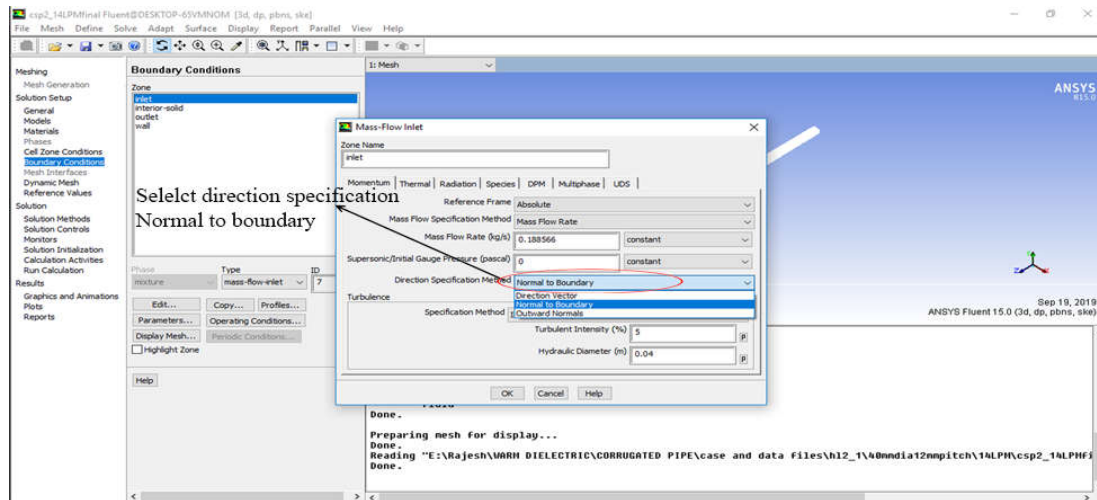


Figure 3.18 Defining the flow direction with normal to boundary

In turbulence, intensity and hydraulic diameter method is specified as shown in Figure 3.19. The turbulence intensity is specified as 5% and the hydraulic diameter of the computational domain is specified as 0.04 m and click on OK. Further, at the inlet the inlet temperature of the LN₂ is specified.

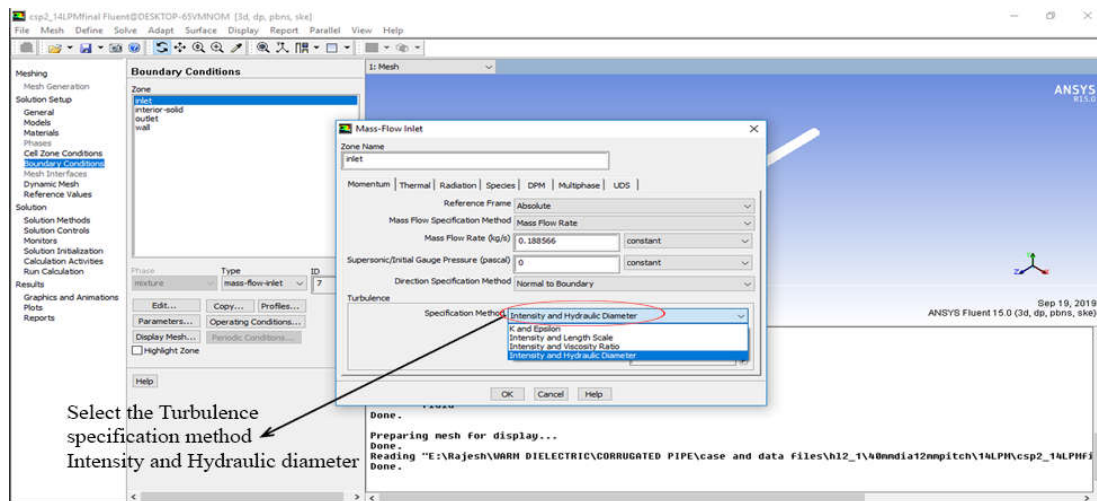


Figure 3.19 Specifying the turbulence specification method with intensity and hydraulic diameter

Since at cryogenic temperature, behavior of the fluid vary with minor change in temperature and pressure. Hence it is necessary to provide the inlet temperature of the LN₂. The inlet temperature of the LN₂ ranges from 65-77K and it is defined in the inlet

boundary condition by clicking on thermal. The inlet temperature is specified as constant at the inlet. At the inlet the required boundary conditions are specified and in the computational domain the fluid follows the polynomial behavior as defined in the material properties.

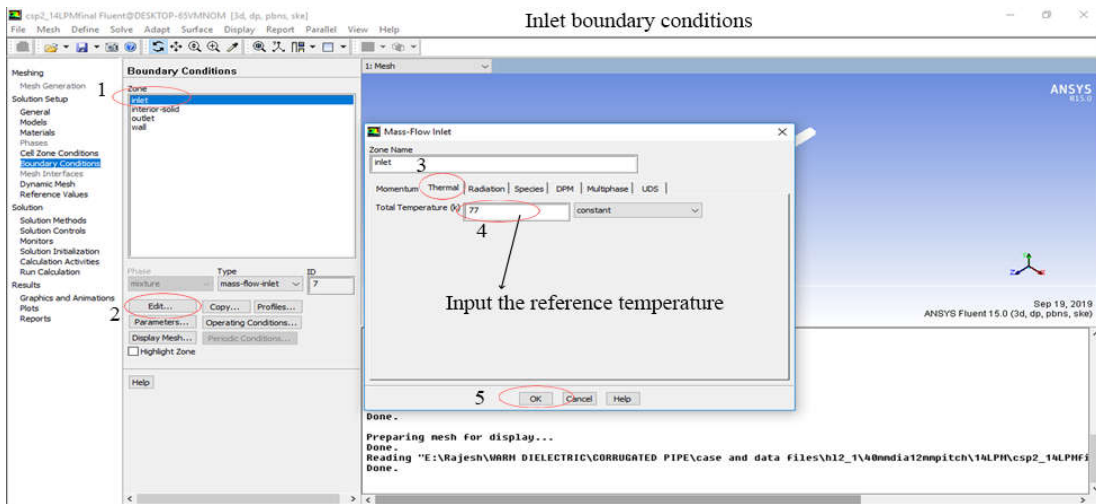


Figure 3.20 Defining the inlet boundary condition with inlet temperature (reference temperature) of 77 K

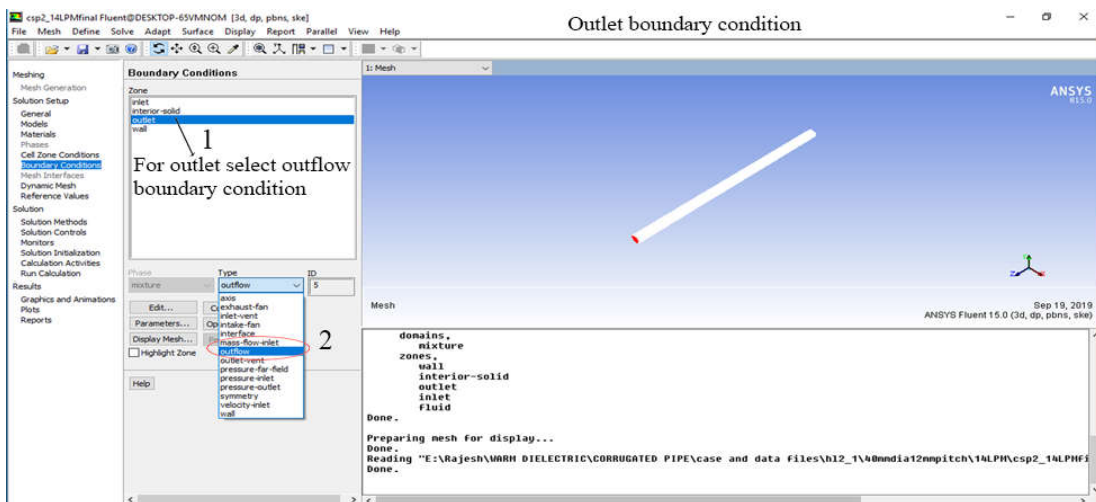


Figure 3.21 Defining the outlet boundary condition

In FLUENT, pre-defined boundary conditions are available such as mass flow inlet boundary at the inlet and outflow at the outlet, velocity inlet at the inlet and pressure outlet at the outlet etc. For solving the thermohydraulic characteristics in the computational domain, outlet pressure and velocities are unknown. Hence, mass flow inlet boundary condition and outflow conditions are used for evaluating the thermohydraulic characteristics. Figure 3.21 shows in boundary condition, at outlet zone outflow boundary condition is selected.

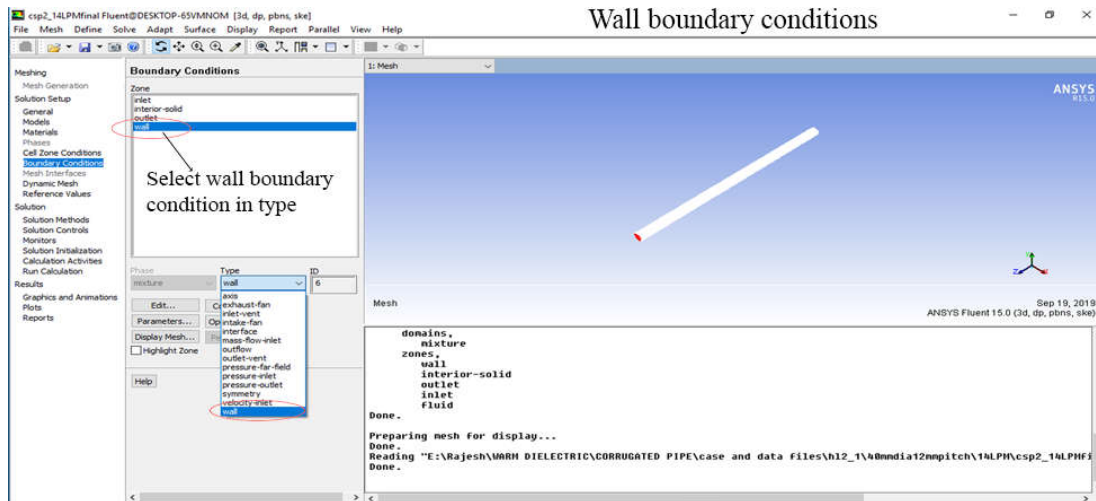


Figure 3.22 Defining the wall with wall boundary condition

In practical conditions HTS cables undergo different heat load conditions such as AC losses from the HTS tapes, dielectric losses from dielectric materials, heat in leaks from ambient and few other minor losses. Hence HTS cables are cooled internally forced cooled from the ambient cryogenic cooling station. Since, the HTS cables are laid under the earth there is no chance for external cooling from the ambient. Hence, the heat loads accommodated in the corrugated former for LN₂ flow through HTS cable should be calculated accurately. In Figure 3.22 the heat loads encountered by the HTS cables are distributed uniformly on the wall by selecting the wall type in the boundary conditions.

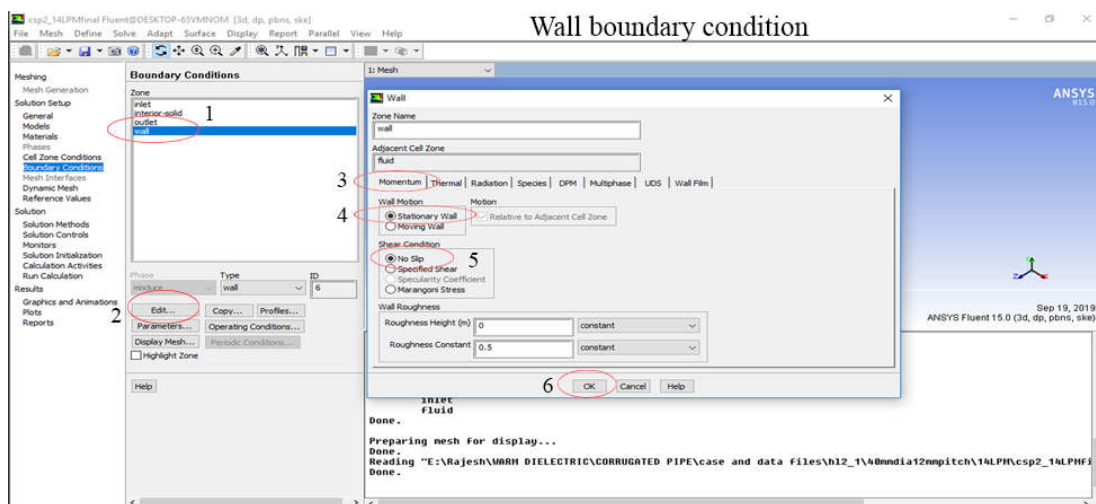


Figure 3.23 Specifying the wall zone with stationary wall and no slip boundary condition

In the wall boundary condition, the adjacent zone is selected as fluid. The stationary all motion and no slip shear condition is applied at the wall in momentum option as shown in Figure 3.23. Mathematically in no slip condition the heat transfer due to conduction should

be equal to the heat transfer due to convection. The wall roughness constant is maintained as 0.5 which is pre-defined in the ANSYS.

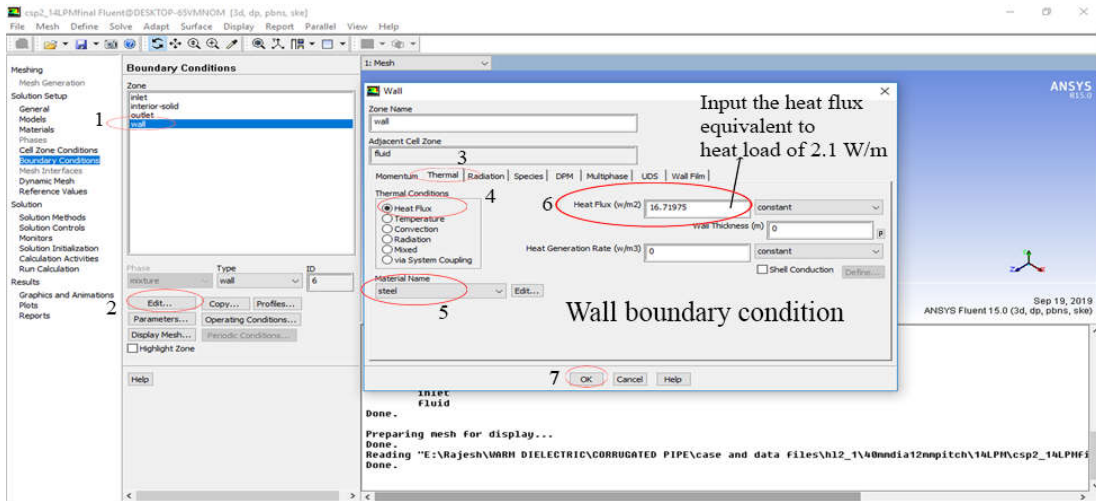


Figure 3.24 Defining the wall boundary condition with uniform heat flux

The heat fluxes related to AC losses and heat in leaks corresponds to power ratings of 0.5 kA to 1.2 kA and voltage rating of 66 kV are estimated approximately 1-3 W/m. In thermal option thermal condition is selected as heat flux and the heat flux equivalent to heat load 1-3 W/m is specified as shown in Figure 3.24. Further at the wall zone condition the material is selected as Steel and its material properties are defined in the material properties section.

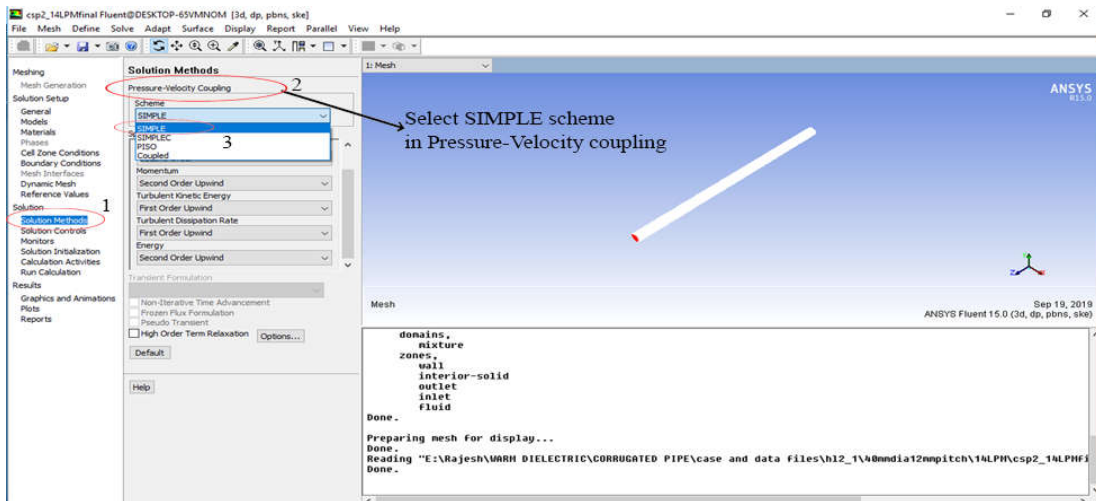


Figure 3.25 Specifying the Pressure-Velocity coupling with SIMPLE scheme

In solution methods, Semi Implicit method for pressure linked equation (SIMPLE) algorithm is employed in solving the pressure-velocity coupling of computational fluid

domain as shown in Figure 3.25. This is due to the superior numerical ability for solving the Reynolds Averaged Navier Stokes (RANS) equation with less compute expenses.

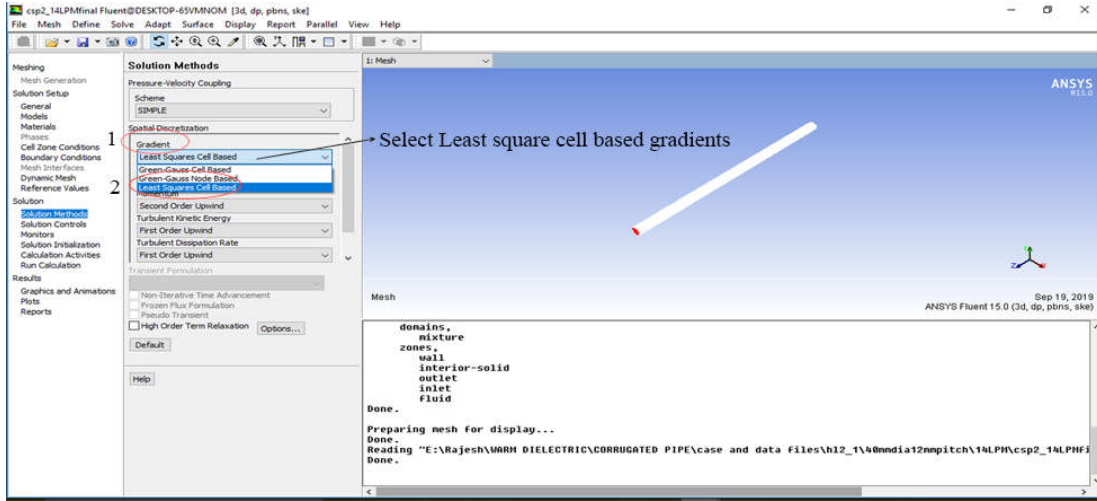


Figure 3.26 Selection of least square cell based gradients in solution discretization

In solution discretization, for solving the gradients least square cell based are selected as shown in Figure 3.26. This discretization method utilizes the concept of least square considering the linear variation between the gradients available at the cell centers. Further, this method presents accuracy with higher order and less computation time for calculating the results.

The necessity of finite difference schemes used in the discretization is to replace the partial derivative equations (PDE's) into algebraic equations using Taylor's Series expansions. For instance, if Taylor's Series expansion is utilized for solving the velocity in a grid, $v_{i,j}$ is the velocity of along the y-direction at any point (i, j) then the velocity at a point $(i+1, j)$ is expressed as

$$v_{i+1,j} = v_{i,j} + \left(\frac{\partial v}{\partial y}\right)_{i,j} \left(\frac{\Delta y}{1!}\right) + \left(\frac{\partial^2 v}{\partial y^2}\right)_{i,j} \left(\frac{(\Delta y)^2}{2!}\right) + \left(\frac{\partial^3 v}{\partial y^3}\right)_{i,j} \left(\frac{(\Delta y)^3}{3!}\right) + \dots \quad (3.76)$$

The finite difference representation of the derivatives in equation (3.76)

$$\left(\frac{\partial v}{\partial y}\right)_{i,j} = \underbrace{\frac{v_{i+1,j} - v_{i,j}}{\Delta y}}_{\text{Finite difference representation}} - \underbrace{\left(\frac{\partial^2 v}{\partial y^2}\right)_{i,j} \left(\frac{\Delta y}{2!}\right) - \left(\frac{\partial^3 v}{\partial y^3}\right)_{i,j} \left(\frac{(\Delta y)^2}{3!}\right)}_{\text{Truncation error}} \quad (3.77)$$

If equation (3.77) is approximated, the PDE in algebraic form can be written as

$$\left(\frac{\partial v}{\partial y}\right)_{i,j} \approx \frac{v_{i+1,j} - v_{i,j}}{\Delta y} \quad (3.78)$$

$$\left(\frac{\partial v}{\partial y}\right)_{i,j} \approx \frac{v_{i+1,j} - v_{i,j}}{\Delta y} + O(\Delta y) \quad (3.79)$$

In the equation (3.79) the information in the left cell of the (i, j) is not used. Therefore, the finite difference is termed as *forward difference*. Further, the first order accurate difference representation is defined in the derivative $\left(\frac{\partial v}{\partial y}\right)_{i,j}$. Hence, it is termed as *first order forward difference*.

Similarly writing the Taylor's expression for $v_{i-1,j}$ with respect to the adjacent cell $v_{i,j}$ is

$$v_{i-1,j} = v_{i,j} + \left(\frac{\partial v}{\partial y}\right)_{i,j} \left(\frac{-\Delta y}{1!}\right) + \left(\frac{\partial^2 v}{\partial y^2}\right)_{i,j} \left(\frac{(-\Delta y)^2}{2!}\right) + \left(\frac{\partial^3 v}{\partial y^3}\right)_{i,j} \left(\frac{(-\Delta y)^3}{3!}\right) + \dots \quad (3.80)$$

$$\left(\frac{\partial v}{\partial y}\right)_{i,j} \approx \frac{v_{i+1,j} - v_{i,j}}{\Delta y} + O(\Delta y) \quad (3.81)$$

For solving the algebraic equation, the finite difference is evaluated with reference to the left cell of (i, j) and no information is utilized from the right side. Therefore, the finite difference is termed as *backward difference*. Further, the first order accurate difference representation is defined in the derivative $\left(\frac{\partial v}{\partial y}\right)_{i,j}$. Hence, it is termed as *first order backward difference*.

In CFD applications for predicting the results accurately, it is observed that first order is not sufficient for solving accurately. Second order can be obtained by subtracting equation (3.76) from equation (3.80)

$$v_{i+1,j} - v_{i-1,j} = 2\left(\frac{\partial v}{\partial y}\right)_{i,j} \left(\frac{(\Delta y)}{1!}\right) + 2\left(\frac{\partial^3 v}{\partial y^3}\right)_{i,j} \left(\frac{(\Delta y)^3}{3!}\right) + \dots \quad (3.82)$$

Simplifying the above equation

$$\left(\frac{\partial v}{\partial y}\right)_{i,j} = \frac{v_{i+1,j} - v_{i-1,j}}{2(\Delta y)} + O(\Delta y)^2 \quad (3.83)$$

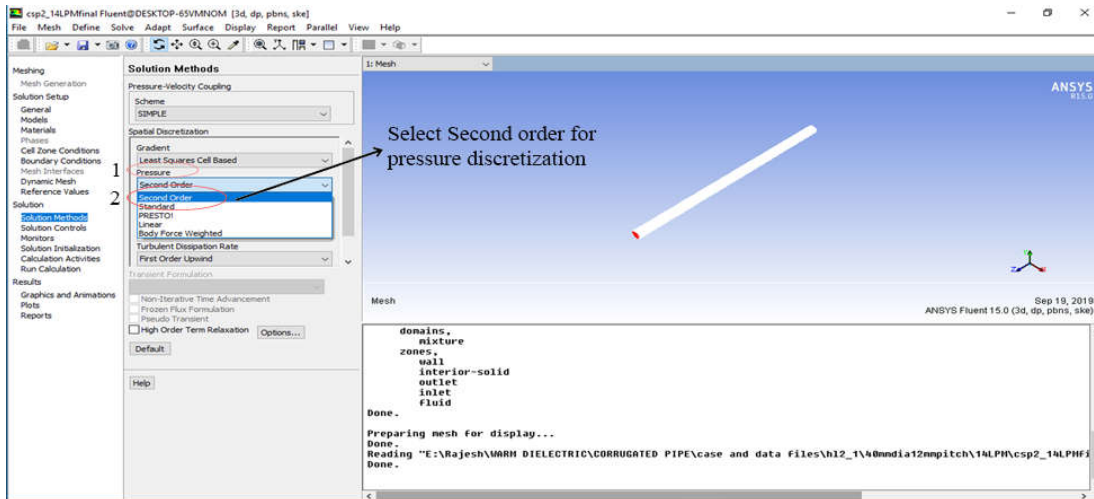


Figure 3.27 Selection of second order pressure discretization

For solving the equation, the information is utilized from right and left side cells of the grid with reference to (i, j) . Further the truncation error is considered in second order in equation (3.83). Hence, it is termed as *second order central difference*.

For instance, if momentum and energy equation discussed in section 3.2 are assumed, $\partial^2 v / \partial x \partial y$, $\partial^2 v / \partial y^2$, $\partial^2 T / \partial y^2$ are derived. Consequently, for solving such PDE's, second order derivatives are required for discretization and such finite difference expressions can be solved using Taylor's series expansions.

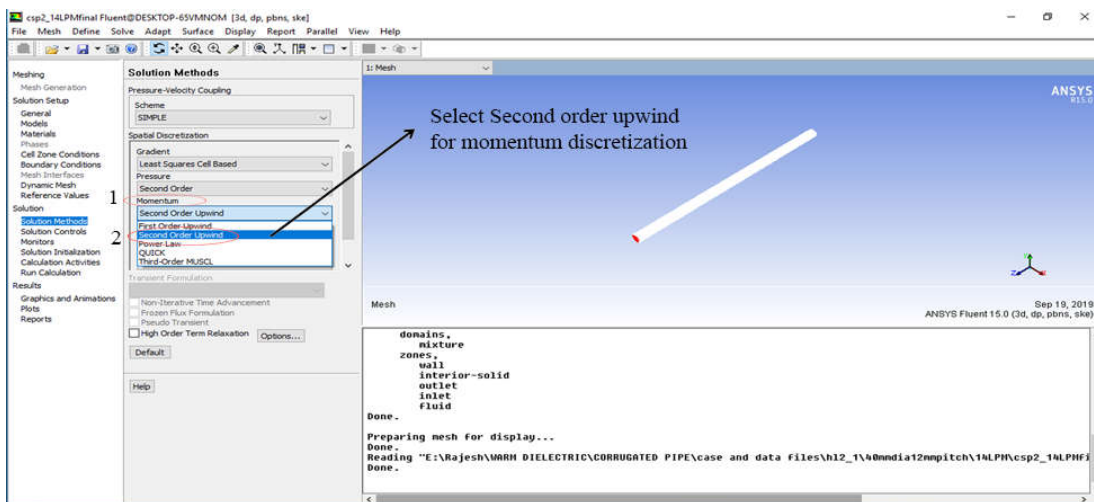


Figure 3.28 Selection of second order upwind for momentum discretization

The pressure gradients in axial and radial direction are required for estimating the flow direction. The negative direction in the axial pressure gradients show forward flow and the negative direction in radial pressure gradients show the radial outward flow of LN_2 in the

computational domain. Hence, for solving pressure second order gradients are selected as shown in Figure 3.27.

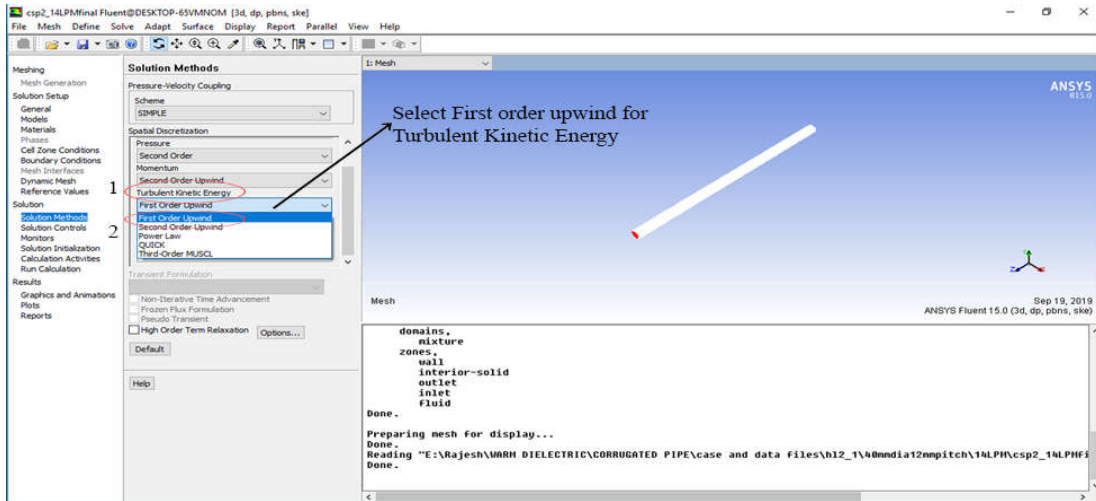


Figure 3.29 Selection of first order upwind for turbulent kinetic energy in solution discretization

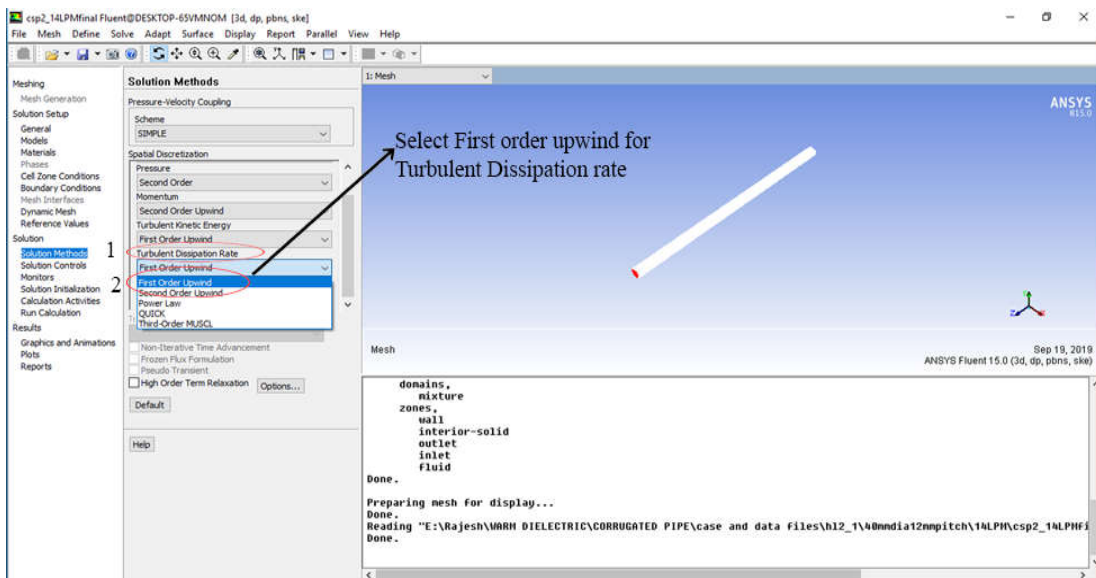


Figure 3.30 Selection of first order upwind for turbulent dissipation rate in solution discretization

Momentum equation is derived in section 3.2.2. In the expression, both first order and second order velocity gradients, first order pressure gradients are available. Second order derivatives is more accurate than first order derivatives. Hence, second order upwind derivative is employed for solving the solution higher order of accuracy as shown in Figure 3.28. The rate of change of velocity gradients and average shear stresses in the fluid flow are responsible for the turbulent viscosity in any turbulent fluid flows. The Turbulent kinetic energy (TKE) is defined as the mean kinetic energy per unit mass in association

with the eddies that are developed in the turbulent flow of computational domain. It is the root mean square of the velocity fluctuations due to eddies in the turbulent flow. The first order upwind is selected for estimating the TKE in the computational domain as shown in the Figure 3.29.

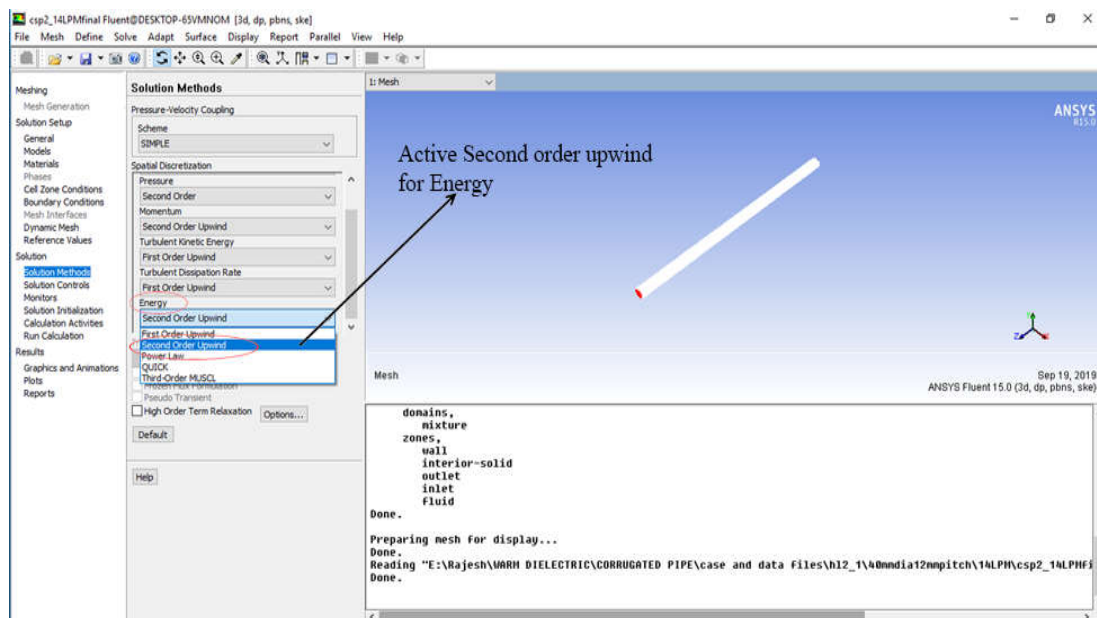


Figure 3.31 Selection of second order upwind for energy in solution discretization

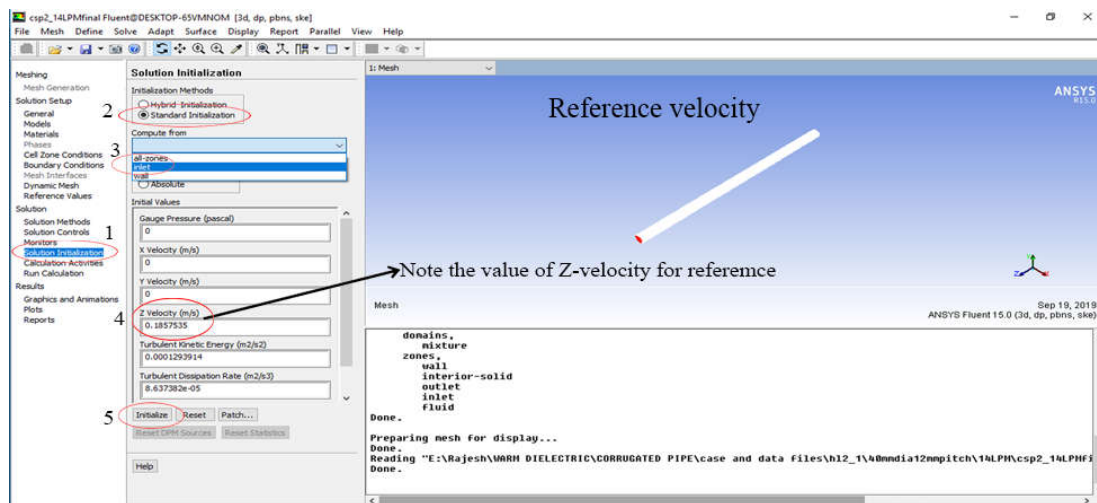


Figure 3.32 Initializing the solution with standard initialization and computing from the inlet

The turbulent dissipation rate is defined as the rate at which the turbulent energy in the computational domain is absorbed by breaking down the large eddies generated into smaller eddies. These smaller eddies are converted into heat energy by viscous forces that

are generated in the LN₂. The turbulent dissipation rate in the computational domain is estimated by selecting the first order upwind derivatives as shown in Figure 3.30.

Energy equation is derived in section 3.2.3. In the expression, first order velocity gradients, second order temperature gradients are available. Second order derivatives is more accurate than first order derivatives. Hence, second order upwind derivative is employed for solving the solution higher order of accuracy as shown in Figure 3.31.

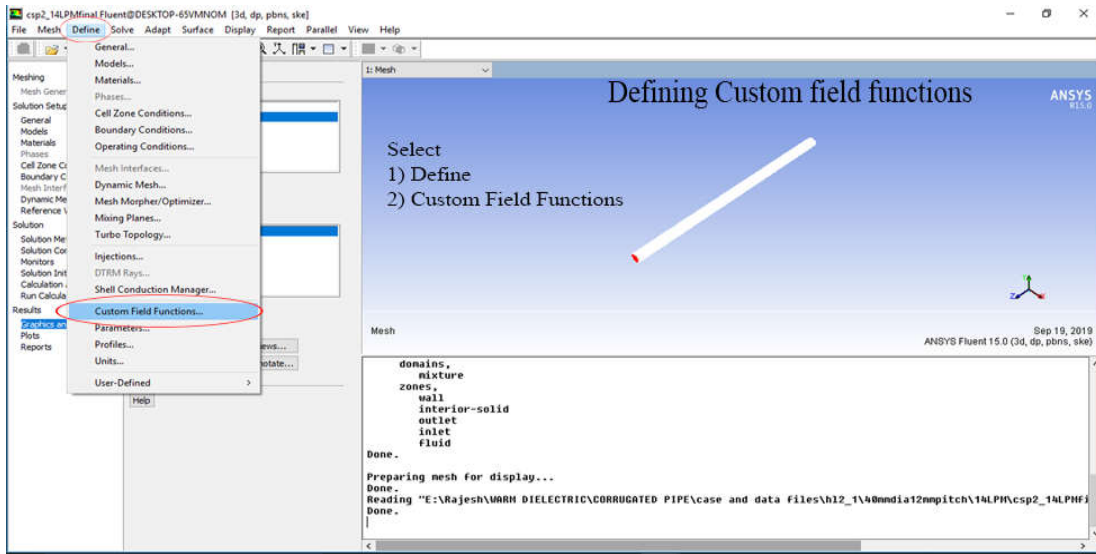


Figure 3.33 Selecting the custom field functions

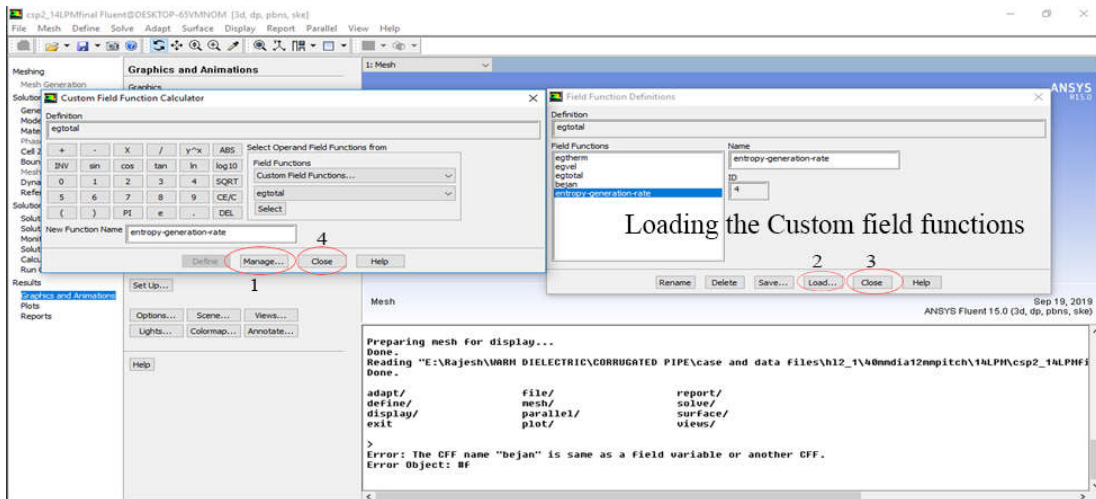


Figure 3.34 Defining the custom field functions for volumetric entropy generation rate

In solution initialization, standard initialization is selected and the solution is computed from inlet of the computational domain. Here the value related to z-direction velocity is noted as shown in Figure 3.32. This value is utilized for calculating the friction factor,

and click on manage as shown in Figure 3.34. The required custom field functions are loaded in to the ANSYS-FLUENT.

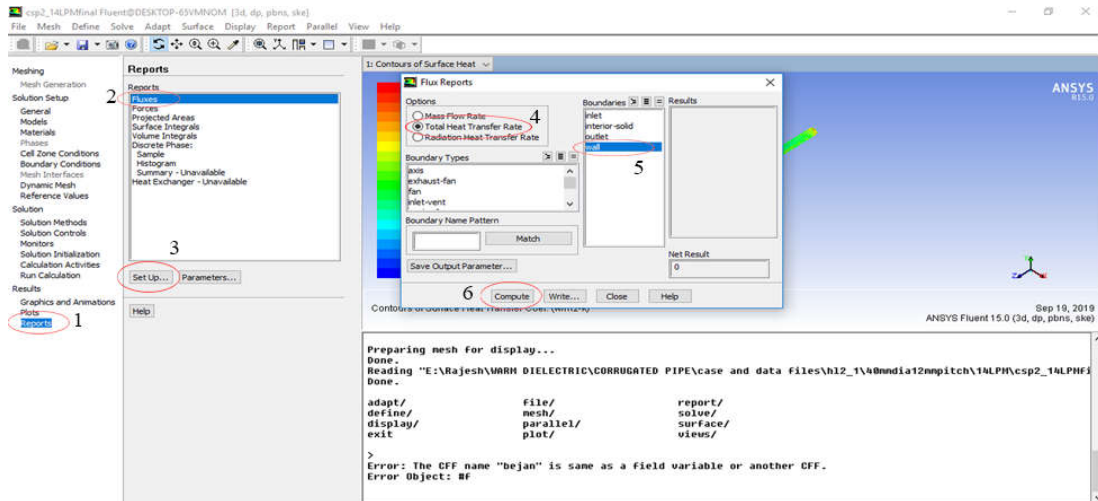


Figure 3.37 Retrieving the heat transfer rate from the wall of the computational domain

Click on graphics and animations, select contours and click on wall fluxes and surface heat transfer coefficient as shown in Figure 3.35. Select the wall option and click on display to visualize the heat load distribution on the wall of computational domain. Note down the maximum and minimum values of the contour for further calculations to verify the Nusselt number. The temperature distribution in the computational domain is retrieved by selecting the temperature and total temperature in contours as shown in Figure 3.36. Select inlet and outlet surfaces and note the value for further reference to calculate cooling capacity.

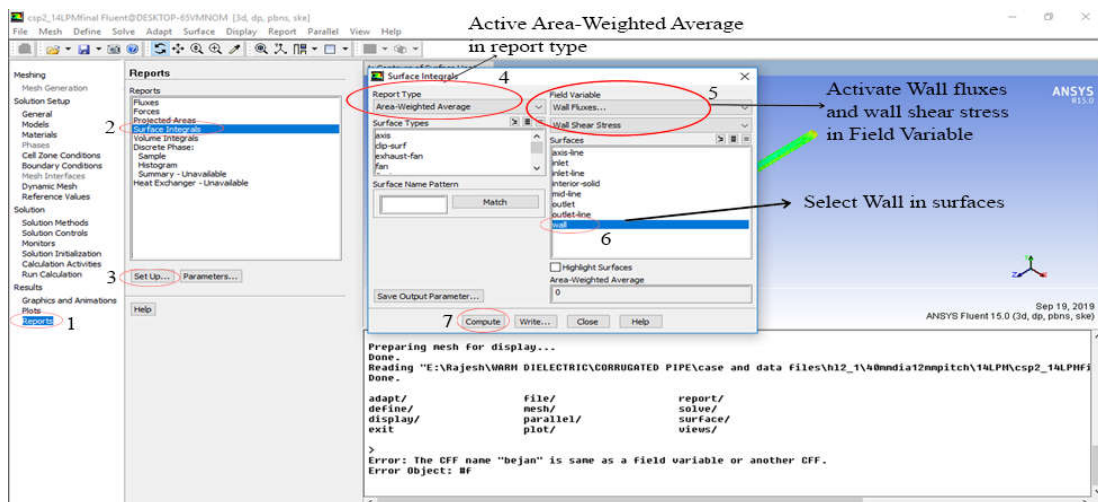


Figure 3.38 Retrieving the shear stresses in the computational domain

The heat transfer rate in the computational domain is retrieved from reports as shown in Figure 3.37. Select fluxes in report and click on total heat transfer rate. Select all in boundaries and click on compute. The net result displayed provides the heat transfer rate with reference to the wall heat loads provided in the wall boundary conditions. Further, in reports select average weighted average in report type and activate wall fluxes and wall shear stress in field variables as shown in Figure 3.38. Select wall in the surfaces and click on compute. The retrieved wall shear stress is used for calculating friction factor of LN₂ in computational domain.

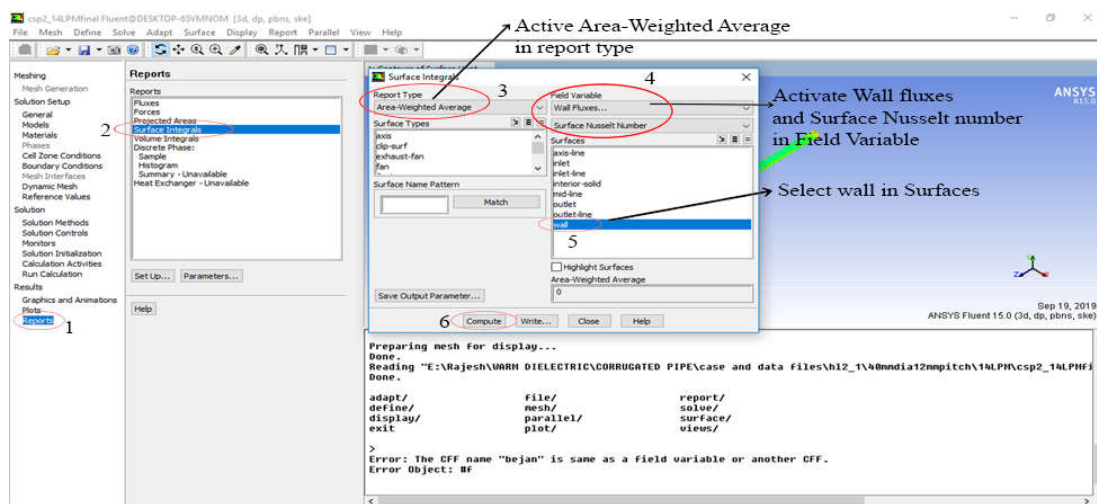


Figure 3.39 Retrieving the surface Nusselt number in the computational domain

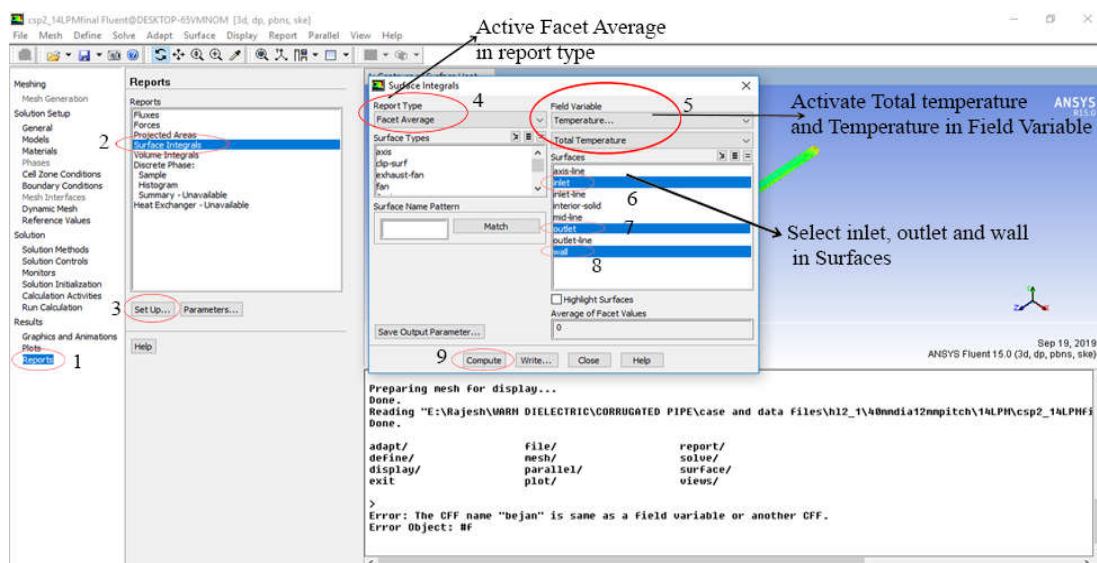


Figure 3.40 Retrieving the total temperature at the inlet and outlet of the computational domain

In reports select average weighted average in report type and activate wall fluxes and surface Nusselt number in field variables as shown in Figure 3.39. Select wall in the surfaces and click on compute. The retrieved surface Nusselt number is used for calculating convective heat transfer rate.

In reports select facet average in report type and activate temperature and total temperature in field variables as shown in Figure 3.40. Select inlet and outlet in the surfaces and click on compute. The retrieved temperature is used for calculating cooling capacity of LN₂ in computational domain.

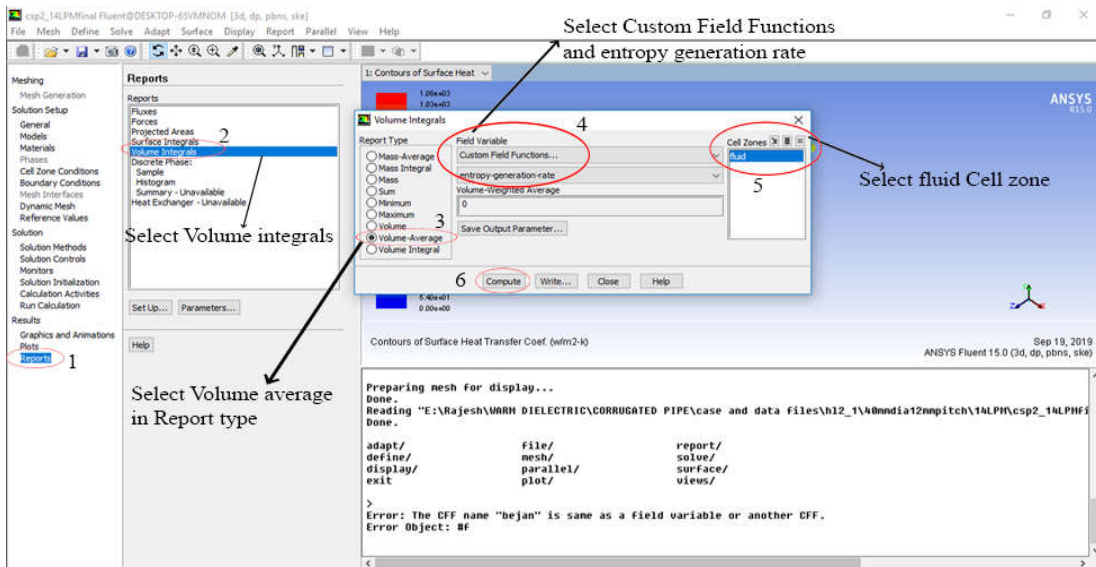


Figure 3.41 Retrieving the volumetric entropy generation rate in the computational domain

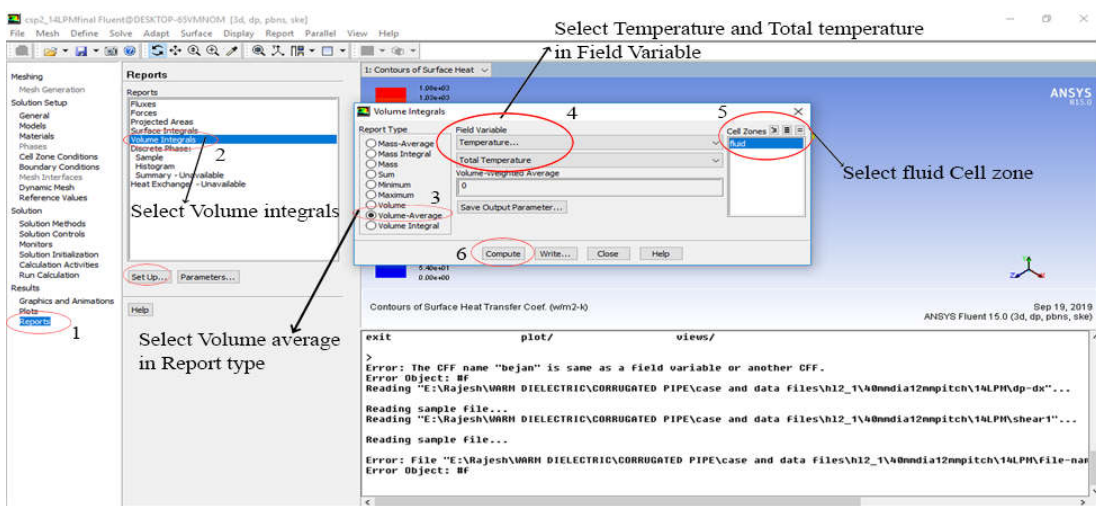


Figure 3.42 Retrieving the bulk temperature of LN₂ in the computational domain

Select volume integrals, activate volume average and select custom field functions. Activate volumetric entropy generation rate to calculate the total entropy generation rate as shown in Figure 3.41. Similarly select temperature and total temperature to retrieve the total temperature in entire volume of the computational domain as shown in Figure 3.42.

3.6.1 Thermohydraulic characteristics

The former and cryostat in HTS cables are corrugated due to these large frictional factors are observed. The shear stresses and drag forces on the corrugated walls of the HTS cable increases the pressure drop. Friction inside the computational domains is due to the shear forces between the cryogenic fluid molecules and between the wall and the cryogenic coolant. The friction factor for different mass flow rates at given heat flux is given in eqn(3.84).

$$f_{csp} = \frac{8\tau_{wall}}{\rho_{LN_2} v_{avg}^2} \quad (3.84)$$

In the past, Pisareco [295] investigated and reported, the numerical analysis on friction factor considering various turbulence models and corrugation depths in corrugated pipes. Herwig [296] discussed about pressure drop and friction factor for corrugated geometry, considered turbulent flow of an incompressible fluid.

The Reynolds number can be estimated by eqn(3.85).

$$Re = \frac{D_h v_{avg} \rho_{LN_2}}{\mu_{LN_2}} \quad (3.85)$$

Pressure drop in the HTS cable former can be calculated by using

$$\Delta P = \frac{\rho_{LN_2} f_{csp} v_{avg}^2}{2D_h} \quad (3.86)$$

The amount of the power needed for transporting cryogenic coolant from refrigeration system is given by [204]

$$W = \Delta p \dot{V} = \Delta p \frac{\dot{m}_{LN_2}}{\rho_{LN_2}} \quad (3.87)$$

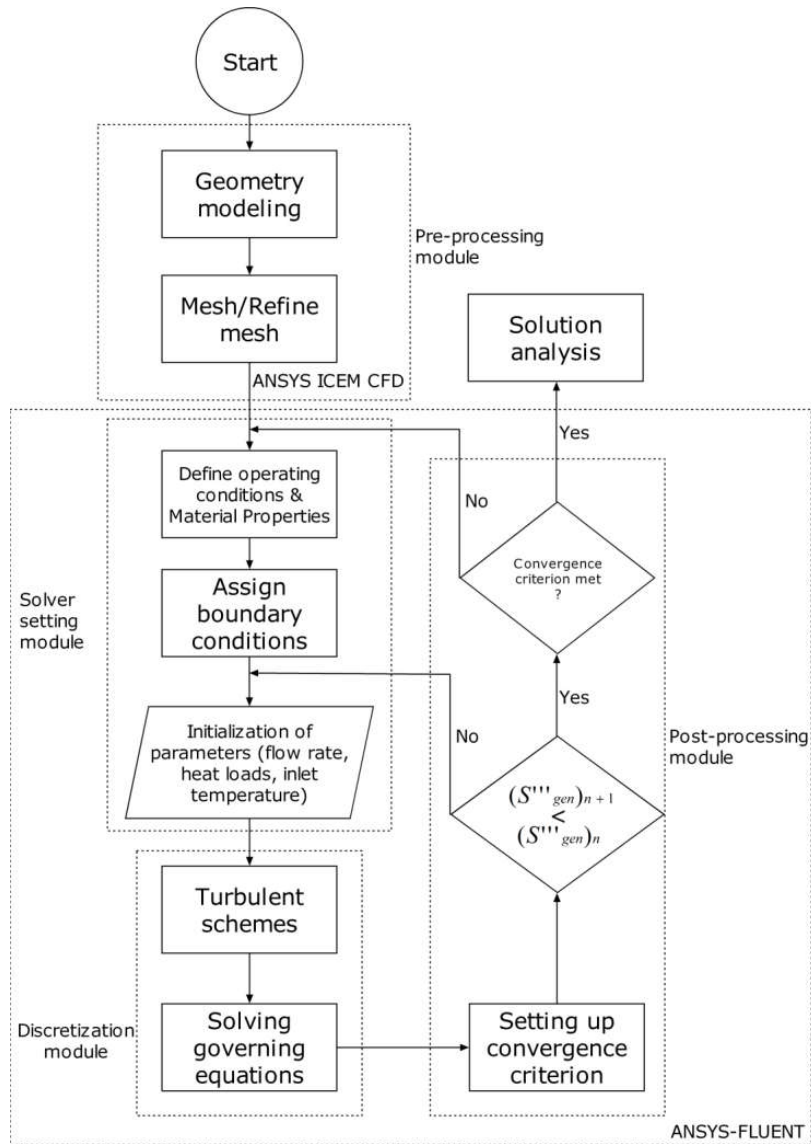


Figure 3.43 Flow chart of the methodology used for the analysis

where, f_{cp} is frictional faction in corrugated steel pipe, ρ_{LN_2} = density (kg/m^3) of LN_2 , v_{avg} = average velocity inside the pipe (m/s), D_h = hydraulic diameter, Δp = pressure drop (Pa/m), volume flow rate (L/sec), $\dot{V} = v_{avg} * A$, A = area of cross section (m^2).

Heat transfer can be increased effectively by using corrugated geometry due to the turbulence of cryocoolant in fluid domain larger cooling capacity can be attained. The heat transfer rate at the surface is calculated from the dimensionless number called Nusselt number by following equation (3.88)

$$Nu = \frac{h_c L}{k} \quad (3.88)$$

Where, h_c denotes the convective heat transfer coefficient (W/m²K) and k refers to thermal conductivity (W/m-K)

The heat transfer rate is estimated by using

$$q'' = h_c \Delta T \quad (3.89)$$

Cooling capacity of the cryogenic coolant is given by

$$Q = \dot{v} \rho C_p (T_{outlet} - T_{inlet}) \quad (3.90)$$

Where, h_c =convective heat transfer rate, q'' = heat flux (W/m²), $\Delta T = T_{wall} - T_{bulk}$, temperature difference from inlet to outlet in K, C_p = specific heat, T_{outlet} , T_{inlet} are temperatures of LN₂ in K and extracted from ANSYS-FLUENT.

3.6.2 Volumetric entropy generation rate

The conservation of energy contributes to thermal gradients that are to be discretized using Finite Volume Method (FVM) in FLUENT. The temperature gradients developed at each node in computational domain are extracted from the FLUENT and the volumetric average of entropy generation rate due to thermal gradients is calculated using equation (3.91). The momentum equation constitutes contribution of pressure gradients that are to be discretized using Finite Volume Method (FVM) in FLUENT. Further it is reported that, transportation of eddies during turbulent flow results in pressure gradients and temperature rise [297]. Hence, the estimation of pressure gradients is necessary to calculate the entropy generation rate due to velocity gradients. The pressure drop in the corrugated former, results in velocity gradients in the computational domain. The velocity gradients developed at each node in computational domain are extracted from the FLUENT and the volumetric average of entropy generation rate due to velocity gradients is calculated using equation (3.91).

$$S_{gen,Thermal}''' = \frac{K}{T_{ref}^2} \left[\left(\frac{\partial \bar{T}}{\partial x} \right)^2 + \left(\frac{\partial \bar{T}}{\partial y} \right)^2 + \left(\frac{\partial \bar{T}}{\partial z} \right)^2 \right]$$

$$S_{frictional}''' = \frac{\mu}{T_{ref}} \left[2 \left(\left(\frac{\partial \bar{u}}{\partial x} \right)^2 + \left(\frac{\partial \bar{v}}{\partial y} \right)^2 + \left(\frac{\partial \bar{w}}{\partial z} \right)^2 \right) + \left(\frac{\partial \bar{u}}{\partial y} + \frac{\partial \bar{v}}{\partial x} \right)^2 + \left(\frac{\partial \bar{u}}{\partial z} + \frac{\partial \bar{w}}{\partial x} \right)^2 + \left(\frac{\partial \bar{w}}{\partial y} + \frac{\partial \bar{v}}{\partial z} \right)^2 \right] \quad (3.91)$$

The volumetric entropy generation rate in the HTS cable is calculated by using the entropy generation rate due to the thermal and velocity gradients. Further, minimum entropy generation is evaluated at different flow rates of LN₂, different inlet temperature of LN₂ and different heat loads encountered by the HTS cable during operation.

3.7 Grid independence study

The necessity of grid independence study is to predict the appropriate element size for meshing the computational domain used for the analysis which is independent of node position. This study is carried with the different element sizes ranging from 1.1 mm to 0.8 mm using ANSYS.

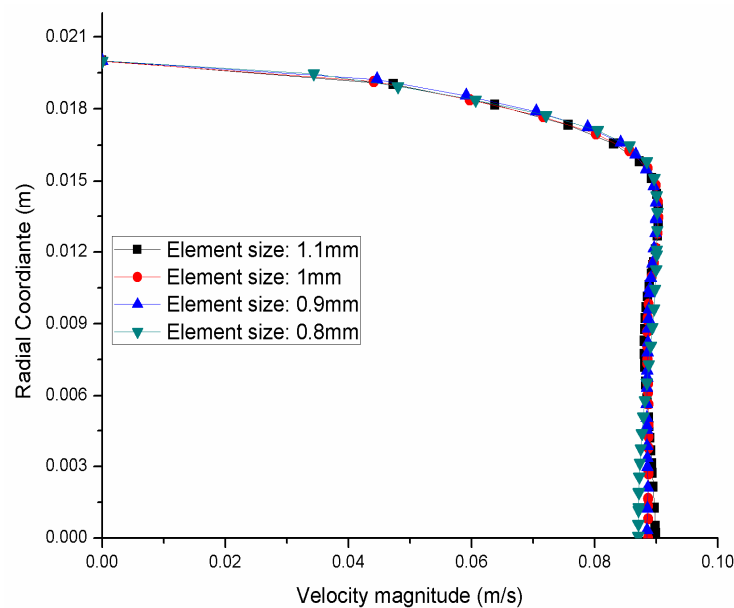



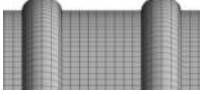

Figure 3.44 Velocity profiles at the outlet of the corrugated pipe in HTS cables for different mesh sizes

Figure 3.44 shows the results obtained from the grid independence study on velocity distribution at the outlet of the HTS cable along radial direction. From the figure it is observed that, varying the element size from 0.9 mm to 0.8 mm there is no significant variation in the velocity magnitude at the outlet. Hence, 0.9 mm mesh is chosen for the further analysis because it is independent of the node position. In the computational domain, the developed grid constitutes 13723002 nodes and 3358383 elements.

In addition to the velocity distribution, entropy generation rate is calculated with different mesh topologies for studying the grid independency of HTS cable modeled for the present analysis with different element sizes shown in Table 3.6. From the study, it is observed that the relative difference in the total entropy generation rate is 0.8% for the element size of 1

mm and 0.9 mm. Hence, the mesh topology with 0.9 mm element size is selected for the analysis to avoid solution instability in HTS cables at different heat loads, inlet temperature and flow rate.

Table 3.6 Different mesh topologies used for grid independent study

Element Size (mm)	Mesh Topology	Number of nodes	Entropy Generation Rate (W/m ³ K)	Difference in Entropy Generation Rate (%)
1.1		2408005	0.008023	29.31
1		3044076	0.0113	0.8
0.9		3816244	0.0114	-

The mathematical formulation for solving the closure problem of the present is discussed. The grid independence study is done and the computational domain with selected mesh topology is used for calculating the results. Further, the practical boundary conditions are imposed on the computational domain for analyzing thermohydraulic characteristics, entropy generation rate and exergy destruction rate. The results pertained to the different cases such as influence of mass flow rate, influence of heat loads and influence of inlet temperature are discussed in the further chapters.

4 HYDRAULIC CHARACTERISTICS OF HTS CABLES

4.1 Introduction

The capacity of power handled by the compact HTS cable is very higher compared to the conventional cable. Hence, critical study on HTS cables is necessary to meet the rated power demand. In order to meet the demand, HTS cable encounters heat loads which are imposed on cryogenic coolants. These cables are force convection cooled internally to accommodate the inevitable heat loads from heat-in-leaks, AC losses, dielectric losses etc using LN₂. The critical temperatures in the HTS cable should be maintained in order to transmit the power efficiently. Hence, a critical investigation is required while designing the HTS cable. The estimation of pressure drop and cooling capacity of HTS cable depends on the inlet temperature and rate of cryocoolant supplied from the terminal of refrigeration system.

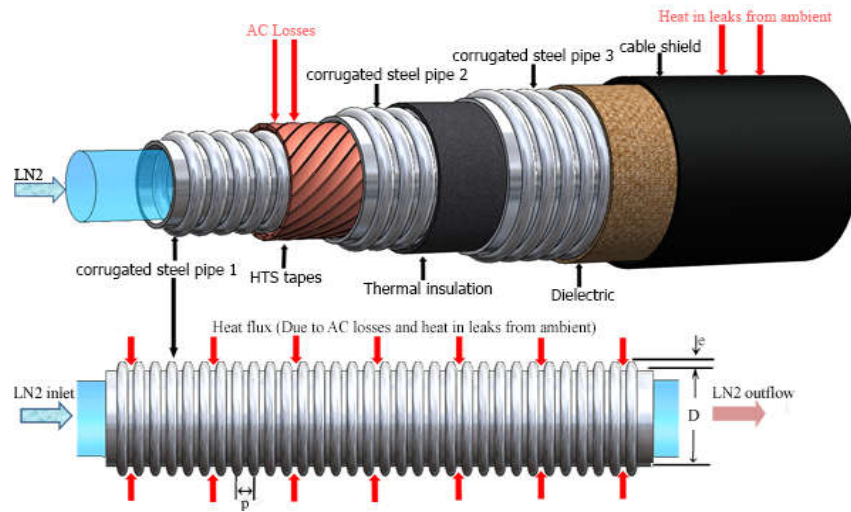


Figure 4.1 Geometry of HTS cable and schematic of corrugated former used for computational analysis with boundary conditions

The estimation of Thermohydraulic performance in HTS cables is required for efficient operation under heat loads. The HTS cable (see Figure 4.1) comprises of HTS tapes wound around spirally on inner corrugated steel former. LN₂ flows internally through the corrugated former and thermal insulation is used to restrict heat infiltrations from the ambient to retain the superconductivity of HTS tapes under operation. Further, to protect the HTS cable from short circuit dielectric layer is used and the cable shield is used as an outer layer for protecting the HTS cable from surrounding. Due to the complexity in the

geometry of HTS cable, in the past, researchers carried computational analysis on estimation of thermal and hydraulic characteristics [242], [283]. In this section, a detailed description on computational domain used for the analysis for estimating the hydraulic characteristics such as friction factor, pressure drop and pumping power is discussed. Further, the thermophysical properties of LN₂ are extracted and the coefficients of fitted data are calculated. These coefficients are used in the material properties of LN₂ during the simulation (discussed in section 3.4.1). Later, the governing equations are solved by imposing the boundary conditions similar to the practical conditions. The results obtained in the post processing are used in the estimation of pumping power and cooling capacity for LN₂ flow in HTS cable former. Flow rates ranging from 1-20 L/min, heat loads ranging from 1-3 W/m and inlet temperature of LN₂ ranging from 65-77 K (shown in Table 3.1) are utilized for estimating the hydraulic characteristics in HTS cables.

4.2 Validation

To validate the thermohydraulic performance of present results obtained from CFD at different heat load is presented in this section. The calculated results obtained from CFD are validated with the existing literature shown in Figure 4.2. From the Figure 4.2 (a) it is observed that, with the increase in the Reynolds number, friction factor decreases at different heat loads. Further, the influence of the heat loads on the friction factor remains unaltered. From equation (3.84) it is observed that the friction factor is in proportion to the wall shear stresses and inversely proportion to the square of the velocity. The variation of the wall shear stress and velocity distribution in the corrugated former (see Figure 4.5) are unaltered. Hence, the friction factor may unaltered under the influence of heat load.

From Figure 4.2(b), it is observed that with the increase in flow rate, temperature difference between the outlet and the inlet of the HTS cable is decreasing. Further, with the increase in the heat load the temperature at the outlet of the HTS cable increased. Furthermore, the results of friction factor are showing good agreement with the simulation results of Gadekula et al. [298] and experimental results of Ivanov et al. [290] and the thermal results are showing good agreement with the simulation results of Gadekula et al. [298] and Kalsia et al. [280].

The pressure drop at different flow rates at a heat load of 2.1 W/m is shown in Figure 4.3. From the figure, it is observed that the pressure drop is increasing with the increase in the flow rate at a particular heat load. The computational results of the present work is

validated with the experimental results of Ivanov et al. [290]. Further, the simulation results are less than 5% of the experimental results of Ivanov et al.

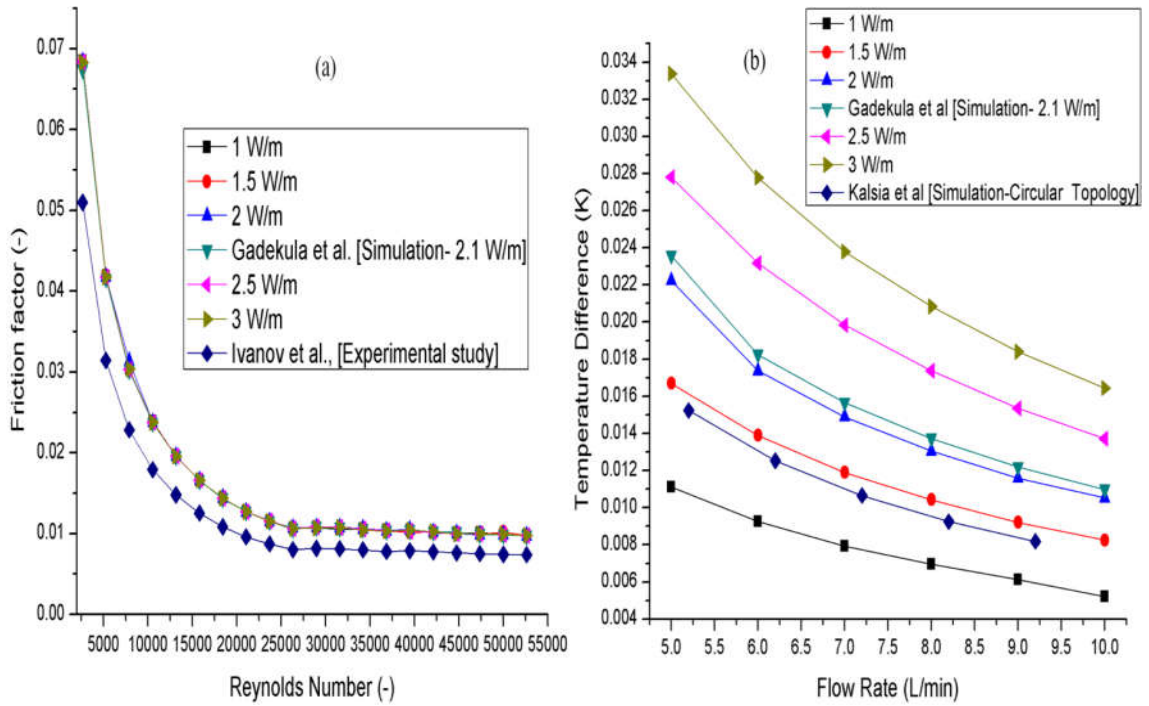


Figure 4.2 Validation of present CFD study at different heat loads (a) friction factor versus Reynolds number with simulation results of Gadekula et al. [298] and experimental results of Ivanov et al. [290] (b) Temperature difference versus flow rate with the simulation results of Gadekula et al. [298] and Kalsia et al. [280]

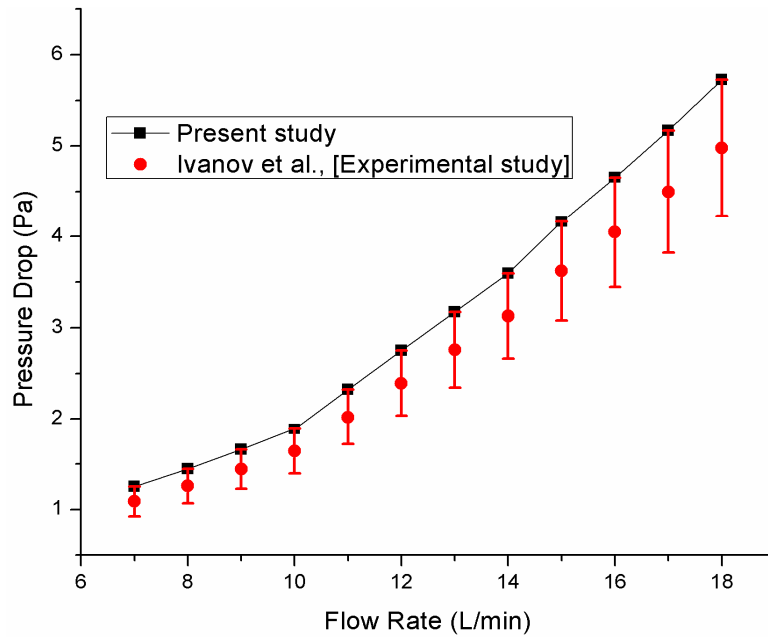


Figure 4.3 Validation of Computational results with the experimental results of Ivanov et al. [290]

4.3 Velocity profiles

The velocity profiles that are developed at different flow rates with a heat load of 2.1 W/m is at two different locations one at the center and other at the outlet are shown in Figure 4.4. From the figure it is evident with the increase in flow rate velocity magnitudes are increasing. Further, fully developed velocity profiles are not attained at the captured locations. Hence, these fluctuations leads to turbulence flow of LN₂ in HTS cables and thereby contributes to higher wall shear stresses [242].

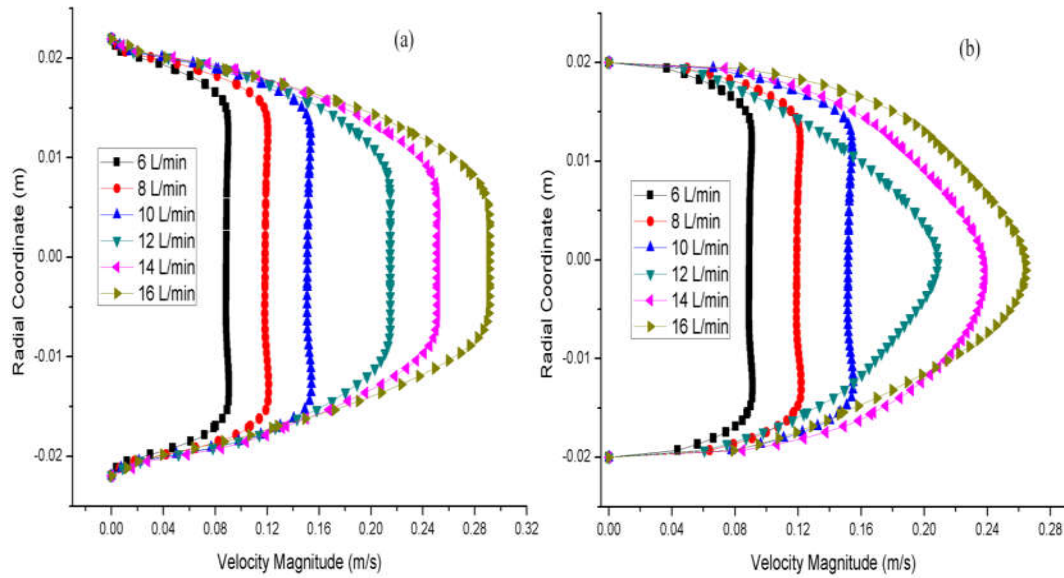


Figure 4.4 Velocity profiles at various flow rates in HTS cable with a heat load of 2.1 W/m (a) center (b) outlet

The effect of heat loads and the temperature dependent thermophysical properties on the hydraulic performance such as friction factor, pressure drop and pumping power in HTS cable with internal forced convective cooling of LN₂ is presented. Figure 4.5 shows that the velocity profiles at the center and at the outlet of the HTS cable. From the figure, it can be seen that at the center of the HTS cable the variation of the velocity at different heat loads remain unaltered.

Further, the profiles are seems to be fully developed at the outlet of HTS cable for different heat loads at a flow rate of 19 L/min. The fluctuations in the velocity result in the turbulence of LN₂ and thereby contributing to the shear stresses at the wall of HTS cable. Hence, it contributes to entropy generation due to frictional flow of LN₂ which affects the performance of HTS cable.

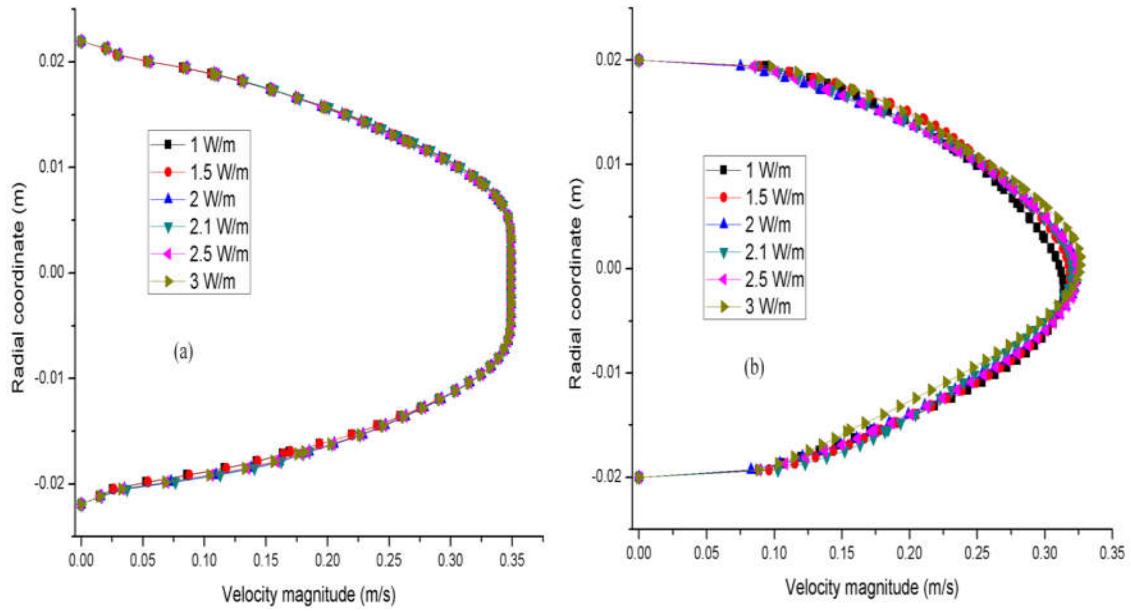


Figure 4.5 Velocity profiles at various heat loads in corrugated steel former with a flow rate of 19 LPM (a) center (b) outlet

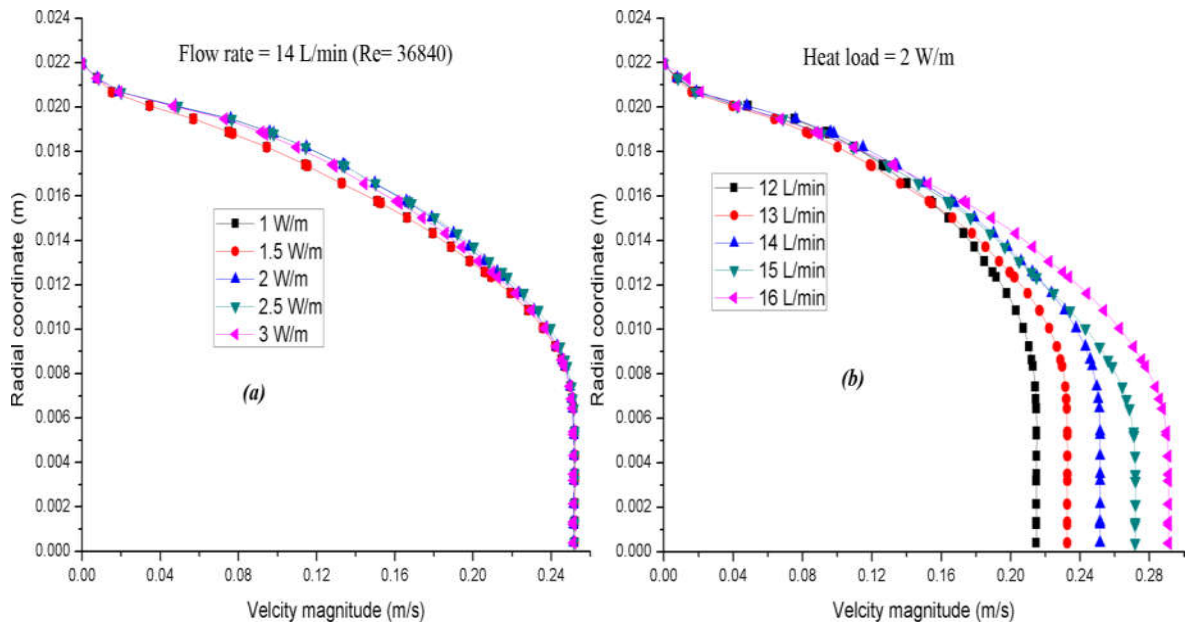


Figure 4.6 Radial velocity distribution at a distance of $z = 0.5$ m in the HTS cable (a) for different heat loads at a flow rate of 14 L/min (b) for different flow rates at a heat load of 2 W/m

The radial velocity distribution for temperature dependent LN_2 flow through HTS corrugated former at different heat loads is presented in this section. In order to capture the results in the computational domain two locations are selected one is at a distance of 0.5 m where a corrugation exist and other location is at a distance of 1 m from the inlet.

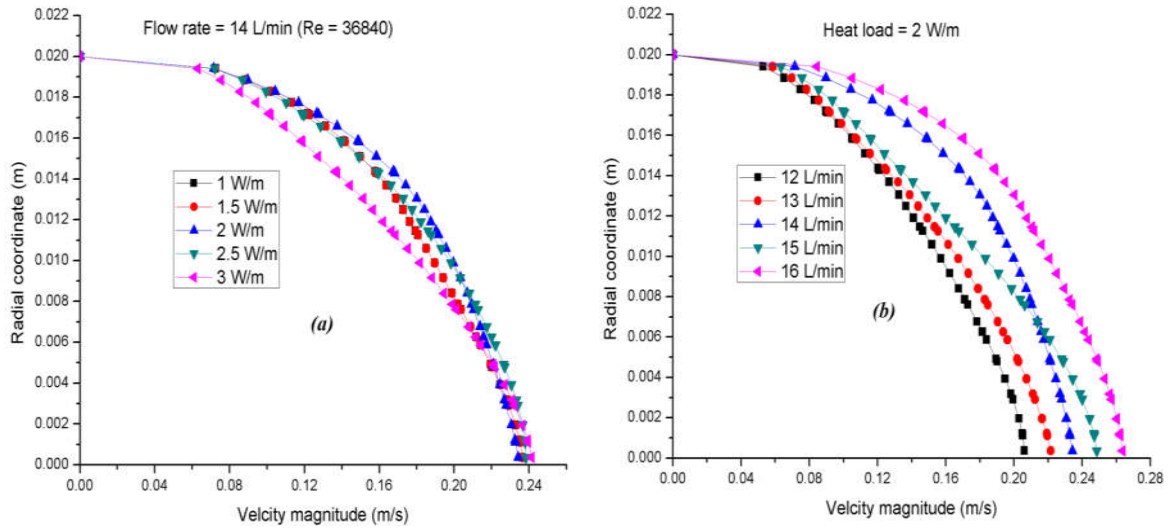


Figure 4.7 Radial velocity distribution at a distance of $z = 1$ m in the HTS cable (a) for different heat loads at a flow rate of 14 L/min (b) for different flow rates at a heat load of 2 W/m

The radial velocity distribution at a distance of 0.5 m from the inlet of the computational domain at a flow rate of 14 L/min is shown in Figure 4.6 (a) and at a heat load of 2 W/m is shown in Figure 4.6 (b). It is observed that the effect of heat loads on the radial velocity distribution at a particular flow rate is negligible and with the increase in the flow rate at a particular heat load the radial velocity increases at a distance of 0.5m. Further, the radial velocity distribution at a distance of 1 m from the inlet of the computational domain at a flow rate of 14 L/min is shown in Figure 4.7 (a) and at a heat load of 2 W/m is shown in Figure 4.7 (b). The radial velocity distribution follows similar trend as observed at 0.5m.

4.4 Velocity gradients

The average velocity gradients in axial direction and radial direction together contribute to the development of entropy generation rate due to velocity gradients as discussed in chapter 3. In this section, the average axial and radial velocity gradients are presented at different flow rates and at different locations in the HTS cable.

4.4.1 Axial Velocity gradients

The average axial velocity gradients for different flow rates at a heat load of 2.1 W/m in x , y and z -direction is shown in Figure 4.8. From the figure it is evident that the contribution of average axial velocity gradients for entropy generation rate due to velocity gradients is higher at higher flow rates in x , y and z -directions.

The average transverse axial velocity gradients for different flow rates at a heat load of 2.1 W/m in x , y and z -direction is shown in Figure 4.9. From the figure it is evident that the

contribution of average transverse axial velocity gradients for entropy generation rate due to velocity gradients is higher at higher flow rates in x, y and z-directions. Further, no variations in the velocity gradients are observed till the center of HTS cable. The average transverse velocity gradients in the z- direction at higher flow rates are compensating the entropy generation rate as shown in Figure 4.9 (e-f).

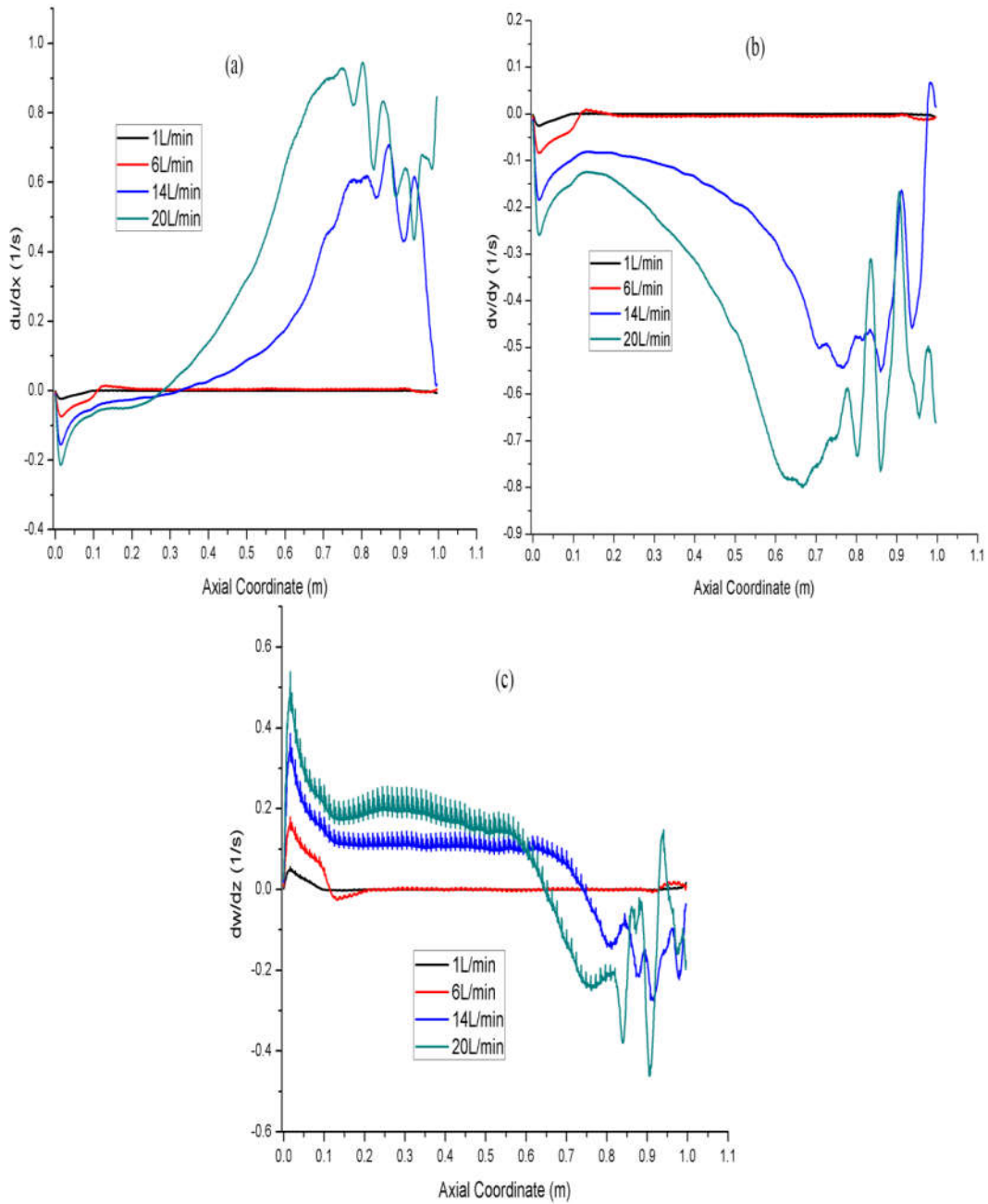


Figure 4.8 Axial velocity gradients for different flow rates at heat load of 2.1 W/m in (a) x-direction (b) y-direction (c) z-direction

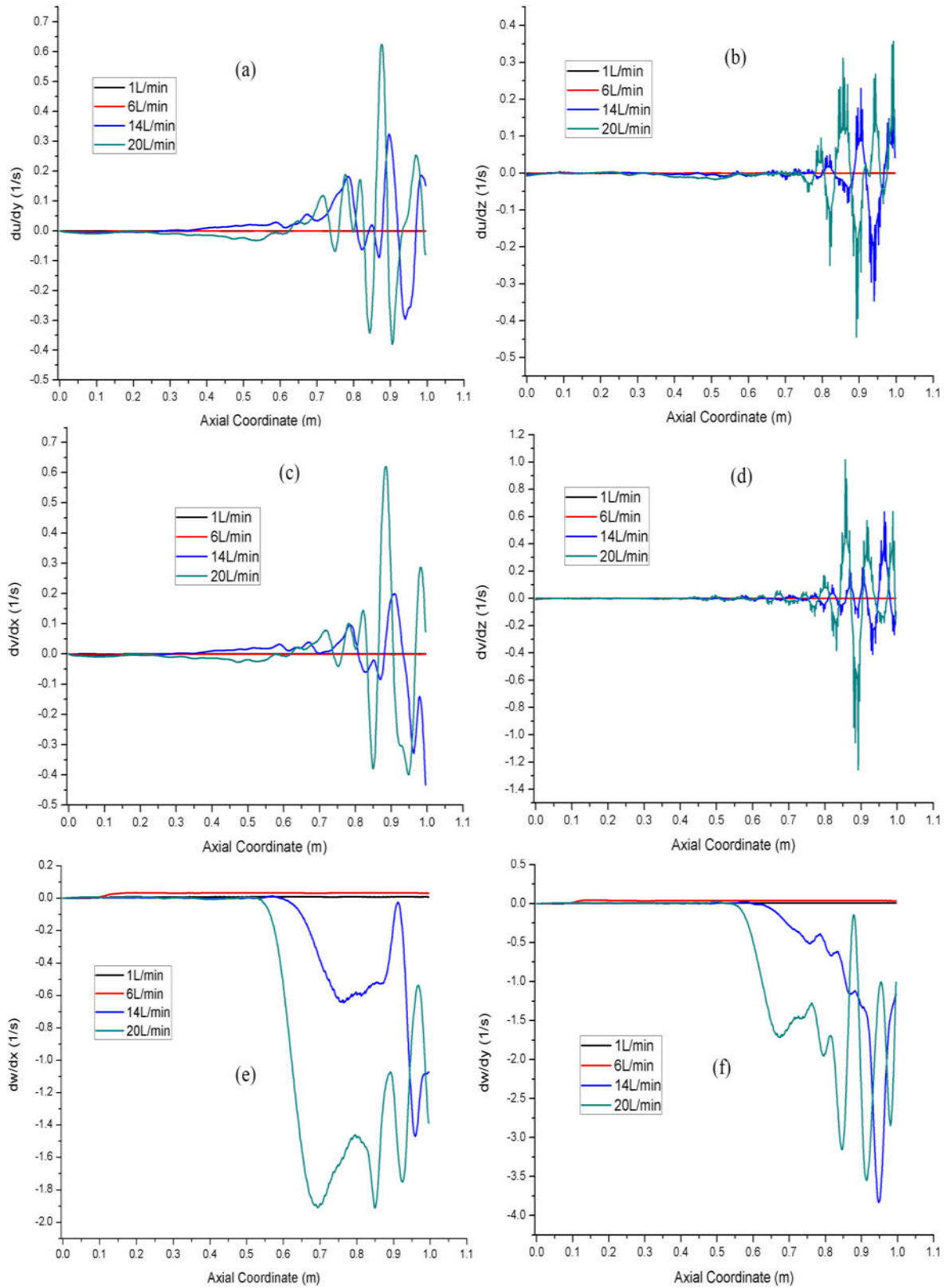


Figure 4.9 Transverse axial velocity gradients at different mass flow rates at a heat flux of 2.1 W/m (a-b) x-direction (c-d) y-direction (e-f) z-direction

4.4.2 Radial velocity gradients

The average radial velocity gradients at a flow rate of 14 L/min and a heat load of 2.1 W/m is shown in Figure 4.10. From the figure, it is observed that velocity gradients in y-direction are contributing higher to entropy generation rate. Further, at the corrugations the velocity gradients are higher than the locations without corrugations.

The average transverse radial velocity gradients at a flow rate of 14 L/min and a heat load of 2.1 W/m is shown in Figure 4.11. From the figure, it is observed that z-direction velocity gradients are contributing higher for the entropy generation rate. Further, at the corrugations the velocity gradients are higher than the locations without corrugations.

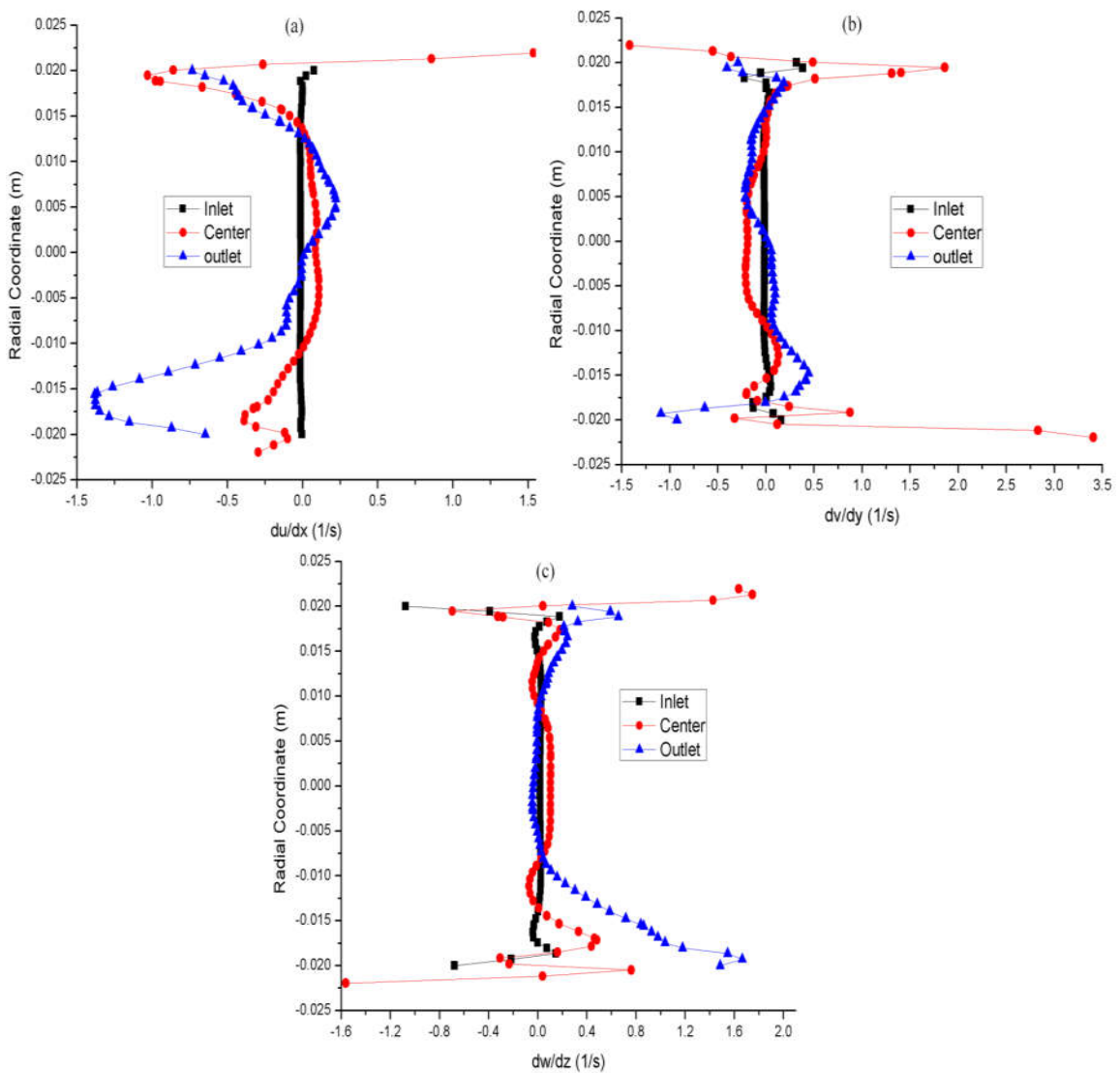


Figure 4.10 Radial Velocity gradients at the flow rate of 14 L/min in (a) x-direction (b) y-direction (c) z-direction

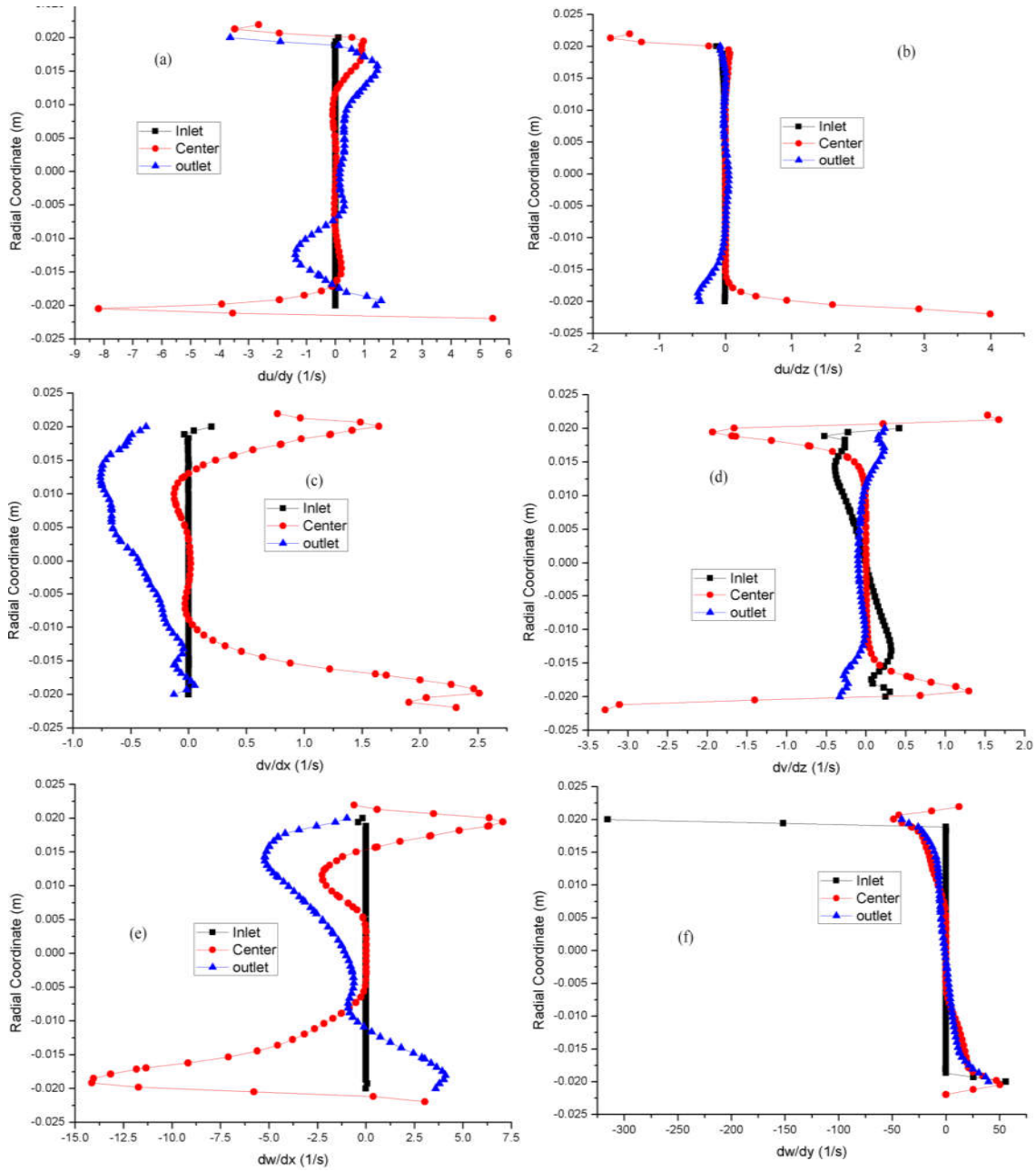


Figure 4.11 Transverse radial velocity gradients at a flow rate of 14 L/min and a heat load of 2.1 W/m (a-b) x-direction (c-d) y-direction (e-f) z-direction

4.5 Pressure gradients

The momentum equation constitutes contribution of pressure gradients that are to be discretized using Finite Volume Method (FVM). Further it is reported that, transportation of eddies during turbulent flow results in pressure gradients and temperature rise [297]. Hence, the estimation of pressure gradients are necessary to calculate the entropy generation rate. In this section, the axial and radial pressure gradients are presented at different flow rates and at different locations in the HTS cable.

4.5.1 Axial Pressure gradients

Figure 4.12 shows the axial pressure gradients in the x-direction for different flow rate. From the figure it is observed that the pressure gradients along the x-direction encounters the reversed flow at the flow rate of 20 L/min along the length of the HTS cable compared to the lower flow rates.

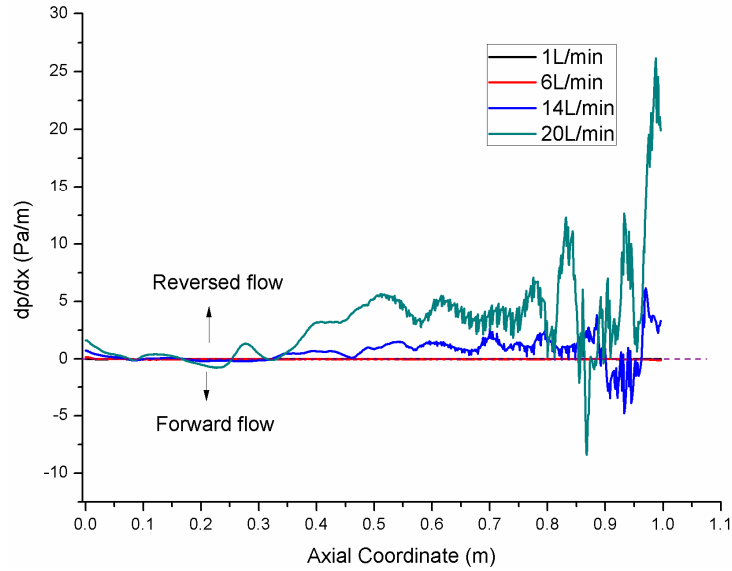


Figure 4.12 Axial pressure gradient in x-direction for different flow rates at heat load of 2.1 W/m

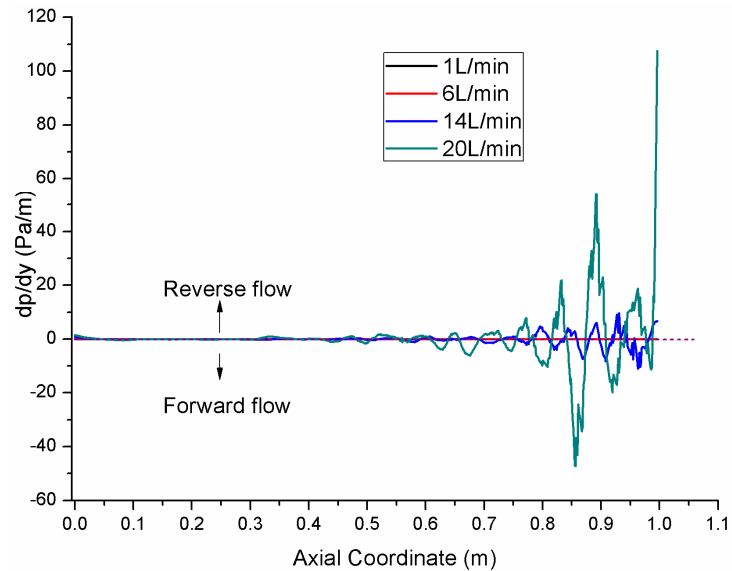


Figure 4.13 Axial pressure gradient in y-direction for different flow rates at heat load of 2.1 W/m

Figure 4.13 shows the axial pressure gradients in the y-direction for different flow rate. From the figure it is observed that the pressure gradients along the y-direction encounters

the reversed flow at the flow rate of 20 L/min along the length of the HTS cable compared to the lower flow rates. Further at 20 L/min higher pressure gradients are observed.

Figure 4.14 shows the axial pressure gradients in the z-direction for different flow rate. From the figure it is observed that the pressure gradients along the z-direction flow in the forward direction at different flow rates along the length of the HTS cable. The pressure gradients in the z-direction are higher compared to x and y-directions.

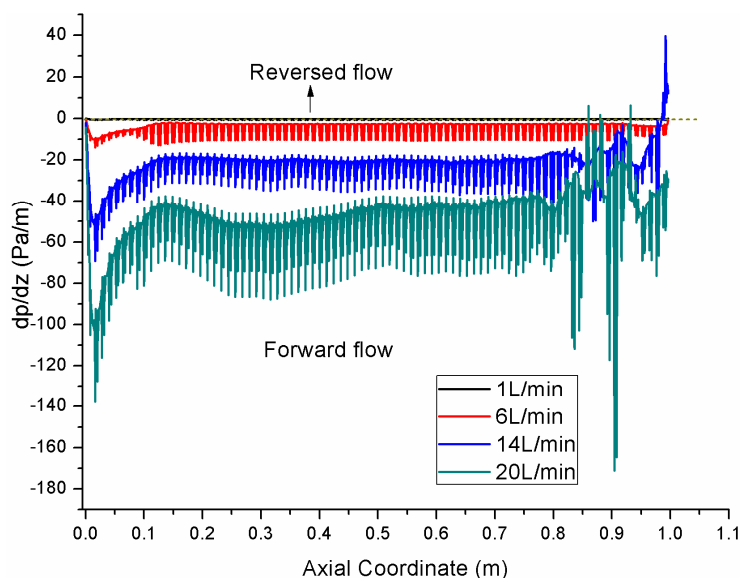


Figure 4.14 Axial pressure gradient in z-direction for different flow rates at heat load of 2.1 W/m

4.5.2 Radial Pressure gradients

The radial pressure gradients along the x-direction along the different locations in the HTS cable is shown in Figure 4.15. From the figure it is observed that, at the inlet radial inward flow is observed due to this the transportation of LN₂ takes place. Further, at the corrugations higher pressure gradients are observed compared at locations without corrugations (inlet and outlet).

The radial pressure gradients along the y-direction along the different locations in the HTS cable is shown in Figure 4.16. From the figure it is observed that, radial inward flow is observed at the center with corrugation and at the inlet due to this the transportation of LN₂ takes place. Further, at the corrugations higher pressure gradients are observed compared at locations without corrugations (inlet and outlet). The pressure gradients in the y-direction are higher compared to the x and z-directions.

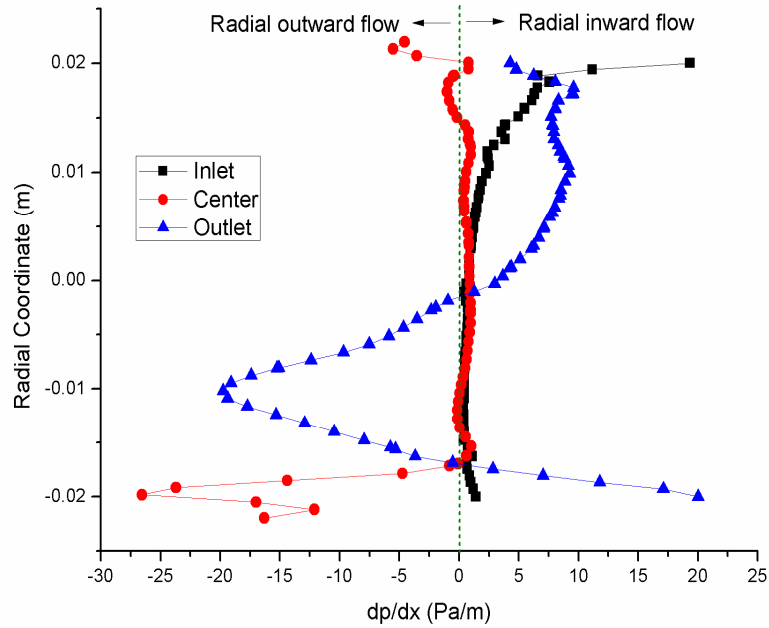


Figure 4.15 Radial pressure gradient in x-direction for different flow rates at heat load of 2.1 W/m

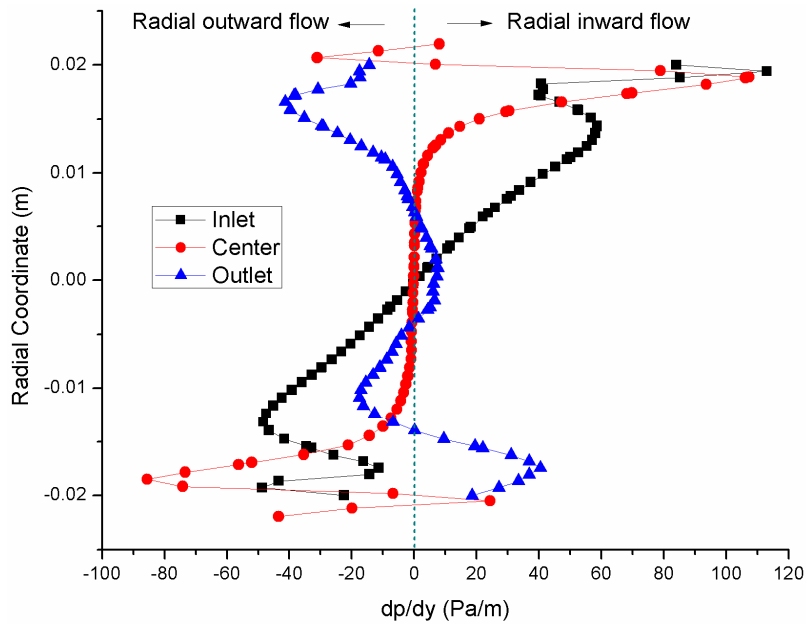


Figure 4.16 Radial pressure gradient in y-direction for different flow rates at heat load of 2.1 W/m

The radial pressure gradients along the z-direction along the different locations in the HTS cable is shown in Figure 4.17. From the figure it is observed that, radial inward flow is observed at the outlet and radial outward flow is observed at the inlet and center. Further, at the corrugations higher pressure gradients are observed compared at locations without corrugations (inlet and outlet) and in the corrugation radial inward flow is observed.

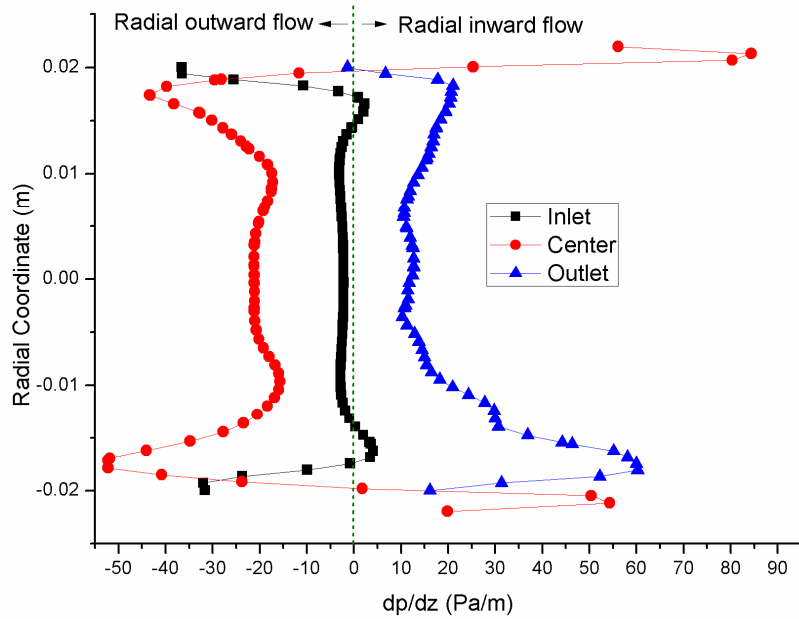


Figure 4.17 Radial pressure gradient in z-direction for different flow rates at heat load of 2.1 W/m

4.6 Friction factor

The friction factor at different flow rates and heat loads for different Reynolds numbers at an inlet temperature of 77 K is calculated using equation (3.84) and shown in Figure 4.18. From the figure, it is observed that with the increase in Reynolds number at a particular heat load, friction decreases slowly.

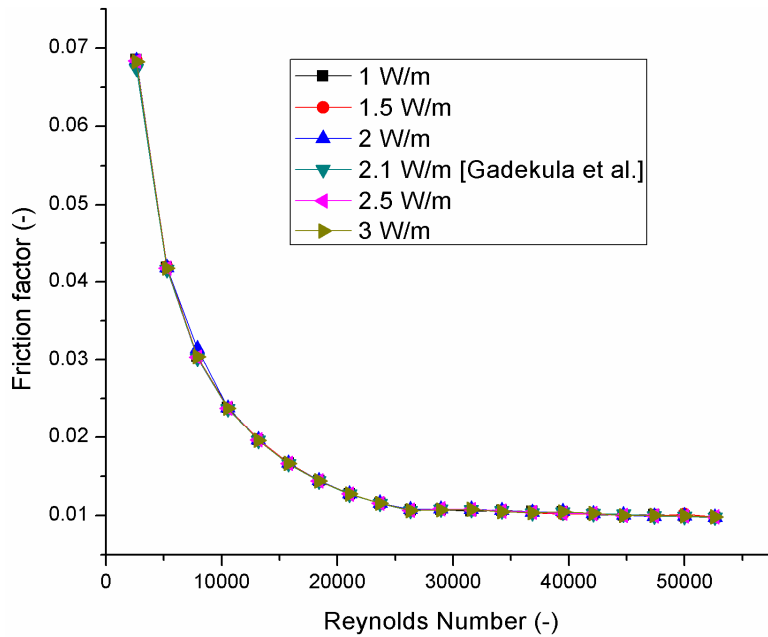


Figure 4.18 Friction factor versus Reynolds number at different heat loads

Further, with the increase in the heat load the friction factor at different Reynolds number is varying slightly. This may be due to insignificance in velocity distribution at different heat loads. Since the friction factor is square the velocity of the LN₂ in the corrugated former. Hence, the influence of the heat loads in the friction factor is insignificant. At the lower flow rates higher friction factor is observed and decreasing slowly with increase in Reynolds number (similar trends can be seen in the Moody diagram).

The friction factor at different flow rates and inlet temperatures for various heat loads is calculated using equation (3.84) and shown in Figure 4.19. From the figure, it is observed that with the increase in flow rate at a particular inlet temperature, friction decreases slowly. Further, at higher inlet temperature, lower friction factor of LN₂ in the corrugated former of the HTS cable is observed. Since, the Reynolds number increases with increase in flow rate, the friction factor decreases slowly.

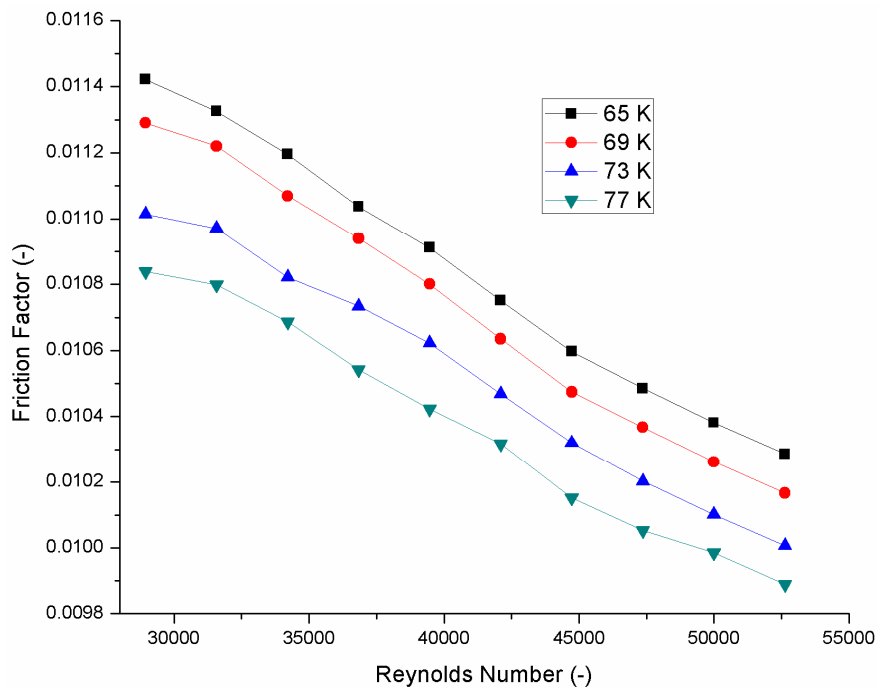


Figure 4.19 Friction Factor versus Reynolds Number at various inlet temperatures

4.7 Pressure drop

The pressure drop at various flow rates and inlet temperatures for different heat loads is calculated using equation (3.86) and shown in Figure 4.20. From the figure, it is observed that with increase in flow rate pressure drop increases at constant heat load. However, the variation in pressure drop is unaltered with the increase in heat load at constant flow rate.

This may be due to insignificancy in velocity distribution and friction factor under the influence of heat loads (see Figure 4.2(a), Figure 4.5).

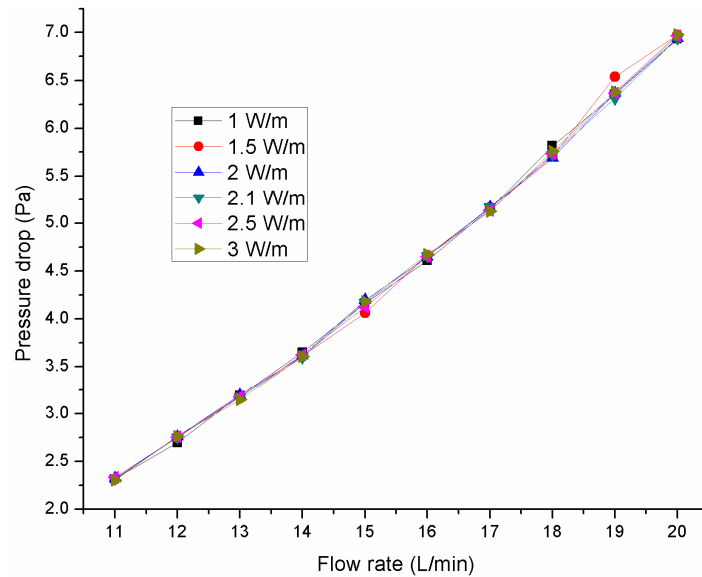


Figure 4.20 Variation of pressure drop with respect to flow rate for different heat loads

The pressure drop at various flow rates and inlet temperatures for different heat loads is calculated using equation (3.86) and shown in Figure 4.21. It can be observed that as Reynolds numbers increase with the increased flow rates, the friction factors decrease slowly (see Figure 4.19). This is due to the overcoming of inertial forces over the viscous forces in the range of considered flow rates.

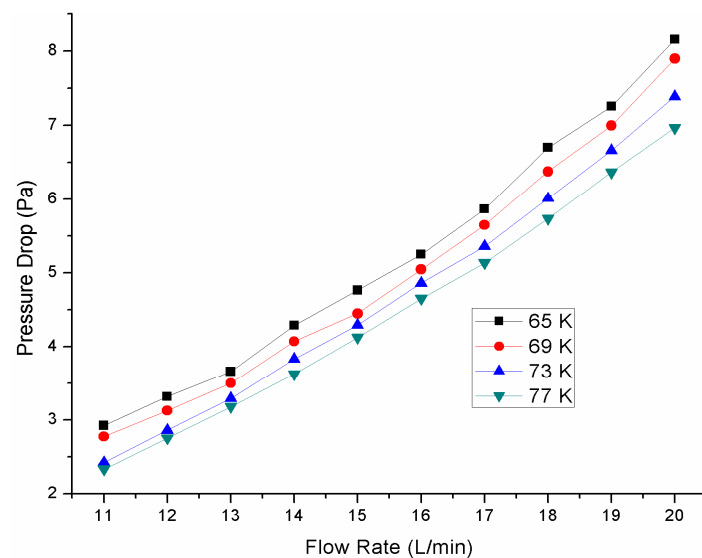


Figure 4.21 Pressure drop along the HTS cable at various flow rates and inlet temperatures

From equation (3.86), it is observed that pressure drop increases in proportion to the friction factor times the squared velocity. From the figure, it is observed that at a particular

flow rate, higher the inlet temperature, lower the pressure drop along the length of the HTS cable. This is due to lower frictional forces developed in the HTS cables at higher inlet temperatures (see Figure 4.19). Further, at a particular inlet temperature with the increase in flow rate pressure drop increases along the length of the HTS cable.

4.8 Pumping power

The pumping power at different flow rates for various heat loads is calculated using equation (156) and shown in Figure 4.22. Since, the Reynolds number increases with increase in flow rate, the friction factor decreases slowly. From equation (156) it is observed that pressure drop increases in proportion to the friction factor times the squared velocity. The squared velocity is responsible for the increase in pumping power. Further, the results indicate that at a particular flow rate, the pumping power remains unaltered for increase in the heat load. This may be due to, velocity distribution at different locations in HTS cable are similar at different heat loads as shown in Figure 4.5.

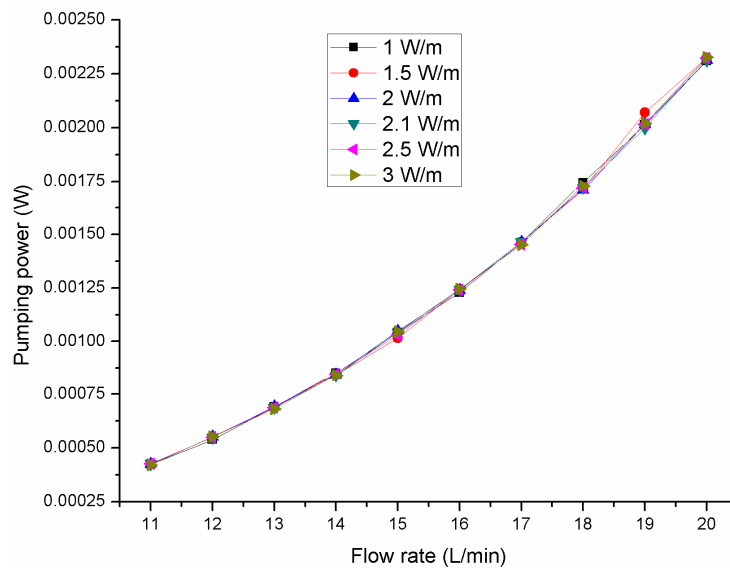


Figure 4.22 Pumping power versus flow rate for various Heat loads

The pumping power at different flow rates for various heat loads is calculated using equation (3.87) and shown in Figure 4.23. As the Reynolds number increases with increase in flow rate, the friction factor decreases slowly (see Figure 4.19). From equation (156), it is observed that pressure drop increases in proportion to the friction factor times the squared velocity. The squared velocity is responsible for the increase in pumping power. Further, the results indicate that at a particular flow rate, the pumping power increases with increase in inlet temperatures. Further at a particular inlet temperature with the increase in

flow rate pumping power increases. Hence, HTS cable need to be operated at higher temperatures of LN₂ compared to lower inlet temperatures of LN₂ for better performance.

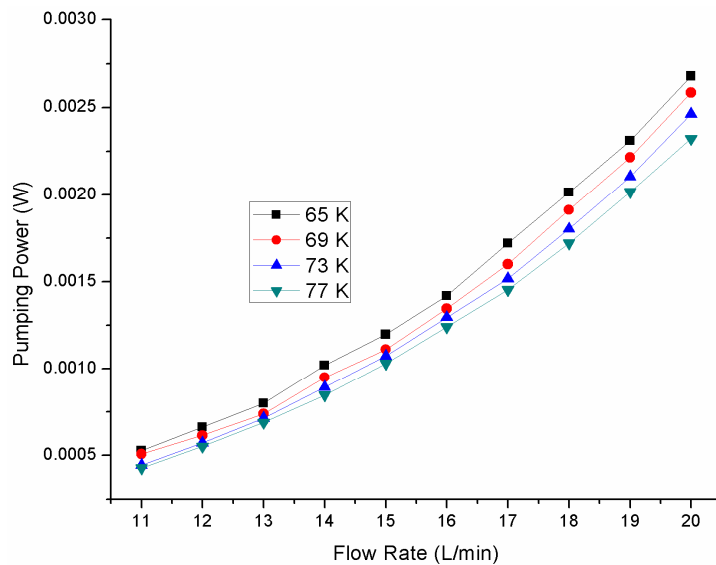


Figure 4.23 Pumping power versus flow rate for various inlet temperatures

The velocity gradients and pressure gradients in axial as well as radial directions in this chapter are to be utilized for predicting the volumetric entropy generation rate due to velocity gradients in HTS cables (Chapter 6). Further, the hydraulic characteristics estimated at different flow rates, heat loads and inlet temperatures in this chapter are to be utilized in the estimating the performance of HTS cable using entropy generation minimization approach (Chapter 7). The performance of the HTS cable not only depends on hydraulic characteristics, it also depends on the thermal characteristics of LN₂ that are discussed in the next chapter.

5 THERMAL CHARACTERISTICS OF HTS CABLES

5.1 Introduction

High Temperature Superconducting (HTS) cables have potential merits of large current carrying capacity and compactness with reduced transmission losses and Right-of-Way (RoW) compared to conventional transmission power cables. However, internal forced convective cooling is necessary to cool HTS cables using cryogenic coolant such as liquid nitrogen (LN_2) to retain the superconductivity for efficient power transmission. A corrugated steel pipe is used as former, around which HTS tapes are wound as shown in Figure 5.1. These HTS tapes carry large current densities which encounter AC losses [28]–[32], [34]–[36], [287] and dielectric losses [38]–[42]. In addition, losses such as heat-in-leaks[43]–[47] hinders the thermal performance of HTS cables. Hence, to accommodate such losses higher mass flow of LN_2 is required to cool the HTS cables which require higher pumping power for the circulation of LN_2 between the end terminations.

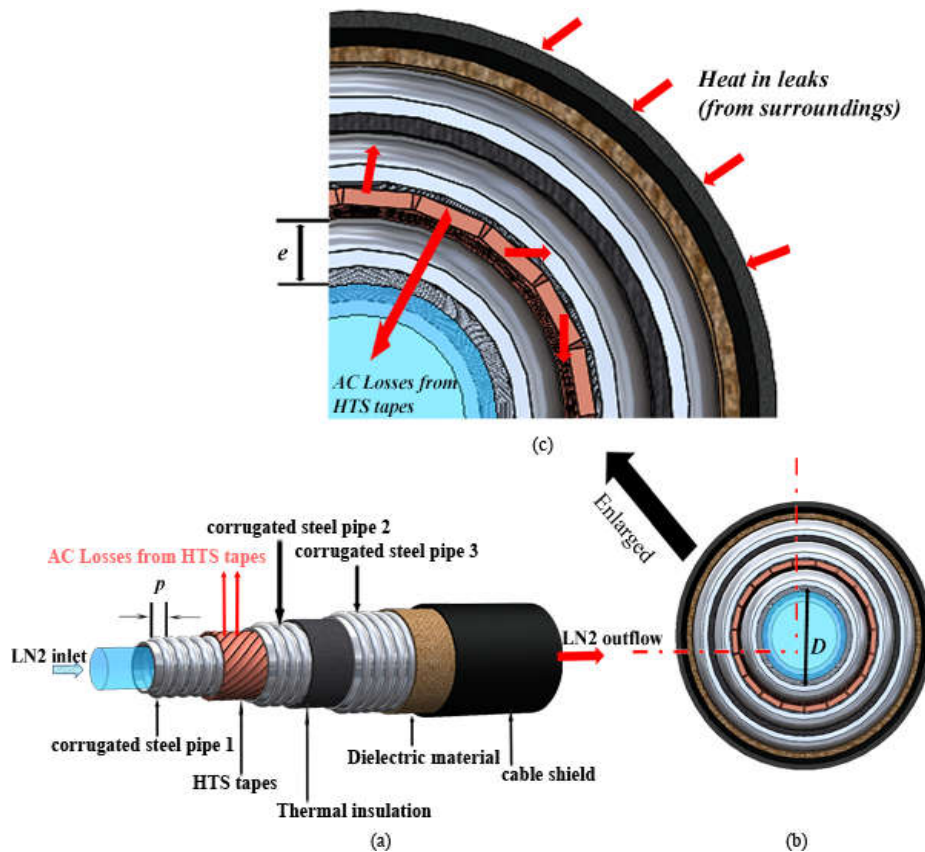


Figure 5.1 High Temperature Superconducting (HTS) cable configuration with heat loads employed for thermal characteristic analysis

In this context, the cooling requirement in HTS cables is associated with the estimation of pressure drop and heat transfer rate for predicting the pumping power and cooling capacity. The AC losses and heat-in-leaks encountered by the HTS cables are estimated (discussed in chapter 2). The heat loads are applied uniformly on the computational domain similar to the practical conditions of LN₂ flow through the corrugated former of HTS cables. Figure 5.1 shows the schematic of HTS cable and the computational domain used for analyzing the thermal characteristics of HTS cable. Flow rates ranging from 1-20 L/min, heat loads ranging from 1-3 W/m and inlet temperature of LN₂ ranging from 65-77 K (shown in Table 3.1) are utilized for estimating the thermal characteristics in HTS cables. In this chapter the temperature gradients, temperature profiles that are developed in the computational domain are discussed. Further, Nusselt number is estimated for analyzing the heat transfer rate and cooling capacity for the specified boundary in the HTS cables is discussed.

5.2 Temperature profile

The radial temperature distribution in HTS cables are investigated to observe the behavior of temperature dependent thermophysical properties of LN₂ for various heat loads. Figure 5.2 (a) shows the radial temperature distribution at a location of $z = 0.5$ m for different heat loads at flow rate of 14 L/min.

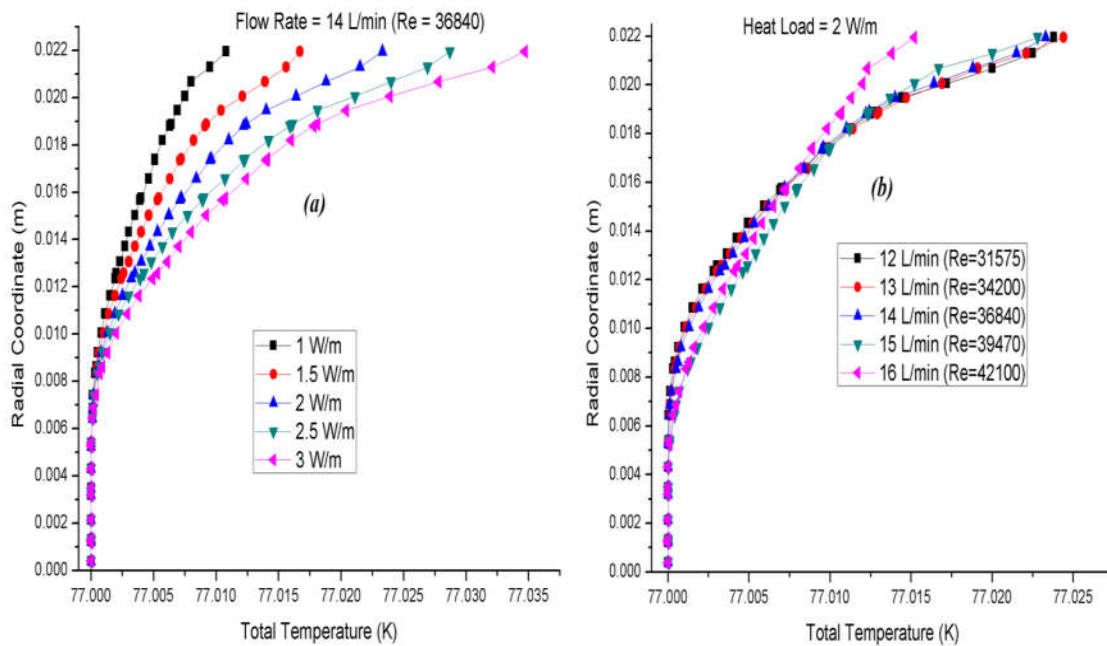


Figure 5.2 Radial temperature distribution at a distance of $z = 0.5$ m in the HTS cable (a) for different heat loads at a flow rate of 14 L/min (b) for different flow rates at a heat load of 2 W/m

From the figure, it is observed that the influence of heat loads is higher at the wall of the HTS cable. Further, at a flow rate of 14 L/min, higher the heat loads higher the temperature rise is observed. Figure 5.2 (b) shows the radial temperature distribution at a location of $z = 0.5$ m for different flow rates at a heat load of 2 W/m. From the figure, it is evident that with the increase in the flow rate the temperature at the wall decreases. Further, it is observed that the influence of temperature distribution can affect the entropy generation rate significantly.

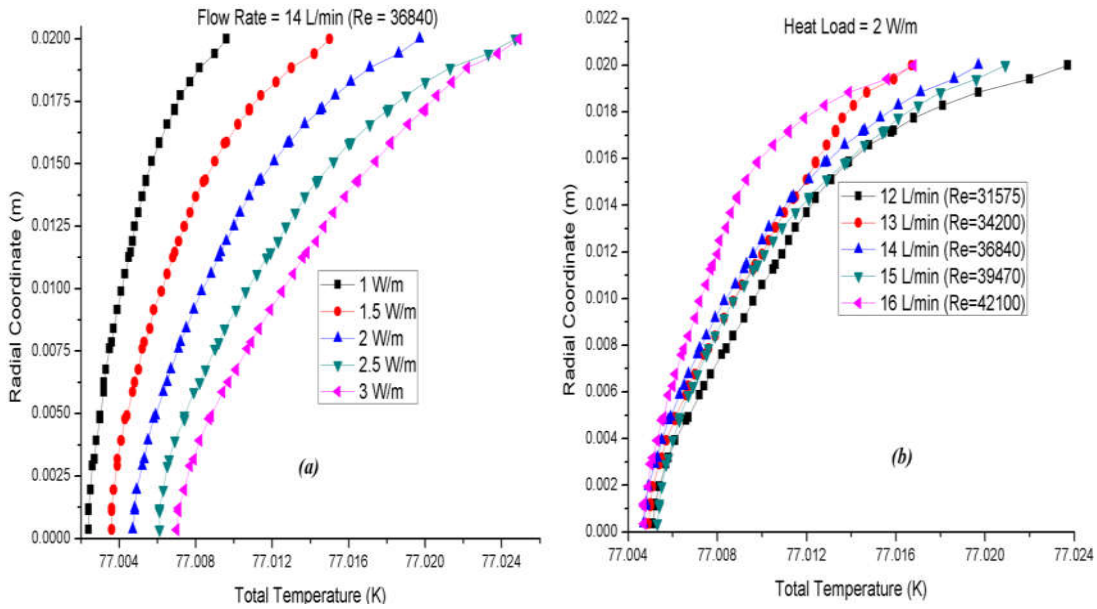


Figure 5.3 Radial temperature distribution at a distance of $z = 1$ m in the HTS cable (a) for different heat loads at a flow rate of 14 L/min (b) for different flow rates at a heat load of 2 W/m

Figure 5.3 (a) shows the radial temperature distribution of LN₂ flow through the HTS cable at an axial distance of $z = 1$ m. From the figure, it is observed that there is a temperature rise at the axis of the HTS cable compared to $z = 0.5$ m at a flow rate of 14 L/min for higher heat loads. Further, higher temperatures are observed at the wall of the HTS cable signifies that the thermal gradients are higher at the wall at higher heat loads.

Figure 5.3 (b) shows the temperature distribution of LN₂ flow through HTS cables in radial direction at a heat load of 2 W/m for various flow rates. From the figure, it is evident that with the increase in flow rate the temperature decreases. The temperature distribution follows the similar trend as observed at $z = 0.5$ m. Furthermore, the temperature rise at $z = 0.5$ m is higher compared to the $z = 1$ m, due to availability of corrugation at that section. Hence, the corrugations can also affect the temperature distribution that contributes to the entropy generation rate. The total temperature distribution in the HTS cable is less than the

critical temperature of HTS tapes at different heat loads. Hence, HTS tapes are safe from quenching. Further, the temperature at the outlet of the HTS cable is less than the boiling temperature of the LN₂. Hence, central flow cooling with specified geometry and boundary conditions can be used for long length cable applications.

5.3 Temperature gradients

The average temperature gradients in axial direction and radial direction together contribute to the development of entropy generation rate due to temperature gradients as discussed in Chapter 3. In this section, the average axial and radial temperature gradients are presented at different flow rates and at different locations in the HTS cable.

5.3.1 Axial temperature gradients

The average axial temperature gradients in the x-direction for different flow rates at a heat load of 2.1 W/m is shown in Figure 5.4. From the figure, it is observed that at different flow rate the temperature gradients are not showing significant effect till the center of the HTS cable. Later, there is a significant variation in the temperature gradients at the higher flow rates. Further, higher the flow rate, higher the contribution of temperature gradients.

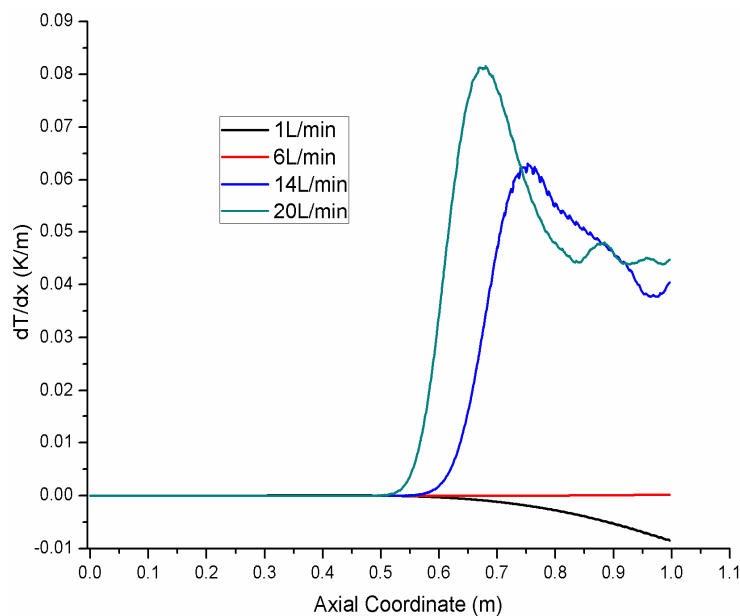


Figure 5.4 Axial temperature gradient in x-direction for different flow rates at heat load of 2.1 W/m

Figure 5.5 shows the average axial temperature gradients in the y-direction for different flow rates at a heat load of 2.1 W/m. From the figure, it is evident that for various flow rates the temperature gradients are not varying till the center of the HTS cable. Later, there

is a significant variation in the temperature gradients at the higher flow rates. Further, higher the flow rate higher the contribution of temperature gradients.

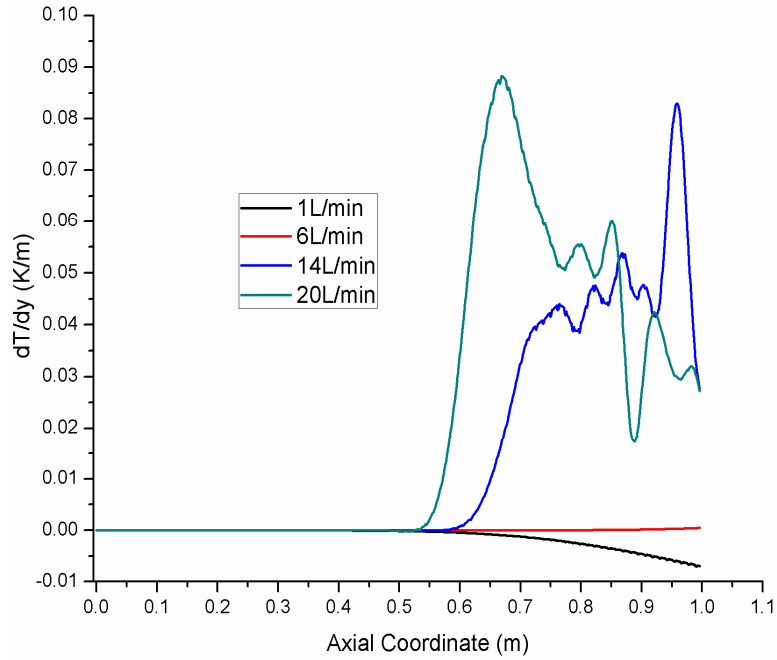


Figure 5.5 Axial temperature gradient in y-direction for different flow rates at heat load of 2.1 W/m

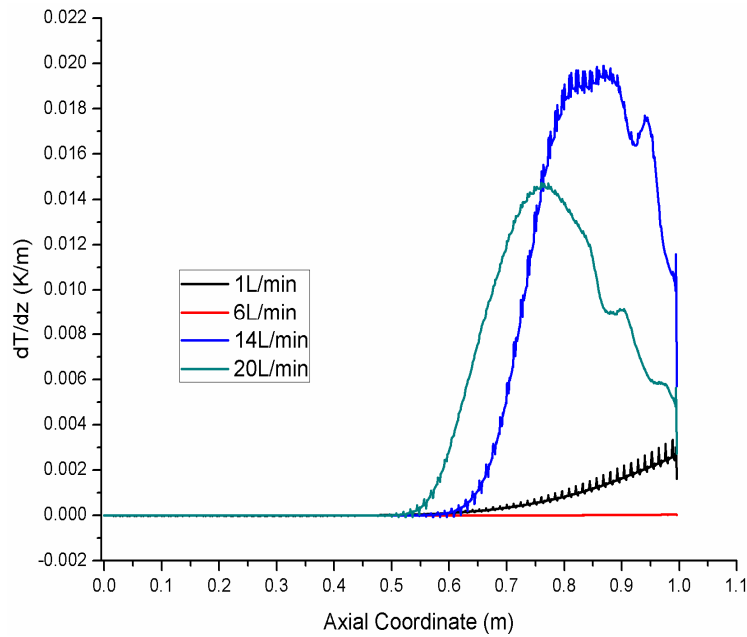


Figure 5.6 Axial temperature gradient in z-direction for different flow rates at heat load of 2.1 W/m

The average axial temperature gradients in the z-direction for different flow rates at a heat load of 2.1 W/m is shown in Figure 5.6. From the figure, it is observed that at different flow rate the temperature gradients are not showing significant effect till the center of the

HTS cable. Later, there is a significant variation in the average temperature gradients at the higher flow rates. Further, higher the flow rate higher the contribution of temperature gradients due to frictional heat losses and heat loads due to losses from HTS cable. Furthermore, it is observed that 14 L/min is having the higher contribution on entropy generation rate compared to 20 L/min.

5.3.2 Radial temperature gradients

The average radial temperature gradients at three different locations are captured one at the inlet, second at the center and third at the outlet of the HTS cable. Figure 5.7 shows the temperature gradients in the radial x-direction. From the figure it is observed that, higher average temperature gradients are observed at the corrugations than the locations without corrugations. Further, the contribution of temperature gradients is observed to be minimum than the temperature gradients in y and z-direction.

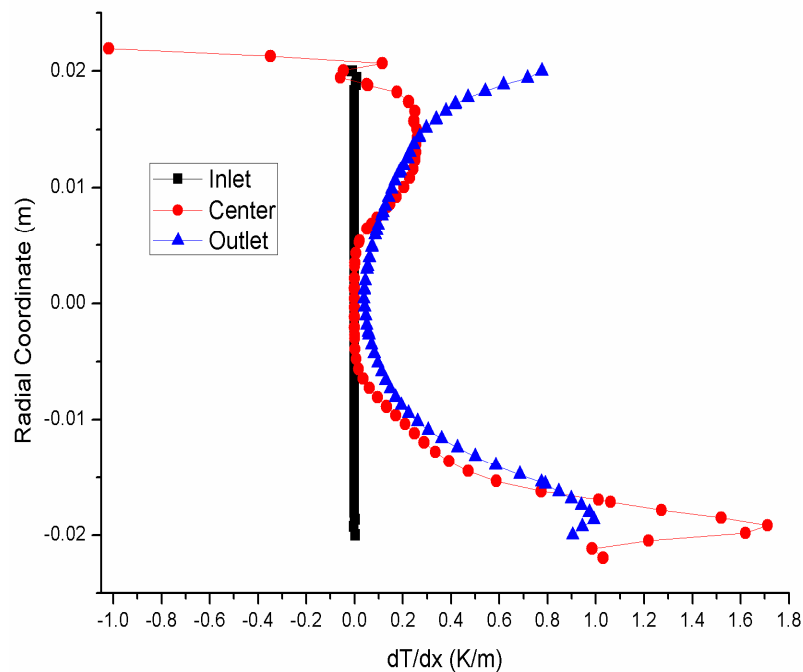


Figure 5.7 Radial temperature gradient in x-direction for different flow rates at heat load of 2.1 W/m

The average radial temperature gradients at three different locations are captured one at the inlet, second at the center and third at the outlet of the HTS cable. Figure 5.8 shows the temperature gradients in the radial y-direction. From the figure it is observed that, higher temperature gradients are observed at the center and outlet. The variation of the temperature gradients from the axis of the HTS cable is lower and the temperature

gradients are higher at the wall. Further, the contribution of temperature gradients is observed to be maximum than the temperature gradients in x and z-direction.

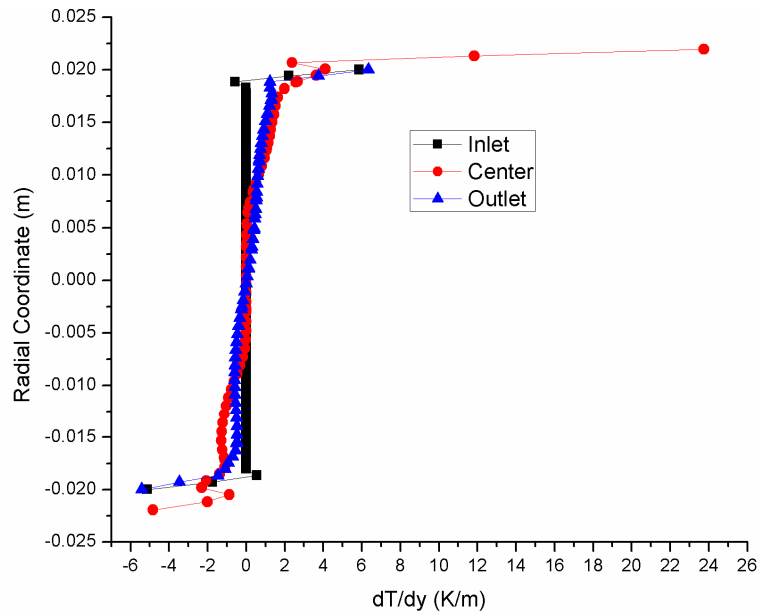


Figure 5.8 Radial temperature gradient in y-direction for different flow rates at heat load of 2.1 W/m

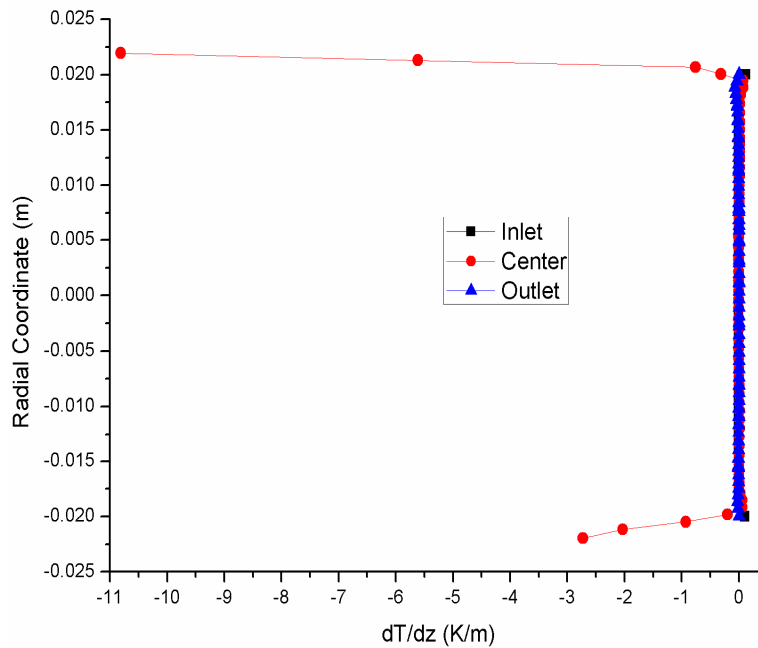


Figure 5.9 Radial temperature gradient in z-direction for different flow rates at heat load of 2.1 W/m

The average radial temperature gradients at three different locations are captured one at the inlet, second at the center and third at the outlet of the HTS cable. Figure 5.9 shows the temperature gradients in the radial z-direction. From the figure it is observed that, higher temperature gradients are observed at the corrugations than the locations without

corrugations. Further, the contribution of average temperature gradients is observed to be minimum at all the locations in the HTS cable. The contribution of the temperature gradients in the z-direction is not significant.

5.4 Temperature difference

The temperature difference between the outlet and inlet temperature of the HTS cable is shown in Figure 5.10. From the figure, it is observed that at a constant heat load with the increase in flow rate temperature difference is decreased. The lower temperature difference signifies that the distance between the terminations of HTS cable can be increased and the installation cost of cryogenic cooling station can be reduced.

The temperature difference between the outlet and inlet temperature of the HTS cable for different inlet temperatures is shown in Figure 5.11. From the figure, it is observed that at a constant inlet temperature with the increase in flow rate temperature difference is decreased. Further, at constant flow rate with increase in inlet temperature the temperature difference decreases between the inlet and outlet of the HTS cable. The lower temperature difference at higher inlet temperature signifies that the distance between the terminations of HTS cable can be increased and the installation cost of cryogenic cooling station can be reduced.

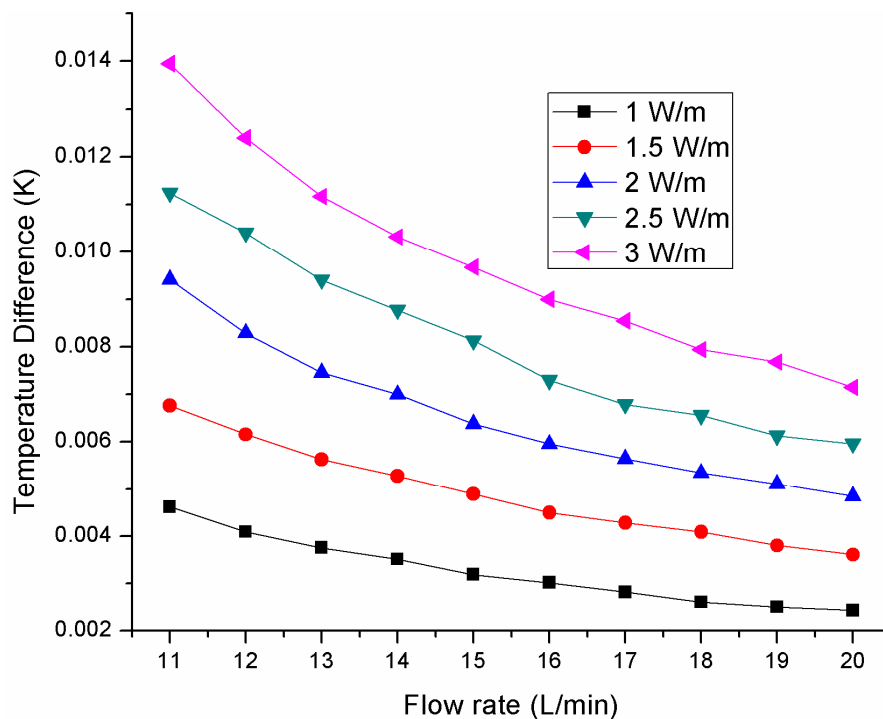


Figure 5.10 Temperature difference between the outlet and inlet of HTS cable for different Heat loads and mass flow rates at inlet temperature of 77 K

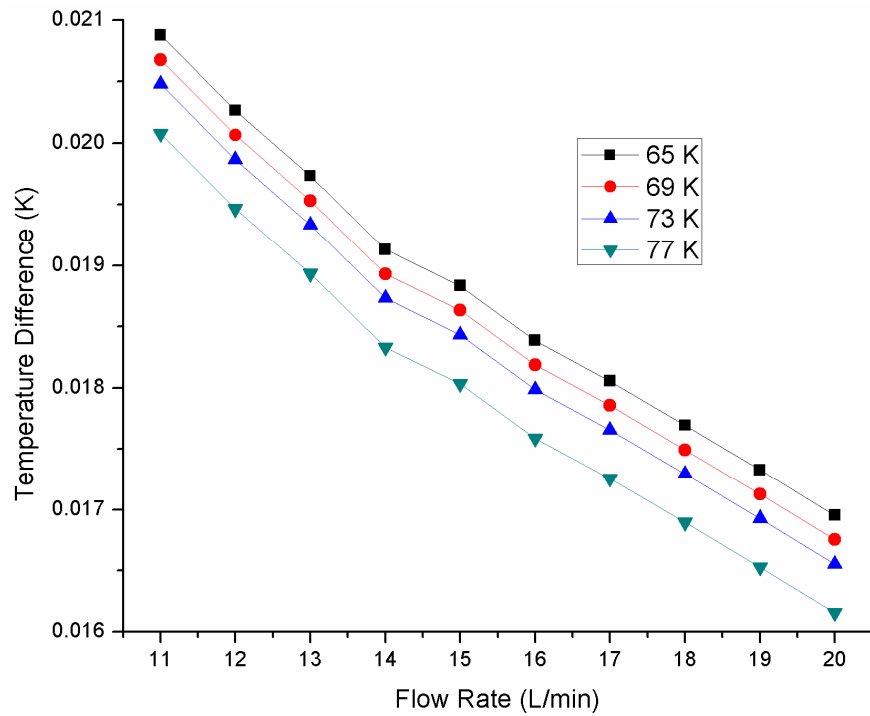


Figure 5.11 Temperature difference between the outlet and inlet of HTS cable for different inlet temperatures and mass flow rates at heat load of 2.5 W/m

5.5 Nusselt number

Nusselt number at different heat loads is calculated by solving the equation (3.88) and the results are shown in Figure 5.12. From the figure, it is evident that at a particular heat load, with the increase in Reynolds number, Nusselt number increases due to increase in the convective heat transfer rate in HTS cables.

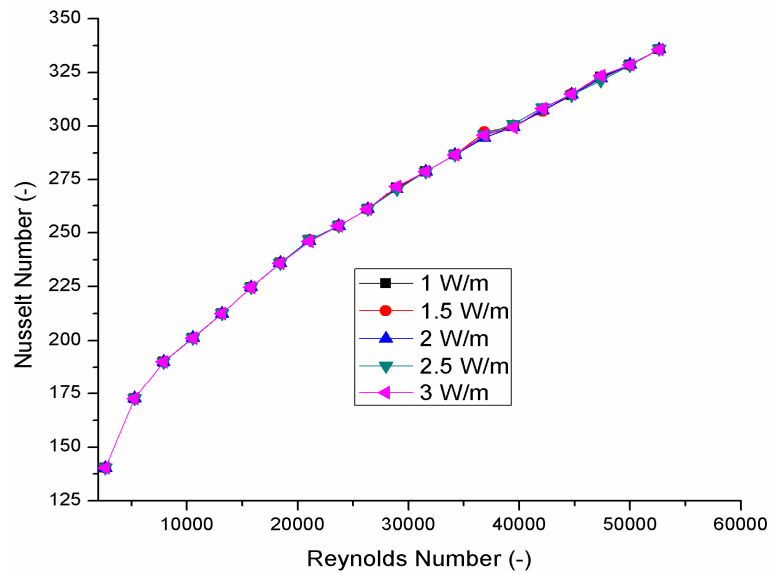


Figure 5.12 Nusselt Number versus Reynolds Number at different heat loads

However, at different heat loads, the variation in the Nusselt number is small. This may be due to the small change in the temperature drop at a given heat flux. However, the small change in the temperature drop alters the entropy generation due to thermal gradients (see Figure 6.9) and thereby total entropy generation rate increases.

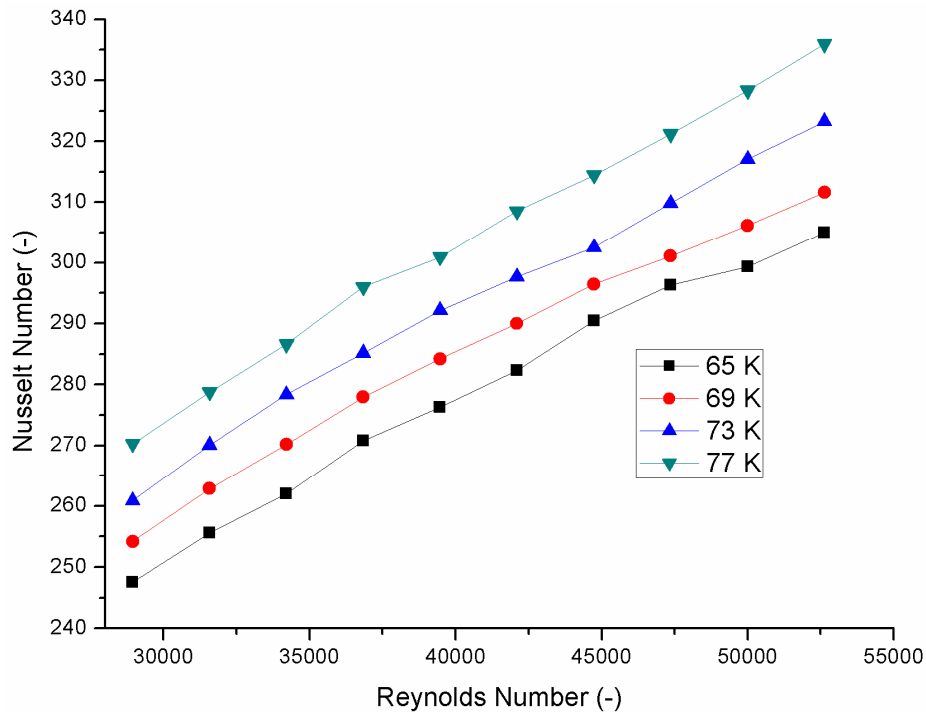


Figure 5.13 Nusselt Number versus Reynolds Number at different inlet temperatures

Nusselt numbers for different flow rates and inlet temperatures at various heat loads is calculated by solving the equation (3.88) and the results are shown in Figure 5.13. From the figure, it is evident that at a particular flow rate, with the increase in Reynolds number, Nusselt number increases due to increase in the convective heat transfer rate in HTS cables. Further, at a particular Reynolds number, Nusselt number is higher at higher inlet temperature of LN₂. Hence, HTS cable need to be operated at higher temperatures of LN₂ compared to lower inlet temperatures of LN₂ for better performance.

5.6 Cooling capacity

The temperature difference calculated in section 5.4 and equation (3.90) are used for calculating cooling capacity of HTS cable with forced convection cooling. Figure 5.14 shows the variation of the cooling capacity for different flow rates at various heat loads. It can be seen that, at a constant heat load with the increase in the flow rate cooling capacity

increases. Furthermore, at constant flow rate with the decrease in heat load may be cooling capacity decreases due to increase in the outlet temperature of LN₂.

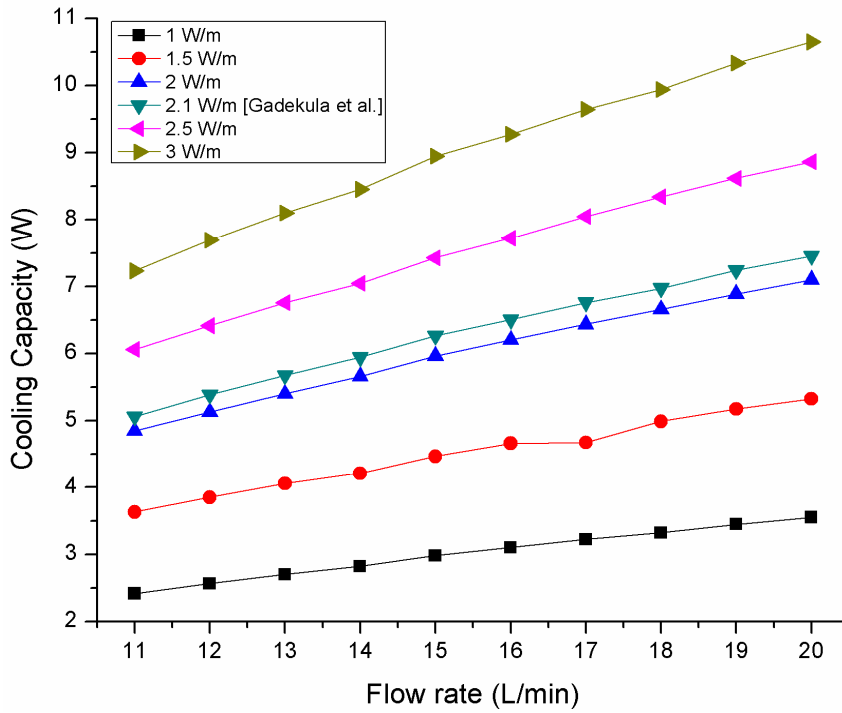


Figure 5.14 Cooling capacities versus flow rate for different Heat loads

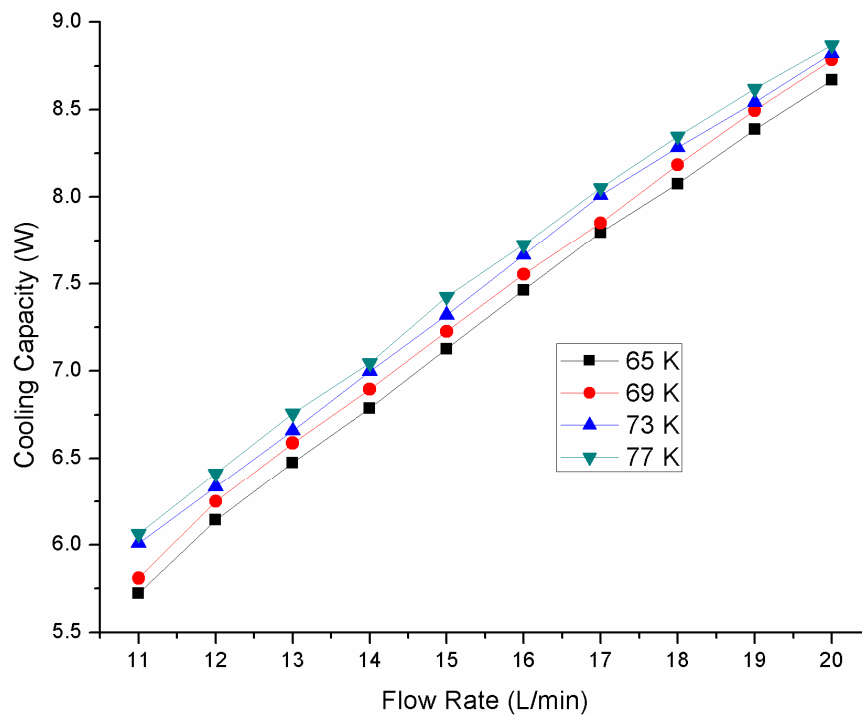


Figure 5.15 Cooling capacities versus flow rate for different inlet temperatures

The temperature difference estimated in section 5.4 and equation (3.90) are used for calculating cooling capacity of HTS cable with forced convection cooling. Figure 5.15 shows the variation of cooling capacity for different flow rates at various inlet temperatures. It can be seen that, at a particular inlet temperature, with the increase in the flow rate cooling capacity increases. Furthermore, at a particular flow rate with the increase in inlet temperature, cooling capacity of the HTS cable increases. Hence, HTS cable need to be operated at higher temperatures of LN₂ compared to lower inlet temperatures of LN₂ for better performance.

The thermal gradients in axial and radial directions in this chapter are to be utilized for predicting the volumetric entropy generation rate due to thermal gradients in HTS cables (Chapter 6). Further, the thermal characteristics estimated at different flow rates, heat loads and inlet temperatures in this chapter are to be utilized in the estimating the performance of HTS cable using entropy generation minimization approach(Chapter 7).

6 ENTROPY GENERATION RATE IN HTS CABLES

6.1 Introduction

In engineering systems, estimation of entropy generation rate is vital for evaluating the performance of the systems. Entropy is generated in such systems due to finite temperature difference, frictional fluid flow and mass diffusion in the fluid. The entropy generated in the system hinders the performance thereby the efficiency of the system reduces. In HTS cables, during the flow of LN₂ through corrugated pipe various dissipative mechanisms such as the formation of eddies causes in the development of velocity and temperature gradients leading to entropy generation. Entropy generation rate is combination of entropy generation rate due to velocity gradients and entropy generation rate due to thermal gradients. Hence, to obtain higher cooling capacity along with minimum pumping power, the estimation of entropy generation is an essential procedure.

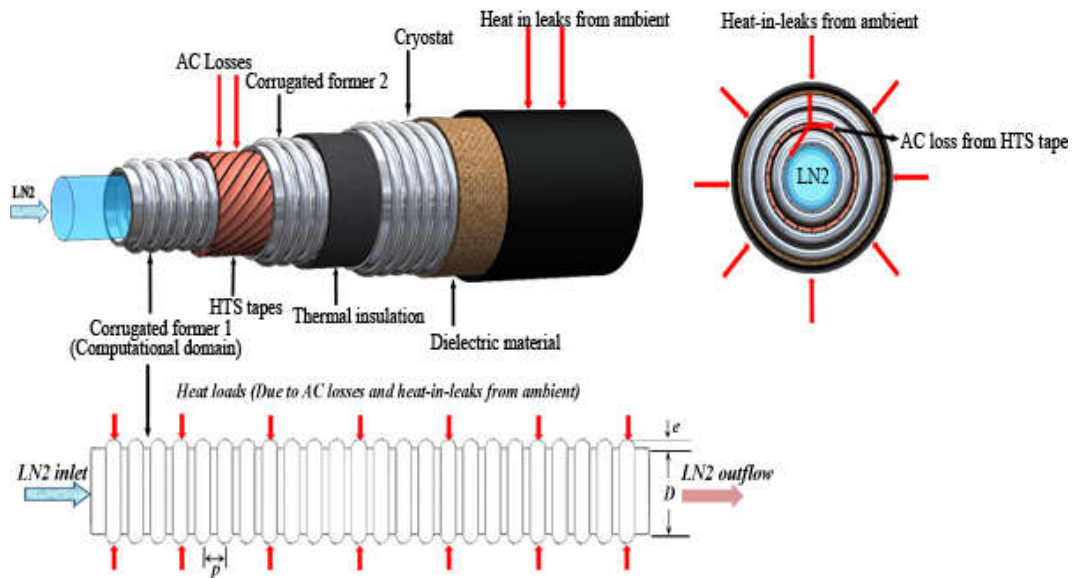


Figure 6.1 Schematic of HTS cable and computational domain used for estimating the entropy generation rate. The volumetric entropy generation rate is presented in this section and the results are obtained from the CFD analysis of corrugated former in HTS cable using FLUENT. Efforts are made to calculate the volumetric average of entropy generation rate on the entire computational domain. Further Bejan number is also estimated to evaluate the significance of volumetric entropy generation rate due to thermal gradients and velocity gradients on total volumetric entropy generation rate. Figure 6.1 shows the schematic of HTS cable and computational domain employed for estimating the entropy generation rate.

Flow rates ranging from 1-20 L/min, heat loads ranging from 1-3 W/m and inlet temperature of LN₂ ranging from 65-77 K (shown in Table 3.1) are utilized for estimating the entropy generation rate in HTS cables.

The volumetric entropy generation rate S'''_{gen} (W/m³K) for steady state operation in HTS cables can be calculated as [5]

$$S'''_{gen} = S'''_{Thermal\ source} + S'''_{frictional\ source} \quad (6.1)$$

$$S'''_{Thermal\ source} = \frac{K}{T_{ref}^2} \left[\left(\frac{\partial \bar{T}}{\partial x} \right)^2 + \left(\frac{\partial \bar{T}}{\partial y} \right)^2 + \left(\frac{\partial \bar{T}}{\partial z} \right)^2 \right] \quad (6.2)$$

$$S'''_{frictional\ source} = \frac{\mu}{T_{ref}} \left[2 \left(\left(\frac{\partial \bar{u}}{\partial x} \right)^2 + \left(\frac{\partial \bar{v}}{\partial y} \right)^2 + \left(\frac{\partial \bar{w}}{\partial z} \right)^2 \right) + \left(\frac{\partial \bar{u}}{\partial y} + \frac{\partial \bar{v}}{\partial x} \right)^2 + \left(\frac{\partial \bar{u}}{\partial z} + \frac{\partial \bar{w}}{\partial x} \right)^2 + \left(\frac{\partial \bar{v}}{\partial y} + \frac{\partial \bar{w}}{\partial z} \right)^2 \right] \quad (6.3)$$

where, T_{ref} is reference temperature in Kelvin.

The thermal source is due to the thermal gradients and the frictional source is due to velocity gradients. The thermal gradients and velocity gradients obtained from CFD analysis at all locations in computational domain and averaged over the volume for the calculation of S'''_{gen} . Further various flow rates are used to estimate the minimum entropy generation rate for identifying the lower pumping power and higher cooling capacity.

The ratio of entropy generation rate due to the thermal gradients to the total entropy generation rate in the corrugated former of HTS cable is defined as Bejan number.

$$Be = \frac{\frac{K}{T_{ref}^2} \left[\left(\frac{\partial \bar{T}}{\partial x} \right)^2 + \left(\frac{\partial \bar{T}}{\partial y} \right)^2 + \left(\frac{\partial \bar{T}}{\partial z} \right)^2 \right]}{\frac{K}{T_{ref}^2} \left[\left(\frac{\partial \bar{T}}{\partial x} \right)^2 + \left(\frac{\partial \bar{T}}{\partial y} \right)^2 + \left(\frac{\partial \bar{T}}{\partial z} \right)^2 \right] + \frac{\mu}{T_{ref}} \left[2 \left(\left(\frac{\partial \bar{u}}{\partial x} \right)^2 + \left(\frac{\partial \bar{v}}{\partial y} \right)^2 + \left(\frac{\partial \bar{w}}{\partial z} \right)^2 \right) + \left(\frac{\partial \bar{u}}{\partial y} + \frac{\partial \bar{v}}{\partial x} \right)^2 + \left(\frac{\partial \bar{u}}{\partial z} + \frac{\partial \bar{w}}{\partial x} \right)^2 + \left(\frac{\partial \bar{v}}{\partial y} + \frac{\partial \bar{w}}{\partial z} \right)^2 \right]} \quad (6.4)$$

6.2 Volumetric entropy generation rate due to velocity gradients

Volumetric entropy generation rate due to velocity gradients are shown in Figure 6.2 for different mass flow rates at the center and outlet of corrugated former with LN₂ flow. From the figure, it is observed that at the center there is a drastic variation in the entropy generation rate due to velocity gradients because of corrugations. Further, the entropy

generation is observed to be negligible at the peak of corrugation eddies are formed and the retarding of transporting fluid (LN₂) occurs.

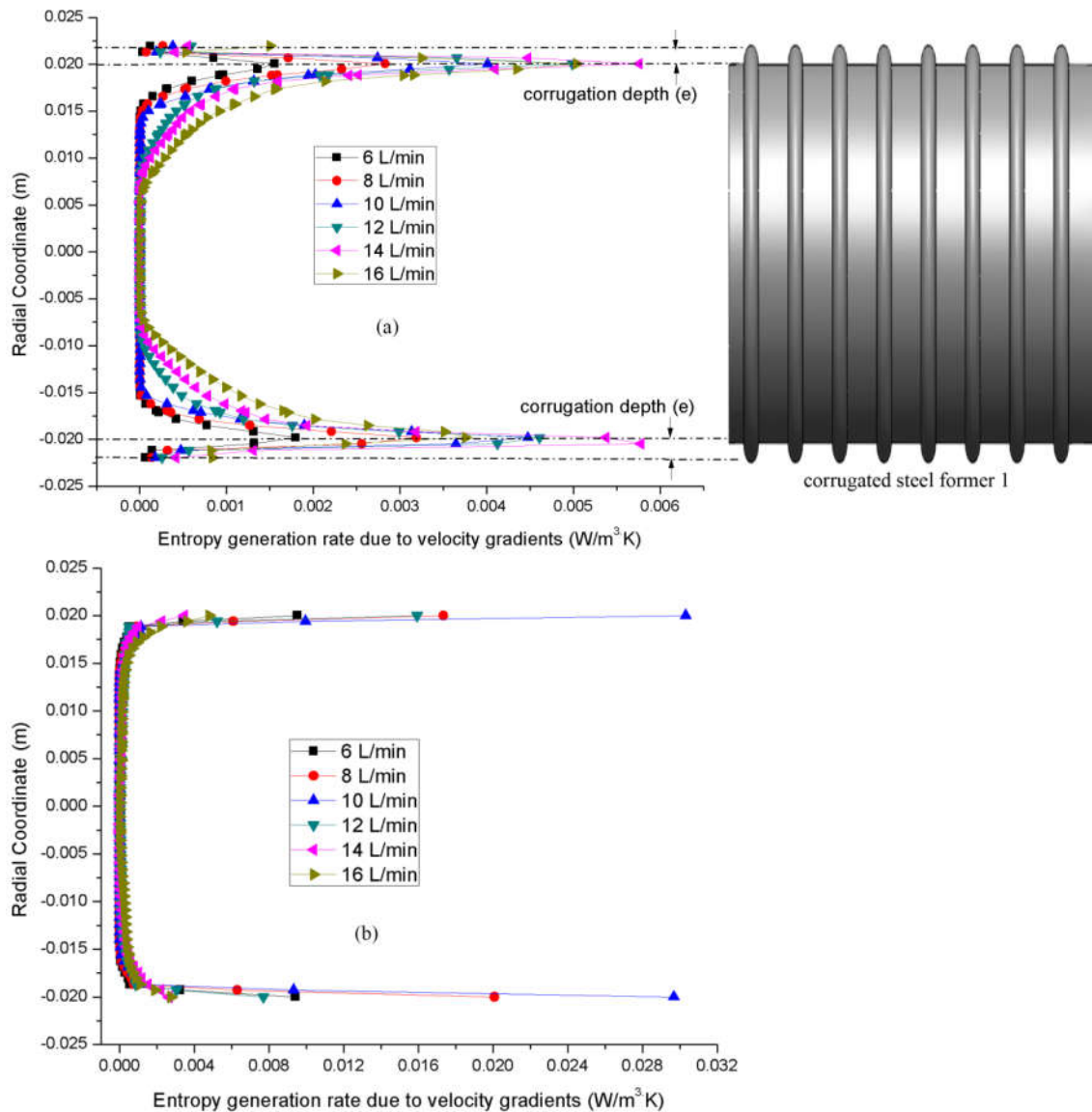


Figure 6.2 Entropy generation due to velocity gradients for different flow rates (a) at the center and (b) at the outlet at a heat load of 2.1 W/m

In the radial direction the velocity gradients along the x, y and z-direction shows negative magnitudes which indicates the fluid flow retards at the corrugation and eddies are formed. Due to this, wall shear stresses are increased. Further, eddies that are formed dissipates the turbulent kinetic energy (TKE) during transportation results in the pressure gradients and temperature raise. The entropy generation rates at the center of corrugated former is higher compared at outlet of the corrugated former due to the presence of corrugation and increase in flow rate increase the viscous forces.

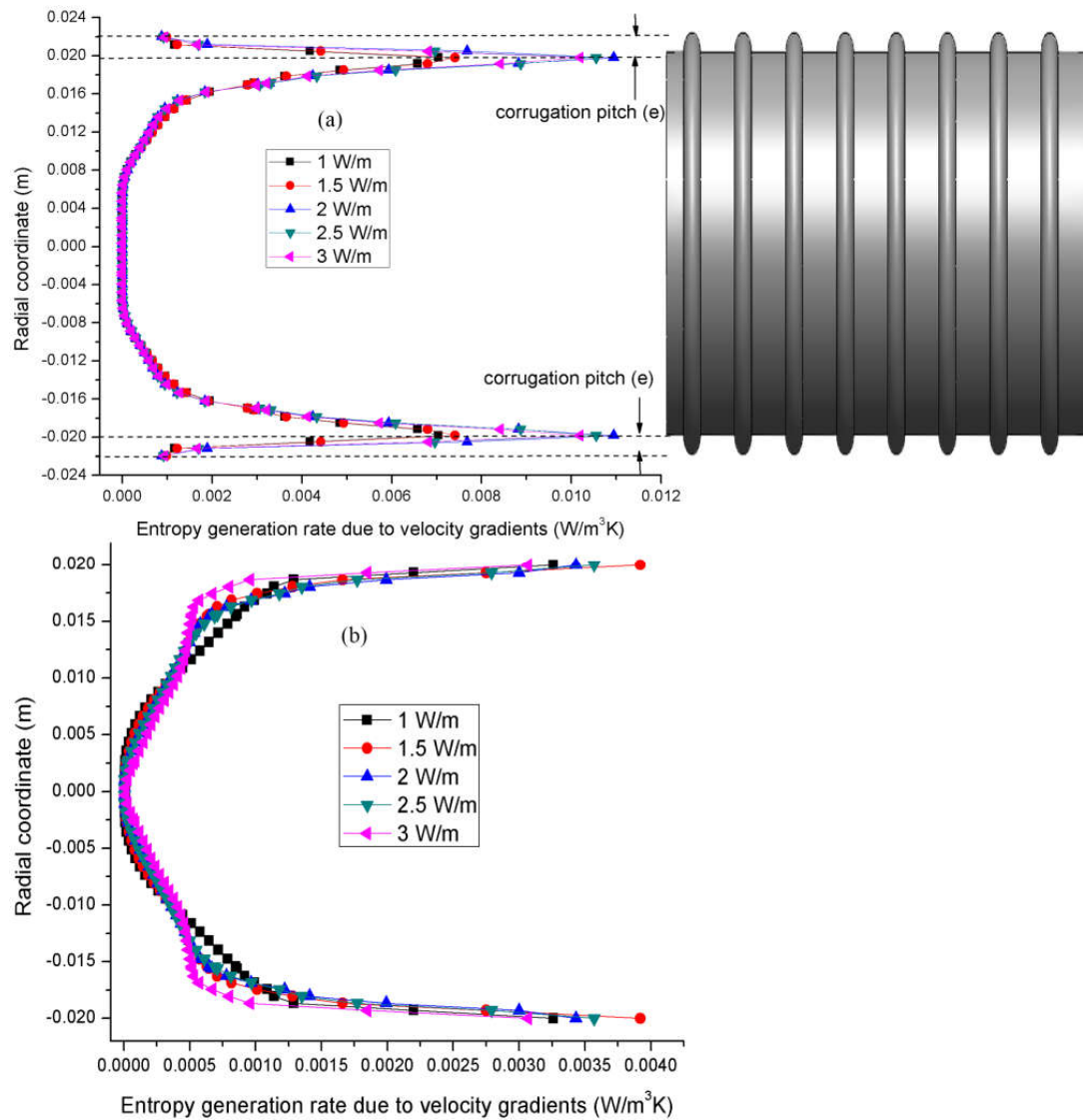


Figure 6.3 Entropy generation due to velocity gradients for different heat loads at a flow rate of 19 L/min (a) at the center and (b) at the outlet

The pressure gradients that are developed due to velocity gradients are higher in y and z-directions and also negative. These pressure gradients enable the fluid flow by counteracting the retarding effects of shear stresses at the wall. In axial direction the velocity gradients are lower for smaller mass flow rate and the magnitude of these gradients changes drastically at the length of 0.6m. The contribution of velocity gradients to total entropy generation rate is lesser compared to the temperature gradients.

The contribution of velocity gradients to the volumetric entropy generation rate with different mass flow rates and at various heat loads is shown in Figure 6.3. The results are presented at two different locations, one at the center of HTS cable where corrugation is

available and second at the outlet of HTS cable without corrugation for a flow rate of 19 L/min. From the Figure 6.3.a, it is identified that the entropy generation rate at the corrugation is higher because the velocity gradients are maximum reflecting to the wall condition where the gradients are maximum and similar results are observed at the outlet of the HTS cable at the wall in Figure 6.3.b. Furthermore, with the increase in the heat load at constant flow rate volumetric entropy generation rate due to velocity gradients remains unaffected.

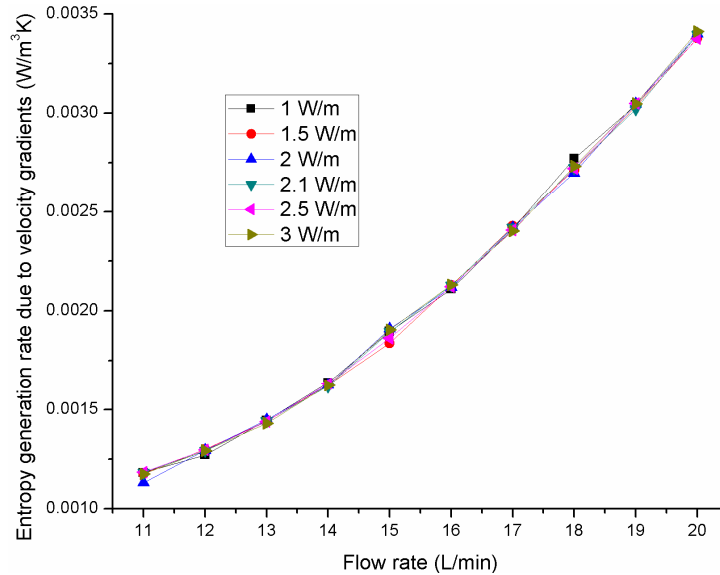


Figure 6.4 Entropy generation rate due to velocity gradients for different flow rates and heat loads

The volume average of entropy generation rate due to the velocity gradients over the entire volume of HTS cable for different mass flow rates and heat loads are shown in Figure 6.7. From the figure, it is observed that at constant heat load with the increase in the flow rate volumetric entropy generation rate due to the velocity gradients increases. Further, at constant flow rate with the increase in the heat load, volumetric entropy generation rate due to the velocity gradients are not significantly increased.

The frictional entropy generation rate is due to the velocity gradients that are developed in the computational domain. These are may be due to the turbulent frictional flow in the corrugated former. The radial distribution of entropy generation rate due to velocity gradients are at a flow rate of 14 L/min for different heat loads at $z = 1$ m are shown in Figure 6.5 (a). The entropy generation rate due to velocity gradients are higher at a heat load of 3 W/m and lower at the heat load of 2 W/m at a flow rate of 14 L/min. Hence, the contribution of velocity gradients to the entropy generation rate is lower at the 2 W/m at a

constant flow rate of 14 L/min. Figure 6.5 (b) shows the entropy generation rate due to velocity gradients at $z = 1$ m in the radial direction for various flow rates at a heat load of 2 W/m. From the figure, it is observed that with the increase in the flow rate the velocity gradients are increased at constant heat load. Further, the intensity of velocity gradients at the wall of HTS cable is higher for different heat loads and flow rates.

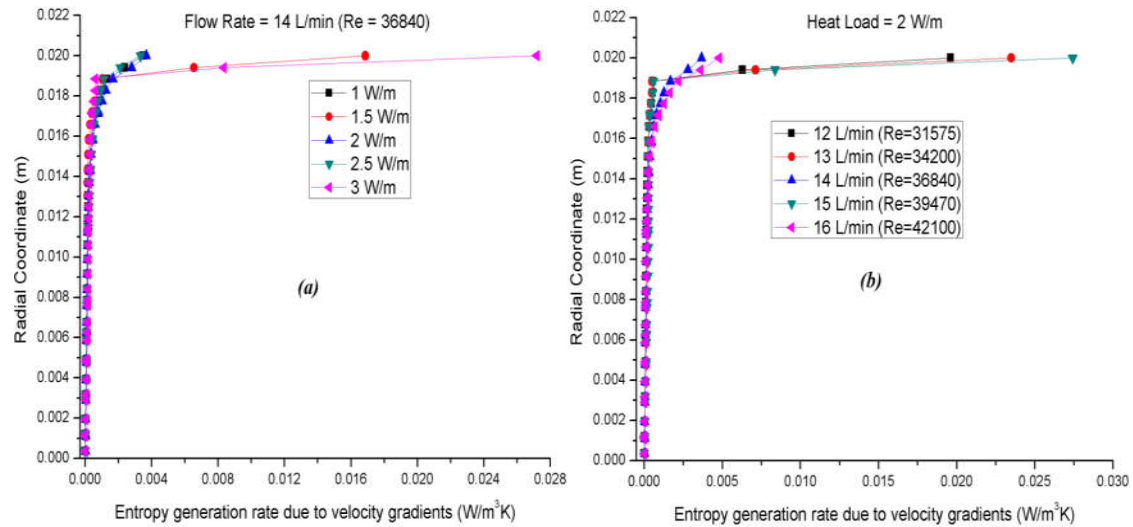


Figure 6.5 Entropy generation rate due to velocity gradients at a distance of $z = 1$ m in the HTS cable (a) for different heat loads at a flow rate of 14 L/min (b) for different flow rates at a heat load of 2 W/m

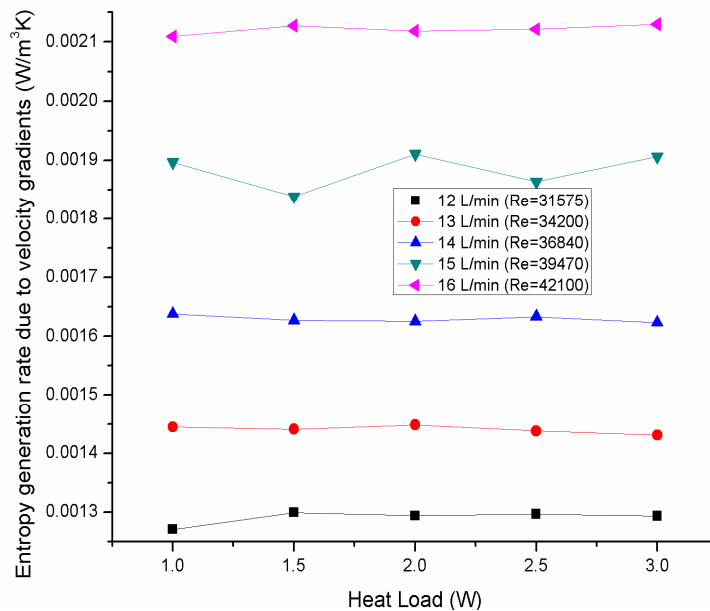


Figure 6.6 Volumetric entropy generation rate due to velocity gradients for various heat loads and different flow rates in HTS cable

The volumetric entropy generation rate due to velocity gradients at different heat loads and flow rates are shown in Figure 6.6. It is observed that at a particular heat load, higher the

flow rate higher the contributing to the volumetric entropy generation rate due to velocity gradients. Further, at a particular flow rate, with the increase in heat load slight increase in the volumetric entropy generation due to thermal gradients are observed. Hence, the influence of the heat loads on the volumetric entropy generation rate due to velocity gradients is lower compared than that of different flow rates.

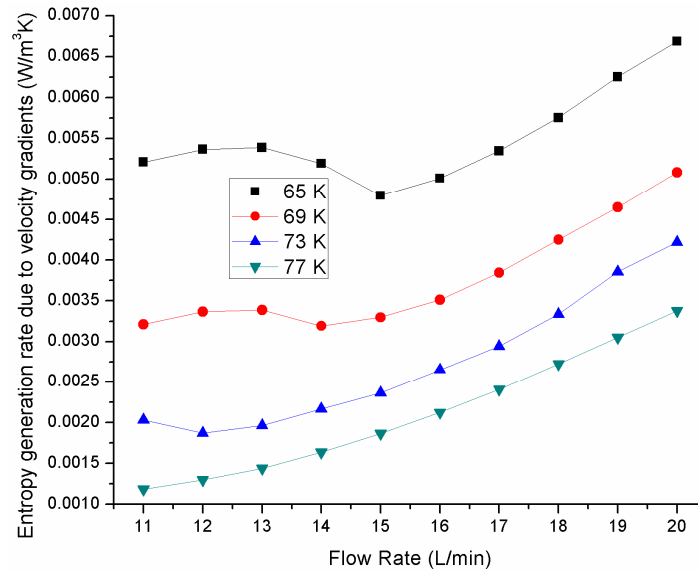


Figure 6.7 Entropy generation rate due to velocity gradients for different flow rates and inlet temperature

The volume average of entropy generation rate due to the velocity gradients over the entire volume of HTS cable for different mass flow rates and inlet temperature are shown in Figure 6.7. From the figure, it is observed that at particular inlet temperature with the increase in the flow rate at a range of 11 L/min to 20 L/min, volumetric entropy generation rate due to the velocity gradients increases at inlet temperatures of 73 K and 77 K. Further, at the inlet temperatures of 65 K and 69 K, the average volumetric entropy generation rate due to velocity gradients decreases till 15 L/min and 14 L/min respectively and later increases. The increase in the average volumetric entropy generation rate due to velocity gradients may be due to increase in the frictional forces that lead to higher velocity gradients at that particular inlet temperature. From the figure it is observed that, the volumetric entropy generation rate due to velocity gradients is lower at higher inlet temperature (77 K) compared to lower inlet temperature (65 K). Hence, HTS cable need to be operated at higher temperatures of LN₂ compared to lower inlet temperatures of LN₂ for better performance.

6.3 Volumetric entropy generation rate due to thermal gradients

The thermal gradients that are obtained from the ANSYS-FLUENT presented in the section 5.3 is used to calculate the entropy generation rate due thermal gradients. The results are shown at two different locations one at the center where there exist a corrugation (see Figure 6.8(a)) and other location is at outlet where no corrugation exists (see Figure 6.8 (b)).

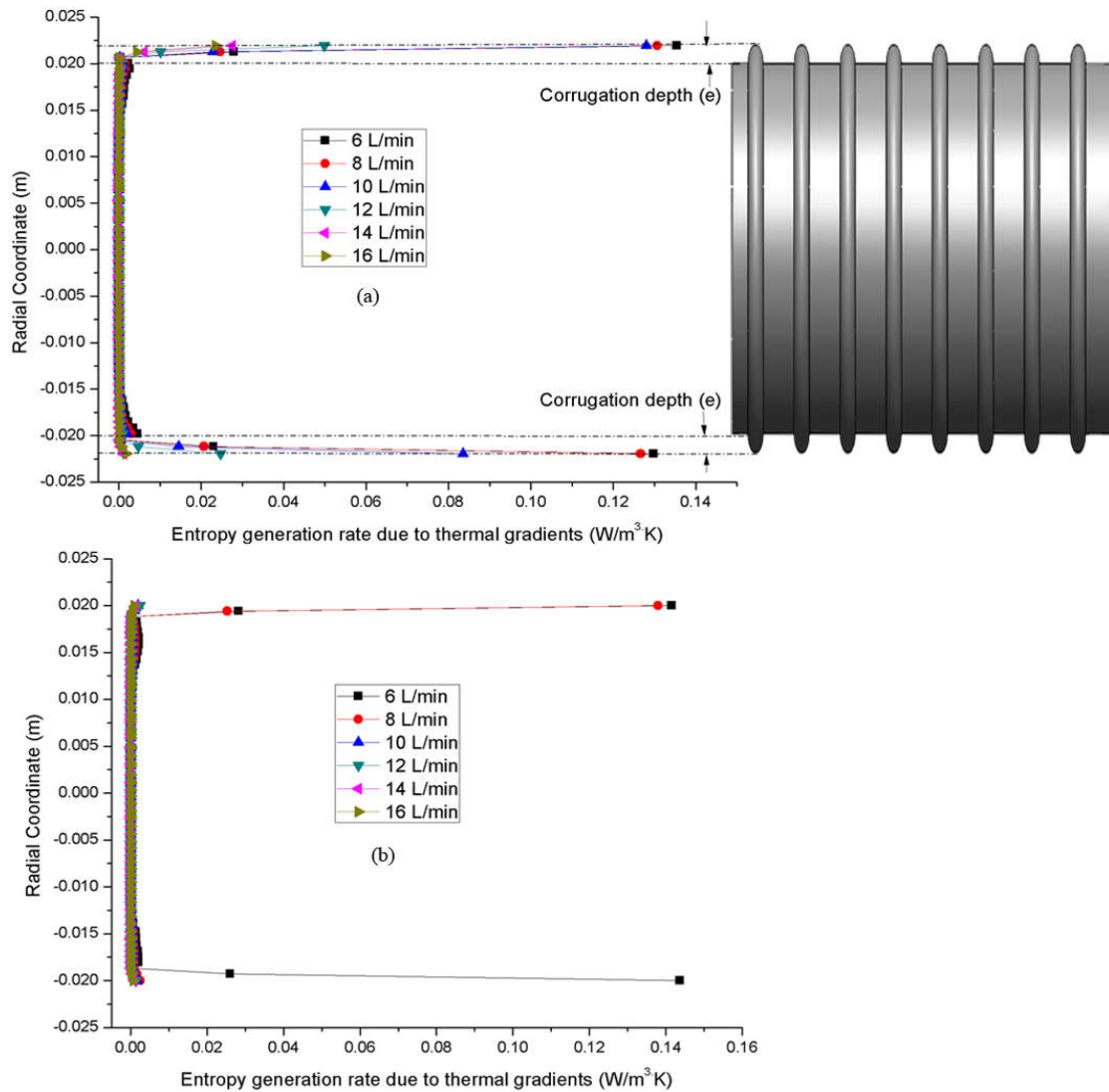


Figure 6.8 Entropy generation due to thermal gradients for different flow rates at a heat load of 2.1 W/m (a) at the center and (b) at the outlet

Volumetric entropy generation rate due to thermal gradients are shown in Figure 6.8 for different mass flow rates at the center and outlet of corrugated former with LN₂ flow. From the figure, it is observed that, higher the mass flow rate lower the entropy generation due to thermal gradients. Further, at the corrugations entropy generation rate is the maximum at

the center due to higher thermal gradients. The radial temperature gradients along the x, y and z- directions are positive which indicates that the heat is transferred from the wall of corrugated former to the bulk fluid. However, in axial thermal gradients are remains constant till the center of the corrugated former and then increases with the increase in flow rate. Negative temperature gradients are observed in the y-direction due to the formation of eddies the temperature at the wall of corrugated former increases and the fluid flowing at the axis acts as a heat sink. Hence the temperature gradients are negative for lower mass flow rates. The temperature gradients in z-direction are comparatively lower than x and y-direction gradients.

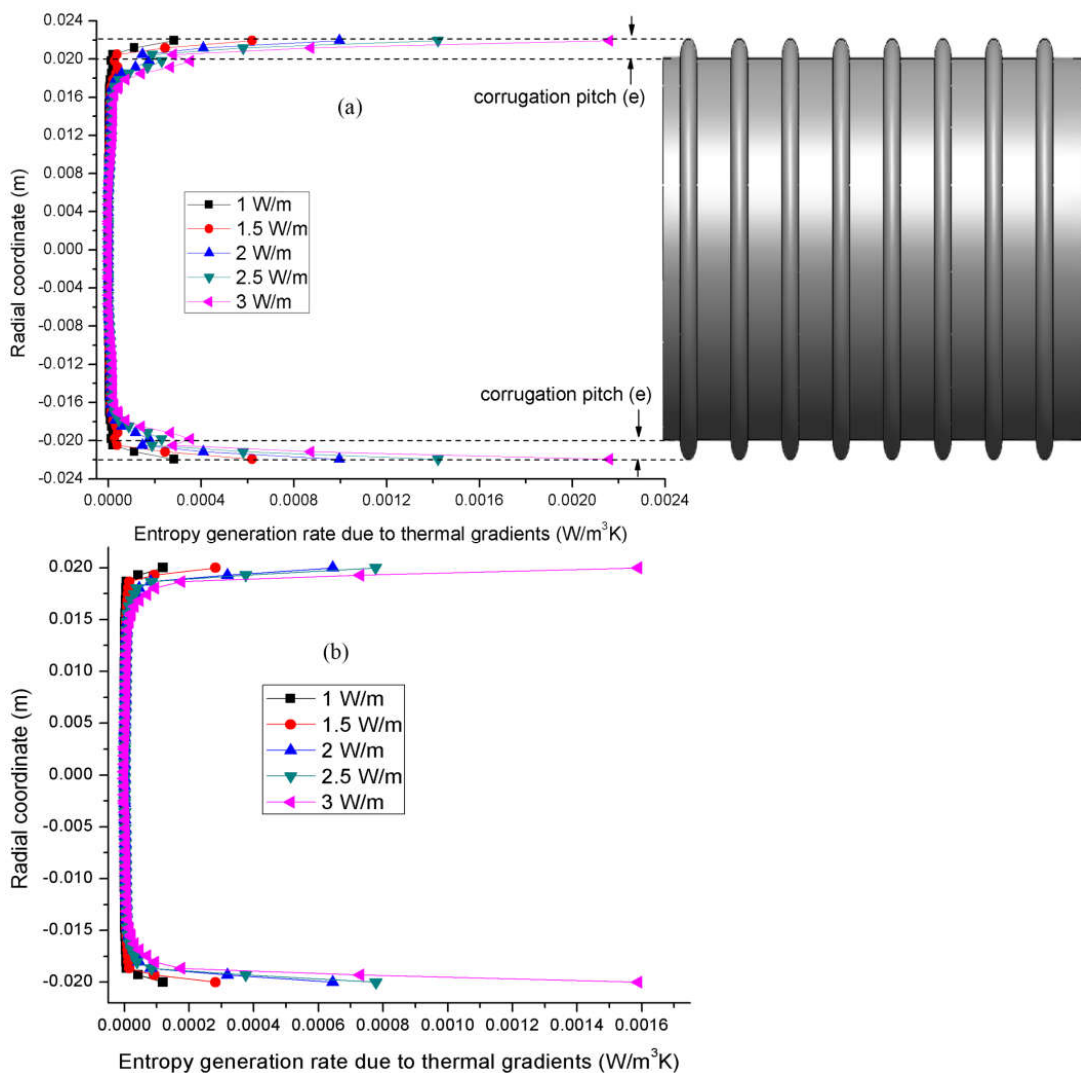


Figure 6.9 Entropy generation due to thermal gradients for different heat loads at a flow rate of 19 LPM (a) at the center and (b) at the outlet

The contribution of temperature gradients to the volumetric entropy generation rate with different mass flow rates and at various heat loads is shown in Figure 6.9. The results are presented at two different locations, one at the center of HTS cable where corrugation is available and second at the outlet of HTS cable without corrugation for a flow rate of 19 L/min. From the Figure 6.9a, it is identified that the entropy generation rate at the corrugation is higher because the temperature gradients are maximum reflecting to the wall condition where the gradients are maximum and similar results are observed at the outlet of the HTS cable at the wall in Figure 6.9b. Furthermore, with the increase in the heat load at constant flow rate higher entropy generation rate due to thermal gradients is observed.

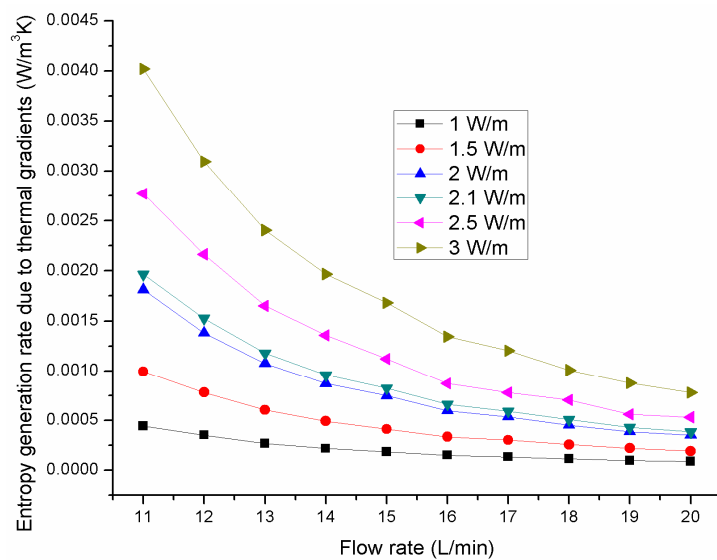


Figure 6.10 Entropy generation rate due to thermal gradients for different flow rates and heat loads

The volume average of entropy generation rate due to the thermal gradients over the entire volume of HTS cable for different mass flow rates and heat loads are shown in Figure 6.10. From the figure, it is observed that at constant heat load with the increase in the flow rate volumetric entropy generation rate due to the thermal gradients decrease. Further, at constant flow rate with the increase in the heat load, higher the heat load higher the volumetric entropy generation rate due to the thermal gradients.

The thermal entropy generation rate is due to the thermal gradients that are developed in the computational domain. These are may be due to the heat loads and the frictional losses for the flow of LN₂ in the HTS cable. The radial entropy generation rate due to thermal gradients for different heat loads at a flow rate of 14 L/min at $z = 1$ m is shown in Figure 6.11 (a). From the figure, it is observed that the entropy generation rate due to thermal gradients is higher at the higher heat loads. Figure 6.11 (b) shows the radial entropy

generation rate due to thermal gradients at $z = 1$ m for various flow rates at a heat load of 2 W/m. The entropy generation rate due to thermal gradients is lower at the higher flow rates for a constant heat load. Further, the thermal gradients at the wall are higher than that at the axis for different heat loads and flow rates. Furthermore, the contribution of entropy generation rate due to thermal gradients to the total entropy generation rate is lower than the entropy generation rate due to velocity gradients at higher flow rates.

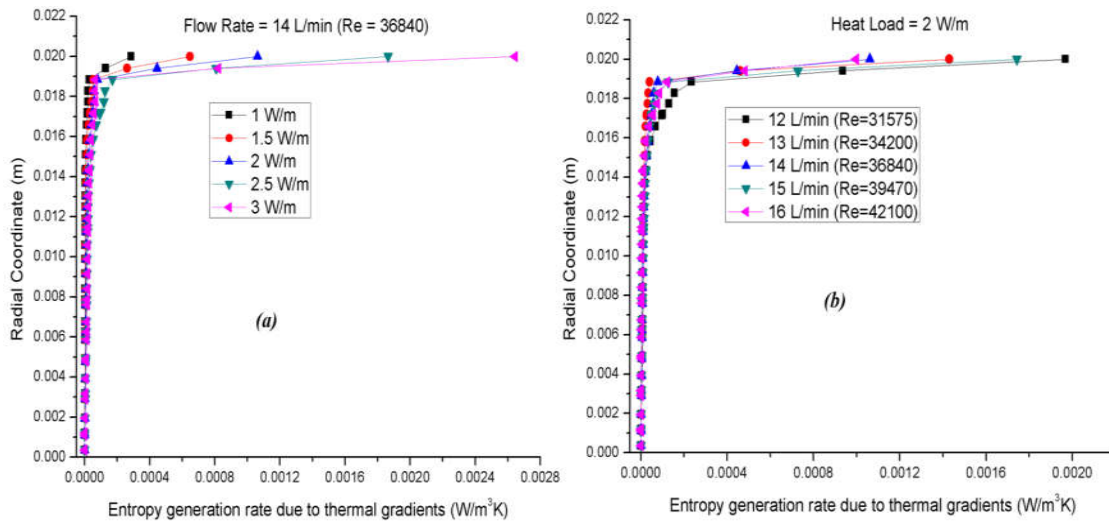


Figure 6.11 Entropy generation rate due to thermal gradients at a distance of $z = 1$ m in the HTS cable (a) for different heat loads at a flow rate of 14 L/min (b) for different flow rates at a heat load of 2 W/m

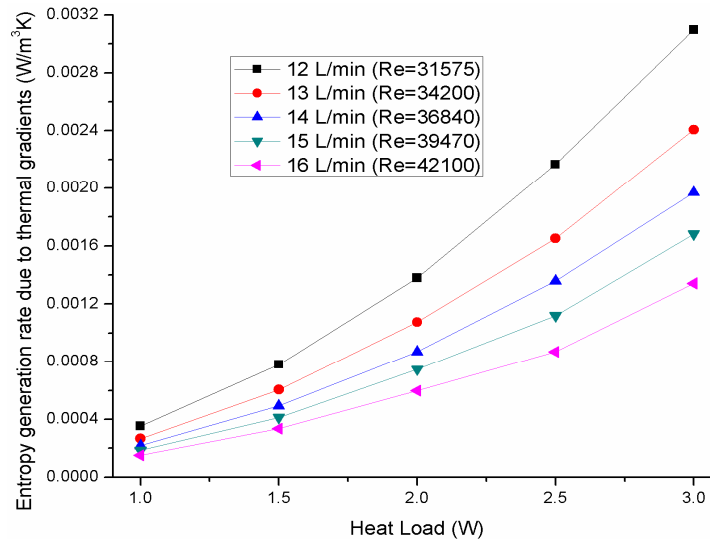


Figure 6.12 Entropy generation rate due to thermal gradients for various heat loads and different flow rates. The volumetric entropy generation rate due to the thermal gradients for different heat loads and flow rates are shown in Figure 6.12. From the figure, it is evident that at a particular heat load with the decrease in the flow rate the volumetric entropy generation rate due to thermal gradients increases. Further, at a particular flow rate, with the increase in heat

loads, the volumetric entropy generation rate due to thermal gradients increases. Furthermore, it is observed that the volumetric entropy generation rate due to thermal gradients is lower at the higher flow rate this may be due to slower thermal boundary layer development in higher flow rates [299].

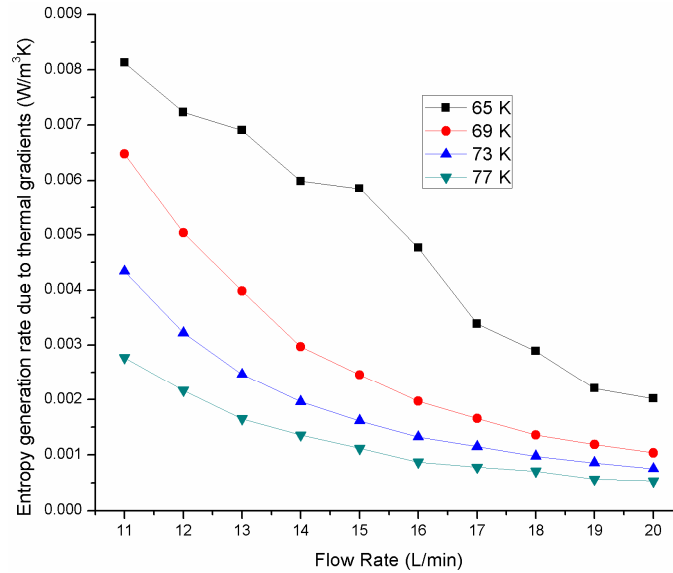


Figure 6.13 Entropy generation rate due to thermal gradients for different flow rates and inlet temperatures

The volume average of entropy generation rate due to the thermal gradients over the entire volume of HTS cable for different mass flow rates and inlet temperature are shown in Figure 6.13. From the figure, it is observed that at particular inlet temperature with the increase in the flow rate volumetric entropy generation rate due to the thermal gradients decreases. Further, at a particular flow rate, increase in the inlet temperature of the LN₂, the average volumetric entropy generation rate due to thermal gradients decreases. From the figure it is observed that, the volumetric entropy generation rate due to thermal gradients is lower at higher inlet temperature (77 K) compared to lower inlet temperature (65 K). Hence, HTS cable need to be operated at higher temperatures of LN₂ compared to lower inlet temperatures of LN₂ for better performance.

6.4 Bejan Number

When the thermal gradients are dominating $Be > 0.5$ and if velocity gradients are dominating $Be < 0.5$. The Bejan number is calculated across the entire computational domain and the maximum global Bejan number is 0.89 at 1L/min. Figure 6.14 shows the Bejan number contours at the inlet, center and outlet for a flow rate of 14 L/min. From the

analysis, it is identified that $Be > 0.5$ till the flow rate is 7L/min, confirm that entropy generation rate due to thermal gradients are dominating than velocity gradients.

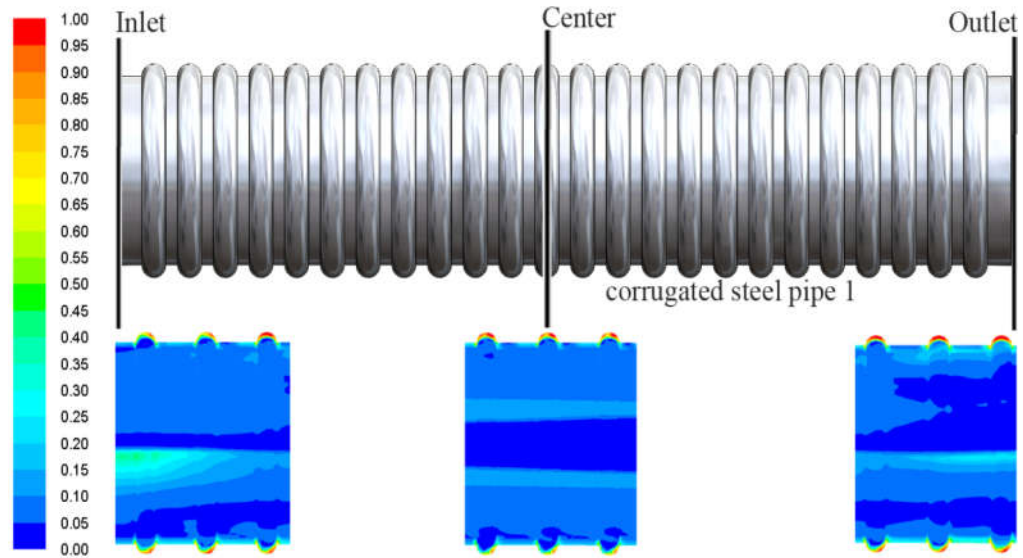


Figure 6.14 Bejan number contours at the inlet, center and outlet for flow rate of 14 L/min and heat load of 2.1W/m

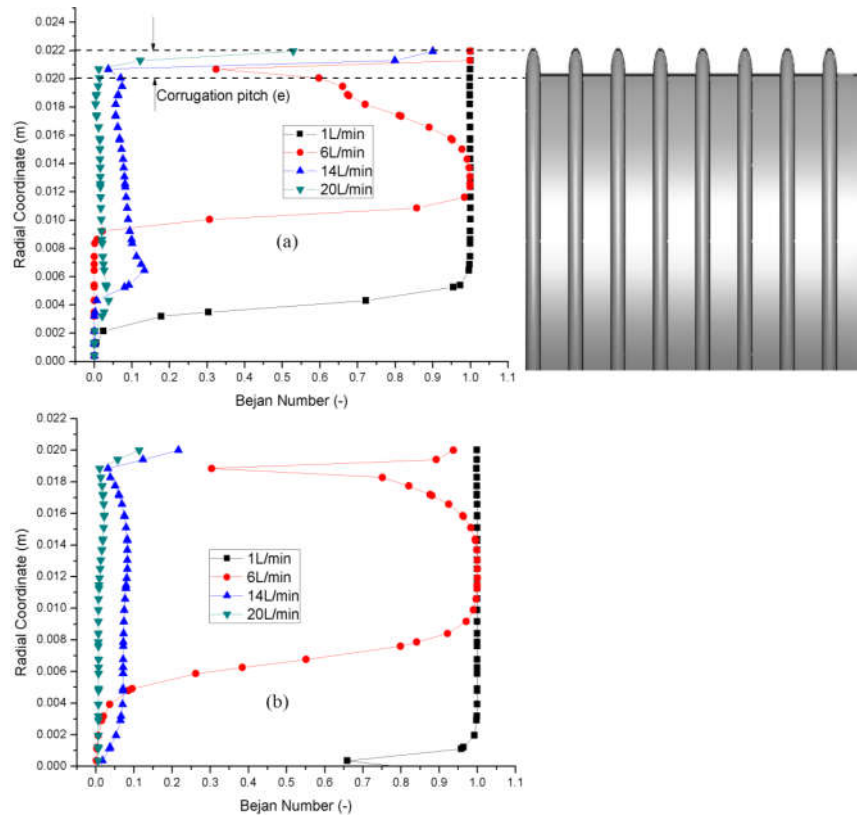


Figure 6.15 Bejan number for different flow rates (a) at the center and (b) at the outlet at a heat load of 2.1 W/m

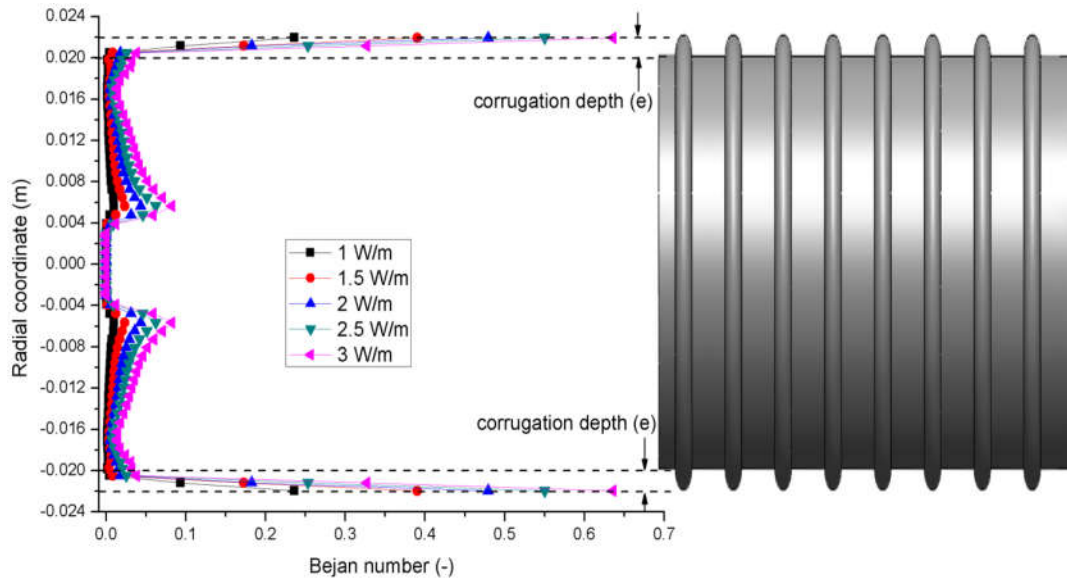


Figure 6.16 Bejan number for different heat loads at a flow rate of 19 L/min at center

Furthermore, $Be < 0.5$ with the increase in flow rate higher than 7L/min, signifies that entropy generation rate due to velocity gradients are dominating than temperature gradients. However, the magnitude of temperature gradients is higher than velocity gradients at higher flow rates also (see Figure 6.2 and Figure 6.8). This shows that the volumetric entropy generation rate is dominated by temperature gradients than velocity gradients.

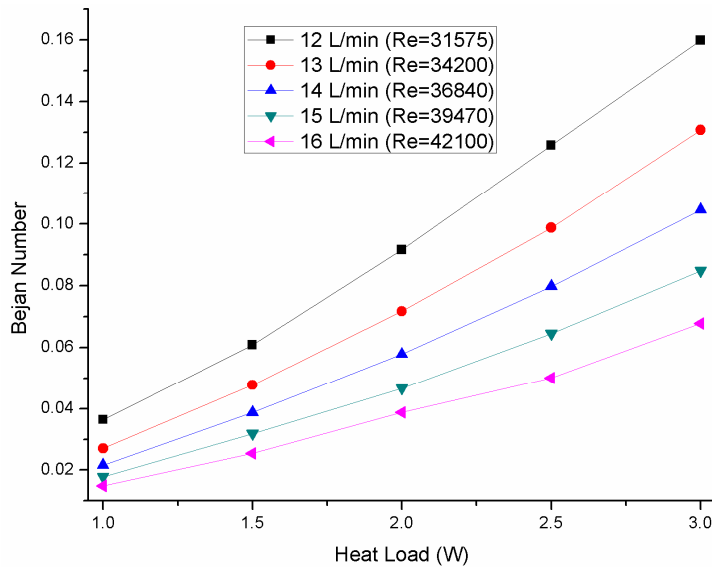


Figure 6.17 Bejan number for different heat loads and flow rates at an inlet temperature of 77K

Bejan number is a dimensionless number that used to predict the influence of temperature gradients and velocity gradients on the entropy generation rate due to flow of LN₂ in HTS

cable. A location in the HTS cable is considered at the center where corrugation is available to observe the Bejan number.

Figure 6.16 shows the variation of Bejan number at center location for a flow rate of 19 L/min and different heat loads ranging from 1 W/m to 3 W/m. From the figure, it is observed that higher the heat load higher the Bejan number. Further, at the corrugations domination of temperature gradients is higher than the velocity gradients. Hence, higher Bejan number is observed at the corrugations than that at the axis of the HTS cable.

The variation of Bejan number for different heat loads and flow rates at an inlet temperature of 77K is shown in Figure 6.17. From the figure, it is observed that higher the heat loads, higher the Bejan number at constant flow rate. Further, at the constant heat load, with increase in the flow rate, Bejan number is decreasing due to the contribution of velocity gradients in total entropy generation rate which signifies that temperature gradients are reduced significantly.

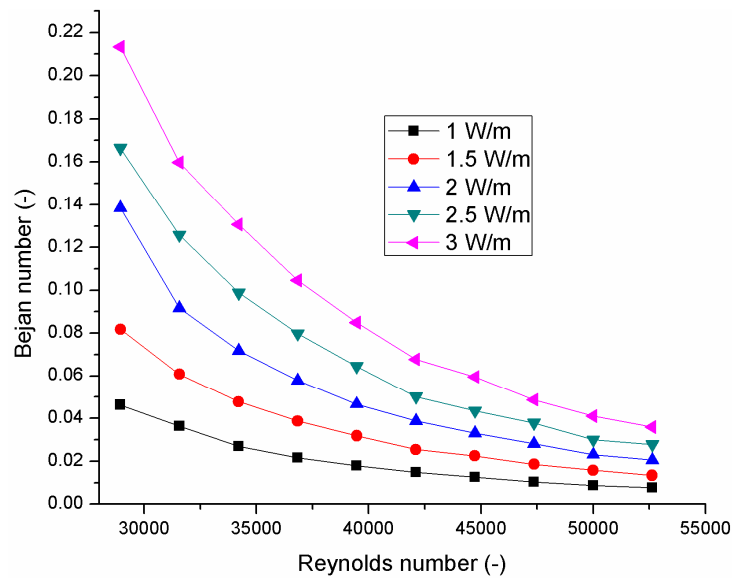


Figure 6.18 Bejan number versus Reynolds number at different heat loads

The variation of Bejan number as a function of Reynolds number at different heat loads is shown in Figure 6.18. From the figure, it is observed that higher the heat loads, higher the Bejan number at constant flow rate. Further, at the constant heat load, with increase in the Reynolds number, Bejan number is decreasing due to the contribution of velocity gradients in total entropy generation rate which signifies that temperature gradients are reduced significantly.

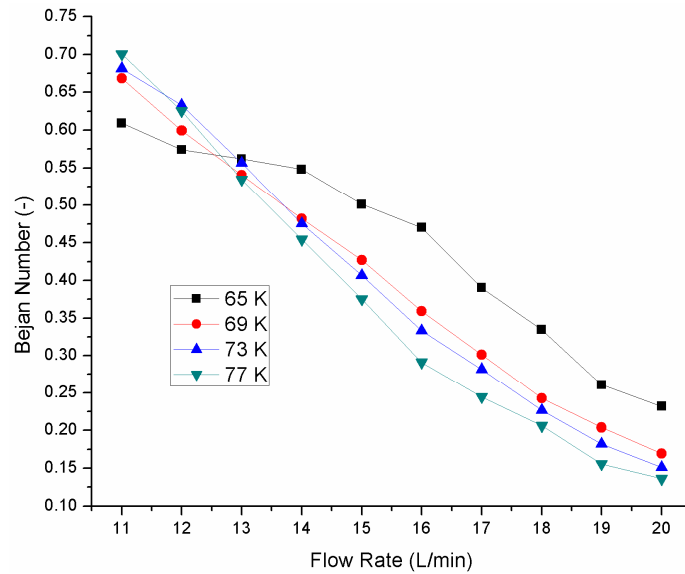


Figure 6.19 Bejan number for different flow rates and inlet temperatures at a heat load of 2.5 W/m

From the figure it is observed that, at a particular inlet temperature with the increase in flow rate the Bejan number decreases which indicate the entropy generation rate due to thermal gradients are lower compared to entropy generation rate due to velocity gradients. At a flow rate of 11 L/min, Bejan number is higher at inlet temperature of 77 K. Further increase in flow rate till 14 L/min at different inlet temperature, the Bejan number is gradually decreases and higher Bejan number is observed for inlet temperature of 65K. Later the trend of higher Bejan number at lower inlet temperature is observed.

The entropy generation rate is estimated using pressure gradients, velocity gradients and thermal gradients for different heat loads, flow rates and inlet temperatures. The estimated entropy generation rate is utilized in optimizing the thermohydraulic performance of HTS cable and discussed in the Chapter 7.

7 ENTROPY GENERATION MINIMIZATION IN HTS CABLES

7.1 Introduction

Optimization studies pertaining to engineering systems have been gaining prominence around the world to develop energy efficient devices. Entropy Generation Minimization (EGM) studies is one such popular method employed to interpret the thermohydraulic losses thereby recommending the necessary modifications in the design and operating conditions to enhance the efficiency of engineering systems and flow processes.

Entropy Generation Minimization (EGM) technique is most predominantly used for analyzing the exergy of the system for increasing the effectiveness and efficiency of a system. Optimization is defined as the technique that determines the optimized value for the desired design variables which maximize or minimize the objective by satisfying all constrains.

Optimization is majorly classified into types

1) Static optimization

This process refers to maximization of benefits or minimization of cost, for the design variables which are fixed with respect to time.

- ❖ Examples are Linear and Non-linear programming, Transportation, Portfolio selection etc
- ❖ Examples of optimization techniques are Direct Search Technique, Downhill Simplex and Gradient Search

A static optimization problem uses various methods for solving they are

a) Search methods

In this method the objective function is determined by using number of combination values of independent variables for optimum solution. Derivatives are not used in this method for optimizing the solution.

b) Calculus or Gradient Methods

In this method the first and second derivatives are used for optimizing the solution.

c) Stochastic or Evolutionary methods

In this method different optimal methods and algorithms are used such as Genetic Algorithms (GA), Particle Swarm Optimization (PSO), Simulating Annealing (SA) and Neural Networks etc. The combination of Stochastic algorithms with

deterministic algorithms such as Generalized Reduced Gradient (GRG) and Sequential Quadratic Programming (SQP) are used.

2) Dynamic optimization

This process refers to maximization of benefits or minimization of cost, for the design variables which are function of time

Examples are Cost functions, Euler-Lagrange equation etc

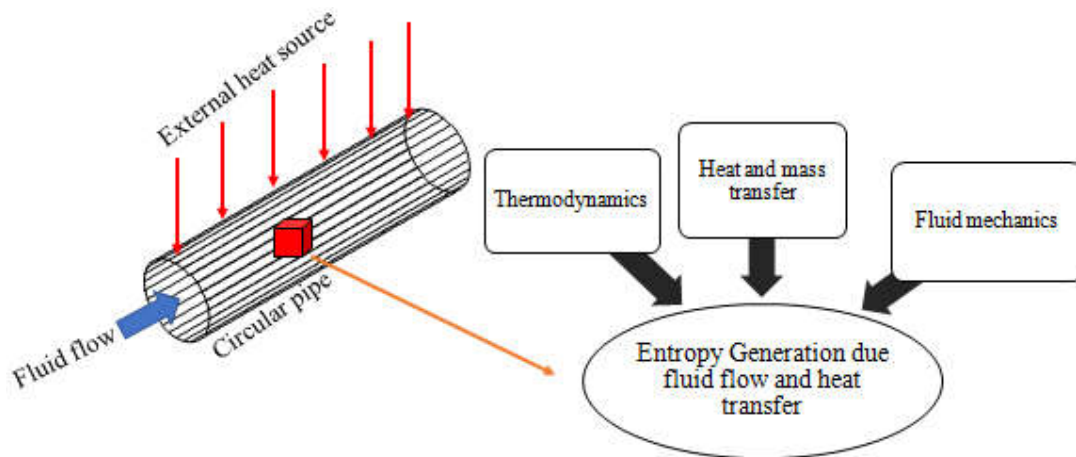


Figure 7.1 Entropy generation analysis (EGA) interdisciplinary fields

Entropy Generation Minimization (EGM) is a thermodynamic optimization technique which plays a major role in problem formulation, modeling, designing and optimization in research and engineering. This technique is used majorly due to its interdisciplinary fields which owe thermodynamic irreversibility in fluid mechanics, heat and mass transfer, thermodynamics and other transport processes[300] as shown in Figure 7.1.

The major objective of the EGM method is to identify the design or configuration in which the entropy generation rate (EGR) is minimal. This technique is used in this present research because it owes thermodynamic irreversibility in fluid mechanics, heat and mass transfer, thermodynamics and other transport processes. EGR is a function of overall physical characteristics of the subsystems where the entropy is generated at the boundaries due to the heat, mass transfer and fluid flow currents. In this project the interactions of the heat transfer and fluid flow are considered while mass transfer is neglected (no mixing of fluids or concentration differences are considered). In order to calculate the EGR the variation in the temperature drop (from relations of heat fluxes) and pressure drop (from relations of mass flow rate) are need to be calculated. For example, if mass flow rate of LN_2 is increased, pressure loss and heat transfer coefficients are increased at the same instance. Hence, the combined effect of pressure drop and heat transfer influences the

thermohydraulic characteristics of HTS cable for minimizing the EGR. The three dimensional EGR per unit volume is summarized as continuous fluid flow of LN₂ with flow velocity and temperature in space [5]. Entropy generation analysis (EGA) is a Heuristic approach and entropy generation minimization (EGM) is a deterministic approach of optimization [301].

7.2 Entropy Generation Minimization

Optimization studies pertaining to engineering systems have been gaining prominence around the world to develop energy efficient devices. Entropy Generation Minimization (EGM) studies is one such popular method employed to interpret the thermohydraulic losses thereby recommending the necessary modifications in the design and operating conditions to enhance the efficiency of engineering systems and flow processes [300], [302]–[305]. Various researchers have implemented the EGM technique to enhance the thermohydraulic performance of solar collectors [270] for different volume flow rates and reported that total entropy generation is higher in flat plate collectors as compared to that in evacuated tube collectors. Further, EGM algorithm in heat exchangers is implemented [255] in the past to reduce the annual cost of operation. In addition, entropy generation in micro channels [306] due to the flow of nano fluids was estimated and found that the increase in concentration of nano particles would reduce thermal entropy generation thereby aiding effective heat transfer. Moreover, fin arrangement is modified in shell and tube heat exchanger employed for thermal energy storage using phase change material with the help of entropy generation studies [266]. Recently, such studies were also used in developing superconducting magnets used for nuclear fusion reactors [5], [307]. Hence, such studies may be used in power transmission applications, where superconducting tapes are employed in the transmission of larger current densities.

The objective of the present work is to estimate the volumetric entropy generation rate for optimizing the thermohydraulic performance of HTS cable with higher heat transfer rate and lower pumping power. This analysis is carried for various mass flow rates until the minimum entropy generation rate is achieved. The volumetric entropy generation rate obtained due to velocity and thermal gradients at each location of the corrugated domain from the post processor of ANSYS-FLUENT is used to estimate the minimum entropy generated in the HTS cable using Entropy Generation Minimization (EGM) technique. Critical estimations are made by calculating the volume average of entropy generation at the entire length of HTS cable. Flow rates ranging from 1-20 L/min, heat loads ranging

from 1-3 W/m and inlet temperature of LN₂ ranging from 65-77 K (shown in Table 3.1) are utilized for optimizing the entropy generation rate in HTS cables.

The entropy generation rate was initially estimated from 5 L/min to 8 L/min and from the analysis it is identified that total volumetric entropy generation rate is decreasing with the increase in mass flow rate. Further, the efforts are made to extend the analysis till 20 L/min to identify the lower entropy generation rate. Figure 7.3 shows the cooling capacity and pumping power corresponding to minimum entropy generation rate in HTS cable. It is found that the total volumetric entropy generation rate is minimal at a flow rate of 14 L/min and further increase in the flow rate sharply increases the entropy generation rate. At a heat load of 2.1 W/m and LN₂ flow rate of 14 L/min, the corresponding performance of HTS cable constitute higher cooling capacity and lower pumping power. In order to avoid the quench of HTS tape at heat load of 2.1 W/m, the HTS cable is recommended to be operated at a flow rate of 14 L/min

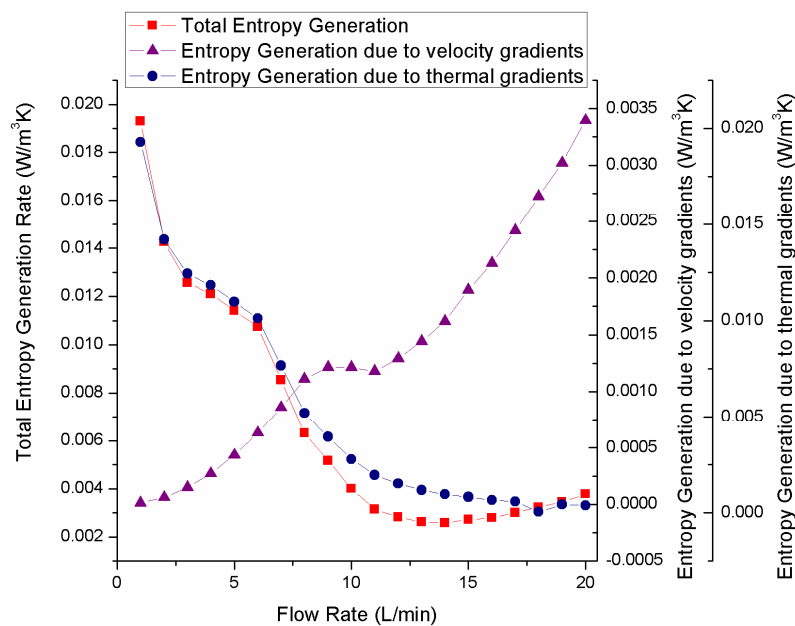


Figure 7.2 Entropy generation due to velocity gradients, Entropy generation due to thermal gradients and Total Entropy Generation, for different flow rates at a heat load of 2.1 W/m

The total volumetric entropy generation rate is the combination of volume average of volumetric entropy generation rate due to velocity gradients and volumetric entropy generation rate due to thermal gradients developed in the corrugated former of HTS cable. In this section the influence of inlet temperature on the total volumetric entropy generation rate in HTS cable is discussed.

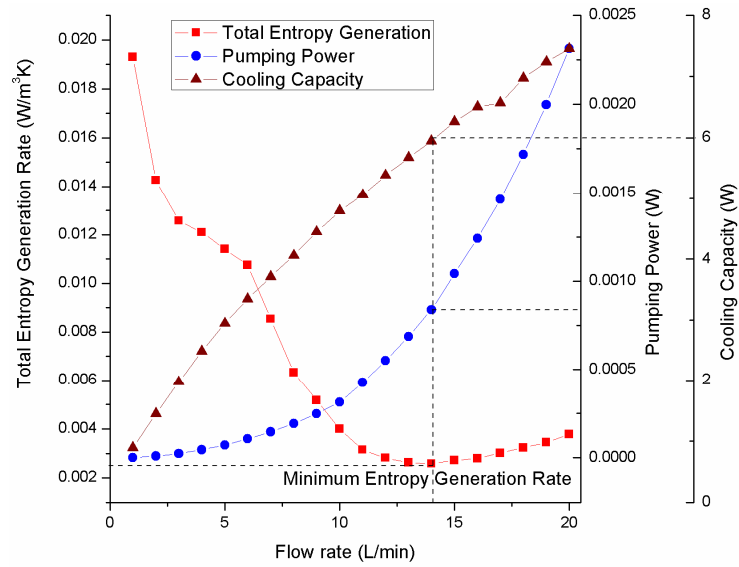


Figure 7.3 Total Entropy Generation, pumping power and cooling capacity for different flow rates at a heat load of 2.1 W/m

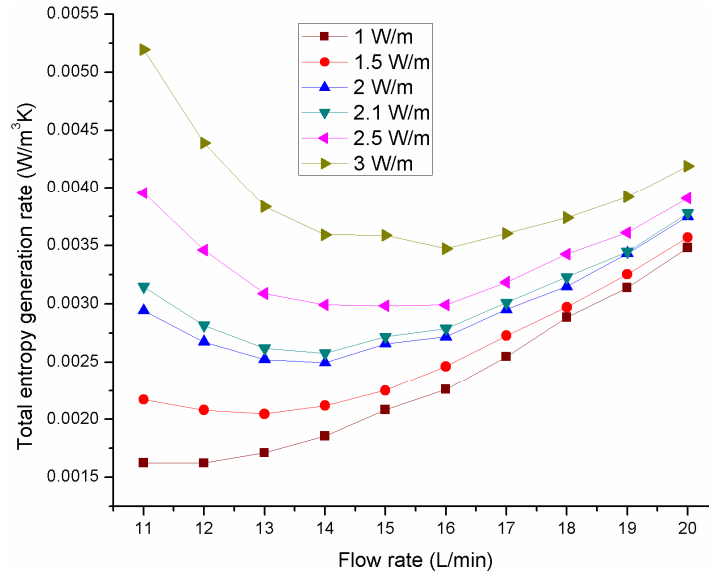


Figure 7.4 Total entropy generation rate for various heat loads and flow rates

The volumetric entropy generation rate in the HTS cable at a flow rate of 16 L/min for inlet temperature of LN₂ ranging from 65 K to 77 K and heat loads ranging from 1 W/m to 3 W/m is shown in Figure 7.5. From the figure, it is observed that at a particular inlet temperature, the total volumetric entropy generation rate increases with increase in heat load. Further, at a particular heat load, the total volumetric entropy generation rate decreases with increase in inlet temperature of LN₂. Hence, HTS cable need to be operated

at higher temperatures of LN₂ compared to lower inlet temperatures of LN₂ for better performance because the total volumetric entropy generation rate is noticeably lower.

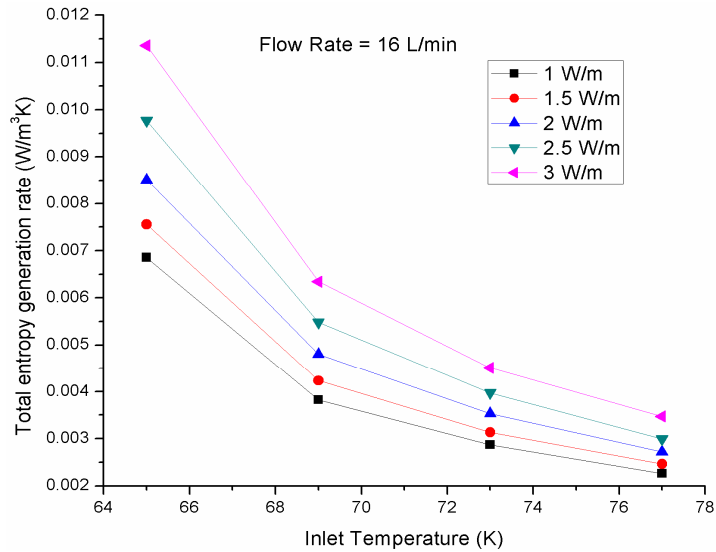


Figure 7.5 Total entropy generation rate at a flow rate of 16 L/min for different inlet temperatures and heat loads

The volumetric entropy generation rate in the HTS cable at a heat load of 2.5 W/m for inlet temperature of LN₂ ranging from 65 K to 77 K and flow rate ranging from 12 L/min to 16 L/min is shown in Figure 7.6.

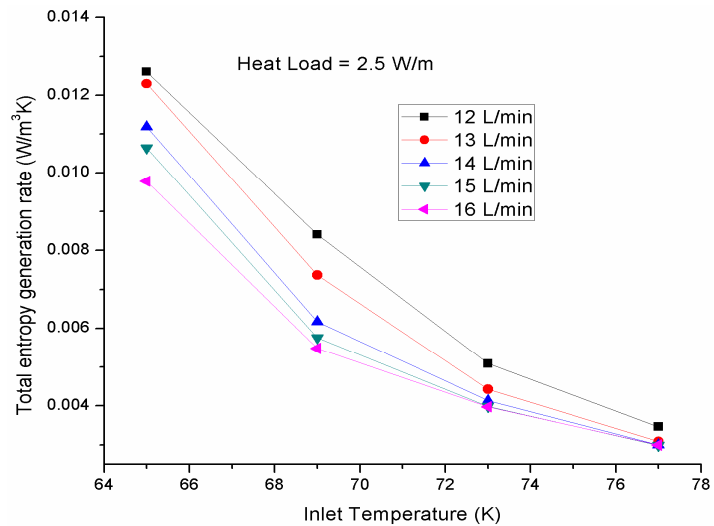


Figure 7.6 Total entropy generation rate at a heat load of 2.5 W/m for different inlet temperatures and flow rates

From the figure, it is observed that at a particular inlet temperature, the total volumetric entropy generation rate decreases with increase in flow rate. Further, at a particular flow rate, the total volumetric entropy generation rate decreases with increase in inlet

temperature of LN₂. Furthermore, at inlet temperature of 77 K, the difference in the total volumetric entropy generation rate is less for different flow rates. Hence, HTS cable need to be operated at higher temperatures of LN₂ compared to lower inlet temperatures of LN₂ for better performance because the total volumetric entropy generation rate is noticeably lower.

The total entropy generation rate is due to the combine contribution of entropy generation rate due to the thermal gradients (Thermal entropy generation rate) and entropy generation rate due to velocity gradients (frictional entropy generation rate) for the flow of LN₂ through the HTS cable. The total entropy generation rate for different heat loads at different flow rates is shown in Figure 7.7.

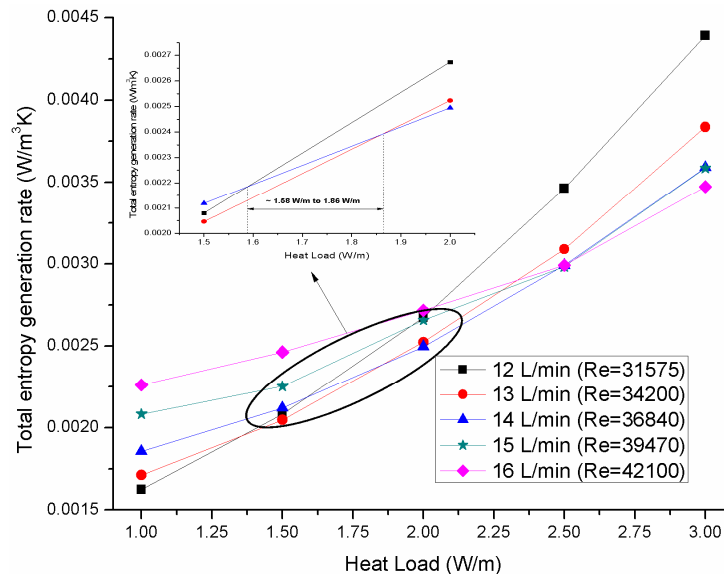


Figure 7.7 Total entropy generation rate for various heat loads and different flow rates in HTS cable.

From the figure, it is observed that at different flow rates, the lowest entropy generation rate at a particular heat load corresponds to minimum possible total entropy generation rate. Further, the minimum total entropy generation rate corresponds to optimum flow rate at which the HTS cable can be operated at a particular flow rate. The global minimum of total entropy generation rate is possible at 12 L/min for a heat load of 1 W/m for particular flow rates and heat loads. Furthermore, the intersection points in total entropy generation rate at different heat loads for various flow rates have been observed. From the Entropy Generation Minimization (EGM) point of view, for an instance, a flow rate of 13 L/min may be used for approximately from 1.5 W/m to 1.86 W/m heat load for efficient operation of the HTS cable with lower pumping power and higher cooling capacity.

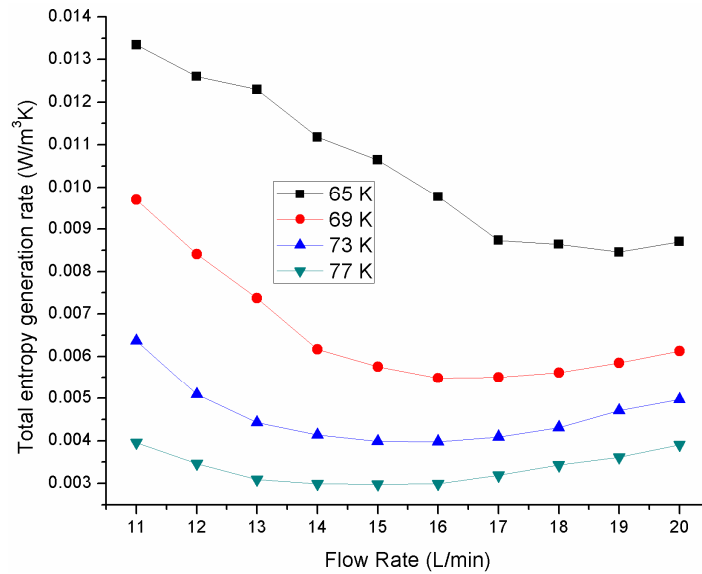


Figure 7.8 Total entropy generation rate for various inlet temperatures and flow rates

The present work focused on the effect of temperature dependent thermophysical properties of LN₂ inlet temperature and the heat loads on the entropy generation rate in HTS cables. The analysis is carried out to predict the optimum thermohydraulic performance of HTS cable for efficient operation under various heat loads. Efforts are made to calculate the volumetric average of entropy generation rate in HTS cables using the computational fluid dynamics with the imposed boundary conditions and the minimum entropy generation rate for different mass flow rates at various heat loads is presented.

The volumetric entropy generation rate due to thermal and velocity gradients are calculated in chapter are used to calculate the volume average of total entropy generation rate in HTS cable. The volumetric average of total entropy generation rate in HTS cable for various flow rates at different inlet temperatures and heat loads is presented in Figure 7.8. From the figure, it is observed that with the increase in flow rate of LN₂ at a particular inlet temperature, total entropy generation rate is decreased and then it increases sharply. Further, at a particular flow rate, higher the inlet temperature lower total entropy generation rate is observed.

The entropy generation rate was initially estimated at inlet temperature of 77 K for flow rates ranging from 1 L/min to 20 L/min and heat loads ranging from 1 W/m to 3 W/m. Further, the efforts are made to extend the analysis for different inlet temperatures to identify the lower entropy generation rate. Figure 7.9 shows the volume average of entropy generation rate due to thermal gradients and velocity gradients and total entropy generation rate in HTS cables at an inlet temperature of 65 K. From the figure, it is observed that

increase in flow rate the contribution of thermal gradients in entropy generation rate decreased. Further with the increase in flow rate contribution of velocity gradients in entropy generation rate increased first till 13 L/min and decreases till 15 L/min. Later, it increases steeply with the increase in flow rate. The minimum entropy generation rate is observed at flow rate of 19 L/min at an inlet temperature of 65 K.

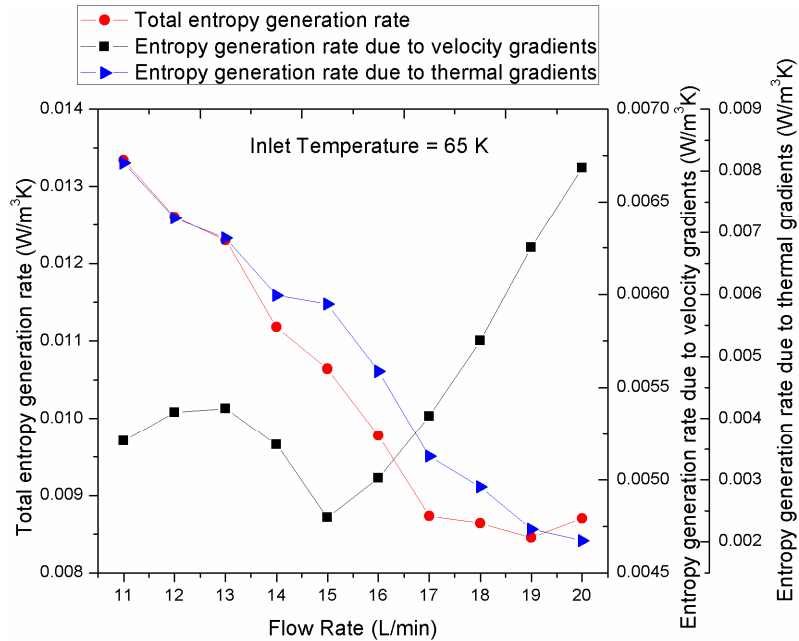


Figure 7.9 Entropy generation rate due to velocity gradients, Entropy generation rate due to thermal gradients and Total Entropy Generation rate, for different flow rates at an inlet temperature of 65 K

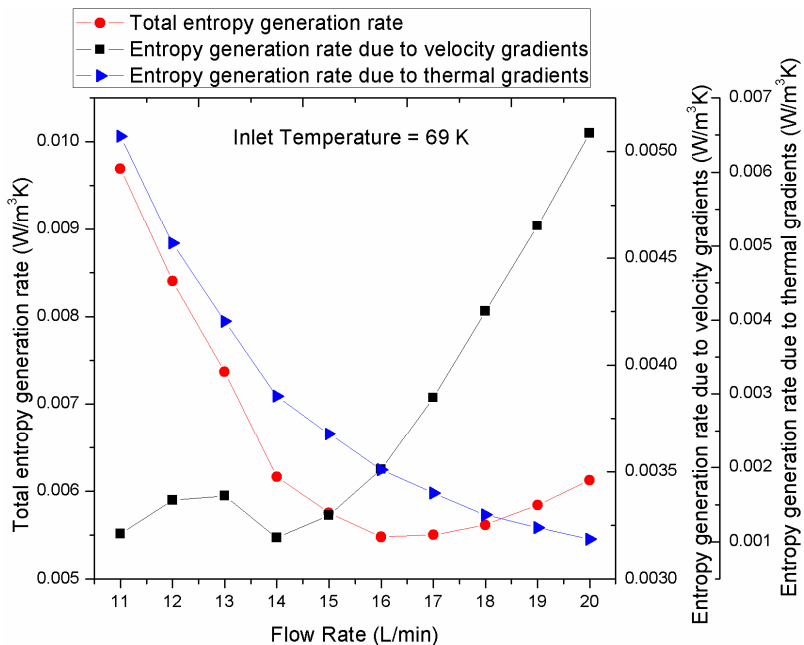


Figure 7.10 Entropy generation rate due to velocity gradients, Entropy generation rate due to thermal gradients and Total Entropy Generation rate, for different flow rates at an inlet temperature of 69 K

Figure 7.10 shows the volume average of entropy generation rate due to thermal gradients and velocity gradients and total entropy generation rate in HTS cables at an inlet temperature of 69 K. From the figure, it is observed that increase in flow rate the contribution of thermal gradients in entropy generation rate decreased. Further with the increase in flow rate contribution of velocity gradients in entropy generation rate increased first till 13 L/min and decreased at 14 L/min. Later, it increases steeply with the increase in flow rate. The minimum entropy generation rate is observed at flow rate of 16 L/min at an inlet temperature of 69 K.

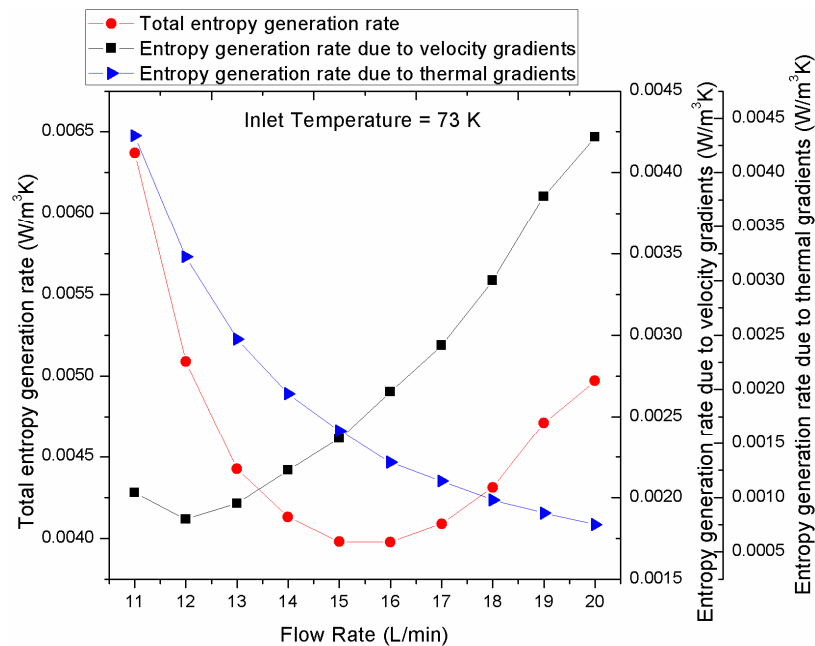


Figure 7.11 Entropy generation rate due to velocity gradients, Entropy generation rate due to thermal gradients and Total Entropy Generation rate, for different flow rates at an inlet temperature of 73 K

Figure 7.11 shows the volume average of entropy generation rate due to thermal gradients and velocity gradients and total entropy generation rate in HTS cables at an inlet temperature of 73 K. From the figure, it is observed that increase in flow rate the contribution of thermal gradients in entropy generation rate decreased. Further with the increase in flow rate contribution of velocity gradients in entropy generation rate decreased till 12 L/min and increases steeply with the increase in flow rate. The minimum entropy generation rate is observed at flow rate of 16 L/min at an inlet temperature of 73 K.

Figure 7.12 shows the volume average of entropy generation rate due to thermal gradients and velocity gradients and total entropy generation rate in HTS cables. From the figure, it is observed that increase in flow rate the contribution of thermal gradients in entropy

generation rate decreased. Further with the increase in flow rate contribution of velocity gradients in entropy generation rate increased. The minimum entropy generation rate is observed at flow rate of 15 L/min at an inlet temperature of 77 K.

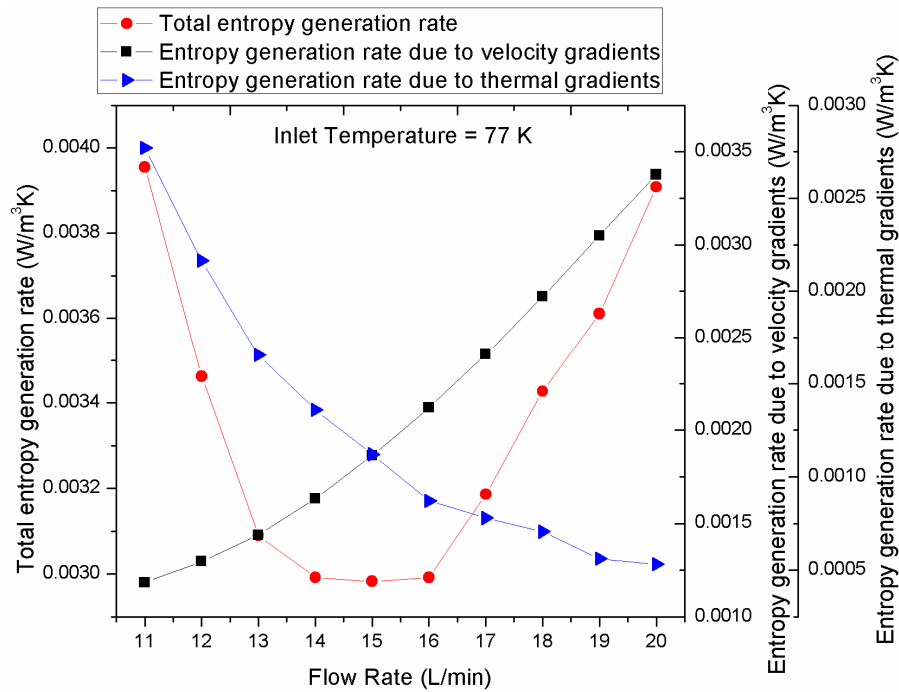


Figure 7.12 Entropy generation rate due to velocity gradients, Entropy generation rate due to thermal gradients and Total Entropy Generation rate, for different flow rates at an inlet temperature of 77 K

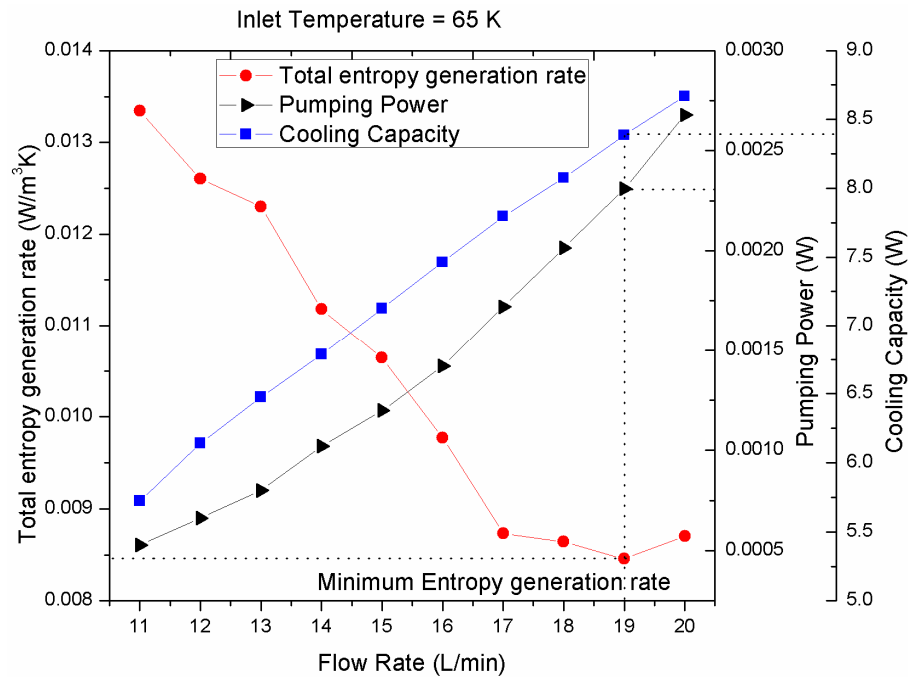


Figure 7.13 Total Entropy Generation, pumping power and cooling capacity for different flow rates at a heat load of 2.5 W/m and inlet temperature of 65 K

Figure 7.13 shows the cooling capacity and pumping power corresponding to minimum entropy generation rate in HTS cable. It is found that the total volumetric entropy generation rate is minimal at a flow rate of 19 L/min and further increase in the flow rate sharply increases the entropy generation rate. At a heat load of 2.5 W/m and 65 K inlet temperature LN₂ flow rate of 19 L/min, the corresponding performance of HTS cable constitute higher cooling capacity and lower pumping power.

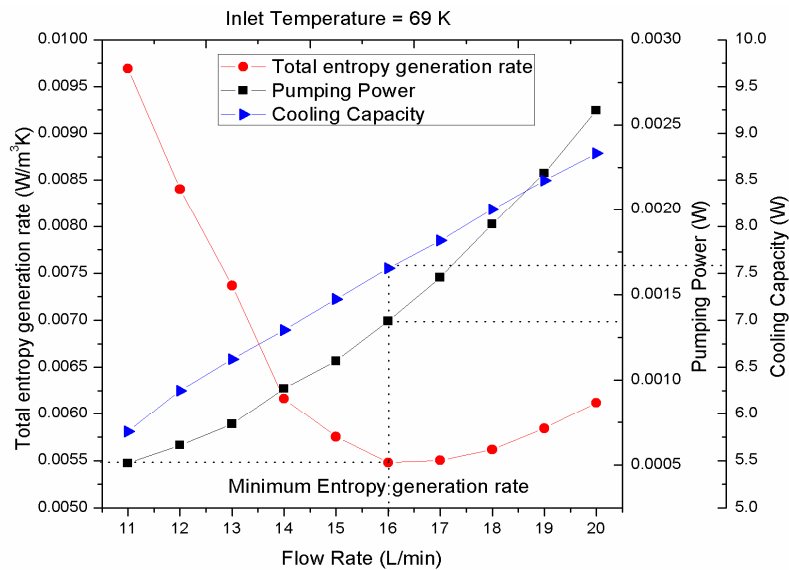


Figure 7.14 Total Entropy Generation, pumping power and cooling capacity for different flow rates at a heat load of 2.5 W/m and inlet temperature of 69 K

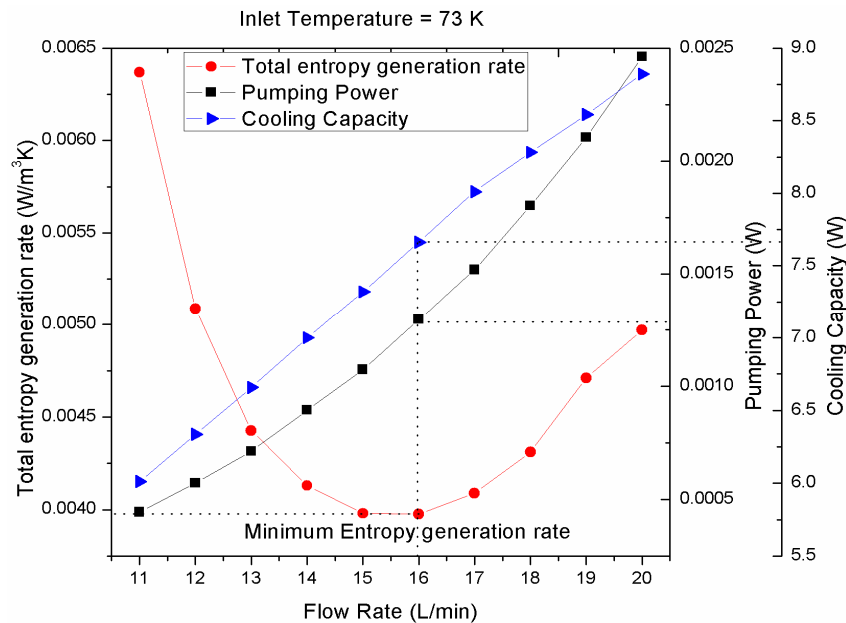


Figure 7.15 Total Entropy Generation, pumping power and cooling capacity for different flow rates at a heat load of 2.5 W/m and inlet temperature of 73 K

Figure 7.14 shows the cooling capacity and pumping power corresponding to minimum entropy generation rate in HTS cable. It is found that the total volumetric entropy generation rate is minimal at a flow rate of 16 L/min and further increase in the flow rate sharply increases the entropy generation rate. At a heat load of 2.5 W/m and 69 K inlet temperature of LN₂ flow rate of 16 L/min, the corresponding performance of HTS cable constitute higher cooling capacity and lower pumping power.

Figure 7.15 shows the cooling capacity and pumping power corresponding to minimum entropy generation rate in HTS cable. It is found that the total volumetric entropy generation rate is minimal at a flow rate of 16 L/min and further increase in the flow rate sharply increases the

Table 7.1 Optimum flow rate at different inlet temperatures and heat loads with minimum entropy generation rate of the HTS cables

Inlet Temperature (K)	Heat Loads (W/m)	Minimum Entropy Generation Rate (W/m ³ K)	Optimum flow Rate (L/min)
65	1	0.00363	16
	1.5	0.00695	17
	2	0.00771	17
	2.5	0.00846	19
	3	0.00938	19
69	1	0.00369	14
	1.5	0.00418	15
	2	0.00481	16
	2.5	0.00548	16
	3	0.00625	17
73	1	0.00239	13
	1.5	0.00285	13
	2	0.00342	15
	2.5	0.00397	16
	3	0.00451	16
77	1	0.00163	12
	1.5	0.00205	13
	2	0.00249	14
	2.5	0.00298	15
	3	0.00347	16

entropy generation rate. At a heat load of 2.5 W/m and 69 K inlet temperature of LN₂ flow rate of 16 L/min, the corresponding performance of HTS cable constitute higher cooling

capacity and lower pumping power. Figure 7.16 shows the cooling capacity and pumping power corresponding to minimum entropy generation rate in HTS cable. It is found that the total volumetric entropy generation rate is minimal at a flow rate of 15 L/min and further increase in the flow rate sharply increases the entropy generation rate. At a heat load of 2.5 W/m and 77 K inlet temperature of LN₂ flow rate of 15 L/min, the corresponding performance of HTS cable constitute higher cooling capacity and lower pumping power.

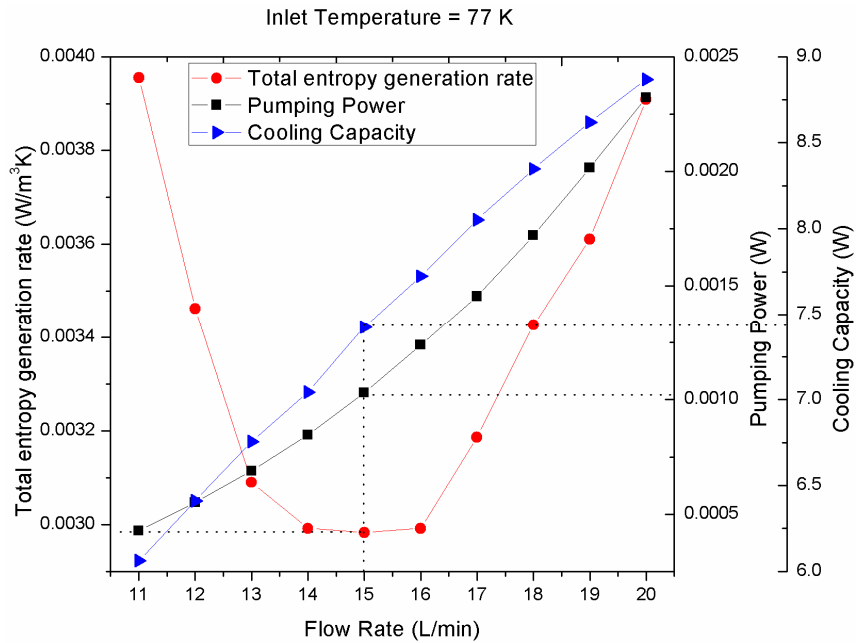


Figure 7.16 Total Entropy Generation, pumping power and cooling capacity for different flow rates at a heat load of 2.5 W/m and inlet temperature of 77 K

The optimum flow rate at different inlet temperatures and heat loads with minimum entropy generation rate of the HTS cables is shown in the Table 7.1. From the table, for different operating conditions such as heat loads, inlet temperature the optimum flow rate for efficient operation of HTS cables can be identified with minimum entropy generation rate. The optimum thermohydraulic characteristics for efficient operation the HTS cable with lower pumping power and higher cooling capacity with optimized flow rates can be seen at minimum entropy generation rate for different inlet temperatures ranging from 11 L/min to 20 L/min and heat loads ranging from 1 W/m to 3 W/m.

CHAPTER VIII

8 SUMMARY AND CONCLUSIONS

The present work focused on the influence of temperature dependent thermophysical properties of LN₂ at various heat loads ranging from 1 W/m to 3 W/m, inlet temperature ranging from 65 K to 77 K and flow rates ranging from 11 L/min to 20 L/min in HTS cables. The analysis is carried out to predict the optimum thermohydraulic performance of HTS cable for efficient operation. Efforts are made to calculate the volumetric average of entropy generation rate in HTS cables using the computational fluid dynamics with the imposed boundary conditions and the minimum entropy generation rate for different mass flow rates, inlet temperatures and heat loads is presented. Entropy generation minimization is the approach that signifies the optimum thermohydraulic performance of HTS cable for efficient operation under normal operation. From the present work, the following conclusions are drawn

- ✓ It can be concluded that, at a heat load of 2.1 W/m, inlet temperature of 77 K and flow rates ranging from 1 L/min to 20 L/min, the optimum thermohydraulic characteristics are observed at minimum entropy generation rate of 14 L/min.
- ✓ The temperature gradients are contributing higher rate of entropy generation as compared to that due to velocity gradients.
- ✓ The hydraulic performance and the entropy generation rate due to velocity gradients at different heat loads are not significantly increased for various mass flow rates.
- ✓ The temperature rise of LN₂ flow through HTS cable is below to the critical temperature at an operating pressure of 2.7 bar at different heat loads. Hence, HTS tapes are safe from quenching. The central flow cooling can be used for long length cable applications.
- ✓ For heat loads ranging from 1-3 W/m and flow rates ranging from 11-20 L/min, the global minimum total entropy generation rate is observed at a flow rate of 12 L/min and at a heat load of 1 W/m.
- ✓ The entropy generation rate due to velocity gradients are decreasing initially at lower flow rate and increasing with further increase in the flow rate. However, the

entropy generation rate due to thermal gradients is decreasing for the flow rates ranging from 11 L/min to 20 L/min.

- ✓ From the analysis, it is observed that for efficient operation of HTS cables, the inlet temperature of LN₂ is to be maintained at 77 K that pertains to better thermohydraulic performance and minimum entropy generation rate.
- ✓ The temperature rise of LN₂ flow through HTS cable is below to the critical temperature at an operating pressure of 2.7 bar at different heat loads and inlet temperatures. Hence, HTS tapes are safe from quenching. The central flow cooling can be used for long length cable applications.
- ✓ For heat loads ranging from 1-3 W/m, inlet temperatures ranging from 65 K to 77 K and flow rates ranging from 11-20 L/min, the global minimum total entropy generation rate is observed at a flow rate of 12 L/min and at a heat load of 1 W/m and an inlet temperature of 77 K.
- ✓ The minimum entropy generation rate for heat loads ranging from 1-3 W/m, inlet temperatures ranging from 65 K to 77 K and flow rates ranging from 11-20 L/min, is possible at the optimum flow rates ranging from 12-19 L/min.
- ✓ Higher the inlet operating temperature of LN₂ higher the efficiency of HTS cable at an operating pressure of 2.7 bar and the inlet temperature ranging from 65 K to 77 K.
- ✓ HTS cables should be operated at the higher inlet temperature of 77 K and lower heat load of 1 W/m for efficient operation with lower entropy generation rate and better thermohydraulic characteristics.

FUTURE SCOPE

- ✓ In future, the effect of corrugation pitch and depth on thermohydraulic characteristics, for different corrugation domains needs further to be studied for developing an efficient cooling system for HTS cables.
- ✓ The entropy generation rate in different HTS cable configurations are to be studied for estimating the optimum thermohydraulic characteristics.
- ✓ A novel cryogenic coolant can be prepared by dispersion of nano particles in the LN₂ for enhancing the thermal characteristics. Thereby, minimum entropy generation rate in HTS cables can be achieved.
- ✓ The transient analysis of HTS cables in operation must be studied in detail for understanding the challenges in real time operation
- ✓ Superconducting Fault Current Limiters (SFCL) must be integrated to HTS power cables so that the stability of HTS cables may be enhanced. Thereby, the extra cooling required incorporation of HTS-SFCL may be estimated.
- ✓ Superconducting Magnetic Energy Storage (SMES) system attached to HTS power cables would impose fluctuation in current carrying capacity of HTS cables. Hence, the coolant which has to be circulated must be sufficient enough to take care of these fluctuations. Such studies help the users in designing reliable transmission systems.

9 REFERENCES

- [1] P. Seidel, *Applied Superconductivity, Handbook on Devices and Applications*. 2015.
- [2] W. Paul and M. Chen, "Superconducting control for surge currents," *IEEE Spectr.*, vol. 35, no. May, pp. 49–54, 1998.
- [3] R. S. Dondapati and V. V. Rao, "CFD Analysis of Cable-In-Conduit Conductors (CICCs) for Fusion Grade Magnets," *IEEE Trans. Appl. Supercond.*, vol. 22, no. 3, 2012.
- [4] D. Raja Sekhar and V. V. Rao, "Three dimensional CFD analysis of Cable-in-Conduit Conductors (CICCs) using porous medium approach," *Cryogenics (Guildf.)*, vol. 54, pp. 20–29, Feb. 2013.
- [5] R. S. Dondapati and V. V. Rao, "Entropy generation minimization (EGM) to optimize mass flow rate in dual channel cable-in-conduit conductors (CICCs) used for fusion grade magnets," *Fusion Eng. Des.*, vol. 89, no. 6, pp. 837–846, Jun. 2014.
- [6] R. S. Dondapati and V. V. Rao, "Influence of mass flow rate on Turbulent Kinetic Energy (TKE) distribution in Cable-in-Conduit Conductors (CICCs) used for fusion grade magnets," *Fusion Eng. Des.*, vol. 88, no. 5, pp. 341–349, Jun. 2013.
- [7] S. Hahn *et al.*, "Design Study on a 100-kA / 20-K HTS Cable for Fusion Magnets," *IEEE Trans. Appl. Supercond.*, vol. 25, no. 3, 2015.
- [8] D. Uglietti, N. Bykovsky, R. Wesche, and P. Bruzzone, "Development of HTS Conductors and Magnets for Fusion Reactors," *IEEE Trans. Appl. Supercond.*, vol. 25, no. 3, pp. 4–9, 2015.
- [9] T. Nitta, M. Chiba, and H. Uematsu, "Characteristic of AC surface spark voltage in LN₂ and LHe," *IEEE Trans. Appl. Supercond.*, vol. 10, pp. 1325–1328, 2000.
- [10] A. B. Abrahamsen, N. Magnusson, B. B. Jensen, and M. Runde, "Large superconducting wind turbine generators," *Energy Procedia*, vol. 24, no. January, pp. 60–67, 2012.
- [11] T. Oka, K. Yokoyama, and K. Noto, "Construction of strong magnetic field generators by high T_c bulk superconductors and its applications," *IEEE Trans. Appl. Supercond.*, vol. 14, no. 2, pp. 1058–1061, 2004.
- [12] A. B. Abrahamsen *et al.*, "Feasibility study of 5 MW superconducting wind turbine generator," *Phys. C Supercond. its Appl.*, vol. 471, no. 21–22, pp. 1464–1469, 2011.
- [13] P. Tixador, "Superconducting electrical motors," *Int. J. Refrig.*, vol. 22, pp. 150–157, 1999.
- [14] K. Kajikawa, R. Osaka, H. Kuga, T. Nakamura, and T. Wakuda, "Proposal of new structure of MgB₂ wires with low AC loss for stator windings of fully superconducting motors located in iron core slots," *Phys. C Supercond. its Appl.*, vol. 471, no. 21–22, pp. 1470–1473, 2011.
- [15] T. Ki and S. Jeong, "Stirling-type pulse tube refrigerator with slit-type heat exchangers for HTS superconducting motor," *Cryogenics (Guildf.)*, vol. 51, no. 6, pp. 341–346, 2011.

- [16] A. Kim *et al.*, “Operating Characteristic Analysis of HTS SMES for Frequency Stabilization of Dispersed Power Generation System,” vol. 20, no. 3, pp. 1334–1338, 2010.
- [17] W. Yao, L. Jiang, J. Fang, J. Wen, S. Cheng, and Q. H. Wu, “Adaptive power oscillation damping controller of superconducting magnetic energy storage device for interarea oscillations in power system,” *Int. J. Electr. Power Energy Syst.*, vol. 78, pp. 555–562, Jun. 2016.
- [18] Y. Kito, O. Tsukamoto, and S. Fukui, “AC Transport Current Loss of High Temperature Superconducting Tapes in Single Layer Arrangements,” *Int. Conf. Magn. Technol.*, pp. 1214–1217, 1997.
- [19] V. V. Zubko, A. A. Nosov, N. V. Polyakova, S. S. Fetisov, and V. V. Vysotsky, “Hysteresis Loss in Power Cables Made of 2G HTS Wires With NiW Alloy Substrate,” *IEEE Trans. Appl. Supercond.*, vol. 21, no. 3, pp. 988–990, 2011.
- [20] Z. Zhou *et al.*, “Magnetic-Thermal Coupling Analysis of the Cold Dielectric High Temperature Superconducting Cable,” *IEEE Trans. Appl. Supercond.*, vol. 23, no. 3, p. 5400404, 2013.
- [21] J. He *et al.*, “Thermal analysis of HTS power cable using 3-D FEM model,” *IEEE Trans. Appl. Supercond.*, vol. 23, no. 3, pp. 1–4, 2013.
- [22] D. Homa, G. Kaur, G. Pickrell, and Y. Liang, “Efficient cooling of superconducting fiber core via holey cladding,” *Cryogenics (Guildf.)*, vol. 61, pp. 25–30, 2014.
- [23] Z. Li, Y. Li, W. Liu, J. Zhu, and M. Qiu, “Comparison of Liquid Nitrogen Flow Resistance in Corrugated Pipe With Smooth Pipe for HTS Cable,” *IEEE Trans. Appl. Supercond.*, vol. 25, no. 3, p. 5401304, 2015.
- [24] R. S. Dondapati, A. Kumar, G. R. Kumar, P. R. Usurumarti, and S. Dondapati, “Superconducting magnetic energy storage (SMES) devices integrated with resistive type superconducting fault current limiter (SFCL) for fast recovery time,” *J. Energy Storage*, vol. 13, pp. 287–295, Oct. 2017.
- [25] L. Chen, Y. Tang, J. Shi, and Z. Sun, “Simulations and experimental analyses of the active superconducting fault current limiter,” *Phys. C Supercond.*, vol. 459, pp. 27–32, 2007.
- [26] J. Zhu, X. Zheng, M. Qiu, Z. Zhang, J. Li, and W. Yuan, “Application Simulation of a Resistive Type Superconducting Fault Current Limiter (SFCL) in a Transmission and Wind Power System,” *Energy Procedia*, vol. 75, pp. 716–721, 2015.
- [27] F. Grilli, E. Pardo, A. Stenvall, D. N. Nguyen, W. Yuan, and F. Gomory, “Computation of losses in HTS under the action of varying magnetic fields and currents,” *IEEE Trans. Appl. Supercond.*, vol. 24, no. July, pp. 1–57, 2014.
- [28] H. Noji, K. Ikeda, K. Uto, and T. Hamada, “Calculation of the total AC loss of high-T_C superconducting transmission cable,” *Phys. C*, vol. 448, pp. 1066–1068, 2006.
- [29] F. Grilli, F. Sirois, S. Member, M. Laforest, and S. P. Ashworth, “Periodic Space-Time Formulation for Numerical AC Loss Computation in Superconductors,” *IEEE Trans. Appl. Supercond.*, vol. 19, no. 3, pp. 3565–3568, 2009.
- [30] Z. Hong and T. A. Coombs, “Numerical Modelling of AC Loss in Coated

- Conductors by Finite Element Software Using H Formulation,” *J Supercond NovMagn*, vol. 23, pp. 1551–1562, 2010.
- [31] Z. Hong, A. M. Campbell, and T. A. Coombs, “Numerical solution of critical state in superconductivity by finite element software,” *Supercond. Sci. Technol.*, vol. 19, no. 12, p. 1246, 2006.
- [32] F. Grilli, “Magnetization AC losses of stacks of YBCO coated conductors,” *Phys. C*, vol. 434, pp. 185–190, 2006.
- [33] D. Miyagi, S. Yamashita, and N. Takahashi, “Study of AC Loss Characteristics of HTS-coated Conductor with Magnetic Substrate Using FEM Analysis,” *J Supercond NovMagn*, vol. 24, pp. 43–48, 2011.
- [34] D. A. Nguyen, S. P. Ashworth, R. Duckworth, W. Carter, and S. Fleshler, “Measurements of AC Losses and Current Distribution in Superconducting Cables,” *IEEE Trans. Appl. Supercond.*, vol. 21, no. 3, pp. 996–1000, 2011.
- [35] H. Noji, “Numerical analysis of the AC losses of 500-m HTS power cable in Super-ACE project,” *Cryog. 47*, vol. 47, pp. 94–100, 2007.
- [36] J. Rieger, M. Leghissa, J. Wiezoreck, H. Kramer, G. Ries, and H. Neumuller, “AC losses in a flexible 10 m long conductor model for a HTS power transmission cable,” *Phys. C*, vol. 310, pp. 225–230, 1998.
- [37] M. Siahtrang, S. Fr´ed´eric, D. N Nguyen, and S. P Ashworth, “Assessment of alternative design schemes to reduce the edge losses in HTS power transmission cables made of coated,” *Supercond. Sci. Technol.*, vol. 14001, no. 25, pp. 1–8, 2012.
- [38] J. Choi, J. Choi, H. Kim, J. Cho, S. Kim, and A. High-temperature, “Manufacture and Insulating Test of a Mini-Model,” *IEEE Trans. Appl. Supercond.*, vol. 19, no. 3, pp. 1789–1792, 2009.
- [39] S. Mukoyama, M. Yagi, N. Fujiwara, and H. Ichikawa, “Conceptual design of 275 kV class high-T_c superconducting cable,” *Phys. C Supercond. its Appl.*, vol. 470, no. 20, pp. 1563–1566, 2010.
- [40] Y. Kim, D. Kwag, H. Kim, J. Cho, K. Seong, and S. Kim, “Research on Insulation Design of 22 . 9-kV High- T_c Superconducting Cable in Korea,” *IEEE Trans. POWER Deliv.*, vol. 20, no. 2, pp. 554–559, 2005.
- [41] D. S. Kwag, V. D. Nguyen, S. M. Baek, H. J. Kim, J. W. Cho, and S. H. Kim, “A Study on the Composite Dielectric Properties for an HTS Cable,” *IEEE Trans. Appl. Supercond.*, vol. 15, no. 2, pp. 1731–1734, 2005.
- [42] J. Choi *et al.*, “A Study on Insulation Characteristics of Laminated Polypropylene Paper for an HTS Cable,” *IEEE Trans. Applied Supercond.*, vol. 20, no. 3, pp. 1280–1283, 2010.
- [43] B. Zajaczkowski, A. J. M. Giesbers, M. Holtrust, E. Haenen, and R. Den Heijer, “Feasibility of inline cooling in long distance HTS power line,” *Cryogenics (Guildf.)*, vol. 51, no. 4, pp. 180–186, 2011.
- [44] A. Posada, Y. I. Kim, and V. Manousiouthakis, “On conduction-cooling of a high-temperature superconducting cable,” *Cryogenics (Guildf.)*, vol. 46, pp. 458–467, 2006.

- [45] S. P. Ashworth and D. W. Reagor, "A novel cooling scheme for superconducting power cables," *Cryogenics (Guildf)*, vol. 51, no. 4, pp. 161–167, 2011.
- [46] M. Furuse, S. Fuchino, and N. Higuchi, "Investigation of structure of superconducting power transmission cables with LN₂ counter-flow cooling," *Phys. C Supercond. its Appl.*, vol. 386, pp. 474–479, 2003.
- [47] J. A. Demko and R. C. Duckworth, "Cooling Configuration Design Considerations for Long-Length HTS Cables," *IEEE Trans Appl. Supercond.*, vol. 19, no. 3, pp. 1752–1755, 2009.
- [48] J. Fleiter, M. Sitko, and a. Ballarino, "Analytical formulation of I_c dependence on torsion of YBCO and BSCCO conductors," *IEEE Trans. Appl. Supercond.*, vol. 23, no. 3, pp. 3–6, 2013.
- [49] P. Skov-Hansen and Z. Han Nordic, "Stresses and strains in multi-filament hts tapes," *IEEE Trans. Appl. Supercond.*, vol. 9, no. 2, pp. 2617–2620, 1999.
- [50] C. W. Bumby, R. a Badcock, and N. J. Long, "Critical Current Behavior of HTS Roebel Cable Under Tensile Stress," *Appl. Supercond. IEEE Trans.*, vol. 23, no. 3, p. 4801805, 2013.
- [51] D. E. Daney *et al.*, "Single-phase AC losses in prototype HTS conductors for superconducting power transmission lines," *Phys. C*, vol. 310, pp. 236–239, 1998.
- [52] J. Yoo *et al.*, "Calculations of AC magnetic losses from the experimental field profiles in various types of coated conductors under applied fields," *J. Phys. Conf. Ser.*, vol. 97, no. 2, pp. 1341–1344, 2008.
- [53] W. Ta and Y. Gao, "Numerical simulation of the electro-thermo-mechanical behaviors of a high-temperature superconducting cable," *Compos. Struct.*, vol. 192, pp. 616–625, 2018.
- [54] X. Wang *et al.*, "Over-current characteristics of a 20-m-Long YBCO model cable," *IEEE Trans. Appl. Supercond.*, vol. 19, no. 3, pp. 1722–1726, 2009.
- [55] R. C. Duckworth *et al.*, "On the Effect of NiW on the Inductance and AC Loss of HTS Cables," *IEEE Trans. Applied Supercond.*, vol. 15, no. 2, pp. 1578–1582, 2005.
- [56] J. H. Kim *et al.*, "Investigation of the over current characteristics of HTS tapes considering the application for HTS power devices," *IEEE Trans. Appl. Supercond.*, vol. 18, no. 2, pp. 1139–1142, 2008.
- [57] L. J. Rostila *et al.*, "AC Losses and Current Sharing in an YBCO Cable," *IEEE Trans. Applied Supercond.*, vol. 17, no. 2, pp. 1688–1691, 2007.
- [58] O. Maruyama, T. Ohkuma, and T. Izumi, "Numerical analysis of heat transfer and fluid characteristics in long distance HTS cable," *Phys. Procedia*, vol. 45, pp. 285–288, 2013.
- [59] N. Magnusson and A. Wolfbrandt, "AC losses in high-temperature superconducting tapes exposed to longitudinal magnetic fields," *Cryogenics (Guildf)*, vol. 41, no. 2001, pp. 721–724, 2002.
- [60] M. Kalsia, R. S. Dondapati, and P. R. Usurumarti, "AC losses and dielectric losses in high temperature superconducting (HTS) power cables for smart grid

- applications: A comprehensive review,” *Int. J. Control Theory Appl.*, vol. 9, no. 41, pp. 309–317, 2016.
- [61] Epri, “Superconducting Cable Construction and Testing,” pp. 1–168, 2000.
- [62] P. Tixador, “Development of superconducting power devices in Europe,” *Phys. C Supercond. its Appl.*, vol. 470, no. 20, pp. 971–979, 2010.
- [63] J. F. Maguire *et al.*, “Progress and status of a 2G HTS power cable to be installed in the Long Island Power Authority (LIPA) grid,” *IEEE Trans. Appl. Supercond.*, vol. 21, no. 3, pp. 961–966, 2011.
- [64] J. F. Maguire *et al.*, “Development and demonstration of a HTS power cable to operate in the long island power authority transmission grid,” *IEEE Trans. Appl. Supercond.*, vol. 17, pp. 2034–2037, 2007.
- [65] F. Schmidt, J. Maguire, T. Welsh, and S. Bratt, “Operation Experience and further Development of a High- Temperature Superconducting Power Cable in the Long Island Power Authority Grid,” *Phys. Procedia*, vol. 36, pp. 1137–1144, 2012.
- [66] R. S. dole H. Yang, Hyung Suk; Dong Lak, Kim; Song Ho, Sohn; Ji Hyun, Lim; Ha Ok, Choi; Yeon Suk, Choi; Byoung Seob, Lee; Won Moog, Jung; Hee Suk, “Long Term Performance Test of KEPCO HTS Power Cable,” *IEEE Trans. Appl. Supercond.*, vol. 19, no. 3, pp. 1782–1784, 2009.
- [67] S. J. Lee, M. Park, I. K. Yu, Y. Won, Y. Kwak, and C. Lee, “Recent Status and Progress on HTS Cables for AC and DC Power Transmission in Korea,” *IEEE Trans. Appl. Supercond.*, vol. 28, no. 4, pp. 1–5, 2018.
- [68] S. H. Sohn *et al.*, “The results of installation and preliminary test of 22.9 kV, 50 MVA, 100 m class HTS power cable system at KEPCO,” *IEEE Trans. Appl. Supercond.*, vol. 17, no. 2, pp. 2043–2046, 2007.
- [69] F. Herzog, T. Kutz, M. Stemmler, and T. Kugel, “Cooling unit for the AmpaCity project – One year successful operation,” *Cryogenics*, vol. 80, pp. 204–209, 2016.
- [70] S. Honjo *et al.*, “Status of superconducting cable demonstration project in Japan,” *IEEE Trans. Appl. Supercond.*, vol. 21, no. 3, pp. 967–971, 2011.
- [71] H. Yumura *et al.*, “Update of YOKOHAMA HTS cable project,” *IEEE Trans. Appl. Supercond.*, vol. 23, no. 3, 2013.
- [72] T. Masuda *et al.*, “A New HTS Cable Project in Japan,” *IEEE Trans. Applied Supercond.*, vol. 19, no. 3, pp. 1735–1739, 2009.
- [73] H. X. Xi *et al.*, “China ’ s 33 . 5 m , 35 kV / 2 kA HTS ac power cable ’ s operation in power grid,” *Phys. C*, vol. 448, pp. 1054–1057, 2006.
- [74] S. J. Lee, M. Park, I. K. Yu, Y. Won, Y. Kwak, and C. Lee, “Recent Status and Progress on HTS Cables for AC and DC Power Transmission in Korea,” *IEEE Trans. Appl. Supercond.*, vol. 28, no. 4, pp. 1–5, 2018.
- [75] T. Masuda *et al.*, “Fabrication and Installation Results for Albany HTS Cable,” *IEEE Trans. Appl. Supercond.*, vol. 17, no. 2, pp. 1648–1651, 2007.
- [76] C. S. Weber, C. T. Reis, a. Dada, T. Masuda, and J. Moscovic, “Overview of the underground 34.5 kV HTS power cable program in Albany, NY,” *IEEE Trans.*

- Appl. Supercond.*, vol. 15, no. 2, pp. 1793–1797, 2005.
- [77] S. Mukoyama *et al.*, “Manufacturing and Installation of the World ’ s Longest HTS Cable in the Super-ACE Project,” *IEEE Trans. Appl. Supercond.*, vol. 15, no. 2, pp. 1763–1766, 2005.
- [78] S. Honjo, K. Matsuo, T. Mimura, and Y. Takahashi, “High- T c superconducting power cable development,” *Phys. C*, vol. 360, pp. 1234–1240, 2001.
- [79] Y. Wang *et al.*, “A Novel Approach for Design of DC HTS Cable,” *IEEE Trans. Applied Supercond.*, vol. 21, no. 3, pp. 1042–1045, 2011.
- [80] a. P. Malozemoff, J. Yuan, and C. M. Rey, *High-temperature superconducting (HTS) AC cables for power grid applications*. Elsevier Ltd, 2015.
- [81] J. F. Maguire *et al.*, “Development and Demonstration of a Long Length Transmission Voltage Cold Operate in the Long Island Power Authority,” *IEEE Trans. Applied Supercond.*, vol. 17, no. 2, pp. 1–13, 2007.
- [82] Y. Zheng, Y. Wang, W. Pi, P. Ju, and Y. Wang, “Current Distribution among Layers of Single Phase HTS Cable Conductor,” *Phys. C SUPER Conduct.*, no. September, 2014.
- [83] A. N. Ozcivan, K. Shimoyama, S. Soeda, T. Yagai, M. Tsuda, and T. Hamajima, “AC loss in a tri-axial HTS cable with balanced current distribution,” *Phys. C*, vol. 468, pp. 2033–2036, 2008.
- [84] Y.-S. Choi, S.-W. Yim, J. Sim, H.-R. Kim, S.-H. Sohn, and S.-D. Hwang, “Application of IPTs to HTS Cable Conductor for Uniform Current Distribution Between Their Layers,” *IEEE Trans. Applied Supercond.*, vol. 15, no. 2, pp. 1739–1742, 2005.
- [85] W. T. Norris, “Calculation of hysteresis losses in hard superconductors carrying ac: Isolated conductors and edges of thin sheets,” *J. Phys. D. Appl. Phys.*, vol. 3, no. 4, pp. 489–507, 1970.
- [86] J. A. Demko, J. W. Lue, M. J. Gouge, J. P. Stovall, U. Sinha, and R. L. Hughey, “Practical AC Loss and Thermal Considerations for HTS Power Transmission Cable Systems,” *IEEE Trans Appl. Supercond.*, vol. 11, no. 1, pp. 1789–1792, 2001.
- [87] J. Voccio, J. H. Kim, and S. Pamidi, “Study of AC losses in a 1-m long, HTS power cable made from wide 2G tapes,” *IEEE Trans. Appl. Supercond.*, vol. 22, no. 3, p. 5800304, 2012.
- [88] G. Coletta *et al.*, “Application of Electrical and Calorimetric Methods to the AC Loss Characterization of Cable Conductors,” *IEEE Trans. Appl. Supercond.*, vol. 9, no. 2, pp. 1053–1056, 2008.
- [89] C. N. Rasmussen *et al.*, “First operation experiences from a 30 kV , 104 MVA HTS power cable installed in a utility substation,” vol. 376, pp. 1571–1579, 2002.
- [90] M. Yagi, “Measurement of AC losses in an HTS conductor by calorimetric method,” *Phys. B Phys. Condens. Matter*, vol. 396, pp. 1124–1128, 2003.
- [91] V. E. Sytnikov, K. A. Shutov, N. V Polyakova, S. S. Fetisov, A. A. Nosov, and V. S. Vysotsky, “The AC Loss Analysis in the 5 m HTS Power Cables,” *IEEE Trans. Appl. Supercond.*, vol. 19, no. 3, pp. 1706–1709, 2009.

- [92] J. Ogawa *et al.*, “Dependence of AC Loss With a Phase Difference Between Transport Current and Applied Magnetic Field,” *IEEE Trans. Appl. Supercond.*, vol. 16, no. 2, pp. 115–118, 2006.
- [93] C. Træholt, E. Veje, F. Gøromøry, M. Døaumling, and O. Tønnesen, “Contactless electrical measurements of transport ac losses in a 3 m long superconducting cable,” *Supercond. Sci. Technol.*, vol. 898, pp. 2–6, 2002.
- [94] H. M. Wen, L. Z. Lin, Y. B. Lin, Z. Y. Gao, S. T. Dai, and L. Shu, “AC losses measurement of 1 m long HTS cable,” *Phys. C*, vol. 386, pp. 52–55, 2003.
- [95] J. Zhu *et al.*, “A Novel AC Loss Measurement Technology for High Temperature Superconducting Cable With Large Current Capacity Using a Compensation Coil,” *IEEE Trans. Applied Supercond.*, vol. 25, no. 3, pp. 3–6, 2015.
- [96] S. Mukoyama *et al.*, “Study on AC loss measurements of HTS power cable for standardizing,” *J. Phys. Conf. Ser.*, vol. 897, no. 1, pp. 1–8, 2017.
- [97] L. Hu *et al.*, “Transport current losses in Bi2223 high temperature superconductors,” *Phys. C*, vol. 396, pp. 1107–1112, 2003.
- [98] H. Kim, K. Sim, J. Cho, S. Kim, J. H. Kim, and H. Y. Jung, “Characteristics of the joint mini-model high temperature superconducting cable,” *Phys. C*, vol. 468, pp. 2028–2032, 2008.
- [99] S. Elschner *et al.*, “New Experimental Method for Investigating AC Losses in Concentric HTS Power Cables,” *IEEE Trans. Appl. Supercond.*, vol. 25, no. 3, pp. 1–5, 2015.
- [100] J. Joo *et al.*, “Characteristics Measurements of HTS Tape with Parallel HTS Tapes,” *IEEE Trans. Applied Supercond.*, vol. 16, no. 2, pp. 119–122, 2006.
- [101] M. Daibo, K. Watanabe, K. Akashi, and H. Hidaka, “Development of a 66 kV-5 kA Class HTS Power Cable With IBAD / PLD REBCO Tapes,” *Phys. Procedia*, vol. 58, pp. 314–317, 2014.
- [102] Y. H. Ma, Z. Y. Li, H. B. Jin, K. Ryu, S. H. Sohn, and S. D. Hwang, “AC loss characteristics of a hex-cable in an azimuthal external AC magnetic field,” *Phys. C Supercond. its Appl.*, vol. 469, no. 15–20, pp. 1722–1725, 2009.
- [103] S. Kim, K. W. Ryu, D. H. Huh, H. J. Kim, J. Joo, and K. J. Song, “Effect of AC Magnetic Field on Transport Current Loss of HTS Tapes,” *IEEE Trans. Applied Supercond.*, vol. 14, no. 2, pp. 646–649, 2004.
- [104] S. Tanaka, T. Hara, K. Miyoshi, N. Ichiyangi, Y. Tanakat, and H. Ishiis, “66 kV-2 kA peak load test of high-T_c superconducting model cable,” *Cryogenics (Guildf.)*, vol. 36, no. 8, pp. 589–598, 1996.
- [105] N. Magnusson, “Semi-empirical model of the losses in HTS tapes carrying AC currents in AC magnetic fields applied parallel to the tape face,” *Phys. C*, vol. 349, pp. 225–234, 2001.
- [106] S. Yamasaki *et al.*, “Transport and AC loss properties of the repaired multifilamentary REBCO superconducting tapes,” *Phys. C Supercond. its Appl.*, vol. 470, no. 20, pp. 1316–1320, 2010.
- [107] M. Siahraang, F. edric Sirois, F. Grilli, S. Babic, and S. Brault, “A new numerical

- approach to find current distribution and AC losses in coaxial assembly of twisted HTS tapes in single layer arrangement,” *J. Phys. Conf. Ser.*, vol. 22034, no. 234, pp. 1–8, 2010.
- [108] M. J. Gouge *et al.*, “Tests of Tri-Axial HTS Cables,” *IEEE Trans. Appl. Supercond.*, vol. 15, no. 2, pp. 1827–1830, 2005.
- [109] S. Safran, J. Šouc, F. Gömöry, P. Kovac, and A. Gencer, “Experimentally Determined Magnetization ac Losses of Mono and Multifilamentary MgB 2 Wires,” *J Supercond NovMagn*, vol. 26, pp. 1557–1561, 2013.
- [110] A. Frank, R. Heller, W. Goldacker, A. Kling, and C. Schmidt, “Roebel Assembled Coated Conductor Cables (RACC): Ac-Losses and Current Carrying Potential,” *J. Phys. Conf. Ser.*, vol. 97, no. 12147, 2008.
- [111] K. Miyoshi *et al.*, “AC Losses of HTS Power Transmission Cables Using Bi-2223 Tapes with Twisted Filaments,” *IEEE Trans. Applied Supercond.*, vol. I, no. 1, pp. 2192–2195, 2001.
- [112] S. Zannella *et al.*, “AC Losses in Transport Current Regime in Applied AC Magnetic Field: Experimental Analysis and Modeling,” *IEEE Trans Appl. Supercond.*, vol. I, no. I, pp. 1–4, 2001.
- [113] J. Kováč, J. Šouc, and P. Kováč, “Experimental study of the AC magnetization loss in MgB 2 superconducting wires at different temperatures,” *Phys. B Phys. Condens. Matter*, vol. 475, pp. 1–4, 2012.
- [114] L. S. Lakshmi *et al.*, “Magnetic and Transport AC Losses in HTS Roebel Cable,” *IEEE Trans. Applied Supercond.*, vol. 21, no. 3, pp. 3311–3315, 2011.
- [115] T. Famakinwa, Q. M. Chen, and S. Yamaguchi, “3D finite element analysis of eddy current losses of HTS tapes—Self field analysis,” *Phys. C Supercond. its Appl.*, vol. 434, no. 1, pp. 71–78, Feb. 2006.
- [116] Z. Hong, L. Ye, Y. Jiang, R. Pei, A. M. Campbell, and T. Coombs, “A two-dimensional finite element method to calculate the AC loss in superconducting cables , wires and coated conductors,” *J. Phys. Conf. Ser.*, vol. 97, no. 12117, pp. 1–6, 2008.
- [117] F. Grilli and M. Šj̄ ostr̄ Om, “Prediction of resistive and hysteretic losses in a multi-layer high- T c superconducting cable,” *Supercond. Sci. Technol.*, vol. 409, 2004.
- [118] T. Famakinwa, Q. M. Chen, and S. Yamaguchi, “3D finite element analysis of eddy current loss of HTS tapes – External field analysis,” *Phys. C Supercond.*, vol. 459, pp. 18–23, 2007.
- [119] B. Shen *et al.*, “Investigation and comparison of AC losses on stabilizer-free and copper stabilizer HTS tapes,” *Phys. C Supercond. its Appl.*, vol. 541, pp. 40–44, 2017.
- [120] B. Shen *et al.*, “Investigation of AC losses in horizontally parallel HTS tapes,” *Supercond. Sci. Technol.*, vol. 30, no. 7, 2017.
- [121] B. Shen, T. Coombs, and F. Grilli, “Investigation of AC Loss in HTS Cross-Conductor Cables for Electrical Power Transmission,” *IEEE Trans. Appl. Supercond.*, vol. 29, no. 2, p. 1, 2019.

- [122] V. V. Zubko, S. S. Fetisov, and V. S. Vysotsky, "Hysteresis Losses Analysis in 2G HTS Cables," *IEEE Trans. Appl. Supercond.*, vol. 26, no. 3, pp. 1–5, 2016.
- [123] M. D. Ainslie, T. J. Flack, and A. M. Campbell, "Calculating transport AC losses in stacks of high temperature superconductor coated conductors with magnetic substrates using FEM," *Phys. C*, vol. 472, no. 1, pp. 50–56, 2012.
- [124] M. K. Song, S. J. Lee, and J. W. Cho, "Research on the Eddy Current Losses in the Stabilizer and Outer-Cryostats of the High-Tc Superconducting Power Cable System," *IEEE Trans. Appl. Supercond.*, vol. 16, no. 2, pp. 1610–1613, 2006.
- [125] E. Demencik *et al.*, "AC magnetization loss and transverse resistivity of striated YBCO coated conductors," *IEEE Trans. Appl. Supercond.*, vol. 25, no. 3, pp. 3–7, 2015.
- [126] M. Majoros, M. D. Sumption, E. W. Collings, and D. C. Van Der Laan, "Magnetization losses in superconducting YBCO conductor-on-round-core (CORC) cables," *Supercond. Sci. Technol.*, vol. 27, no. 12, pp. 1–12, 2014.
- [127] V. M. R. Zermeno, A. B. Abrahamsen, N. Mijatovic, B. B. Jensen, and M. P. Sørensen, "Calculation of alternating current losses in stacks and coils made of second generation high temperature superconducting tapes for large scale applications," *J. Appl. Phys.*, vol. 114, no. 17, pp. 173901–7, 2013.
- [128] J. Sheng, M. Vojenčiak, R. Terzioğlu, L. Frolek, and F. Gömöry, "Numerical Study on Magnetization Characteristics of Superconducting Conductor on Round Core Cables," *IEEE Trans Appl. Supercond.*, vol. 27, no. 4, pp. 1–5, 2017.
- [129] Y. Wang, S. Venuturumilli, J. Sheng, and A. High-temperature, "Influence of Harmonic Current on Magnetization Loss of a Triaxial CORC REBCO Cable for Hybrid," *IEEE Trans. Appl. Supercond.*, vol. 28, no. 4, pp. 4–8, 2018.
- [130] H. Noji, "Numerical study on self-field losses of 30 m BSCCO HTS transmission cable," *Cryogenics (Guildf.)*, vol. 49, no. 1, pp. 34–38, 2009.
- [131] H. Noji, K. Haji, and T. Hamada, "AC loss analysis of 114 MVA high-Tc superconducting model cable," *Phys. C Supercond.*, vol. 392–396, pp. 1134–1139, Oct. 2003.
- [132] H. Noji, K. Haji, and T. Hamada, "Alternating current loss calculation in a high- T C superconducting transmission cable considering the magnetic field," *Supercond. Sci. Technol.*, vol. 16, pp. 14–18, 2003.
- [133] F. Grilli, S. Stavrev, B. Dutoit, and S. Spreafico, "Numerical Analysis of the Effects of the Magnetic Self-Field on the Transport Properties of a Multilayer HTS Cable," *IEEE Trans. Appl. Supercond.*, vol. 14, no. 1, pp. 94–102, 2004.
- [134] S. Sato and N. Amemiya, "Electromagnetic Field Analysis of YBCO Coated," *IEEE Trans. Applied Supercond.*, vol. 16, no. 2, pp. 127–130, 2006.
- [135] L. Dresner, "Incomplete-penetration hysteresis losses in transmission line cables," *Phys. B Phys. Condens. Matter*, vol. 310, pp. 213–217, 1998.
- [136] A. P. Malozemoff, G. Snitchler, and Y. Mawatari, "Tape-Width Dependence of AC Losses in HTS Cables," *IEEE Trans. Applied Supercond.*, vol. 19, no. 3, pp. 3115–3118, 2009.

- [137] H. Noji, K. Ikeda, K. Uto, and T. Hamada, "Numerical analysis of the AC loss in a high- T C superconducting cable measured by calorimetric method," *Phys. C*, vol. 425, pp. 97–100, 2005.
- [138] N. Bykovsky, G. De Marzi, D. Uglietti, P. Bruzzone, and L. Muzzi, "Magnetization loss for stacks of ReBCO tapes," *Supercond. Sci. Technol.*, vol. 30, no. 24010, pp. 1–10, 2017.
- [139] J. Ogawa, S. Fukui, M. Yamaguchi, T. Sato, and O. Tsukamoto, "Magnetization loss in a striated YBCO coated conductor considering the intrinsic critical current distribution," *IEEE Trans. Appl. Supercond.*, vol. 16, no. 2, pp. 111–114, 2006.
- [140] D. Miyagi, H. Kawasaki, O. Tsukamoto, S. Honjo, and Y. Takahashi, "AC loss characteristics of an assembled conductor of round Bi2223 Ag sheathed wires," *Phys. C*, vol. 376, pp. 1727–1729, 2002.
- [141] S. Fukui and O. T. b Takeshi Noguchi a, Jun Ogawa a, Mitsugi Yamaguchi a, Takao Sato a, "Analysis of AC loss and current distribution in multi-layer tri-axial three-phase HTS cable," *Phys. C*, vol. 431, pp. 1374–1379, 2005.
- [142] N. Amemiya, N. Enomoto, and S. Shirai, "FEM analysis of AC loss in twisted Bi-2223 multifilamentary tapes carrying AC transport current in AC transverse magnetic field with arbitrary orientation," *IEEE Trans. Appl. Supercond.*, vol. 14, no. 2, pp. 782–785, 2004.
- [143] M. Takayasu, J. V. Minervini, L. Bromberg, M. K. Rudziak, and T. Wong, "Investigation of twisted stacked-tape cable conductor," *AIP Conf. Proc.*, vol. 1435, no. June 2012, pp. 273–280, 2012.
- [144] L. Chiesa, N. C. Allen, and M. Takayasu, "Electromechanical Investigation of 2G HTS Twisted Stacked-Tape Cable Conductors," *IEEE Trans. Appl. Supercond.*, vol. 24, no. 3, p. 6600405, 2014.
- [145] J. R. Clem and A. P. Malozemoff, "Theory of ac loss in power transmission cables with second generation high high temperature superconductor wires," *Supercond. Sci. Technol.*, vol. 23, no. 34014, pp. 1–6, 2010.
- [146] S. Choi and W. Nah, "The AC Loss Estimation of Bi-2223 / Ag Superconductor Tapes in Polygonal Configuration," *IEEE Trans. Applied Supercond.*, vol. 20, no. 3, pp. 2107–2110, 2010.
- [147] S. Fukui *et al.*, "Numerical Analysis of AC Loss Characteristics of Multi-Layer HTS Cable Assembled by Coated Conductors," *IEEE Trans. Applied Supercond.*, vol. 19, no. 3, pp. 1714–1717, 2009.
- [148] T. Tsukamoto, T. Mifune, Y. Sogabe, Z. Jiang, T. Nakamura, and N. Amemiya, "Influence of Geometrical Configurations of HTS Roebel Cables on Their AC Losses," *IEEE Trans. Appl. Supercond.*, vol. 25, no. 3, 2015.
- [149] H. Zhang *et al.*, "Electromagnetic Analysis of YBCO Superconducting Cables with High Current Transporting for Electric Devices," *IEEE Trans. Appl. Supercond.*, vol. 26, no. 7, 2016.
- [150] S. Schuller, W. Goldacker, A. Kling, L. Krempasky, and C. Schmidt, "Ac-loss measurement of a DyBCO-Roebel assembled coated conductor cable (RACC)," *Phys. C*, vol. 465, pp. 761–765, 2007.

- [151] G. Vyas, R. S. Dondapati, and P. R. Usurumarti, "Parametric Evaluation of AC Losses in 500 MVA/1.1 kA High Temperature Superconducting (HTS) Cable for Efficient Power Transmission: Self Field Analysis," in *Modelling Symposium (EMS), 2014 European*, 2014, pp. 315–319.
- [152] Y. Wang, H. Liu, H. Zhang, and Y. Zheng, "A conceptual design for HTS cable with large current capacity using co-axial configurations," *IEEE Trans. Appl. Supercond.*, vol. 20, no. 3, pp. 1263–1267, 2010.
- [153] M. A. Young *et al.*, "An Investigation of the Current Distribution in the Triaxial Cable and Its Operational Impacts on a Power System," *IEEE Trans. Appl. Supercond.*, vol. 15, no. 2, pp. 1751–1754, 2005.
- [154] P. W. Fisher *et al.*, "Design, analysis, and fabrication of a tri-axial cable system," *IEEE Trans. Appl. Supercond.*, vol. 13, no. 2 II, pp. 1938–1941, 2003.
- [155] M. J. Gelabert-Serra, a. Sumper, X. Granados, a. Sudria-Andreu, and J. Rull-Duran, "Dynamic simulation of HTSC cables with a conventional simulation program," *IEEE Trans. Appl. Supercond.*, vol. 21, no. 3, pp. 1025–1029, 2011.
- [156] N. J. Kelley *et al.*, "Field demonstration of a 24-kV warm dielectric HTS cable," *IEEE Trans. Appl. Supercond.*, vol. 11, no. I, pp. 2461–2467, 2001.
- [157] M. Nassi, N. Kelley, P. Ladié, P. Corsaro, G. Coletta, and D. Von Dollen, "Qualification results of a 50 m-115 kV warm dielectric cable system," *IEEE Trans. Appl. Supercond.*, vol. 11, no. I, pp. 2355–2358, 2001.
- [158] S. T. Dai, F. Y. Zhang, X. Xu, G. Li, L. F. Li, and L. Y. Xiao, "The three-phase 75 m long HTS power cable," *Cryogenics (Guildf.)*, vol. 47, pp. 402–405, 2007.
- [159] K. Shimoyama *et al.*, "Experimental results of tri-axial HTS cable," *Cryogenics (Guildf.)*, vol. 49, no. 8, pp. 398–401, 2009.
- [160] J. Zhu, X. Bao, L. Guo, Z. Xia, M. Qiu, and W. Yuan, "Optimal design of current sharing in transmission conductors of a 110 kV/3 kA cold dielectric superconducting cable consisted of YBCO tapes," *IEEE Trans. Appl. Supercond.*, vol. 23, no. 3, p. 5402505, 2013.
- [161] J. Zhu, M. Qiu, X. Lai, and X. Chen, "Modeling and Analysis of the Power Transmission with an 110kV / 3kA HTS Cable in a Meshed Grid," no. 2, 2014.
- [162] K. Sim, S. Kim, J. Cho, H. Jang, and S. Hwang, "Design and current transporting characteristics of 80 kV direct current high Temperature superconducting cable core," *IEEE Trans. Appl. Supercond.*, vol. 23, no. 3, 2013.
- [163] G. Del-Rosario-Calaf, J. Lloberas-Valls, A. Sumper, X. Granados, and R. Villafafila-Robles, "Modeling of second generation HTS cables for grid fault analysis applied to power system simulation," *IEEE Trans. Appl. Supercond.*, vol. 23, no. 3, pp. 3–6, 2013.
- [164] L. Rostila, J. Lehtonen, M. Masti, and R. Mikkonen, "Circuit analysis model for AC losses of superconducting YBCO cable," *Cryogenics (Guildf.)*, vol. 46, pp. 245–251, 2006.
- [165] D. Miyagi *et al.*, "3-D FEM Analysis of Effect of Twist Pitch and Shielding Layer on Multi-Layered HTS Power Cable," *IEEE Trans. Appl. Supercond.*, vol. 16, no. 2,

pp. 1614–1617, 2006.

- [166] O. Chevtchenko, R. Zuijderduin, J. Smit, I. Melnik, and A. Geschiere, “Low AC loss in a 3 kA HTS cable of the Dutch project,” *Phys. Procedia*, vol. 36, pp. 1285–1289, 2012.
- [167] S. Ha, C. Kim, S. Kim, and M. Dinh, “Design and PHILS-based Transient Analysis of a Tri-axial HTS,” *Phys. Procedia*, vol. 58, pp. 318–321, 2014.
- [168] O. Maruyama, T. Ohkuma, T. Masuda, M. Ohya, S. Mukoyama, and M. Yagi, “Development of REBCO HTS power cables,” *Phys. Procedia*, vol. 36, pp. 1153–1158, 2012.
- [169] T. Sudheer, M. Sarkar, A. S. Gour, V. V. Rao, and B. N. Rao, “Development and testing of a high temperature superconducting (HTS) cable for smart grid applications,” *2017 3rd Int. Conf. Cond. Assess. Tech. Electr. Syst. CATCON 2017 - Proc.*, vol. 2018–Janua, pp. 197–201, 2018.
- [170] T. Kitamura *et al.*, “Development of Tri-axial superconducting cable system for type test,” *J. Phys. Conf. Ser.*, vol. 1054, no. 1, p. 12075, 2018.
- [171] T. Masuda *et al.*, “Design and Experimental Results for Albany HTS Cable,” *IEEE Trans. Appl. Supercond.*, vol. 15, no. 2, pp. 1806–1809, 2005.
- [172] H. Yumura *et al.*, “HTS cable design and evaluation in YOKOHAMA Project,” *J. Phys. Conf. Ser.*, vol. 234, no. PART 3, 2010.
- [173] S. Mukoyama, “Study of an YBCO HTS transmission cable system,” *Phys. C*, vol. 465, pp. 1150–1153, 2007.
- [174] M. Yagi, S. Mukoyama, N. Amemiya, S. Nagaya, N. Kashima, and Y. Shiohara, “Development of YBCO HTS cable with low AC loss,” *Phys. C*, vol. 468, pp. 2037–2040, 2008.
- [175] M. Yagi, S. Mukoyama, and N. Amemiya, “Development of a 10 m long 1 kA 66 / 77 kV YBCO HTS cable with low AC loss and a joint with low electrical resistance,” *Supercond. Sci. Technol.*, vol. 22, no. 85003, 2009.
- [176] J. X. Jin *et al.*, “HTS Power Devices and Systems : Principles , Characteristics, Performance, and Efficiency,” *IEEE Trans. Appl. Supercond.*, vol. 26, no. 7, 2016.
- [177] J. C. Prestigiacomo, R. C. Y. Auyeung, and M. S. Osofsky, “Process for scalable fabrication of low AC loss HTS conductors,” *Supercond. Sci. Technol.*, vol. 31, no. 11, 2018.
- [178] M. Yagi *et al.*, “Recent development of an HTS power cable using YBCO tapes,” *Phys. C*, vol. 465, pp. 1154–1158, 2007.
- [179] D. Miyagi, N. Takata, and N. Takahashi, “Thermal Analysis of Co-Axial Multi-Layered,” *IEEE Trans. Appl. Supercond.*, vol. 21, no. 3, pp. 991–995, 2011.
- [180] J. G. Kim *et al.*, “HTS power cable model component development for PSCAD/EMTDC considering conducting and shield layers,” *IEEE Trans. Appl. Supercond.*, vol. 19, no. 3, pp. 1785–1788, 2009.
- [181] J. G. Kim *et al.*, “Development of a PSCAD/EMTDC model component for AC loss characteristic analysis of HTS power cable,” *IEEE Trans. Appl. Supercond.*, vol. 20,

- no. 3, pp. 1284–1287, 2010.
- [182] J. Bae, S. Choi, S. Lee, K. Sim, J. Cho, and H. Kim, “The Stability Evaluation on HTS Power Cable,” *IEEE Trans. Appl. Supercond.*, vol. 18, no. 2, pp. 1289–1292, 2008.
- [183] F. Grilli and A. Kario, “How filaments can reduce AC losses in HTS coated conductors: A review,” *Supercond. Sci. Technol.*, vol. 29, no. 8, pp. 1–15, 2016.
- [184] M. Wang *et al.*, “An effective way to reduce AC loss of second-generation high temperature superconductors,” *Supercond. Sci. Technol.*, vol. 32, no. 1, p. 01LT01, 2018.
- [185] T. Wass and S. P. Hörnfeldt, “AC Losses in HTS Tapes in Applied Longitudinal Magnetic Fields at Variable Temperatures,” *IEEE Trans. Appl. Supercond.*, vol. 14, no. 1, pp. 22–27, 2004.
- [186] J. W. Lue, M. S. and Lubell, and M. J. Tomsic, “AC Losses of HTS Tapes and Bundles with De-Coupling Barriers,” *IEEE Trans. Applied Supercond.*, vol. 9, no. June, pp. 793–796, 1999.
- [187] J. W. Lue *et al.*, “AC Losses of Prototype HTS Transmission Cables,” *IEEE Trans. Appl. Supercond.*, vol. 9, no. 2, pp. 416–419, 1999.
- [188] X. Z. Zhang, X. H. Zong, Y. W. Han, X. Tian, X. H. Lu, and Z. G. Yu, “Research of the loss of the corrugated stainless steel pipe in HTS cable,” *2015 IEEE Int. Conf. Appl. Supercond. Electromagn. Devices, ASEMD 2015 - Proc.*, no. 1, pp. 576–577, 2016.
- [189] P. J. Lee, M. Park, H. Lim, and H. G. Lee, “Magnetization Loss and Shield Effect in Multi-Stacked Tapes With Various Stacking Configurations,” *Appl. Supercond. IEEE Trans.*, vol. 16, no. 2, pp. 131–134, 2006.
- [190] Y. Xie *et al.*, “Second-Generation HTS Conductor Design and Engineering for Electrical Power Applications,” *IEEE Trans Appl. Supercond.*, vol. 19, no. 3, pp. 3009–3013, 2009.
- [191] L. S. Lakshmi, K. P. Thakur, M. P. Staines, R. A. Badcock, and N. J. Long, “Magnetic AC Loss Characteristics of 2G Roebel Cable,” *IEEE Trans. Appl. Supercond.*, vol. 19, no. 3, pp. 3361–3364, 2009.
- [192] O. Tsukamoto, K. Yamagishi, J. Ogawa, M. Murakami, and M. Tomita, “Mechanism of decay of trapped magnetic field in HTS bulk caused by application of AC magnetic field,” *J. Mater. Process. Technol.*, vol. 161, pp. 52–57, 2005.
- [193] J. Ogawa, S. Fukui, T. Oka, T. Ogawa, and M. Sugai, “AC loss distribution in two-layer HTS cable,” *IEEE Trans. Appl. Supercond.*, vol. 28, no. 3, pp. 3–6, 2018.
- [194] A. N. Petrov, J. A. Pilgrim, and I. O. Golosnoy, “Revisiting the homogenized domain model for fast simulation of AC transport power losses in first generation high temperature superconducting tapes and cables,” *Phys. C Supercond. its Appl.*, vol. 557, no. November 2018, pp. 33–40, 2019.
- [195] G. Escamez *et al.*, “Numerical Modelling of AC Hysteresis Losses in HTS Tubes,” *IEEE Trans. Appl. Supercond.*, vol. 25, no. 3, pp. 3–7, 2015.
- [196] S. Yildiz, F. Inanir, A. Cicek, and F. Gomory, “Numerical study of AC loss of two-

- layer HTS power transmission cables composed of coated conductors with a ferromagnetic substrate,” *Turkish J. Electr. Eng. Comput. Sci.*, vol. 25, no. 5, pp. 3528–3539, 2017.
- [197] Y. Wu, Z. Chen, G. Geng, J. Fang, and Y. Liu, “AC Losses analysis of HTS composite conductors with different current ramp rates,” *IEEE Trans. Appl. Supercond.*, vol. 29, no. 2, pp. 1–5, 2019.
- [198] Y. Wang, M. Zhang, F. Grilli, Z. Zhu, and W. Yuan, “Study of the magnetization loss of CORC® cables using a 3D T-A formulation,” *Supercond. Sci. Technol.*, vol. 32, no. 2, p. 25003, 2019.
- [199] N. Duan, W. Xu, S. Wang, and J. Zhu, “Current Distribution Calculation of Superconducting Layer in HTS Cable Considering Magnetic Hysteresis by Using XFEM,” *IEEE Trans. Magn.*, vol. 54, no. 3, pp. 1–4, 2018.
- [200] S. V Samoilenov *et al.*, “Design versions of HTS three-phase cables with the minimized value of AC losses,” *J. Phys. Conf. Ser.*, vol. 969, p. 12049, 2018.
- [201] W. J. Kim, S. H. Kim, H. J. Kim, J. W. Cho, J. S. Lee, and H. G. Lee, “The fundamental characteristics of PPLP as insulating material for HTS DC cable,” *IEEE Trans. Appl. Supercond.*, vol. 23, no. 3, pp. 3–6, 2013.
- [202] C. Peng *et al.*, “Insulation characteristics of dielectric material for CD HTS cable,” *IEEE Trans. Appl. Supercond.*, vol. 29, no. 2, p. 1, 2019.
- [203] R. Wesche, A. Anghel, B. Jakob, G. Pasztor, and R. Schindler, “Design of superconducting power cables,” *Cryogenics (Guildf.)*, vol. 39, pp. 767–775, 1999.
- [204] J. Oestergaard, J. Okholm, K. Lomholt, and O. Toennesen, “Energy losses of superconducting power transmission cables in the grid,” *IEEE Trans. Applied Supercond.*, vol. 11, no. 1, pp. 2375–2378, Mar. 2001.
- [205] H. J. Kim, D. S. Kwag, Y. S. Kim, and S. H. Kim, “Electrical characteristics of high- T_c superconducting mini-model cable under mechanical stresses in liquid nitrogen,” vol. 45, pp. 45–50, 2005.
- [206] M. Furuse and S. Fuchino, “Analysis and measurement of thermal conductivity of polypropylene laminated paper impregnated with subcooled liquid nitrogen,” *Cryogenics (Guildf.)*, vol. 63, pp. 125–128, 2014.
- [207] D. S. Kwag, J. W. Choi, H. J. Kim, J. W. Cho, and S. H. Kim, “Research on insulation design method of a cold dielectric type superconducting cable,” *Phys. C*, vol. 468, pp. 2023–2027, 2008.
- [208] Y. Kikuchi *et al.*, “Partial discharge characteristics in composite insulation systems with PPLP® for HTS cable,” *IEEE Trans. Dielectr. Electr. Insul.*, vol. 22, no. 2, pp. 1025–1030, 2015.
- [209] J. Šouc *et al.*, “Superconducting HTS coil made from round cable cooled by liquid nitrogen flow,” *Supercond. Sci. Technol.*, vol. 30, no. 10, 2017.
- [210] Y. Zhang, T. Lehner, T. Fukushima, H. Sakamoto, and D. Hazelton, “Progress in production and performance of second generation (2G) HTS wire for practical applications,” *2013 IEEE Int. Conf. Appl. Supercond. Electromagn. Devices*, vol. 24, no. 5, pp. 557–558, 2013.

- [211] R. Soika, F. Schmidt, and A. Allais, "Mechanical requirements for superconducting tapes in HTS power cable applications," *IEEE Trans. Appl. Supercond.*, vol. 17, no. 2, pp. 1730–1733, 2007.
- [212] J. A. Demko *et al.*, "Cryostat Vacuum Thermal Considerations for HTS Power Transmission Cable Systems," *IEEE Trans. Applied Supercond.*, vol. 13, no. 2, pp. 1930–1933, 2003.
- [213] D. Kottonau, E. Shabagin, M. Noe, and S. Grohmann, "Opportunities for High Voltage AC Superconducting Cables as Part of New Long - distance Transmission Lines," *IEEE Trans Appl. Supercond.*, vol. 8223, pp. 1–5, 2017.
- [214] D. Horita, K. Agatsuma, A. Ishiyama, T. Masuda, T. Morimura, and T. Mimura, "Comparison between Simulation and Experimental Results of Liquid Nitrogen Coolant Distribution in a 66-kV 40-m Model HTS Power Cable System Experiencing Short-Circuit Accidents," *IEEE Trans. Appl. Supercond.*, vol. 29, no. 5, pp. 1–5, 2019.
- [215] V. S. Vyatkin, Y. V. Ivanov, H. Watanabe, N. Chikumoto, and S. Yamaguchi, "Temperature Distribution and Critical Current of Long HTS Cables Cooled with Subcooled Liquid Nitrogen," *J. Phys. Conf. Ser.*, vol. 871, no. 1, 2017.
- [216] E. P. Volkov, V. S. Vysotsky, and V. P. Firsov, "First Russian long length HTS power cable," *Phys. C Supercond. its Appl.*, vol. 482, pp. 87–91, 2012.
- [217] H. M. Chang, K. N. Ryu, and H. S. Yang, "Cryogenic design of liquid-nitrogen circulation system for long-length HTS cables with altitude variation," *Cryogenics (Guildf.)*, vol. 83, pp. 50–56, 2017.
- [218] A. S. Gour, M. Sarkar, S. Thadela, and V. V. Rao, "A novel instrumentation scheme based on cold electronics for testing of superconducting cable," *2017 3rd Int. Conf. Cond. Assess. Tech. Electr. Syst. CATCON 2017 - Proc.*, vol. 2018–Janua, pp. 188–190, 2018.
- [219] S. Pamidi, C. H. Kim, and L. Graber, *High-temperature superconducting (HTS) power cables cooled by helium gas*. Elsevier Ltd, 2015.
- [220] N. G. Suttell, J. V. C. Vargas, J. C. Ordonez, S. V. Pamidi, and C. H. Kim, "Modeling and optimization of gaseous helium (GHe) cooled high temperature superconducting (HTS) DC cables for high power density transmission," *Appl. Therm. Eng.*, vol. 143, no. August, pp. 922–934, 2018.
- [221] S. Pamidi, C. H. Kim, J. H. Kim, D. Crook, and S. Dale, "Cryogenic helium gas circulation system for advanced characterization of superconducting cables and other devices," *Cryogenics (Guildf.)*, vol. 52, no. 4–6, pp. 315–320, 2012.
- [222] R. S. Dondapati, J. Ravula, S. Thadela, and P. R. Usurumarti, "Analytical approximations for thermophysical properties of supercritical nitrogen (SCN) to be used in futuristic high temperature superconducting (HTS) cables," *Phys. C Supercond. its Appl.*, vol. 519, pp. 53–59, Dec. 2015.
- [223] M. Kalsia, R. S. Dondapati, and P. R. Usurumarti, "Statistical correlations for thermophysical properties of Supercritical Argon (SCAR) used in cooling of futuristic High Temperature Superconducting (HTS) cables," *Phys. C Supercond. its Appl.*, vol. 536, pp. 30–34, 2017.

- [224] R. K. Gadekula, V. R. Uppada, A. Kumar, and R. S. Dondapati, "Feasibility study on nano cryogenic coolant to be used in futuristic high temperature superconducting (HTS) cables," *Int. J. Mech. Eng. Technol.*, vol. 8, no. 7, pp. 1590–1598, 2017.
- [225] P. Anand, G. Vyas, R. S. Dondapati, and P. K. Seepana, "Feasibility studies on the use of cryogenics in HTS Cables," *Int. J. Mech. Eng. Technol.*, vol. 8, no. 7, pp. 1357–1361, 2017.
- [226] J. Lee *et al.*, "Investigation on cryogenic refrigerator and cooling schemes for long distance HTS cable," *IEEE Trans. Appl. Supercond.*, vol. 25, no. 3, pp. 7–11, 2015.
- [227] D. Kottonau, W. T. B. de Sousa, J. Bock, and M. Noe, "Design Comparisons of Concentric Three-Phase HTS Cables," *IEEE Trans. Appl. Supercond.*, vol. 29, no. 6, pp. 1–8, 2019.
- [228] E. Shabagin, C. Heidt, S. Strauß, and S. Grohmann, "Modelling of 3D temperature profiles and pressure drop in concentric three-phase HTS power cables," *Cryogenics (Guildf.)*, vol. 81, pp. 24–32, 2017.
- [229] S. Fuchino, M. Furuse, and N. Higuchi, "Longitudinal Temperature Distribution in Superconducting Power Cables with," *IEEE Trans. Appl. Supercond.*, vol. 12, no. 1, pp. 1339–1342, 2002.
- [230] D. Miyagi, R. Sakakibara, Y. Shinozaki, M. Tsuda, and T. Hamajima, "Suitable Cable Structure of HTS Triaxial Cable Cooled by Counter Flow Cooling Method for Long-Distance Power Transmission," *IEEE Trans. Appl. Supercond.*, vol. 28, no. 4, pp. 8–12, 2018.
- [231] S. Fuchino, N. Tamada, I. Ishii, and N. Higuchi, "Hydraulic characteristics in superconducting power transmission cables," *Phys. C Supercond. its Appl.*, vol. 354, pp. 125–128, 2001.
- [232] N. Hu, M. Toda, T. Watanabe, M. Tsuda, and T. Hamajima, "Recovery time analysis in a tri-axial HTS cable after an over-current fault," *Phys. C*, vol. 471, pp. 1295–1299, 2011.
- [233] T. Yasui *et al.*, "Temperature and pressure simulation of a 1.5-km HTS power cable cooled by Subcooled LN₂ with a fault current," *IEEE Trans. Appl. Supercond.*, vol. 26, no. 3, pp. 1–5, 2016.
- [234] J. F. Maguire, F. Schmidt, S. Bratt, T. E. Welsh, and J. Yuan, "Installation and testing results of long island transmission level HTS cable," *IEEE Trans. Appl. Supercond.*, vol. 19, no. 3, pp. 1692–1697, 2009.
- [235] O. Maruyama, T. Ohkuma, T. Izumi, and Y. Shiohara, "Numerical analysis of heat transfer and fluid characteristics of flowing liquid nitrogen in HTS cable," *Phys. Procedia*, vol. 58, pp. 330–333, 2014.
- [236] Y. Ivanov, H. Watanabe, M. Hamabe, T. Kawahara, J. Sun, and S. Yamaguchi, "Observation of the thermosiphon effect in the circulation of liquid nitrogen in HTS cable cooling system," *Phys. Procedia*, vol. 27, pp. 368–371, 2012.
- [237] Y. Ivanov *et al.*, "Compact counter-flow cooling system with subcooled gravity-fed circulating liquid nitrogen," *Phys. C Supercond. its Appl.*, vol. 470, no. 20, pp. 1895–1898, 2010.

- [238] S. Thadela, V. V. Rao, R. Agarwal, and R. S. Dondapati, "Computational investigation on thermohydraulic characteristics of High-Temperature Superconducting (HTS) power cables," *Phys. C Supercond. its Appl.*, vol. 559, pp. 25–31, Apr. 2019.
- [239] O. Maruyama and T. Mimura, "Fluid characteristic of liquid nitrogen flowing in HTS cable," *J. Phys. Conf. Ser.*, vol. 1054, no. 1, pp. 1–7, 2018.
- [240] Y. Sato, K. Agatsuma, X. Wang, and A. Ishiyama, "Temperature and Pressure Simulation of a High-Temperature Superconducting Cable Cooled by Subcooled LN₂ With Fault Current," *IEEE Trans. Applied Supercond.*, vol. 25, no. 3, p. 5401805, 2015.
- [241] Z. M. Li *et al.*, "Effect of corrugated characteristics on the liquid nitrogen temperature field of HTS cable," *AIP Conf. Proc.*, vol. 15, no. February, pp. 15–19, 2015.
- [242] R. S. Dondapati and V. V Rao, "Pressure Drop and Heat Transfer Analysis of Long Length Internally Cooled HTS Cables," *IEEE Trans. Appl. Supercond.*, vol. 23, no. 3, pp. 1–5, 2013.
- [243] Y. Ivanov, H. Watanabe, M. Hamabe, and T. Kawahara, "Design study of LN₂ circulation in a long SC power transmission lines," *Phys. Procedia*, vol. 36, pp. 1372–1377, 2012.
- [244] D. K. D. Koh, H. Y. H. Yeom, Y. H. Y. Hong, and K. L. K. Lee, "Performance tests of high temperature superconducting power cable cooling system," *IEEE Trans. Appl. Supercond.*, vol. 14, no. 2, pp. 1746–1749, 2004.
- [245] C. H. Lee, C. D. Kim, K. S. Kim, D. H. Kim, and I. S. Kim, "Performance of heat transfer and pressure drop in superconducting cable former," *Cryogenics (Guildf.)*, vol. 43, no. 10–11, pp. 583–588, Oct. 2003.
- [246] A. Sciacovelli, V. Verda, and E. Sciubba, "Entropy generation analysis as a design tool - A review," *Renew. Sustain. Energy Rev.*, vol. 43, pp. 1167–1181, 2015.
- [247] L. Martyushev, "Entropy and Entropy Production: Old Misconceptions and New Breakthroughs," *Entropy*, vol. 15, no. 4, pp. 1152–1170, 2013.
- [248] A. Bejan, *Advanced Engineering Thermodynamics*. Wiley, 1988.
- [249] A. Bejan, "Fundamentals of exergy analysis , entropy generation minimization , and the generation of flow architecture," *Int. J. ENERGY Res.*, vol. 565, no. January 2001, pp. 545–565, 2002.
- [250] A. Bejan, "Method of entropy generation minimization, or modeling and optimization based on combined heat transfer and thermodynamics," *Rev. Gen. Therm.*, vol. 35, no. 418–419, pp. 637–646, 1996.
- [251] E. Manay, E. F. Akyürek, and B. Sahin, "Entropy generation of nanofluid flow in a microchannel heat sink," *Results in Physics*, vol. 9, pp. 615–624, 2018.
- [252] J. Li and C. Kleinstreuer, "Entropy Generation Analysis for Nanofluid Flow in Microchannels," *J. Heat Transfer*, vol. 132, no. 12, p. 122401, 2010.
- [253] N. Sahiti, F. Krasniqi, X. Fejzullahu, J. Bunjaku, and A. Muriqi, "Entropy generation minimization of a double-pipe pin fin heat exchanger," *Appl. Therm.*

Eng., vol. 28, no. 17–18, pp. 2337–2344, 2008.

- [254] M. Arivazhagan and S. Lokeswaran, “Entropy generation minimization of shell and tube heat exchanger with porous medium,” *Exp. Tech.*, vol. 37, no. 5, pp. 74–82, 2013.
- [255] S. Genić, B. Jaćimović, and A. Petrovic, “A novel method for combined entropy generation and economic optimization of counter-current and co-current heat exchangers,” *Appl. Therm. Eng.*, vol. 136, pp. 327–334, 2018.
- [256] J. R. Trevizoli, Paulo Vinicius and Barbosa JR, “Entropy Generation Minimization Analysis of Active Magnetic Regenerators,” *An. Acad. Bras. Cienc.*, vol. 89, no. 1, pp. 717–743, 2017.
- [257] G. Türkakar, T. Okutucu-özyurt, and S. G. Kandlikar, “Entropy generation analysis of a microchannel-condenser for use in a vapor compression refrigeration cycle,” *Int. J. Refrig.*, vol. 70, pp. 71–83, 2016.
- [258] G. Türkakar and T. Okutucu-Ozyurt, “Entropy generation analysis and dimensional optimization of an evaporator for use in a microscale refrigeration cycle,” *Int. J. Refrig.*, vol. 56, pp. 140–153, 2015.
- [259] C. Seckin, “Thermodynamic analysis of a combined power/refrigeration cycle: Combination of Kalina cycle and ejector refrigeration cycle,” *Energy Convers. Manag.*, vol. 157, no. August 2017, pp. 631–643, 2018.
- [260] K. Thu, Y. D. Kim, A. Myat, W. G. Chun, and K. C. Ng, “Entropy generation analysis of an adsorption cooling cycle,” *Int. J. Heat Mass Transf.*, vol. 60, no. 1, pp. 143–155, 2013.
- [261] D. Aparecida *et al.*, “Diagrams of entropy for ammonia – water mixtures : Applications to absorption refrigeration systems,” *Int. J. Refrig.*, vol. 82, pp. 335–347, 2017.
- [262] A. J. White, J. D. Mctigue, and C. N. Markides, “Analysis and optimisation of packed-bed thermal reservoirs for electricity storage applications,” *J. Power Energy*, vol. 230, no. 7, pp. 1–19, 2016.
- [263] S. V Garimella, “Second-Law Analysis of Molten-Salt Thermal Energy Storage in Thermoclines,” *Sol. Energy*, vol. 86, no. 5, pp. 1621–1631, 2012.
- [264] A. Pizzolato, A. Sciacovelli, and V. Verda, “Transient local entropy generation analysis for the design improvement of a thermocline thermal energy storage,” *Appl. Therm. Eng.*, vol. 101, pp. 622–629, 2016.
- [265] Y. Bi, T. Guo, L. Zhang, L. Chen, and F. Sun, “Entropy generation minimization for charging and discharging processes in a gas-hydrate cool storage system,” *Appl. Energy*, vol. 87, no. 4, pp. 1149–1157, 2010.
- [266] E. Guelpa, A. Sciacovelli, and V. Verda, “Entropy generation analysis for the design improvement of a latent heat storage system,” *Energy*, vol. 53, pp. 128–138, 2013.
- [267] R. Laskowski, A. Smyk, J. Lewandowski, A. Rusowicz, and A. Grzebielec, “Selecting the cooling water mass flow rate for a power plant under variable load with entropy generation rate minimization,” *Energy*, vol. 107, pp. 725–733, 2016.
- [268] S. C. Kaushik, V. S. Reddy, and S. K. Tyagi, “Energy and exergy analyses of

- thermal power plants: A review,” *Renew. Sustain. Energy Rev.*, vol. 15, no. 4, pp. 1857–1872, 2011.
- [269] Y. Haseli, “Efficiency improvement of thermal power plants through specific entropy generation,” *Energy Convers. Manag.*, vol. 159, no. July 2017, pp. 109–120, 2018.
- [270] J. J. Ramírez-Minguela *et al.*, “Comparison of the thermo-hydraulic performance and the entropy generation rate for two types of low temperature solar collectors using CFD,” *Sol. Energy*, vol. 166, no. March, pp. 123–137, 2018.
- [271] M. Charjouei Moghadam, M. Edalatpour, and J. P. Solano, “Numerical Study on Conjugated Laminar Mixed Convection of Alumina/Water Nanofluid Flow, Heat Transfer, and Entropy Generation Within a Tube-on-Sheet Flat Plate Solar Collector,” *J. Sol. Energy Eng.*, vol. 139, no. 4, p. 41011, 2017.
- [272] O. Mahian, A. Kianifar, A. Z. Sahin, and S. Wongwises, “Heat Transfer, Pressure Drop, and Entropy Generation in a Solar Collector Using SiO₂/Water Nanofluids: Effects of Nanoparticle Size and pH,” *J. Heat Transfer*, vol. 137, no. 6, p. 61011, 2015.
- [273] M. A. Alim, Z. Abdin, R. Saidur, A. Hepbasli, M. A. Khairul, and N. A. Rahim, “Analyses of entropy generation and pressure drop for a conventional flat plate solar collector using different types of metal oxide nanofluids,” *Energy Build.*, vol. 66, pp. 289–296, 2013.
- [274] R. S. Dondapati, “Role of Supercritical Nitrogen (SCN) on the hydraulic and thermal characteristics of futuristic High Temperature Superconducting (HTS) cables,” *Cryogenics (Guildf.)*, vol. 111, no. May, p. 103166, 2020.
- [275] J. Li, L. Zhang, X. Ye, F. Xia, Y. Cao, and A. C. F. Design, “Demonstration Project of 35 kV / 1 kA Cold Dielectric High Temperature Superconducting Cable System in Tianjin,” *IEEE Trans Appl. Supercond.*, vol. 30, no. 2, p. 5400205, 2020.
- [276] W. Pi, Q. Yang, Q. Shi, and Y. Wang, “Insulation Design for 10 kV Three-Phase Concentric High-Temperature Superconducting Cable,” *IEEE Trans Appl. Supercond.*, vol. 30, no. 4, p. 4800405, 2020.
- [277] R. S. Dondapati and V. V. Rao, “Parametric studies on entropy generation rate in dual channel cable-in-conduit conductors (CICCs) with supercritical helium (SHe) using computational fluid dynamics,” *Fusion Eng. Des.*, vol. 142, no. April, pp. 63–69, 2019.
- [278] S. Lee, H. Sung, M. Park, D. Won, J. Yoo, and H. S. Yang, “Analysis of the Temperature Characteristics of according to a Liquid Nitrogen Circulation Method for Real-Grid Application in Korea,” *Energies*, vol. 12, no. 1740, pp. 1–11, 2019.
- [279] C. Lee, D. Kim, S. Kim, D. Y. Won, and H. S. Yang, “Thermo-Hydraulic Analysis on Long Three-Phase Coaxial HTS Power Cable of Several Kilometers,” *IEEE Trans Appl. Supercond.*, vol. 29, no. 5, p. 5402805, 2019.
- [280] M. Kalsia and R. S. Dondapati, “Influence of corrugation topology on thermohydraulic performance of cold dielectric counter cooled High Temperature Superconducting cable,” *Phys. C Supercond. its Appl.*, vol. 566, no. November, p. 1353525, 2019.

- [281] C. Peng *et al.*, “Insulation Characteristics of Dielectric Material for CD HTS Cable,” *IEEE Trans Appl. Supercond.*, vol. 29, no. 2, p. 7700405, 2019.
- [282] M. Kalsia and R. S. Dondapati, “Thermohydraulic analysis of cold dielectric high temperature superconducting cable with counter-flow cooling,” *Phys. C Supercond. its Appl.*, vol. 564, no. June, pp. 59–67, 2019.
- [283] S. Thadela, V. V. Rao, R. Agarwal, and R. S. Dondapati, “Computational investigation on thermohydraulic characteristics of High Temperature Superconducting (HTS) power cables,” *Phys. C Supercond. its Appl.*, vol. 559, no. April, pp. 25–31, 2019.
- [284] M. Kalsia and R. S. Dondapati, “Influence of Flow Rate and Heat Flux on the Temperature Distribution in Long Length Counter Flow Cooled Cold Dielectric HTS Cables,” *Phys. C Supercond. its Appl.*, vol. 567, no. December, p. 1353549, 2019.
- [285] P. Anand, R. K. Gadekula, U. V. Ramana, and R. S. Dondapati, “Effect of Diameter of Nanoparticles on the thermophysical properties of LN 2 based Cryocoolants,” *Mater. Today Proc.*, vol. 5, no. 14, pp. 28279–28287, 2018.
- [286] W. T. B. De Sousa, J. Bock, and M. Noe, “Investigation of a Concentric Three-Phase HTS Cable Connected to an SFCL Device,” *IEEE Trans Appl. Supercond.*, vol. 28, no. 4, p. 5400105, 2018.
- [287] D. Miyagi, S. Yamashita, and N. Takahashi, “Study of AC Loss Characteristics of HTS-coated Conductor with Magnetic Substrate Using FEM Analysis,” pp. 43–48, 2011.
- [288] A. Bejan, *Convection heat transfer, Fourth edition*. 2013.
- [289] O. B. Adeyinka and G. F. Naterer, “Modeling of Entropy Production in Turbulent Flows,” *J. Fluids Eng.*, vol. 126, no. November 2004, pp. 893–899, 2016.
- [290] Y. V Ivanov, H. Watanabe, M. Hamabe, J. Sun, T. Kawahara, and S. Yamaguchi, “Circulation pump power for 200 m cable experiment,” *Phys. C Supercond. its Appl.*, vol. 471, no. 21–22, pp. 1308–1312, 2011.
- [291] E. W. Lemmon, M. L. Huber, and M. O. McLinden, *NIST Reference Fluid Thermodynamic and Transport Properties — REFPROP*. 2013.
- [292] *ANSYS-Fluent Theory Guide*. Canonsburg, PA: Ansys Inc, 2013.
- [293] H. K. Versteeg and W. Malalasekera, *An Introduction to Computational Fluid Dynamics*, 2nd ed. Pearson Education, 2007.
- [294] M. J. S. De Lemos and R. A. Silva, “Turbulent flow over a layer of a highly permeable medium simulated with a diffusion-jump model for the interface,” *Int. J. Heat Mass Transf.*, vol. 49, no. 3–4, pp. 546–556, 2006.
- [295] M. Pisarenco, B. van der Linden, A. Tijsseling, E. Ory, and J. Dam, “Friction Factor Estimation for Turbulent Flows in Corrugated Pipes with Rough Walls,” *J. Offshore Mech. Arct. Eng.*, vol. 133, no. 1, p. 11101, Feb. 2011.
- [296] H. Herwig, D. Gloss, and T. Wenterodt, “A new approach to understanding and modelling the influence of wall roughness on friction factors for pipe and channel flows,” *J. Fluid Mech.*, vol. 613, pp. 35–53, Oct. 2008.

- [297] R. S. Dondapati and V. V. Rao, “Entropy generation minimization (EGM) to optimize mass flow rate in dual channel cable-in-conduit conductors (CICCs) used for fusion grade magnets,” *Fusion Eng. Des.*, vol. 89, no. 6, pp. 837–846, 2014.
- [298] R. K. Gadekula and R. S. Dondapati, “Entropy Generation Minimization (EGM) in High Temperature Superconducting (HTS) cables for Optimization of Thermohydraulic Performance,” *Phys. C Supercond. its Appl.*, vol. 566, p. 1353541, 2019.
- [299] M. Bahiraei, M. Jamshidmofid, M. Amani, and R. Barzegarian, “Investigating exergy destruction and entropy generation for flow of a new nanofluid containing graphene–silver nanocomposite in a micro heat exchanger considering viscous dissipation,” *Powder Technol.*, vol. 336, pp. 298–310, 2018.
- [300] A. Bejan, “Entropy generation minimization: The new thermodynamics of finitesize devices and finitetime processes,” *J. Appl. Phys.*, vol. 79, no. 3, pp. 1191–1218, 1996.
- [301] G. Giangaspero and E. Sciubba, “Application of the entropy generation minimization method to a solar heat exchanger: A pseudo-optimization design process based on the analysis of the local entropy generation maps,” *Energy*, vol. 58, pp. 52–65, 2013.
- [302] A. Bejan, “Fundamentals of exergy analysis, entropy generation minimization, and the generation of flow architecture,” *Int. J. Energy Res.*, vol. 26, no. 7, pp. 545–565, 2002.
- [303] A. Bejan, “Study of Entropy Generation in Fundamental Convective Heat Transfer,” *J. Heat Transfer*, vol. 101, no. 4, pp. 718–725, 1979.
- [304] A. Bejan, *Entropy generation minimization: the method of thermodynamic optimization of finite-size systems and finite-time processes*. Boca Raton: CRC Press., 1996.
- [305] A. Bejan, *Entropy generation through heat and fluid flow*. New York: Wiley, 1982.
- [306] E. Manay, E. F. Akyürek, and B. Sahin, “Entropy generation of nanofluid flow in a microchannel heat sink,” *Results Phys.*, vol. 9, pp. 615–624, 2018.
- [307] R. S. Dondapati and V. V. Rao, “Parametric studies on entropy generation rate in dual channel cable-in-conduit conductors (CICCs) with supercritical helium (SHe) using computational fluid dynamics,” *Fusion Eng. Des.*, vol. 142, pp. 63–69, 2019.

10 PUBLICATIONS FROM PRESENT WORK

- 1) R. K. Gadekula, R. S. Dondapati, “Investigation on the thermohydraulic performance of high temperature superconducting (HTS) cables with heat loads using Entropy Generation Minimization (EGM) approach,” *Phys. C Supercond. its Appl.*, vol. 571, 1353618, 2020.
- 2) R. K. Gadekula, R. S. Dondapati, “Influence of thermohydraulic irreversibilities on the efficiency of high temperature superconducting (HTS) cables,” *Phys. C Supercond. its Appl.*, vol. 572, 1353634, 2020.
- 3) R. K. Gadekula, R. S. Dondapati, “Entropy Generation Minimization (EGM) in High Temperature Superconducting (HTS) cables for Optimization of Thermohydraulic Performance,” *Phys. C Supercond. its Appl.*, vol. 566, 1353541, 2019.
- 4) R. K. Gadekula and R. S. Dondapati, “Numerical solution for the effect of variable viscosity on non-newtonian fluid,” *JP J. Heat Mass Transf.*, vol. 18, no. 1, pp. 225–232, 2019.
- 5) R. K. Gadekula and R. S. Dondapati, “Analytical solution on entropy generation in a pipe due to non-newtonian fluid flow,” *JP J. Heat Mass Transf.*, vol. 17, no. 2, pp. 443–450, 2019.

11 VITAE

Gadekula Rajesh Kumar is a research scholar pursuing PhD from Lovely Professional University in School of Mechanical Engineering, Punjab in the field of Superconductivity and its applications. He is also working as a research assistant of a sponsored project funded by Central Power Research Institute (CPRI), Bangalore on the development of superconducting magnetic energy storage devices through funding scheme RSOP. He is graduated from Annamacharya Institute of Technology and Sciences (AITS), Department of Mechanical Engineering, Rajampet in 2014. Later, he pursued post graduation from Lovely Professional University in School of Mechanical Engineering, Punjab in 2016. He received gold medal, academic honor and academic topper from Honorable President of India Sri Pranab Mukarjee in 8th Convocation of LPU for his remarkable grades in academics. He worked as an Assistant Professor in Annamacharya Institute of Technology and Sciences (AITK), Kadapa, Andhra Pradesh and in Lovely Professional University (LPU), Phagwara, Punjab. He is a member of Institute of Electrical and Electronics Engineering (IEEE). He has published a number of technical papers in prestigious journals, book chapter and participated in number of international conferences in the field of Superconductivity, Nano fluids, cryogenics, materials and refrigeration.